Scribe Marks at Fuselage Joints: Determination of Residual Stress and Effects of Fatigue Loading Using Nanoindentation and Snychrotron X-Ray Diffraction

Thesis

The Open University
Department of Materials Engineering
Faculty of MCT

Scribe Marks at Fuselage Joints- Determination of Residual Stress and Effects of Fatigue Loading using Nanoindentation and Synchrotron X-ray Diffraction

October 2009

A thesis submitted to The Open University for the degree of Doctor of Philosophy in the Department of Materials Engineering

By
Muhammad Kashif Khan

DATE OF SUBMISSION: 27.OCT 2009
DATE OF AWARD: 12 FEB 2010

ProQuest LLC.
789 East Eisenhower Parkway
P.O. Box 1346
Ann Arbor, MI 48106 – 1346

Abstract

Empirical understanding of fatigue crack growth from small defects is of tremendous importance and of significant concern for structural integrity of aerospace structures. In fatigue, a crack initiates from a stress concentration location and causes premature failure. In principle fatigue life for scribes and scratches is function of the stress concentration around the root which depends upon the depth and root radius of the scribe, the associated microstructure, the residual stress field, work hardening from plastic deformation during scribing and relaxation or redistribution of these residual stresses in fatigue. The scope of the present work is on determination of the residual stress field around scribe marks of different geometries and the effect of fatigue loading on the residual stress field.

The determination of a local residual stress field in a small area of 100 μm x 100 μm around shallow scribes (<150 μm deep) is a very challenging engineering problem. Additionally, the large grain size of Al 2024-T351 (~20 μm), anisotropy between grains and texture makes further difficulties.

The residual stress field associated with scribes of different geometries produced by different tools has been measured using synchrotron X-ray diffraction. It was found that some tools produce a severe tensile stress field and work hardening around the root of scribe as compared to the other tools which also produce a tensile residual stress field but without work hardening.

Additionally, a method of extraction of residual stress has been developed using the nanoindentation load-displacement data. The method has been applied to extract residual stresses while taking into account the plastic deformation around scribe roots. The residual stress field of twenty nine scribes of different geometries produced from different tools has been determined from the nanoindentation method. Depending upon the tool and root radius, residual stresses were different in magnitude and were found in the range of +100MPa to +200MPa.

The effect of fatigue loading on the relaxation of pre-existing residual stresses was studied. It was found that stress field around scribes is not affected by fatigue loading.

It was concluded that fatigue life of these scribes should be examined with consideration of residual stresses. Any crack initiation and propagation model without consideration of residual stress fields may predict more conservative lives in fatigue.

Acknowledgements

This period of three years (35 months in reality) of my PhD has been a tiring but satisfied period of my life in which I earned a unique experience of working outside my country for the first time in my life. I would like to acknowledge Airbus Deutschland for funding this project. My earnest thanks and sincere gratitude to my supervisors, Prof. Mike Fitzpatrick and Lyndon Edwards. Efforts of Dr. Domenico Furfari from Airbus Deutschland for funding the project and arranging the quarterly progress review meetings are duly acknowledged. I would also like to thanks to Prof. Phil Irving of Cranfield University for providing scribe samples and comments about my work in each review meeting. I would also like to thanks to Prof. Sarah Hainsworth of Leicester University for showing special interest in nanoindentation testing and for providing expert comments. Without constant support, guidance and encouragement of all these people this work would not have been possible.

I would also like to thanks ESRF, Grenoble, France for allocating me beam time at ID31 and help during experiments from beam line scientist Dr. Alex. Evans is also acknowledged.

My sincere thanks to staff of Materials Engineering, Ian Norman, Peter Ledgard, Gordon Imlach and Stan Hiller for their help, support and useful discussions in Nanoindentation testing, fabrication of experimental fixtures, microscopy, specimen preparation and metallography.

I wish to acknowledge all other students, members and staffs in Materials Engineering Department for their friendship and support during all these three years.

Finally my deepest regards to my sisters and deceased parents who taught me the basic principles, "consistency, hardworking and honesty" which turned out keys of my success in every walk of life whether I work, study or play cricket.

I give my final regards to my wife for providing me never ending support during my PhD and for giving me the best gift I have ever had, my daughter "Aamna Khan". I entirely dedicate this thesis to my parents, sisters, wife and daughter.

Preface

This thesis is submitted for the degree of Doctor of Philosophy of The Open University. The work described in this dissertation was carried out in the Department of Materials Engineering of the Faculty of Technology, between December 2006 and October 2009, under the supervision of Prof. M. E. Fitzpatrick and Prof. L. Edwards.

It is an original work of the author except where reference is made to the work of others. None of this work is submitted or is in the process of submission in whole or part for a degree at any other university. Some of the results of this work have been published or about to be published in academic journals and conference proceedings as listed below:

1 - Khan, M. K., S. V. Hainsworth, M. E. Fitzpatrick and L. E. Edwards. Application of the work of indentation approach for the characterization of aluminium 2024-T351 and Al cladding by nanoindentation. Journal of Materials Science, 44(4), 2009, pp 1006-1015.

2 - Khan, M. K., M.E. Fitzpatrick., S. V. Hainsworth and L.E. Edwards. Effect of tool profile and fatigue loading on the local hardness around scratches in clad and unclad aluminium alloy 2024. Materials Science and Engineering A, Volume 527, Issues 1-2, 2009, pp 297-304.

3 - Khan, M. K, M. E. Fitzpatrick, S. V. Hainsworth, L.E. Edwards. Determination of Elastic-plastic and Nanoindentaion properties from Finite Element Analysis. (To be published)

4 - Khan, M. K, M. E. Fitzpatrick, S. V. Hainsworth, L.E. Edwards. Effect of Residual Stress on Nanoindentation Properties of Al 2024-T351 and cladding. (To be published)

5 - Khan, M. K, M. E. Fitzpatrick, S. V. Hainsworth, L.E. Edwards. Determination of Residual Stress around small scale damage in Al-alloys from Synchortron X-rays and Nanoindentation. (To be published)

6 - Khan, M. K, M. E. Fitzpatrick, S. V. Hainsworth, L.E. Edwards. Determination of Residual Stress Field around Scratches using Synchrotron X-rays and Nanoindentation.

Proceedings of the 5th International Conference on Mechanical Stress Evaluation by Neutrons and Synchrotron Radiation, MECA SENS 5, November 2009, Mito, Japan. Published in Materials Science Forum

Muhammad Kashif Khan

October 2009.

Contents

Abstract
Acknowledgements
Preface
Contents
List of notations

Chapter 1: Introduction

1.1 Description of Problem---------- 01
1.2 Scope of This Work---------- 03
1.3 References---------- 05

Chapter 2: Literature Review

2.1 Scribe Marks---------- 06
2.1.1 What are Scribe Marks? ---------- 06
2.1.2 How Scribe Marks are Simulated for Laboratory tests---------- 07
2.1.3 How Different Types of Scribes can be Produced---------- 07
2.2 Fatigue Life of Scribes---------- 10
2.2.1 Role of Residual Stresses in Prediction of Fatigue Life---------- 13
2.3 Measurement of Residual Stresses---------- 16
2.3.1 Methods of Residual Stress Measurement---------- 16
2.3.1.1 Hole Drilling ---------- 17
2.3.1.2 Contour Method ---------- 17
2.3.1.3 Ultrasonic Method---------- 18
2.3.1.4 Magnetic Methods---------- 19
2.3.1.5 Diffraction Methods---------- 19
2.3.1.6 Principle & Methods of Synchrotron X-ray Diffraction---------- 21
2.4 Nanoindentation---------- 24
2.5 Conclusions---------- 25
2.6 References---------- 26

Chapter 3: Characterization of Aluminium-clad and Al 2024-T351 by Nanoindentation

3.1 Introduction---------- 30
3.2 Theoretical Background---------- 32
3.2.1 Oliver and Pharr Method (O-P) ---------- 32
3.2.2 Correction with Atomic Force Microscopy (AFM) ---------- 35
3.2.3 Work of Indentation---------- 36
3.3 Materials and Experimental Method---------- 38
3.3.1 Material Details---------- 38
3.3.2 Surface Roughness---------- 42
3.3.3 Experimental Method---------- 44
3.4 Results and Discussion---------- 45
3.4.1 Characterization from Oliver and Pharr Model---------- 45
3.4.2 Pile-Up Formation and AFM Scanning---------- 47
3.4.3 Calculation of Area ---------- 50
3.4.4 Difference in Elastic Recovery of Al-clad and Al2024-T351--- 53
3.4.5 Anisotropy and Texture---------- 55

3.5 Hardness Comparison from Different Approaches---- 63
3.6. Conclusions---- 66
3.7 References---- 67

Chapter 4: Local Hardness around Scribe Marks of Different Root radii Produced from Different Tools
4.1 Introduction---- 70
4.2 Materials and Experimental Details---- 71
4.2.1 Material Details---- 71
4.2.2 Introduction of Scribes---- 71
4.2.3 Nanoindentation Testing---- 74
4.2.4 Fatigue Testing---- 75
4.3 Results and Discussion---- 76
4.3.1 Profiles of 5 μm Root Radius Scribe---- 76
4.3.2 Scribes with 25 & 50 μm Root Radius---- 80
4.3.3 Hardness Maps around Scribes of 5 μm Root Radius---- 81
4.3.4 Hardness profiles around Scribes of 25 & 50 μm Root Radius---- 86
4.3.5 Effect of Fatigue on Hardness Environment---- 93
4.4 Conclusions---- 98
4.5 References---- 98

Chapter: 5 Finite Element Analysis of Nanoindentation Properties of Al 2024-T351 and Al-cladding

5.1 Introduction---- 102
5.2 Material Properties and Finite Element Simulation Procedure---- 104
5.2.1 Materials Properties---- 104
5.2.2 Finite Element Simulation Procedure---- 104
5.3 Results and Discussion---- 107
5.3.1 Forward Analysis on Al 2024-T351---- 107
5.3.1.1 Comparison of Nanoindentation Properties ---- 108
5.3.1.2 Pile-up Characterization---- 110
5.3.2 - Reverse analysis on Al-cladding---- 112
5.3.2.1 - Indentation Load-displacement Curve---- 114
5.3.2.2 - Error Analysis---- 115
5.4 Conclusions---- 127
5.5 References---- 128

Chapter 6: Effect of Residual Stress on Nanoindentation Response of Al-cladding and Al 2024-T351

6.1 Introduction---- 131
6.2 Materials, Experimental and Finite Element Simulation Details---- 133
6.2.1 Materials Details---- 133
6.2.2 Experimental Details---- 133
5.2.3 Finite Element Simulation Details---- 134
6.3 Results and Discussion---- 137
6.3.1 Experimental Investigation---- 137
6.3.1.1 Uniaxial Stresses---- 137
6.3.1.2 Biaxial Stresses---- 138

6.3.2 Investigation through Finite Element Simulation---------- 141
6.3.2.1 Effect on Load-displacement Curve---------- 142
6.3.2.2 Effect on Loading Curve---------- 143
6.3.2.3 Effect on Unloading Curve---------- 145
6.3.2.4 Effect on Pile-up---------- 147
6.3.2.5 Effect on Contact Area---------- 149
6.3.3 Empirical Model for Estimation of Residual Stress---------- 151
6.4 Conclusions---------- 153
6.5 References---------- 154

Chapter 7: Measurement of Strain and Stress Fields and Local Hardening around Scribe Marks of Different Geometries in Aluminium alloy 5091 and 2024-T351

7.1 Introduction---------- 157
7.2 Materials, Specimen and Experimental Details---------- 159
7.2.1 Materials Details---------- 159
7.2.2 Specimen Details---------- 159
7.2.3 Experimental Setup---------- 160
7.3. Results and Discussion---------- 164
7.3.1 Residual Strains from Synchrotron X-ray Diffraction---------- 164
7.3.1.1 Sample 1---------- 165
7.3.1.2 Sample 2---------- 168
7.3.1.3 Sample 3---------- 171
7.3.1.4 Sample 4---------- 173
7.3.2 Stress Analysis---------- 174
7.3.2.1 Plane Strain Condition---------- 174
7.3.2.2 Plane Stress---------- 179
7.3.3 Peak Width Analysis---------- 183
7.4. Discussion---------- 189
7.4.1. Relation between Components of Strain & Stress---------- 189
7.4.2. Effect of Tool---------- 190
7.4.3. Effect of Material---------- 192
7.4.4. Effect of Root Radius---------- 192
7.5 Conclusions---------- 193
7.6 References---------- 194

Chapter 8: Determination of residual stress around scribe marks from nanoindentation

8.1 Introduction---------- 197
8.2 Materials, Samples and Experimental Details---------- 200
8.2.1 Materials and Sample Details---------- 202
8.2.2 Experimental Details---------- 200
8.3 Load-displacement Curve Analysis---------- 201
8.3.1 Sample 1---------- 201
8.3.2 Sample 2---------- 204
8.3.3 Sample 3---------- 206

8.3.4 Sample 4---------- 208
8.4 Determination of Residual Stresses from Load-displacement Curve------- 210
8.4.1 The Method---------- 210
8.4.2 Assumptions and Limitations---------- 215
8.4.3 Application on scribes---------- 219
8.4.3.1 Sample 1 to 4---------- 219
8.5 Extraction of Residual Stresses on Further Scribes---------- 220
8.5.1 Scribes from tool A and B (5um root radius) ---------- 221
8.5.2 Scribes from tool C and D (25 and 50 μm root radius) ---------- 223
8.6 Effect of Fatigue on Residual Stress---------- 225
8.6.1 Scribes from Tool A and B (5um root radius) ---------- 226
8.7 Conclusions---------- 227
8.8 References---------- 228

Chapter 9: Overall Conclusions and Suggestions for Future Work

9.1 Conclusions---------- 230
9.2 Future Work---------- 232
9.3 References---------- 233

List of Notations

{hkl}	Miller indices describing a family of planes
a	Lattice parameter
a_0	Lattice parameter without strain
a_i	Length of pile-up lobe
A	Area of contact
$A_{O\text{-}P}$	Area form Oliver-Pharr model
A_{PU}	Area with pile-up
A_c	Area of contact
$A_{c'}$	Area of contact with pile-up
β	Indenter's constant
B	Fitting parameter
C	Speed of light
d	Depth of scribe
d	Lattice spacing
d_0	Lattice spacing of unstressed crystals
ε	Constant for indenter's geometry
ε	Strain
ε_{xx}	Strain in x-direction
ε_{yy}	Strain in y-direction
ε_{zz}	Strain in z-direction
e_1, e_2, e_3, e_3	Error
E	Energy of Photon
E	Elastic modulus
E_r	Reduced modulus
E_i	Modulus of Indenter
E_s	Modulus of sample
ϕ	Correction factor
h	Plank's constant
h	Depth of indentation
h_e	Elastic depth of indentation
h_f	Final depth of indentation
h_c	Contact depth of indentation
H	Hardness
k	Stress ratio
λ	Wavelength of incident monochromatic beam
m	Power law fitting parameter
n	Integer
n	Strain hardening
υ	Frequency of beam
ν	Poisson's ratio
ν_i	Poisson's ratio of indenter
ν_s	Poisson's ratio of sample
P	Load of indentation
P_{max}	Maximum load of indentation
ρ	Root radius of scribe
S	Stiffness
σ_r	Residual stress

σ_{xx}	Stress in y-direction
σ_{yy}	Strain in y-direction
σ_{zz}	Stress in z-direction
σ_Y	Yield stress
θ	Angle
$2\theta_0$	Angle between incident abeam and the diffracted beam
W_p	Plastic work
W_t	Total work
W_e	Elastic work
w	Width of scribe

Chapter 1: Introduction

1.1 Description of Problem

Empirical understanding of fatigue crack growth from small defects is of tremendous importance for structural integrity of aerospace structures. In fatigue, a crack initiates from a stress concentration location and propagates under cyclic loading. In principle the fatigue life for scribes or scratches is a function of the stress concentration around the root which depends upon the depth and root radius of the scribe, the associated microstructure, residual stress field, work hardening from plastic deformation during scribing and relaxation or redistribution of these residual stresses in fatigue. Several investigations have been done in the past to address the issues associated with stress concentration and microstructural distortion around small damages but thorough understanding of the effect of residual stress around scribe marks and scratches is yet to be obtained.

There are many circumstances which could cause a scratch on an airframe but the most likely source of scratching is removing aircraft paint and sealant with sharp scriber tools. A maintenance task such as a re-paint or structural repair could necessitate the need to remove sealant from the exterior of the lap splice. Such a task would normally be performed manually using some form of sealant scribing. This scribing process may put scratches or marks that are not easily detected. These sharp tools produced scratches and such marks are called scribes.

The existence of unmonitored scribes on the structure of a large portion of an aircraft act as stress concentration areas and are declared as potential fatigue crack initiation points. In 2003 two Boeing 737 aircraft were found with cracks emanating from scribe lines, one of which had two cracks in adjacent bays [1]. The scratches found ranged in size from 25-150 μm. As a result of the inspections, numerous other aircraft were found with similar damage including two 747 aircraft with 30 inch cracks in butt joints. In November 2003 a

Flight Standard Bulletin for Airworthiness FSAW 03-10B was issued by Boeing, entitled: Fuselage Skin "Scribe Mark" Damage on Boeing 737 Aircraft [1]. This bulletin reports about damages along fuselage skin lap joints, butt joints, and other areas of several aircraft. These damages appear to have been caused by the use of sharp tools used during paint and sealant removal (possibly made of metal, certain woods or hard plastic material) for removal of the sealants at the structural joints in the skin during the repainting process. This use of sharp instruments can result in lines scribed in the fuselage skin. Components with scribe marks cannot be treated as pristine and there may be degradation in life promoted by the defect. So characterization of fatigue lives of scribes of different geometries and depths is of significant importance for the aerospace engineering community. There are countless ways by which scribes can be produced in service but previous research on this topic has generally investigated sharp scratches or scribes which were considered most likely to propagate in fatigue due to sufficient stress concentration around root. All of those scribes can be characterized solely by parameters such as depth, included angle and root radius. Tools used in studies for creating scribes have been rigid steel or cutting tools.

The distribution of damage controls the initiation and early growth of fatigue cracks from scribe marks. Under fatigue, residual stresses are responsible for changing mean stress value and thus accelerate the crack growth if they are tensile or retard crack growth if compressive. Unfortunately the ability to measure local residual stress-strain fields around the scribes is a difficult experimental problem in view of the presence of high stress gradients around the scribe root. To probe these local residual stress fields experimental techniques are required that have spatial resolution of the order of few microns for which synchrotron X-ray diffraction is an ideal technique. Synchrotron X-ray methods are well suited to the investigation of residual stresses in the near-surface regions of engineered components. High intensity and low divergence allows small gauge volumes to be defined in order to study stress fields existing over a range of several hundred microns.

In this study scribes have been produced with diamond-tip cutting tools of root radii 5, 25 and 50 μm.

1.2 Scope of This Work

This thesis will focus on development of a method to measure residual stresses around scribe marks on Al 2024-T351 with and without cladding. This will take into account the effect of the tool with which the scribes were produced along with the depth and root radius of the scribe. It will discuss the development of the technique to measure residual stresses from nanoindentation and subsequently validation of measurement results with synchrotron X-ray diffraction.

The thesis will examine the plastic deformation around scribe marks produced by different tools and the effect of this plastic deformation on method developed for extraction of residual stresses using nanoindentation data will be reported.

Chapter 2 reviews the current literature available relevant to this thesis and explains the type of scribe marks that can be created. It discusses the efforts that have been made in earlier studies towards fatigue life prediction of scratches and scribe marks.

Chapter 3 discusses the characterization of Al 2024-T351 and Al-cladding from nanoindentation. The chapter explains the procedure of getting true mechanical properties including hardness and elastic modulus from nanoindentation load-displacement curves. The study is supported by atomic force microscopy (AFM) and scanning electron microscopy (SEM).

Chapter 4 discusses the type of scribe marks that have been studied in this project. Different scribe marks from 50 to 150 μm of depth and 5 to 50 μm root radius have been

studied and subsequently their local hardness has been reported. This includes investigation of effect of fatigue loading on the hardness around scribes as well.

Chapter 5 explains the development of the finite element model for nanoindentation for Al 2024-T351 and Al cladding. It explains forward and reverse analysis techniques to extract the nanoindentation properties from load-displacement curves from simulation and comparison with experimental results.

Chapter 6 explains the effect of residual stresses on nanoindentation properties. It provides detail about experimental and finite element simulations results for the effect of residual stresses on nanoindentation properties. A methodology has been developed to obtain the correct area of contact from nanoindentation load-displacement data rather than from AFM. Based on true contact area results, an empirical relation has been developed to calculate the residual stresses.

Chapter 7 investigates residual stress fields around scribes using synchrotron X-ray radiation. The chapter discusses the experimental set-up, the significance of the model alloy used and its relevance to the in-service alloy. Residual stress fields around scribes produced from different tools have been investigated and a correlation has been developed for two tools which produced 5 μm root radius scribes.

The chapter also discusses the peak width data from synchrotron X-rays for explanation of plasticity present around scribe roots, which have been validated by nanoindentation hardness measurements.

Chapter 8 discusses application of the developed technique in chapter 6 to residual stress measurement around scribes. Firstly, results of residual stress measurement from the nanoindentation method have been validated using synchrotron X-rays. In the later part of

the chapter, nanoindentation method has been applied for other scribes for which synchrotron data was not available.

The effect of fatigue loading on residual stresses around scribe marks has been investigated as well in this chapter. Two types of mode of fatigue loading have been investigated.

Chapter 9 includes a summary of the investigations carried out in this work and suggestions for further work.

1.3 References

[1] Federal Aviation Authority. Flight Standards Information Bulletin for Airworthiness (FSAW): 03-10B Fuselage Skin "Scribe Mark" Damage on Boeing 737 Aircraft. Effective 20 November 2003, amended 31 March 2004.

Chapter 2: Literature review

2.1 Scribe Marks

2.1.1 What are Scribe Marks?

Degradation processes in terms of mechanical damage, corrosion and fatigue affect service lives of aircraft. During service the damage due to these processes increases continuously. In service life, scratches and corrosion pits on fuselage structural areas may turn into propagating cracks owing to the use of structural materials in thin highly stressed sections to reduce fuel consumption. There are many circumstances which could cause a scratch on an airframe but a typical instance is removing aircraft paint and sealant with sharp scriber tools. A maintenance task such as a re-paint or structural repair could necessitate the need to remove sealant from the exterior of the lap splice. Such a task would normally be performed manually using some form of sealant scribing. The tools used for removal of sealant and paints are normally of sharp geometries with material harder than aluminium. This scribing process may put scratches or marks that are not easily detected. These sharp tools produced scratches and marks are called scribes.

Fig. 2.1 - Scribe mark on a fuselage [29]

2.1.2 How Scribe Marks are Simulated for Laboratory Tests

Components with scribe marks can't be treated as pristine as it is a non-conservative approach and there may be degradation in life caused by the defect. So characterization of fatigue lives of scribes of different geometries and depths is of significant importance for the aerospace community. There are countless ways by which scribes can be produced in service but previous research [2-8] on this topic has generally investigated sharp scratches or scribes which were considered most likely to propagate in fatigue due to a high stress concentration around the root. Such scribes can be characterized solely by parameters such as depth, included angle and root radius. Tools used for creating scribes have been rigid steel or cutting tools.

To replicate sharp in-service scribes in the laboratory, scribe marks can be produced from multiple techniques based on controlled or uncontrolled application of force. Nader [2] and Talia et al. [3-4] produced scratches in Al 2024-T3 by using the sharp corner of an end mill which created neat scratches that had an included angle of 90 degrees and tip radius of 84 μm. Kyle [6] used a high speed steel tool on an automated milling machine to produce scribes in Al 7075-T6 with pure aluminium cladding. Morency [7] used a diamond-tip cutting tool on milling machine and produced scribes of 5 μm root radius in Al 2024-T351 with and without cladding. Walmsley [8] used plastic scrapers, Stanley knife blades and sharpened sheet aluminium strips and produced scribes with manual force in Al 2024-T351 with cladding.

In this study scribes have been produced with a diamond-tip cutting tool with the same set-up used by Morency [7] but with different tools of root radii 5, 25 and 50 μm.

2.1.3 How Different Types of Scribes can be Produced

In the production of scribes using cutting tools, there are several basic attributes included depth of cut, rake angle, clearance angle and wedge angle that define the action of a cutting

tool and hence its influence on the surrounding material [28]. The force involved in removal of material from the sample surface imposes significant changes to the surrounding material due to deformation. The deformed material that surrounds the removed material region is work hardened, the amount of which is proportional to the amount of deformation. The degree of deformation apparent from material removal is dependent on the tool rake angle and the depth of the cut made.

Scribes produced from the tool from a milling machine can be of two types based on the type of wear around scribes. They can be classified as 'cut' or 'ploughed' and have significant differences in their characteristics. For scribes obtained through a 'cut' process, a very smooth scribe track is obtained, with very little deformed material around the scribe. Very little debris around the scribe track is present, so the tool removes the material by a cutting action, rather than by plastic deformation and displacement of material. On the other hand, for 'ploughed' scribes, a large extent of material displaced around the scribe track is obtained with a 'rough' scribe track with deformed material or debris around scribe. The scribing of the surface shows large amount of plastic deformation and displacement of material, rather than a cutting action by which material is simply removed. Kyle [6] used the same tool to produce 'ploughed' and 'cut' scribe by changing the direction of sliding of the tool as shown in Fig.2.2 (a) and (b). This change in direction of sliding effectively changes the characteristics of the scratch.

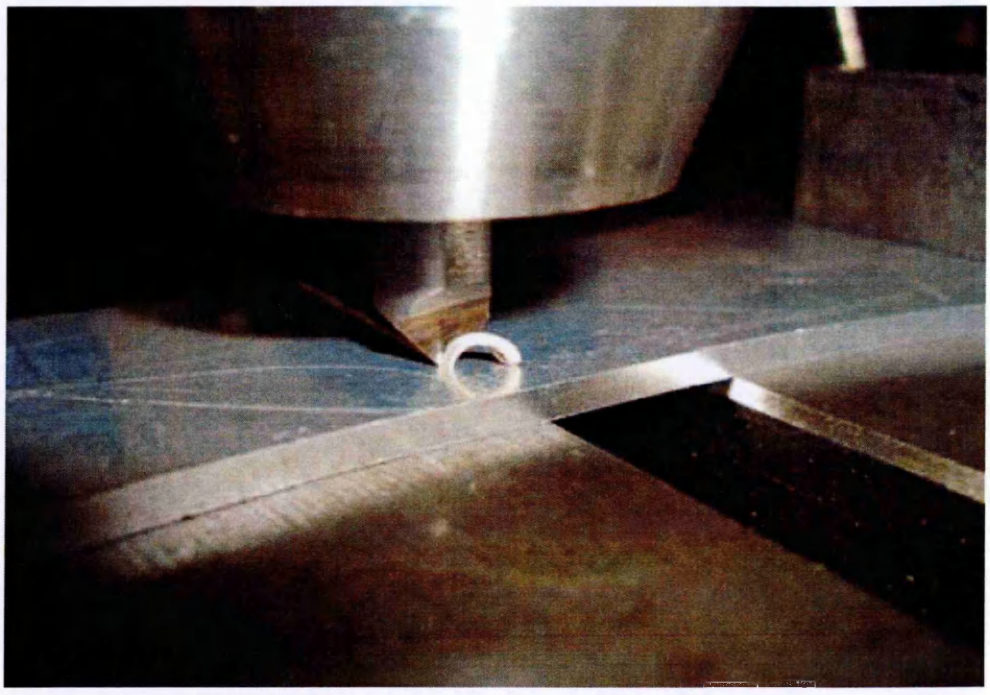

(a)

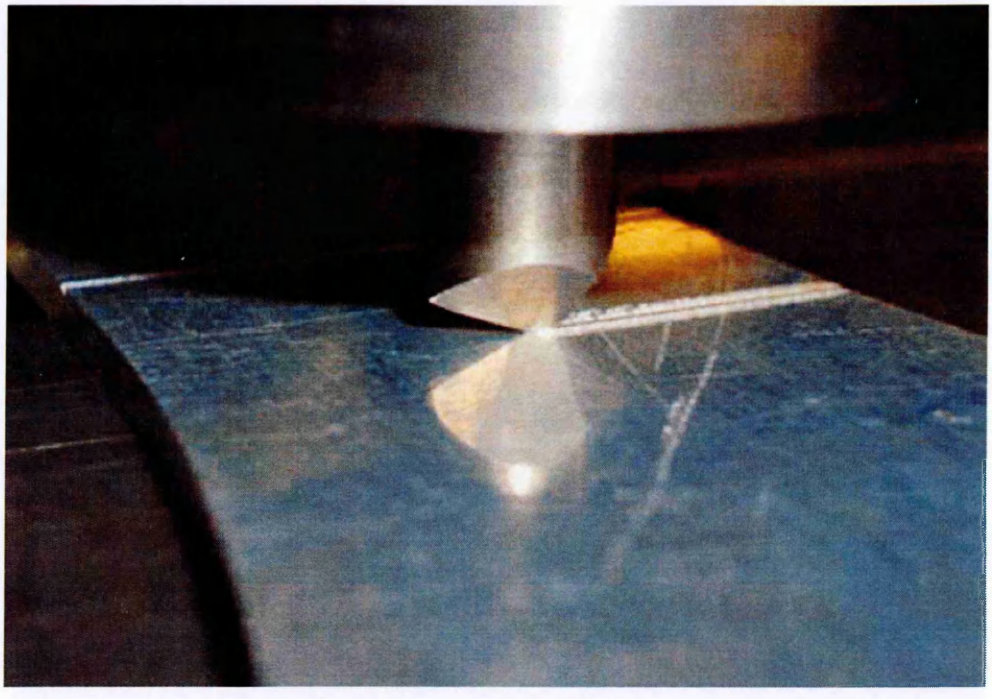

(b)

Fig. 2.2 - Scribe of type (a) Cut and (b) Ploughed (Kyle [6])

Scribes used in this study were produced with different tools capable of producing scribes of different root radii. Two tools were used for scribes of 5 μm root radius designated as tool 'A' and 'B', while tool 'C' and 'D' were used for 25 μm and 50 μm root radius. The

reason for using two different tools for 5μm root radius scribes was the different behaviour of these two tools. It was found that tool A was capable of producing 'ploughed' scribes while tool B produced scribes with 'cutting'. It was found that to get a mechanism of 'ploughing' or 'cutting', direction of sliding does not necessarily need to be changed, but different tools having different rake angles and angle of tip are capable of producing these different mechanisms of wear.

2.2 Fatigue Life of Scribes

Fatigue of a material is the effect of repetitive cyclic loads that are considerably less in magnitude than the yield strength of a material. Fatigue in metals is now well understood and the initiation and growth of fatigue cracks can initiate at stress concentrating features within a structure. These stress concentrations are caused by the geometrical design of the components, local damage such as scribes or scratches, or by localized slip on preferentially-oriented grains during cyclic loading.

Stress concentrations such as scribes, notches or scratches can cause the premature initiation of fatigue cracking and significantly reduce the fatigue life of aircraft structural components [2-4]. The presence of a notch results in an increase of the local stress at the tip of the notch compared to the nominal stress in the component. At sufficiently high nominal stresses the local stress at the notch tip can exceed the material yield strength. This leads to local plastic deformation which in the case of cyclic loading will decrease the fatigue life of the component [19]. Even at lower stresses where there is no plasticity the high local stresses at the notch tip cause earlier fatigue crack initiation. It is therefore important to be able to assess mechanical defects such as notches, scratches and scribes in terms of calculation of the service life at which fatigue cracks are initiated and secondly prediction of the subsequent life to failure.

'Stress life' and 'Strain life' approaches are used to calculate crack initiation. In the 'stress life approach', it is assumed that there is no plastic deformation and all of the stresses present in the region ahead of notch/scribe tip are elastic. This approach quantifies stress concentrations from the elastic stress concentration factor K_t. This approach becomes inapplicable for the case of scribes where cyclic plasticity occurs during fatigue cycles.

The 'Strain life' approach relates the far field strains to strains near notch while considering plasticity. It is based upon the cyclic stress-strain behaviour of the material. From this approach the cycles required to initiate a fatigue crack can be predicted. Although this approach is used extensively for crack initiation, it gives a conservative life for a crack to initiate from shallow notches or scratches of the size same as scribes.

For propagation of a crack, if the scribe is considered as a propagating crack, Linear Elastic Fracture Mechanics (LEFM) can be used to calculate the life to failure. As this approach ignores the number of cycles to create a crack, this approach can give very conservative lives.

It is difficult to predict the initiation and propagation of cracks from scribes and treating the component with a scribe as pristine will be non conservative as there may be degradation in life caused by the defect. In view of these difficulties, earlier experimental studies were carried out to characterize fatigue life of scribes and scratches [2-8]. All of the studies reported a reduction in fatigue life with the presence of surface scratches. Nader [2] investigated the influence of scratch position on the fatigue of Al 2024-T3. Specimens with scratches on one edge, two edges and full width were tested and showed variability in the fatigue lives. He showed that the primary factors influencing the fatigue effects of scratches are the depth, the scratch tip radius and to a lesser extent the included angle of the scratch. He found that scratches as deep as 100 μm could reduce the fatigue life as much as 95%. Talia [3-4] reported for Al 2024-T3 with a scratch of 100 μm depth in 2mm thick plates of clad Al 2024-T3, a reduction in fatigue life of 95% compared to the

undamaged pristine specimen is seen, at a maximum stress of 345MPa. As the maximum stress is decreased, the fatigue life for the same scratch depth increases. It was shown in Talia [4] that the crack growth rate increases with increase in depth of the scratch. For scratch depths of 20μm, 50μm and 100μm, the fatigue crack growth rates were approximately 1.5, 4 and 10 times the rate of unscratched specimens. Inchekel [5] examined the effects of a centre scratch compared to a full width scratch. In terms of overall fatigue life, results from both studies revealed that a centre scratch had virtually no effect when compared to an unscratched specimen. Conversely, a full width scratch produced approximately the same reduction in fatigue life as one or two edge scratches. Kyle [6] used a high speed steel tip and produced scribes of 50μm root radius in Al 7075-T6 with cladding. He concluded that scratches that terminate in the clad layer produce reductions in fatigue life of 40-45% compared to pristine specimens, only for stress concentration factor K_t greater than 3. However, scratches that terminated in the substrate did not produce this reduction in fatigue life as seen in previous research by Nader [2]. Kyle [6] found that for 'plough' scratches the upset clad layer showed signs of work hardening but the substrate remained unchanged. He also found negligible difference between whether a scribe was made by a 'cut' or 'plough' process. However, the results did not show a significant reduction in fatigue life with scribe depth as concluded by Talia et al. [3-4] who observed fatigue life reductions of up to 95% on clad 2024-T3 coupons of 200μm thick clad layer that had scratch depths of 100μm and were cycled at a maximum stress of 345 MPa.

Morency [7] utilised a diamond tip cutting wheel with a 5μm tip radius. He found that clad 2024-T351 was much more susceptible to fatigue crack initiation from any depth of scratch compared to unclad material. Up to 80% life reduction was found for 200μm deep scratches in clad 2024-T351 aluminium. However, for bare 2024-T351, only the deepest scratches (200μm) caused fatigue crack initiation. He also observed that all scratches

initiated some form of fatigue cracking. However, sometimes the cracks propagated slowly or ceased propagating so that the test coupon either ran-out or failed at a location other than the scratch.

Walmsley [8] used plastic scrapers, Stanley knife blades and sharpened aluminium strips to produce scribes in Al 2024-T351 with cladding. He found that plastic scrapers were incapable of producing scribes in clad layer whilst aluminium strips and a Stanley knife blade produced sharp scribes. Scribes from the Stanley knife blade penetrated through the clad layer and into the substrate and were of 'plough' type of scribes with deposition of plastically deformed material around the scribe root. Scribes produced from the aluminium scrapers were different from the Stanley knife. Scribes penetrated only in clad layer and not into the substrate which was attributed to high the hardness of Al 2024-T351. Walmsley tested these scribes in fatigue and found that only 2 out of 8 samples failed from the scribe.

All of these studies showed a random trend of fatigue lives for scribes. In some cases [2-6] samples failed from scribes whilst in some cases failure occurred elsewhere [7-8]. In some cases only initiated cracks from scribes were found which never propagated [7]. All of these different outcomes of fatigue results from different earlier studies make it very difficult to predict fatigue lives of scribe marks.

2.2.1 Role of Residual Stresses in Prediction of Fatigue Life

Further research is being carried out to estimate the fatigue lives of components having small damage [9-17]. Most of the research has been towards characterization of the effect of foreign object damage (FOD) on turbine engine blades in titanium alloy Ti-6Al-4V. In these studies FOD is created with impact on specimen from projectiles of different size and shapes with different velocities. Several aspects including residual stresses, have been discussed and in almost every study residual stresses has been cited as a very important factor in affecting fatigue lives. However, very little work has been made on the

measurement of initial residual stresses around these FODs and the effect of fatigue loading in the relaxation of these residual stresses. Nowell et al. [9] investigated the effect of notches on fatigue life of Ti-6Al-4V. The effect of impact angle which created the notch, leading edge radius and subsequent angle of damage on fatigue life was investigated. They found that with increase in notch depth fatigue life decreased significantly. Their experimental fatigue results were different with different approaches for short cracks and they believed that information about residual stress around root of the notch was necessary in their analysis; but they found it difficult to measure which was the main reason for the difference in their results. Ruschau et al. [10] investigated the fatigue behaviour of the same titanium alloy with FODs resulting from high-speed impact of small glass spheres. They concluded that not only the depth of the damage is correlated to a drop in fatigue life but small tears, notches etc. around damage caused by the FOD impacts changed the residual stress field and appeared to influence the fatigue strength more than the depth. They found that their fatigue data had a large degree of scatter with impact angle and attributed it to residual stresses around the damage. They also investigated the influence of impact angle on the residual stress field around the damage site and found that a $0°$ angle impact creates a large compressive residual stress field while for an angle of impact from $15-16°$, tensile stresses are created and the fatigue strength decreases as much as 60%. Oakley and Nowell [11] working on the same titanium alloy with FOD concluded that without consideration of residual stresses the fatigue results were misleading and even if the residual stresses before fatigue are known then simple elastic superposition of residual stress on the stress ratio (R) did not resolve the problem. It was suggested that the residual stress field generated by the impact may not relax during the first few cycles of fatigue loading and FE analysis of fatigue in presence of damage was recommended. Thompson et al. [12] conducted fatigue testing on the same titanium alloy with FOD and compared the results to fatigue of samples which were stress relieved by annealing. They found that the fatigue strength increased for stress relieved samples. Peters

et al. [13-14] conducted fatigue testing of FOD on the same titanium alloy and observed that the fatigue life decreased by three times as compared to samples without FOD. However, they found that the propagation of small cracks from the damaged zone was slow as compared to naturally initiated small cracks, and attributed this to plastic deformation induced by foreign object impact which suppressed planar slip bands by making slip distribution more homogeneous.

Although all of the studies discussed above mentioned the residual stress field around damage as a main factor for decrease in fatigue life, none of the studies had any measurement of the resulting residual stress field due to FOD, and consequently failed to predict fatigue lives. The residual stress introduced in the material, if significant, will have an effect on the fatigue properties. Tensile or compressive stress may develop in the material depending upon the damage mechanism. Boyce et al. [16] measured the residual stress field around FOD using synchrotron X-ray diffraction and found that the initial residual stress around the damage was high tensile and was 40% of the yield stress. They emphasized that the initial residual stress state is substantially reduced by relaxation or distribution during fatigue loading and may reduce by 30-50% of its initial value after first fatigue cycle. In another study [17], focussing on relaxation of these residual stresses, they concluded that initial residual stress state around FOD can decay significantly in fatigue depending upon the applied stress. For Ti-6Al-4V, they obtained very little relaxation for $0.35\sigma_Y$ but for a higher applied stress of $0.54\sigma_Y$ this relaxation reached 50%. They observed that decay of the residual stress state was only during the first cycle and subsequent cycles showed very little further relaxation.

In view of failures in prediction of fatigue life of FOD components, without consideration of residual stress, it is evident that residual stresses play significant role in fatigue propagation of scribe marks. With the different conclusions of Kyle [6] and Talia et al [3-4] of the dependence of fatigue life on scribe depth, the different behaviour of clad and unclad shown by Morency [7], and no such effect of scribes on fatigue life observed by

Walmsley [8], it can be concluded that there is an important parameter of residual stress which has not been investigated in these studies. Not only the initial residual stress field need to be investigated to accurately predict fatigue life of scribes or FOD, but behaviour of these residual stress fields during fatigue is important and the degree of relaxation of these residual stresses needs to be assessed.

2.3 Measurement of Residual Stresses

There are different techniques of measurement of residual stresses, dependent upon the type and length scale of residual stress field. Residual stresses can be classified into three categories [31]:

1-Type-I residual stresses are stresses which vary continuously over large distances across several grains and may exist over a area of several centimetres. These types of residual stresses are also called Macrostresses.

2- Type-II residual stresses are the stresses which vary over the grain scale, one grain or partial grain of a material. These stresses occur due to anisotropy in the material.

3- Type-III residual stresses are the stresses which vary over submicroscopic areas of a material at the atomic scale.

From earlier studies on residual stress measurement around FOD [9-17] of similar same geometries, it was anticipated that scribe marks of depth ranges 50 μm to 150 μm produced from different tools may have residual stresses up to 1mm around scribe root. So it can be said that scribe marks produce type-I residual stresses but in a very small region around scribe root.

2.3.1 Methods of Residual Stress Measurement

In this section, the techniques currently most widely used for residual stress measurement will be briefly presented and their viability for measurement of small residual stress fields, such as around scribe marks, will be assessed.

Destructive Measurement Techniques

In destructive techniques, material is removed from a sample from the regions of interest and stress relaxation occurred in the remaining material. The change in strain, so obtained, is used to evaluate the residual stress that existed at in the removed material. The change in strain is usually measured by strain gauges.

2.3.1.1 Hole Drilling

In this technique a hole is drilled and strains are measured using a rosette of strain gauges. The stresses are relaxed when any region is drilled, thereby providing data for the back-calculation of residual stresses [30-31]. The diameter of the hole typically ranges from 1-4mm and hence the spatial resolution of this method is not high enough to measure the residual stress field around scribe marks.

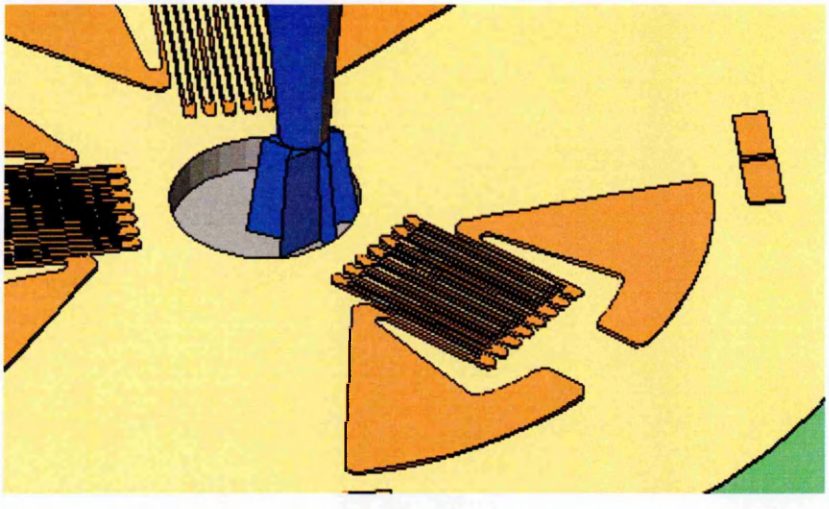

Fig. 2.3 - Drilling of a hole in a strain gauge rosette [30]

2.3.1.2 Contour Method

In this method the surface deformation contour is measured after cutting a component into two parts by the means of electro discharge machining (EDM). With the assumption that the contour is caused by elastic stress relaxation the residual stress normal to the cut

surface in the original sample can be determined using Finite Element Modelling [32-33]. As this technique requires cutting of surface in to two parts and with scribes of even highest depth ~200um it is very difficult to cut so it can not be applied to measure the residual stress fields around scribe marks.

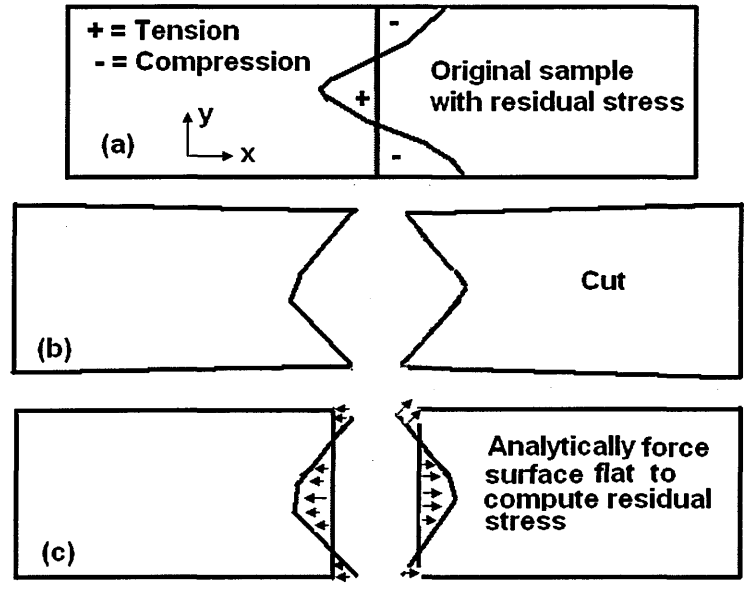

Fig. 2.4 - Principle steps in the contour method

Other destructive techniques included the 'Ring Core Method', 'Curvature Method', 'The Sachs Method', 'Compliance Method' etc., and all of these methods have similar problems of either spatial resolution or removal of material or both [31]; hence no destructive technique is feasible to measure the very small residual stress field around scribe marks.

Non-destructive Measurement Techniques

2.3.1.3 Ultrasonic Method

In this method ultrasonic waves are passed through a material and the velocity of the wave is affected by the variation of stress in the material [31]. This effect is used for residual strain measurement. As this technique gives an averaged stress along the entire ultrasonic path, it is hence not suitable for scribe marks.

2.3.1.4 Magnetic Methods

The principle of this method is based on the interaction between magnetization and elastic strain in ferromagnetic materials. The method calculates stresses from abrupt motion of ferromagnetic domain walls [31]. This method is restricted to ferromagnetic materials and as aluminium is non-ferromagnetic, this method can not be applied for scribe marks in aluminium alloys.

2.3.1.5 Diffraction Methods

In diffraction methods, the interplanar atomic spacing is used as a strain gauge. A monochromatic beam of wavelength near to magnitude of atomic spacing is directed to the material under examination. The principle of X-ray diffraction measurement is based on Bragg's law in which shifts in the Bragg peak give the strain for particular $\{hkl\}$ plane. The essential condition which must be met for diffraction is called Bragg's law and can be described as;

$$n\lambda = 2d_0 \sin\theta_0 \qquad (2.1)$$

Where d_0 is the lattice spacing of the unstressed crystal for any given set of hkl planes, $2\theta_0$ is the angle between the incident beam and the diffracted beam on the unstressed crystal, n is an integer and λ is the wavelength of the incident monochromatic beam.

Differentiating eq. 2.1 gives,

$$\varepsilon = \frac{d - d_0}{d_0} = -(\theta - \theta_0)\cot\theta_0 \qquad (2.2)$$

Strains can also be written in terms of lattice parameter as;

$$\varepsilon = \frac{a - a_0}{a_0} \qquad (2.3)$$

Where a is the lattice parameter under strain and a_0 is the lattice parameter without strain.

Different diffraction methods include Synchrotron X-rays, Neutron diffraction, Laboratory X-ray diffraction and Electron diffraction. Fig.2.5 shows an overview of the different

destructive and non-destructive measurement techniques with their spatial resolution capability for measurement of residual stresses. The requirement for scribe marks are that technique should map near surface stress fields up to 1 mm around scribe root and to get sufficient data points in this region a very high spatial resolution of ~10 to 50um is required. Based on these criteria Synchrotron X-rays was selected as measurement technique due to its excellent ability to map near surface measurements. Synchrotron sources with high level of brilliance (e.g ESRF) [18] provide very narrow, intense X-ray beams with very low angular divergence which results in high spatial and angular resolution.

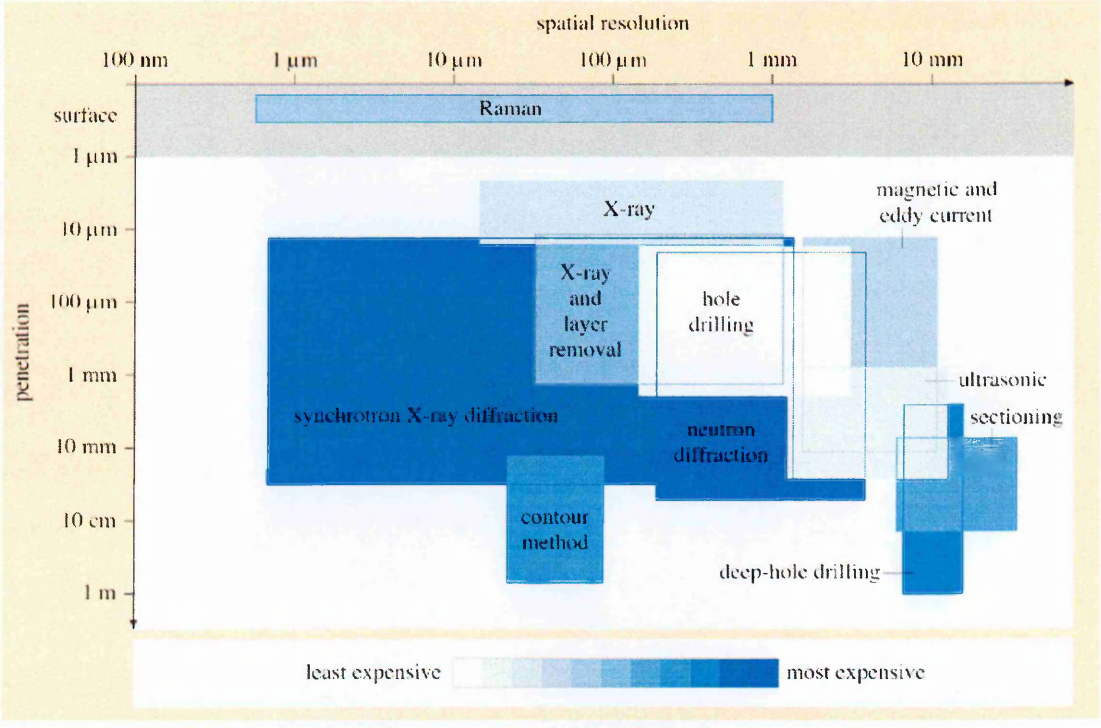

Fig. 2.5 - Comparison of length scales of residual stress measurement techniques (courtesy M. E. Fitzpatrick, Open University course book T357)

Synchrotron X-rays are a relatively new and rapidly developing technique which allows fast internal strain mapping with very high spatial resolution. Synchrotron X-rays are differentiated from conventional laboratory X-rays by their high energy and intense photon flux which increases penetrability to many millimetres as compared to the few tens of microns by laboratory X-rays.

Owing to their high energy the wavelength of synchrotron X-rays are an order of magnitude less than the inter-atomic spacing of normal engineering materials, which makes the diffraction angle much smaller. This characteristic of synchrotron radiation makes it suitable for measurement of in-plane strains in transmission while it is not feasible to measure the out-of-plane strain direction in reflection due to the larger path length in the reflection geometry.

2.3.1.6 Principle & Methods of Synchrotron X-ray Diffraction

A synchrotron consists of a circular vacuum pipe in the horizontal plane through which electrons circulate. This vacuum pipe is known as the storage ring. In synchrotron sources, electrons emitted by an electron gun are first accelerated in a linear accelerator. The electrons are then transmitted to a storage ring where the electron path is bent inside a multiple sided polygon using electromagnets known as bending magnets. The trajectory of electrons inside the storage ring is controlled by powerful electromagnets as shown in Fig. 2.6.

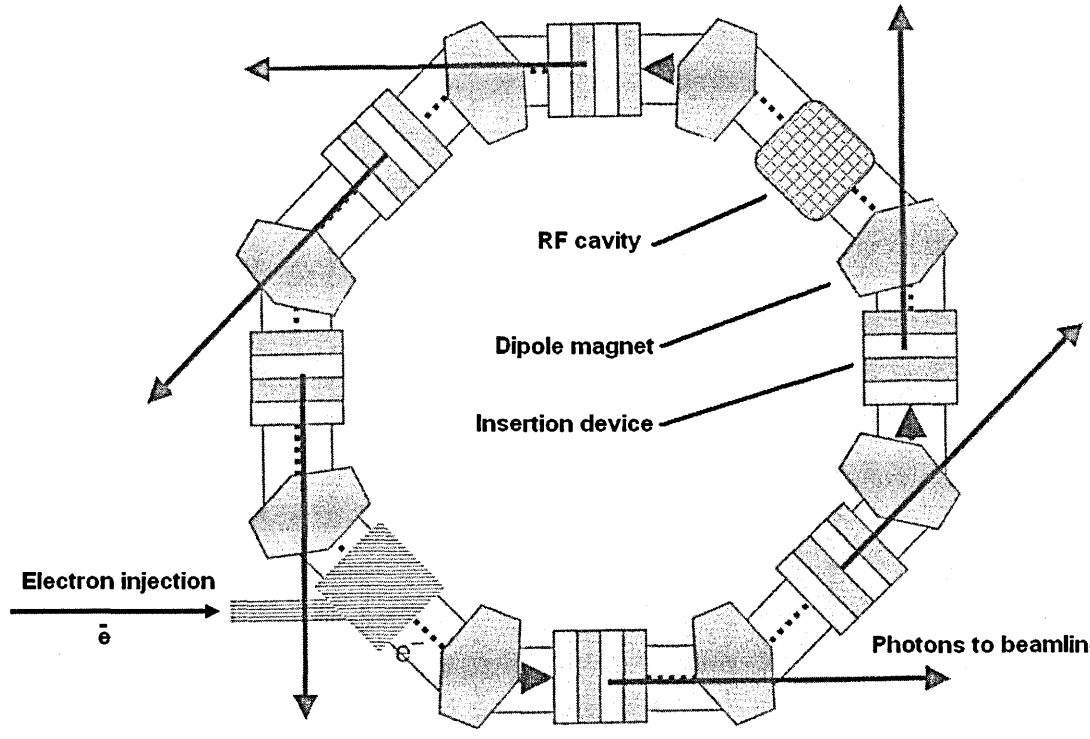

Fig. 2.6 - Schematic diagram of synchrotron X-ray storage ring (Riekel [18])

When the electrons pass through the magnetic fields of the bending magnets the electrons are radially accelerated. When electrons are accelerated they emit electromagnetic radiation which is known as synchrotron radiation. The synchrotron radiation consists of a range of frequencies from infra-red light to hard X-rays.

For electro-magnetic radiation the energy of a photon E in terms of frequency ν is given as

$$E = h\nu \tag{2.4}$$

For an electromagnetic wave the velocity of particles is constant and equal to;

$$C = \lambda\nu \tag{2.5}$$

Equations 2.4 and 2.5 give the relation between energy and wavelength of radiation expressed as

$$E = \frac{hC}{\lambda} \tag{2.6}$$

Where E is in KeV and λ is in angstroms (Å).

Strain measurement by synchrotron X-rays can be done in two ways; by using a polychromatic beam or by using monochromatic beam. Utilising equation 2.2 the lattice strain is measured. Where a monochromatic beam is used the white synchrotron radiation emitted in the storage ring is passed through a crystal monochromator. By adjusting the incidence angle of the monochromator, a particular energy level is selected by Bragg diffraction which is used as an incident synchrotron X-ray beam.

In the experimental set-up, the white synchrotron X-ray beam from the storage ring is first collimated in one plane by passing it through focussing mirrors. The beam is then passed through the monochromator crystal which also helps in collimating the beam in the other plane. In order to reduce the variation of the wavelength range, often two single crystal monochromators are arranged in a manner so that the diffracted beam from the first monochromator becomes the incident beam in the next monochromator at the same angle. The incident beam is then passed through a slit system which controls the incident beam spot size. Due to very high energy and low wavelength in synchrotron X-rays the diffraction angle is very low. The low diffraction angle, as shown in the Fig.2.7, causes significant elongation of gauge volume along the direction of the incident beam. The vertical opening of the incoming and receiving beam slits determine the gauge volume.

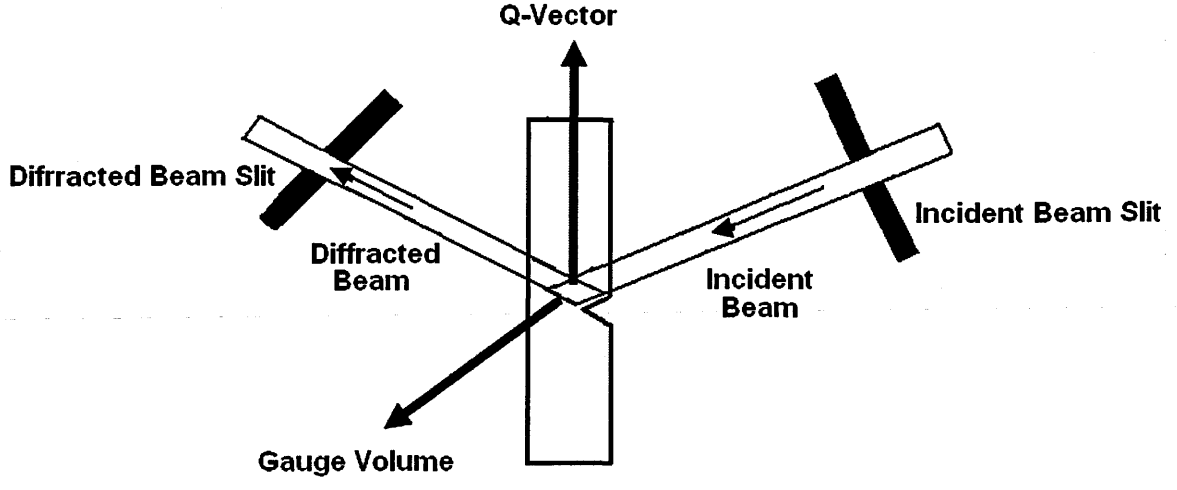

(a)

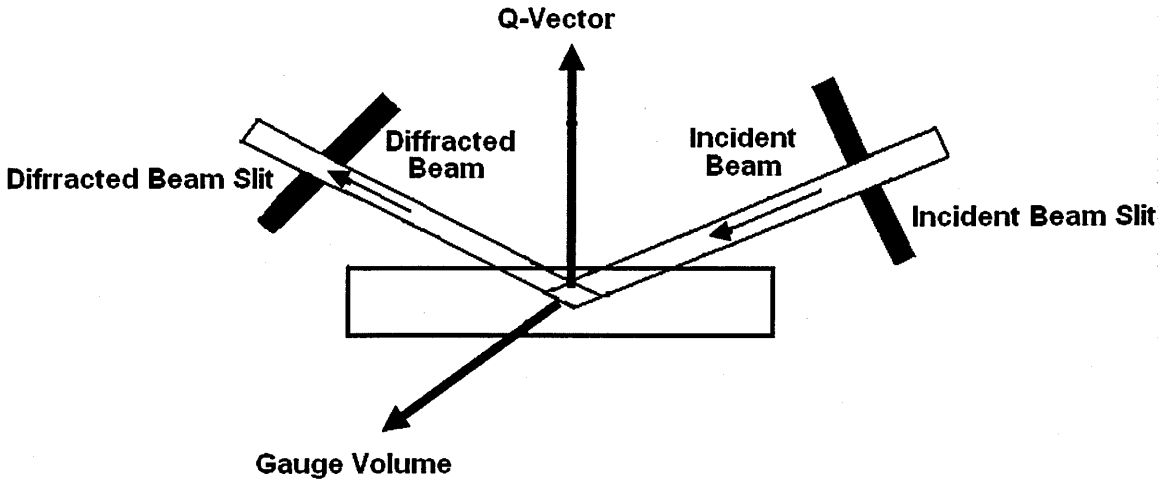

(b)

Fig. 2.7 - Schematic representation of strain measurement in (a) reflection mode (b) transmission mode

In strain scanning the diffracted beam from the sample can be passed through an analyser crystal, which precedes the detector. Analyser crystals are single crystals that stringently define the diffraction angle. The diffracted beam detected after the analyser crystal has high spatial and angular resolution. In the diffraction spectra intensity is plotted as a function of the diffraction angle and accurate angular positioning determines the inter-planar spacing of the selected crystallographic plane.

In a typical experimental 'hutch' at a synchrotron source, detectors are mounted on a circular table in the vertical plane. The sample is mounted on positioner which is placed on a smaller circular table in the vertical plane and concentric with the omega table. With this arrangement the θ-2θ diffraction geometry is maintained by individual movement of the two tables. The sample holder is fitted with a translational motor which can move the sample across the gauge volume and strain maps can be obtained rapidly.

2.4 Nanoindentation

Although synchrotron X-rays diffraction can be used to map local stress field and plasticity around scribe marks, to get good diffraction statistics the gauge volume should contain

sufficient number of grains. Due to the large grain size of Al 2024-T351, a larger gauge volume will be required which will give an average value over that gauge volume. For a very local residual stress field with high gradient around scribes this could lead to conservative measured strain values. Hence, a complementary technique is required which can map residual stress fields and local plasticity with a spatial resolution of 5~10 μm. It has already been discussed that for conventional residual stress measurement techniques, only synchrotron X-rays can be used, which has the highest resolution.

Depth sensing indentation, although not considered as a residual stress measurement technique, allows determination of mechanical properties at very low loads by driving an indenter into the material surface and subsequently recording the load-displacement data. As the indenter is driven into the material, both elastic and plastic deformation processes occur. There have been some studies carried out about sensitivity of nanoindentation load-displacement data with residual stress [20-27]. By keeping the diameter of the indent in the range of 5~10 μm, elastic-plastic information around scribe marks can be obtained. This elastic-plastic information in the form of load-displacement data can be used to extract residual stresses. This will provide an opportunity to measure residual stress field around a number of scribe marks and to compare with synchrotron X-ray diffraction results. Another benefit of nanoindentation over synchrotron X-ray diffraction is that it is readily available in laboratories while Synchrotron sources are highly sophisticated international facilities and beam time is allocated by international peer review. These facilities are heavily over-subscribed and getting beam time is not trivial.

2.5 Conclusions

A brief review of previous studies of the effect of scribes on fatigue life has been presented and the significance of residual stresses in prediction of fatigue life has been discussed. There hasn't been considerable work done so far in determination of residual stresses

around small damages amidst difficulties in determination of such small and local residual stress fields. Consequently, all of the previous studies failed to predict fatigue life of small damages such as scribes and scratches. It has been concluded that to measure such local and small residual stress fields, synchrotron X-ray diffraction along with nanoindentation load-displacement data can be used, however it is a challenging task.

2.6 References

[1] Federal Aviation Authority. Flight Standards Information Bulletin for Airworthiness (FSAW): 03-10B Fuselage Skin "Scribe Mark" Damage on Boeing 737 Aircraft. Effective 20 November 2003, amended 31 March 2004.

[2] N. A. Nader N.A. The effect of scratches on the fatigue life and fatigue crack growth of Al2024-T3 clad. Wichita State University, PhD Thesis, 1994.

[3] M. Talia and J. Talia. Effects of scratches and shot peening on the high cycle fatigue crack growth of aluminium alloy 2024-T3. High Cycle Fatigue of Structural Materials, 14-18 September 1997. The Minerals, Metals and Materials Society. Indianapolis, Indiana, USA.

[4] M. Talia and J. E. Talia. Crack propagation modelling for surface generated scratches in Al 2024-T3 clad alloy. Journal of the Mechanical Behaviour of Materials, Vol. 8, 1997, pp. 117-139.

[5] A. Inchekel and J. E. Talia. Effect of scratches on the fatigue behaviour of an Al-Li alloy. Fatigue Fract. Eng. Mater. Struct. 17(5), 1994, pp 501–507.

[6] Kyle, C. Investigation of the transformation of defects in aircraft structures into cracks. Cranfield University MSc Thesis, 2005.

[7] Morency, R. Fatigue crack initiation and growth from scratches in 2024-T351 aluminium. Cranfield University MSc Thesis, 2006.

[8] Walmsley S.W. Fatigue potential of tool scratches on clad 2024-T351 alumnium alloy. Cranfield University MSc. Thesis, 2007.

[9] Nowell, D., P. Duo, I. F. Stewart. Prediction of fatigue performance in gas turbine blades after foreign object damage. 4th International Conference on Fatigue Damage of Structural Materials, Hyannis, 2002, Massachusetts, Elsevier Sci Ltd.

[10] Ruschau, J. J., T. Nicholas and S. R. Thompson. Influence of foreign object damage (FOD) on the fatigue life of simulated Ti-6Al-4V airfoils. International Journal of Impact Engineering 25(3), 2001, pp 233-250.

[11] Oakley, S. Y. and D. Nowell. Prediction of the combined high- and low-cycle fatigue performance of gas turbine blades after foreign object damage." International Journal of Fatigue 29(1), 2007, pp 69-80.

[12] Thompson, S. R., J. J. Ruschau and T. Nicholas. Influence of residual stresses on high cycle fatigue strength of Ti-6Al-4V subjected to foreign object damage. 3rd International Conference on Fatigue Damage of Structural Materials, 2000, Hyannis, Massachusetts, Elsevier Sci Ltd.

[13] Peters, J. O., B. L. Boyce, Chen X, J. M. McNaney, J. W. Hutchinson and R. O Ritchie. On the application of the Kitagawa-Takahashi diagram to foreign-object damage and high-cycle fatigue. Engineering Fracture Mechanics 69(13), 2002, pp 1425-1446.

[14] Peters, J. O. and R. O. Ritchie. Foreign-object damage and high-cycle fatigue of Ti-6Al-4V. 12th Meeting of the International Conference on the Strength of Materials (ICSMA 12), 2000, Asilomar, California, Elsevier Science Sa.

[15] J. O. Peters, O. Roder, B. L. Boyce, A. W. Thompson and R. O. Ritchie. Role of foreign-object damage on thresholds for high-cycle fatigue in Ti-6Al-4V. Metallurgical and Materials Transactions a-Physical Metallurgy and Materials Science 31(6), 2000, pp 1571-1583.

[16] Boyce, B. L., X. Chen, J. W. Hutchinson and R. O. Ritchie. The residual stress state due to a spherical hard-body impact. Mechanics of Materials 33(8), 2001, pp 441-454.

[17] Boyce, B. L., X. Chen, J. O. Peters, J. W. Hutchinson and R. O. Ritchie. Mechanical relaxation of localized residual stresses associated with foreign object damage. Materials

Science and Engineering a-Structural Materials Properties Microstructure and Processing 349(1-2), 2003, pp 48-58.

[18] C. Riekel. The use of synchrotron radiation for materials research, in M.E. Fitzpatrick and A.Lodini (Eds), Analysis of Residual Stresses by Diffraction Using Neutron and Synchrotron Radiation, Taylor & Francis, London, 2003, pp 28-44.

[19] Peterson, R.E. 1974. Stress Concentration Factors, Wiley and Sons, New York.

[20] Suresh, S. and A. E. Giannakopoulos. 1998. A new method for estimating residual stresses by instrumented sharp indentation. Acta Materialia 46(16): 5755-5767.

[21] Lee, Y. H., W. J. Ji and D. Kwon. Stress measurement of SS400 steel beam using the continuous indentation technique. Experimental Mechanics 44(1), 2004, pp 55-61.

[22] Lee, Y. H. and D. Kwon. Measurement of residual-stress effect by nanoindentation on elastically strained (100) W. Scripta Materialia 49(5), 2003, pp 459-465.

[23] Lee, Y. H. and D. Kwon. Estimation of biaxial surface stress by instrumented indentation with sharp indenters. Acta Materialia 52(6), 2004, pp 1555-1563.

[24] Carlsson, S. and P. L. Larsson. On the determination of residual stress and strain fields by sharp indentation testing. Part I: Theoretical and numerical analysis." Acta Materialia 49(12), 2001, pp 2179-2191.

[25] Xu, Z. H. and X. Li. Estimation of residual stresses from elastic recovery of nanoindentation. Philosophical Magazine 86(19), 2006, pp 2835-2846.

[26] Xu, Z. H. and X. D. Li. Influence of equi-blaxial residual stress on unloading behaviour of nanoindentation. Acta Materialia 53(7), 2005, pp 1913-1919.

[27] Zhao, M. H., X. Chen, J. Yan and A. M. Karlsson, Determination of uniaxial residual stress and mechanical properties by instrumented indentation. Acta Materialia 54(10), 2006, pp 2823-2832.

[28] Chisholm, A.J. 1951. The Action of Cutting Tools, Machinery Publishing Company, London.

[29] Olympus NDT. http://www.olympus-ims.com/en/ndt-application/183 id.209715272.html

[30] http://www.stresscraft.co.uk/hole_drilling.htm.

[31] P. J. Withers and H. K. D. H. Bhadeshia, Residual stress, Part 1 – Measurement techniques. Materials Science and Technology, April 2001, Vol. 17, pp 355.

[32] http://www.lanl.gov/contour/.

[33] M. B. Prime. Cross-Sectional Mapping of Residual Stresses by Measuring the Surface Contour after a Cut. Journal of Engineering Materials and Technology, 123, 2001, pp162-168.

Chapter 3: Characterization of Aluminium-clad and Al 2024-T351 by Nanoindentation

3.1 Introduction

Nanoindentation testing at low loads is a successful technique for the study of mechanical properties of materials. Low load testing allows determination of mechanical properties at penetration depths as low as 20nm, which gives full insight into the mechanical properties of surfaces. The possibility to carry out tests at such small scales makes this technique one of the very few tools capable of characterizing mechanical properties around very small features like scratches, scribes, corrosion pits, cracks etc. Nanoindentation records load-displacement data during the loading and unloading phase of testing and this makes it an ideal technique to study the deformation mechanisms of materials. This load-displacement data works as a finger print for every material. It also shows sensitivity to residual stresses and with careful study of load-displacement data (or curve), residual stresses can be extracted.

The overall aim of this project is to extract residual stresses around scribes with depth of a few hundred microns in Al 2024-T351 and Al-cladding from nanoindentation. This extraction can only be carried out once the response of the stress free or bulk material is known in terms of its characteristic load-displacement curve. So to accurately characterize load-displacement curves obtained from nanoindentation a comprehensive study has been carried out. Nanoindentation has traditionally been developed and applied to hard ceramics materials and coatings, and hence existing methods to analyse raw data of load-displacement do not provide optimized results for relatively soft materials such as aluminium alloys. This chapter discusses the behaviour of low hardness materials for nanoindentation and subsequently required amendments to available methods which work relatively well for hard materials but provide poor estimates for soft materials like

aluminium alloys. To obtain accurate properties from nanoindentation, hardness and modulus were obtained at several depths of penetration. This study will reveal optimized testing parameters like depth of penetration, maximum load, drift rate, area of indent, pile-up around indents for Al 2024-T351 and Al-cladding. These optimized parameters will be used in extraction of residual stresses from nanoindentation load-displacement curves.

The mechanical properties of Al2024-T351 and the Al-cladding over this alloy were calculated from Nanoindentation. Depth sensing indentation technique allows the determination of mechanical properties at very low loads by driving an indenter of known geometry into the material surface by applying a known load and subsequently analyzing the load-displacement data from Oliver-Pharr Model (O-P) [1]. As the indenter is driven into the material, both elastic and plastic deformation processes occur, producing a hardness impression according to the shape of the indenter.

When indenting aluminium alloys, due to their low hardness and small strain hardening exponents, pile-up around indents start to occur even at low loads [8, 13]. This is a process in which some of the deformed material starts to deposit around the edges of the indents. This phenomenon is characteristic of materials with a high E/σ_Y ratio and less work hardening [5, 7, 13]. Earlier studies have shown that for materials with E/σ_Y >100, pile-up starts to occur, and increases continuously with an increase in this ratio [7]. This pile-up critically affects nanoindentation hardness and modulus calculations as the actual contact area between the material and indenter tip includes the area contained in the pile-up. Most models for analysis of nanoindentation data do not take into account pile-up area and underestimate the actual area, which results in an overestimate of the calculated values of modulus and hardness [2, 4, 9, 12-13].

Atomic force microscopy (AFM) can be applied to measure the 'true contact area' of the indentation [2, 8-9]. Hardness calculated using the area measured with AFM is most directly comparable to traditional hardness testing in which residual area is measured using

optical microscope. However, measurement of area from AFM allows material to relax between indentation and scanning with AFM, so AFM measured values of residual depth are less than those measured by the nanoindentation [7] and consequently provides lower values of hardness. Additionally sources of error such as tip convolution effects can lead to errors in the estimation of the area using the O-P model, and the area of the indentation itself cannot always be clearly defined from AFM imaging.

Another approach, which is termed 'work of indentation', can also be used for estimation of the hardness from nanoindentation [2, 13]. In this method, the elastic, plastic or total work of indentation is calculated from the nanoindentation load-displacement curve. These different terms of work of indentation can be used to calculate hardness without the need to calculate the area of indentation.

This chapter presents a comparison of the different available methods to calculate hardness of aluminium alloys which generates pile-up. Comparison was made for the Oliver and Pharr method (O-P), the O-P with area correction from AFM, the plastic work of indentation approach and total work of indentation approach for measurement of hardness of aluminium cladding and Al 2024-T351.

3.2 Theoretical Background

3.2.1 Oliver and Pharr Method (O-P)

In depth-sensing indentation machines, an indenter penetrates into the surface of a material. The total penetration depth is the summation of the elastic and plastic deformations occurring at the indenter tip. The plastic depth corresponds to the contact depth, which is used to determine the contact area. During the unloading stage, only the elastic portion of the displacement is recovered, which effectively allows separation of the elastic properties of the material from the plastic. A schematic representation of indentation load P versus displacement h obtained during one full cycle of loading and unloading is presented in Fig.3.1.

According to elastic contact theory [15], the fundamental relations from which hardness and elastic modulus can be determined are:

$$H = \frac{P}{A} \tag{3.1}$$

where H is hardness, P is the load and A is the projected contact area at that load. Eq.1 is a working definition for the hardness as measured by instrumented indentation testing.

$$E_r = \frac{\sqrt{\pi}}{2\beta}\frac{S}{\sqrt{A}} \tag{3.2}$$

Where E_r is the reduced elastic modulus, S is stiffness and β is a constant that depends on the geometry of the indenter. For triangular cross sections like the Berkovich and cube-corner indenters, $\beta = 1.034$. The reduced modulus, E_r is used to account for the fact that elastic displacements occur in both the indenter and the sample. The elastic modulus of the test material, E_s, is calculated from E_r using:

$$\frac{1}{E_r} = \frac{1-\nu_i^2}{E_i} + \frac{1-\nu_s^2}{E_s} \tag{3.3}$$

Where E_s and ν_s are the elastic modulus and Poisson's ratio for the test material; and E_i and ν_i are the elastic modulus and Poisson's ratio for the indenter. For diamond, the elastic constants E_i = 1140 GPa and ν_i = 0.07 are often used.

One of the more commonly used methods for analyzing nanoindentation load-displacement data is that of Oliver and Pharr [1]. In the Oliver-Pharr method, hardness and elastic modulus are determined from indentation data obtained during one complete cycle of loading and unloading. According to this method, the unloading curve can be fitted by the power-law relation

$$P = B(h - h_f)^m \tag{3.4}$$

where P is the indentation load, h is the displacement, B and m are empirically-determined fitting parameters, and h_f is the final displacement after complete unloading. The depth

along which contact is made between the indenter and the specimen h_c can also be estimated from the load-displacement data using:

$$h_c = h_{max} - \varepsilon \frac{P_{max}}{S} \qquad (3.5)$$

where h_{max} is the maximum depth of penetration at P_{max}, the peak indentation load, and ε is a constant which depends on the geometry of the indenter: for a Berkovich Indenter ε =0.75.

Once the parameters B and m are obtained (by curve fitting), the initial unloading stiffness S can be established by differentiating Eq. (3.4) at the maximum depth of penetration, h = h_{max}:

$$S = \left(\frac{dP}{dh}\right)_{h=h_{max}} = mB\left(h_{max} - h_f\right)^{m-1} \qquad (3.6)$$

With these basic measurements, the projected contact area of the hardness impression, A, is derived by evaluating an empirically determined indenter shape function at the contact depth, h_c; that is, $A = f(h_c)$. The shape function, $A = 24.55\ h_c^2$ relates the cross-sectional area of the indenter to the contact depth. In order to compensate for the effect of the finite tip radius of the Berkovich indenter as well as tip manufacturing differences, additional terms are empirically added as given below.

$$A = 24.5h_c^2 + C_1h_c + C_2hc^{1/2} + C_3hc^{1/4} + C_4hc^{1/8} + C_5hc^{1/16} \qquad (3.7)$$

Where $C_1 - C_5$ are constants for any specific indenter and are determined from nanoindentation experiments on fused quartz silica.

Finally, the hardness, H, and reduced elastic modulus, E_r, are derived from equation (3.1).

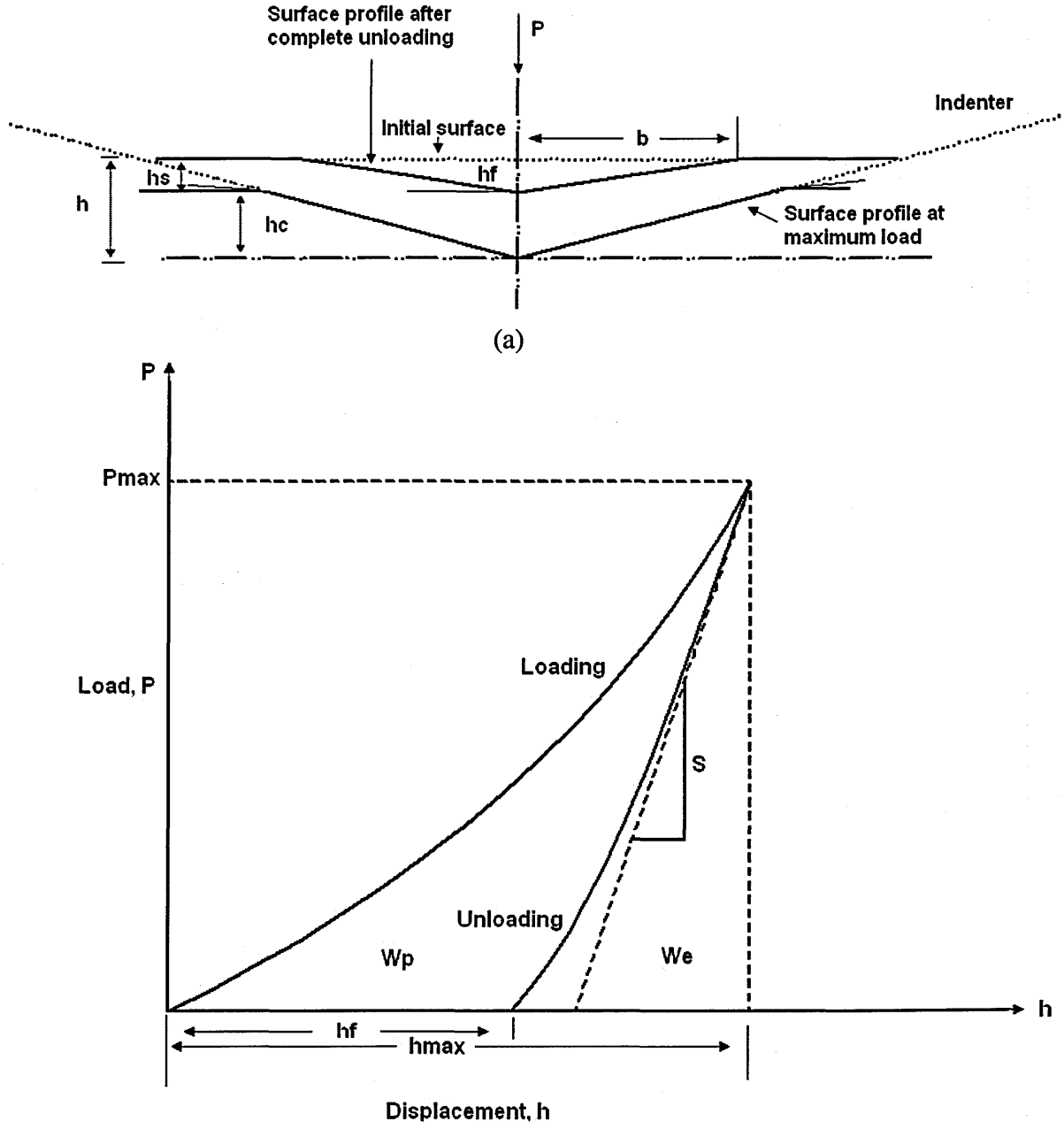

Fig. 3.1 - (a) Indentation process and (b) Load-penetration curve during loading and unloading

3.2.2 Correction with Atomic Force Microscopy (AFM)

One of the problems of the Oliver and Pharr approach is that it can markedly underestimate the true area of contact in cases where significant pile-up occurs. In these cases, the true contact area A can be obtained by combining the results of the Oliver–Pharr method $A_{O\text{-}P}$

with a correction which takes into consideration practical measurement of the pileup area A_{PU}:

$$A = A_{O\text{-}P} + A_{PU} \tag{3.8}$$

This approach has been used by a number of workers including Beegan [4, 8], Saha [10] and Kese [3, 6, 9]. Beegan et al. [4, 8] and Saha [10] calculated the area of the pile-up by considering the pile-up as forming an arc of a certain radius; whilst Kese [3, 6, 9] assumed pileup to be a semi-ellipse with its major axis corresponding to one side of the indent triangle, and the minor axis being the horizontal distance from the vertex of the triangle to the peak height of the pileup.

The area of pile-up is typically obtained from measurements of the pile-up area from scanning electron micrographs or atomic force microscopy images of the indentations.

3.2.3 Work of Indentation

In nanoindentation experiments, the work of indentation can be calculated conveniently from the areas bounded by the loading and unloading curves (Fig. 3.1). The area under the loading curve gives the total work W done by the loading device during indentation. The elastic contribution to the total work, W_e, can be deduced from the area under the unloading curve, and the energy absorbed by plastic deformation is then the difference between these:

$$W_p = W_t - W_e \tag{3.9}$$

Stillwell and Tabor [15] first applied this method to determine hardness. This technique equates the conventional hardness, of maximum applied load divided by the residual area of indent impression, to the plastic work divided by the volume of the indent:

$$\frac{\text{Load}}{\text{Plastic area}} = \frac{\text{Plastic work}}{\text{Plastic volume}} \tag{3.10}$$

The area under the load-penetration curve represents the total work W_t, given by:

$$W_t = \int_0^{h\,max} P\,dh \tag{3.11}$$

For indentation, Kick's Law is given by $P = Ch^2$. Kick's law assumes that the material does not exhibit indentation size effects and that hardness is constant with load. Substituting for P in eq. 11 gives:

$$W_t = \int_0^{h\,max} Ch^2 dh = \frac{Ch_{max}^{\ 3}}{3} = \frac{P_{max}h_{max}}{3} \qquad (3.12)$$

Now according to Tuck [2]:

$$H = kP/h^2 \qquad (3.13)$$

Where k is a constant which takes into account the indenter geometry and the choice of hardness definition; its value is 0.0408 for a Berkovich indenter.

Rearranging equation 3.13 gives:

$$P = \frac{Hh^2}{k} \qquad (3.14)$$

and

$$h = \sqrt{\frac{Pk}{H}} \qquad (3.15)$$

and equation 3.11 thus becomes:

$$W_t = \int_0^{h\,max} \frac{Hh^2}{k} dh = \frac{Hh_{max}^{\ 3}}{3k} \qquad (3.16)$$

If we now substitute h from (3.15) this give,

$$H = \frac{kP^3}{9W_t^{\ 2}} \qquad (3.17)$$

If we consider hardness as a function of only plastic deformation then we need to use the plastic work during the indentation process and thus eq. 3.17 becomes:

$$H = \frac{kP^3}{9W_p^{\ 2}} \qquad (3.18)$$

Hence using Eqs. (3.17 and 3.18) the hardness of a material can be obtained from the work of indentation technique.

Tuck [2, 20] and Beegan [12] applied this technique to ductile materials where significant pile-up occurs at the edges of indentations.

In this paper, we use the work of indentation approach to calculate the hardness using both the total work (i.e. W_e+W_p) and the plastic work W_p alone.

3.3 Materials and Experimental Methods

3.3.1 Material Details

In aerospace structural applications, the use of aluminium alloys leads to an overall reduced weight and, thus, to reduced fuel consumption. Alloy 2024-T351 plate with cladding on both sides is used in fuselage and wing structural areas where stiffness, fatigue performance and good strength are required. Copper and magnesium are the main alloying elements for 2024 plate used to increase the strength of 2024 aluminium alloys by the precipitation hardening which is achieved by post-processing methods. The "T351" describes the post processing which indicates that the sample is solution heat treated, cold worked by stretching and artificially aged.

Aluminium–copper alloys are susceptible to corrosion at the aircraft operating conditions. To prevent corrosion a common practice for the aircraft industry is the roll bonding of protective coatings of pure aluminium on the surface of the material. This is called cladding of substrate. To characterize the fuselage material, the materials used in this study were in the form of plate of Al2024-T351 of 2 mm thickness, with an aluminium cladding of 100μm on both faces as shown in Fig. 3.2.

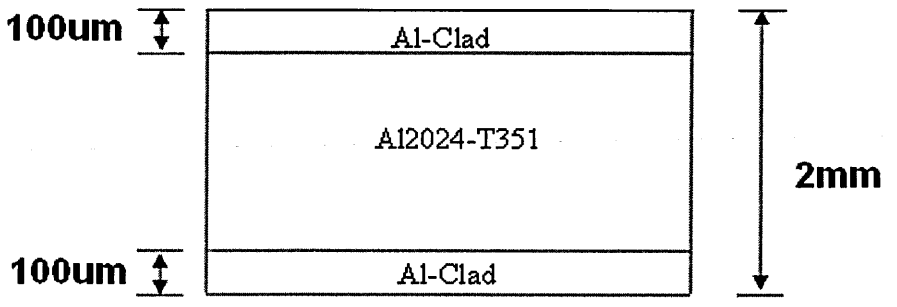

Fig. 3.2 - Sectional view of Al2024-T351 plate

The grain size of the Al2024-T351 was determined by quantitative metallography and electron back scattered diffraction (EBSD), and was found to be 20μm. The grains were equiaxed and showed a random orientation. Fig.3.3 shows the typical grain distribution for Al 2024-T351. The grain size of the Al-clad was not measured directly here owing to the difficulties of preparing metallographic samples of such a thin, soft layer which is difficult to etch and disappears during early stages of grinding, but previous work has shown it to be in the range of 30-70μm (Reference: Professor P.E.Irving, Cranfield University, Personal communication).

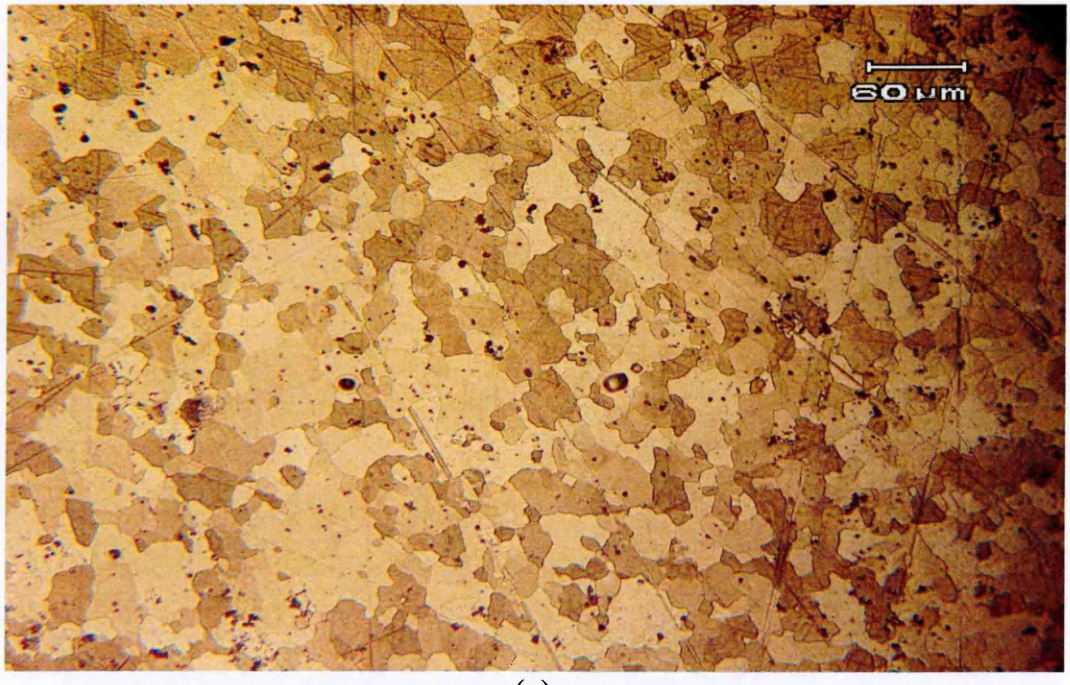

(a)

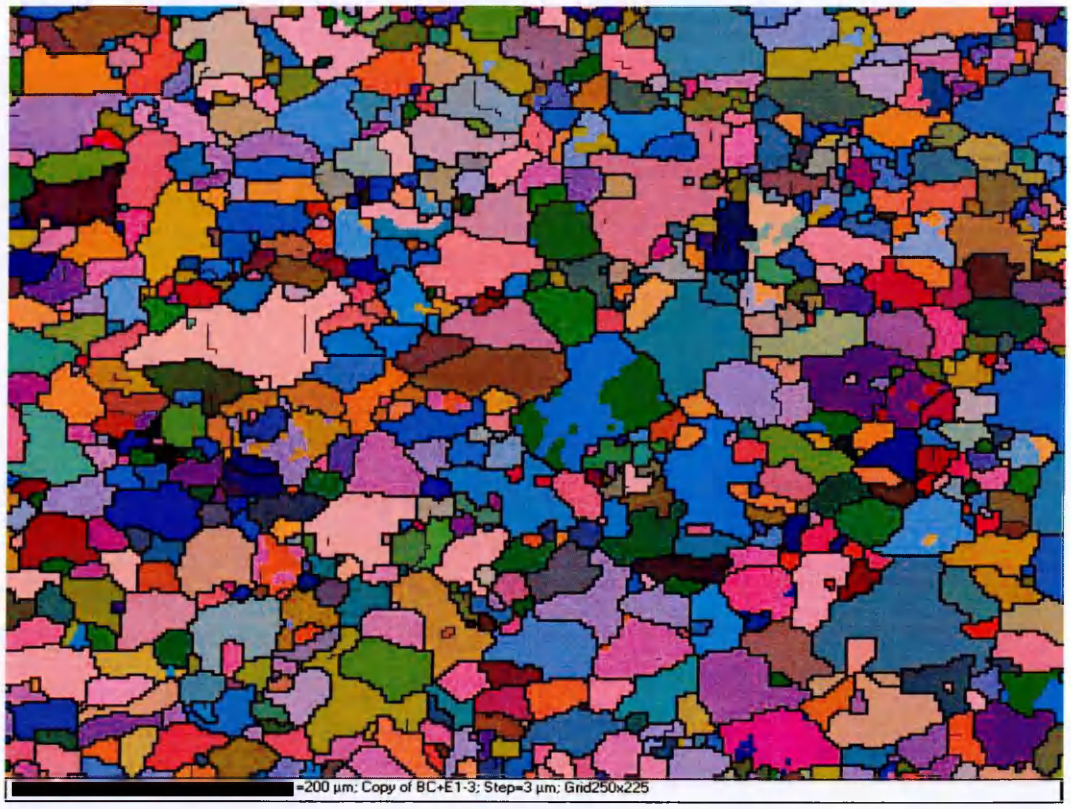

(b)

Fig. 3.3 - Grain size determination from (a) Optical microscopy (b) EBSD.

Material properties of Al 2024-T351 are obtained from tensile testing according to ASTM standard E 8/E 8M-08 [28]. The stress strain curve is shown in Fig.3.4 and the elastic-plastic properties so obtained are given in Table 3.1.

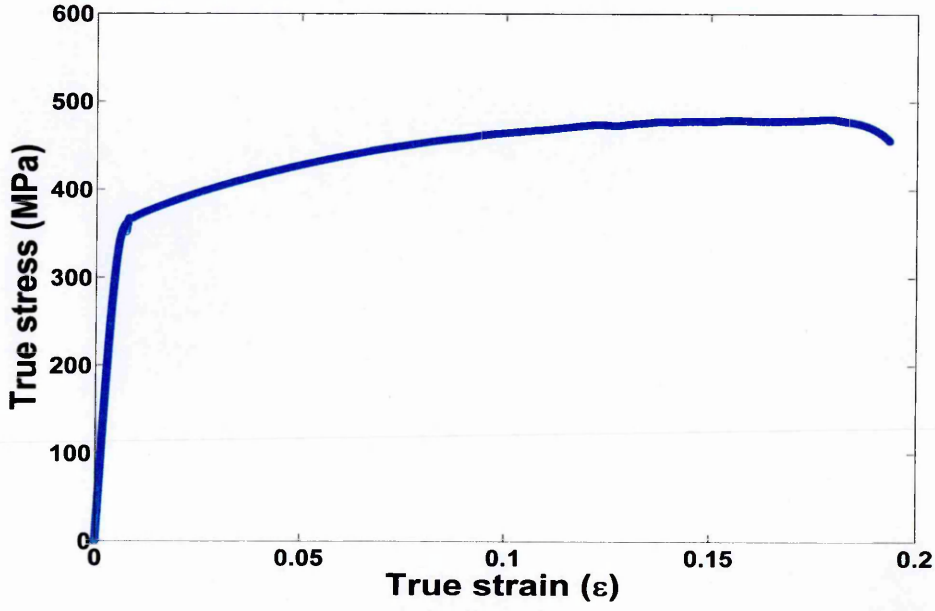

Fig. 3.4 - Stress strain curve of Al 2024-T351.

Material	Composition (Wt%)	Elastic Modulus (GPa)	Yield Stress (MPa)	Strain hardening exponent	E/σ_Y
Al 2024-T351	Cu 3.8-4.9, Mg 1.2-1.8, Mn 0.3-0.9, Zn 0.15max, Cr 0.1max, Si 0.05max, Fe 0.5max, Remaining Al	68	360	0.1	188
Al-cladding	Al-99.99	69	120	0.1	575
AA 5091	Mg 4, Li 1.3, C 1.1, O 0.4, Remaining Al	78	448	0.065	175

Table 3.1 - Mechanical properties of Al 2024-T351, Al-cladding and AA 5091.

Later in this study, aluminium alloy 5091 has been used as a model alloy. It is produced by a powder metallurgy process, which is ideal for synchrotron measurement owing to its fine grain size (~0.6 μm). Aluminium 5091 is a precipitation hardened alloy which contains a dispersion of very fine oxides (Al_2O_3) and carbides (Al_4C). This small grain size allows good diffraction data to be obtained even with a very small sampling gauge volume. Material properties for aluminium alloy 5091 are given in Table 3.1 [16] and Fig.3.5 shows stress strain curve obtained from tensile testing.

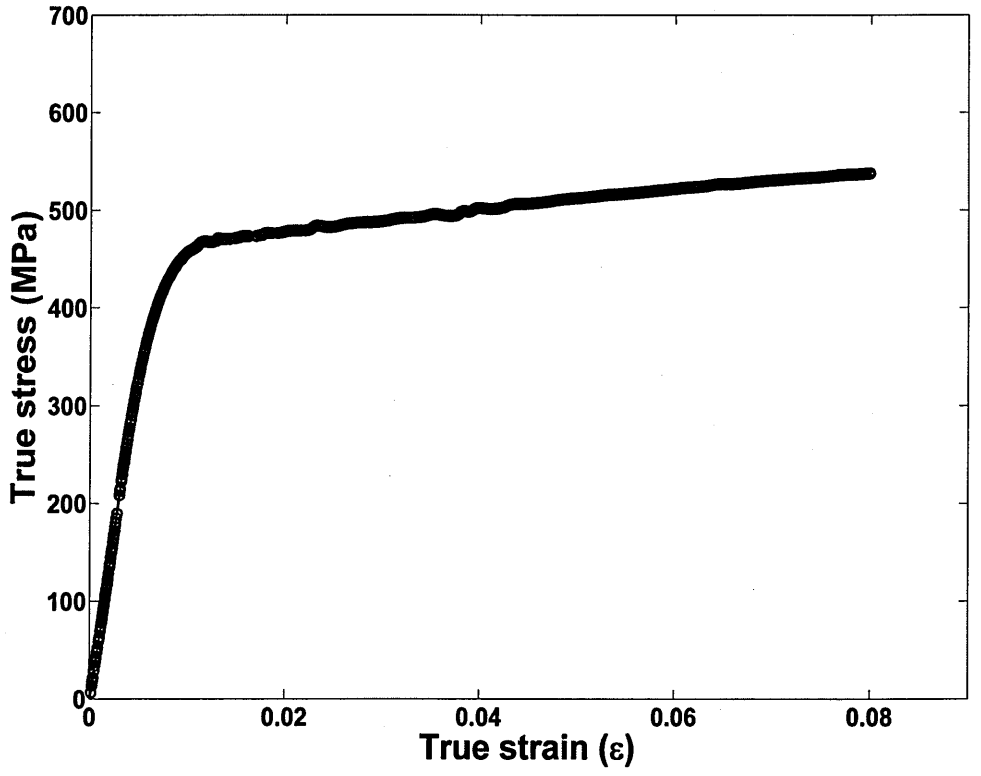

Fig. 3.5 - Stress strain curve of Al 5091.

3.3.2 Surface Roughness

Surface scanning of both materials was performed using atomic force microscopy (AFM), after surface polishing of samples to a 1 micron finish. A DME Dual Scope C-21 AFM was used to perform observations of the indentations and particularly of the pile-up at their periphery. Measured surface profiles are shown in Fig.3.6. which shows the topography of the clad and unclad layers, respectively. The surface roughness of clad was greater than the surface roughness of the Al 2024-T351.

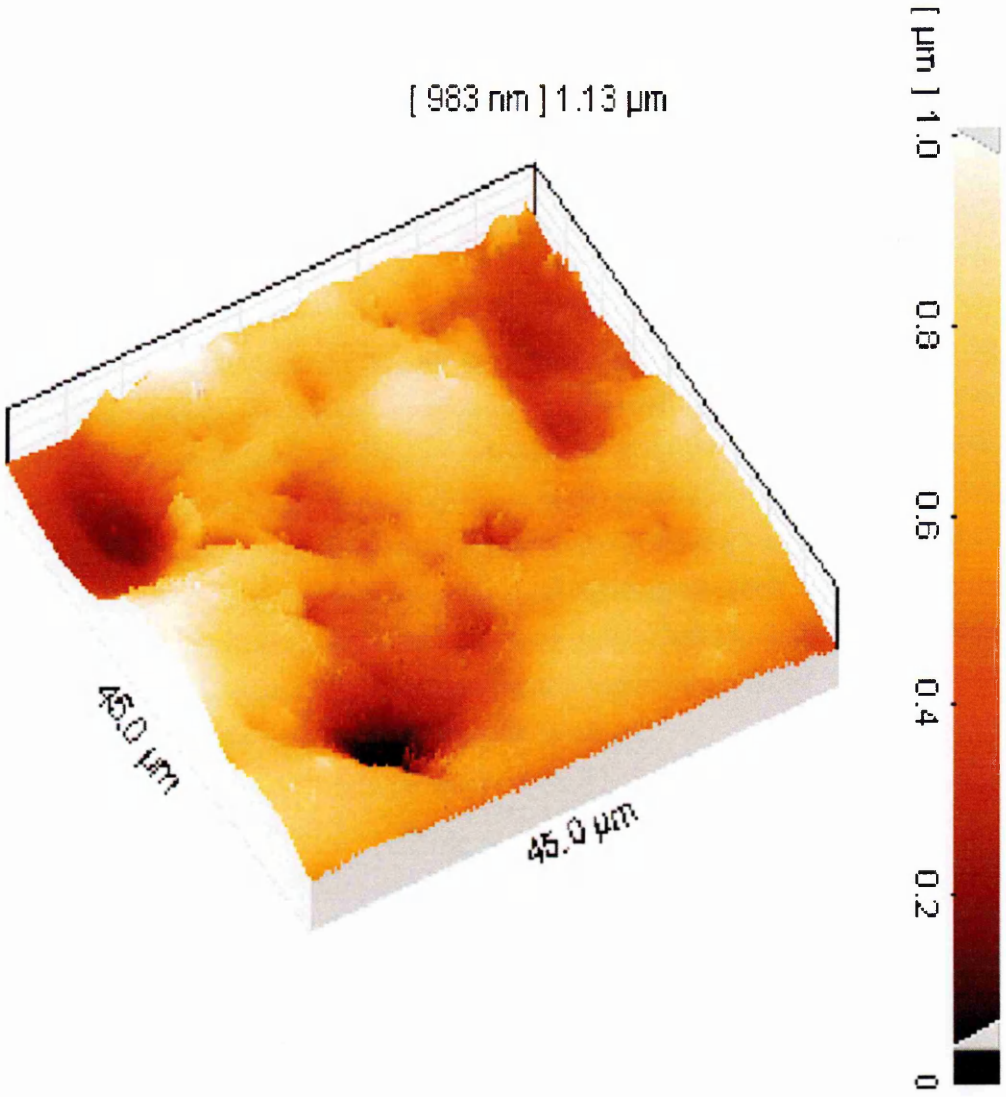

(a)

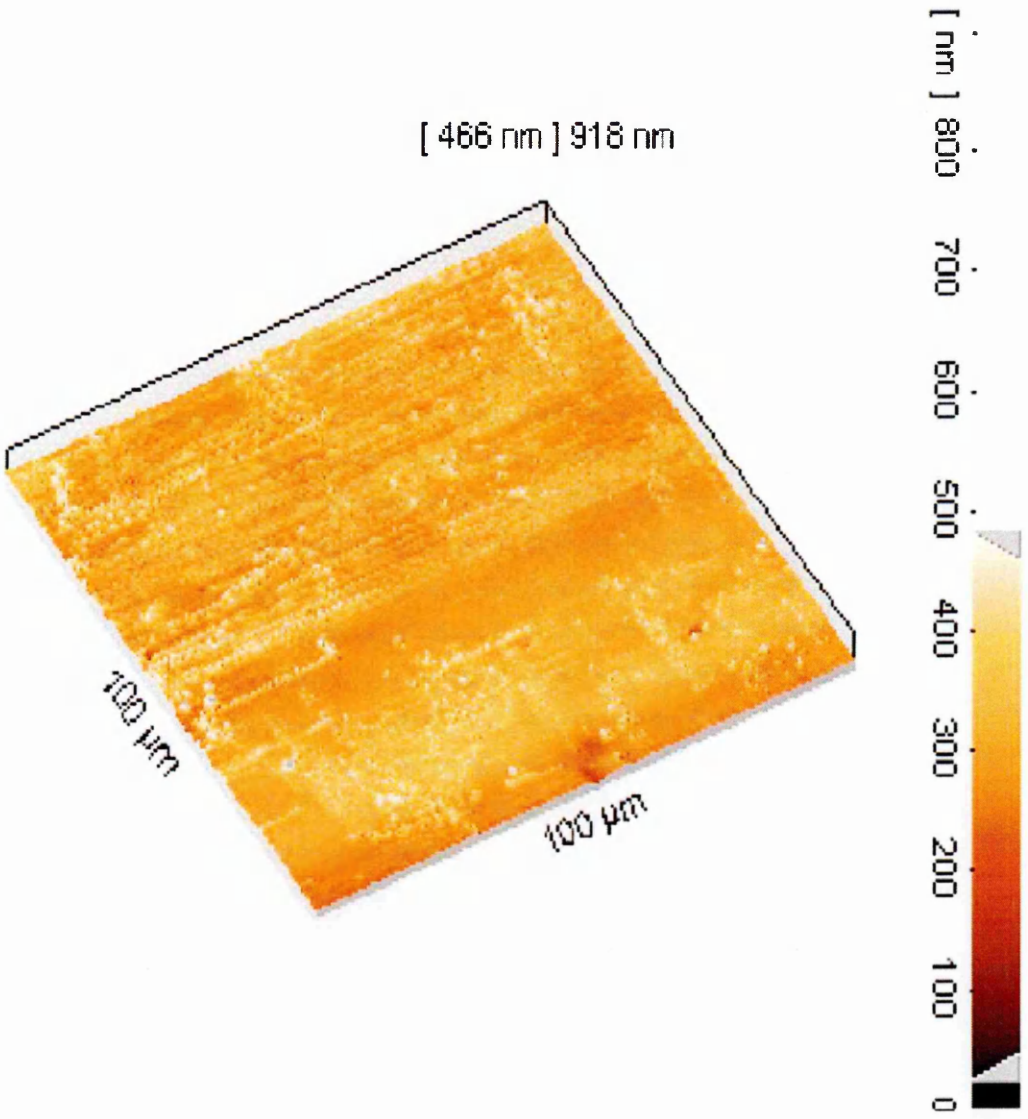

(b)

Fig. 3.6 - Surface scanning of (a) Al-clad and (b) Al 2024-T351

3.3.3 Experimental Method

The mechanical properties of the Al-Clad and substrate Al2024-T351 were characterized using an MTS Nanoindenter XP system with a Berkovich indenter tip (Fig.3.7). The instrument was operated in basic hardness load-displacement mode which simply records load, displacement and time, and contact stiffness mode (CSM) where an oscillating force with a force amplitude generally several orders of magnitude smaller than the nominal load is applied at the same time as the indenter load. This allows the contact stiffness to be obtained at all points on the load-displacement curve and hardness and modulus can be

obtained as function of penetration depth. Indentations were made using a constant nominal strain rate ($\dot{P}/P$) of 0.05 s^{-1} and the drift rate before testing was required to be <0.05nm/s. 25 indents were made at each depth in an array of 5 x 5 with spacing of 100 μm in both axes. The depths of the indentations ranged from 200nm to 2400nm in steps of 200 nm. These indentation depths correspond to applied loads from 1 to 70 mN load for Al-cladding and 2.5 to 220 mN for Al 2024-T351.

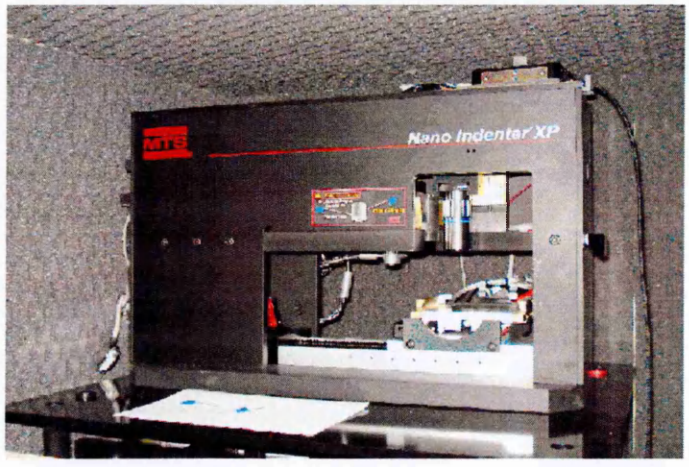

Fig. 3.7 - MTS Nanoindenter used in the study.

3.4. Results and Discussion

3.4.1 Characterization from Oliver and Pharr Model

When the indentation data was analyzed using the Oliver–Pharr (O-P) model, values of both the hardness and modulus were found to be overestimated as shown in Fig.3.8. It can be seen that up to 400nm depth, hardness and modulus values were relatively high. This particular effect is called indentation size effect (ISE) in which the Berkovich indenter's tip bluntness comes in to play and the area fitting function given in eq. 3.7 tries to calculate a best estimate of the area. An ideal Berkovich indenter is assumed to have no roundness at its tip. But tip bluntness occurs in every indenter due to machining capability during manufacturing. This tip blunting effect is more significant for shallow indents of depth of the order of the roundness of the tip. Up to this range of depth, a Berkovich indenter behaves like a spherical indenter, however the O-P model calibrates the area to compensate for tip roundness effect with a polynomial area function as shown in eq. 3.7, but this still

has physical limitations. Tip blunting effects can be obtained by fitting a square root of load and depth curve [22-24] and usually found as 200 to 400nm. So any indentation depth in the range of up to 200~400nm will show indentation size effect in which hardness and modulus would show overestimated values hence these depths of penetration will be avoided in extraction of residual stresses.

The hardness and modulus obtained from O–P for the Al cladding were calculated as 0.48–0.56 GPa and 73–75 GPa, respectively; and for the Al2024-T351, 1.64–1.80 GPa and 77–80 GPa, respectively. Typical literature values of hardness and elastic modulus for hard aluminium (rolled or stretched) are 0.37– 0.50 GPa and 69 GPa, respectively, and for Al 2024-T351 are 1.44–1.7 GPa and 72 GPa, respectively [25]. These hardness values are for bulk materials, measured by traditional macro-Vickers indentation tests which are unsuited to measure the relatively thin clad layers here. The hardness values for the Al-cladding, measured by nanoindentation, were thus 25% higher than the literature values, whilst the values for Al 2024-T351 were 15% higher. This overestimation, for both the hardness and the modulus, can be attributed to the pileup around the indentations, which is not accounted for in the analysis. Pile-up effects on macroindentation measurement are less significant than for nanoindentation as pileup occurs mainly around the edges of the indentations, and macro-indentation measurement is based upon evaluation of the size of the indentation diagonals. Therefore, it is more critical for the accuracy of nanoindentation measurement that pile-up effects are taken into account.

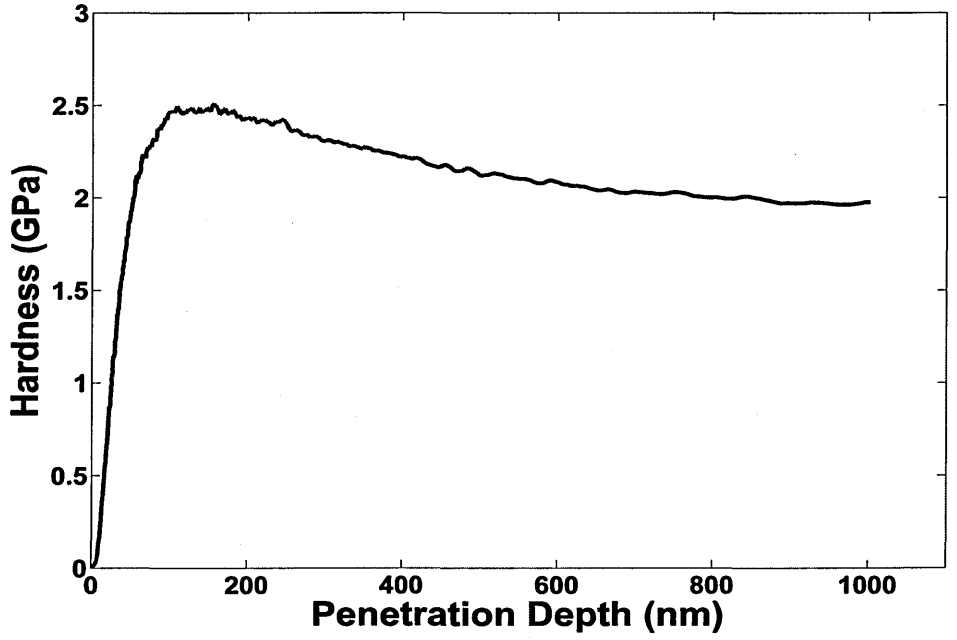

(a)

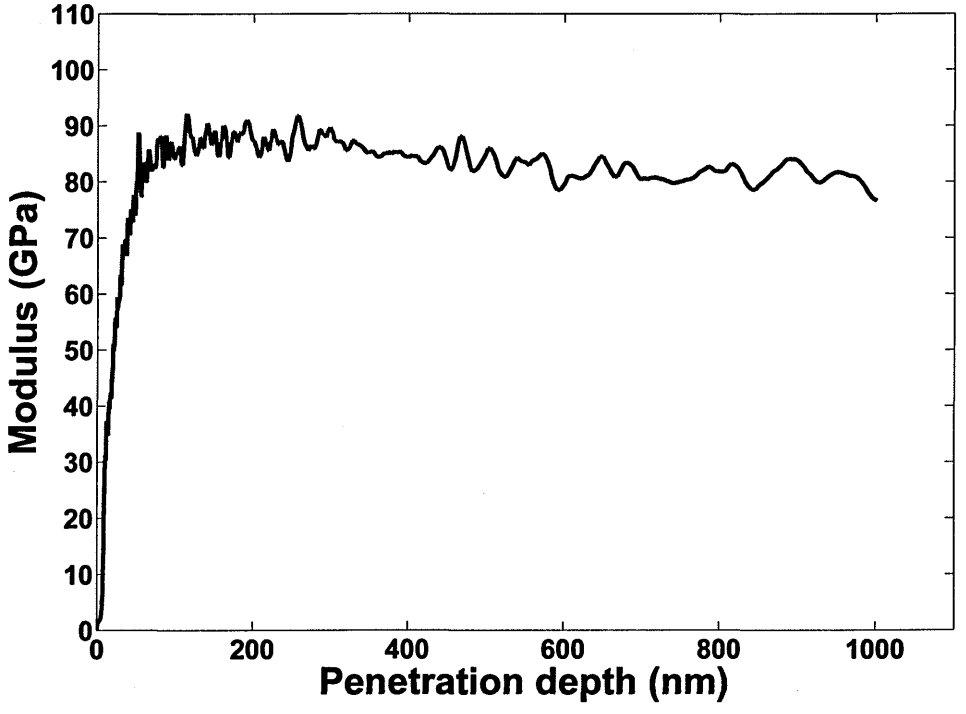

(b)

Fig. 3.8 – (a) Hardness and (b) elastic modulus values of the Al 2024-T351 calculated from the indenter operated in Contact Stiffness Mode

3.4.2 Pile-Up Formation and AFM Scanning

Since aluminium has relatively low hardness and modulus, pileup around the indenter is to be expected, even at small indentation depths. This is shown in Fig.3.9 which shows a scanning electron microscope image of an indentation at load of 500mN in clad Al 2024-

T351. There is clear evidence of pileup around the indentation periphery. Fig.3.10 (a) shows a 3D profile of an indent which shows pileup around every edge of indent. Fig.3.10 (b) shows a line profile though a triangular indent and Fig.3.10 (c) shows the AFM height profile from the corner of an indentation through the midpoint of the edge of the indentation. Pile-up on the edge can be clearly seen in the AFM trace. Hence, the actual contact area includes the area contained in the pileup, and because significant pileup occurred at all the indentations its influence on the determination of the true contact area cannot be ignored. The additional contact area associated with the pileup can contribute significantly to the load bearing capacity of the contact.

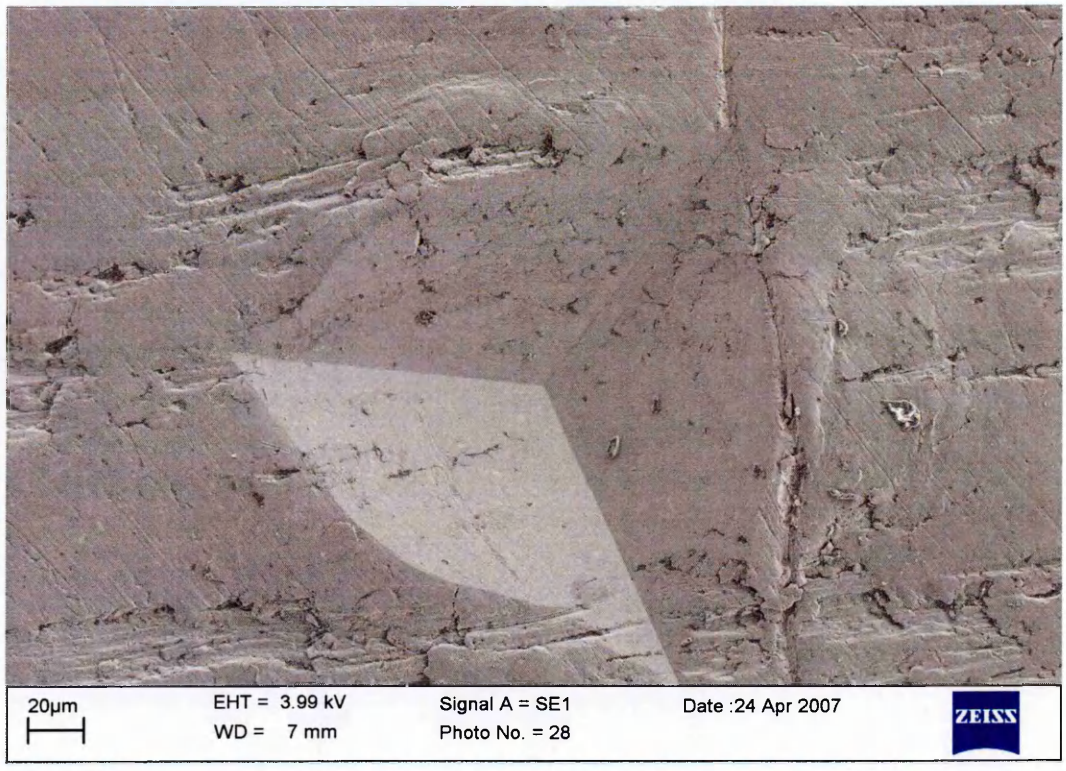

Fig. 3.9 - SEM image of an indent at 500mN load in Al-cladding showing pile-up

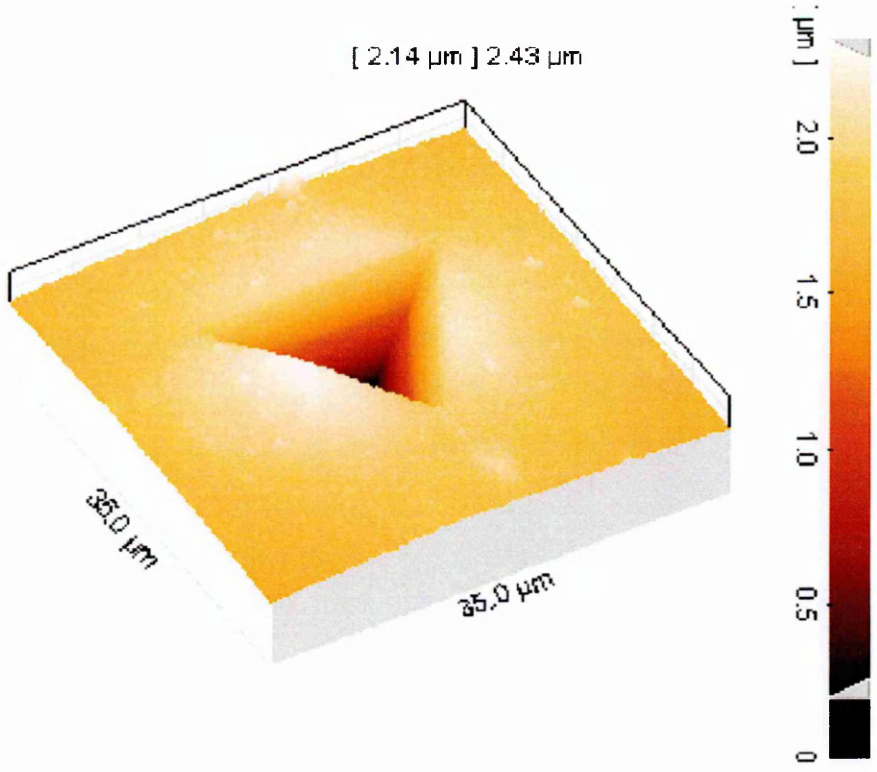
[2.14 µm] 2.43 µm
35.0 µm
35.0 µm
[µm]
2.0
1.5
1.0
0.5
0

(a)

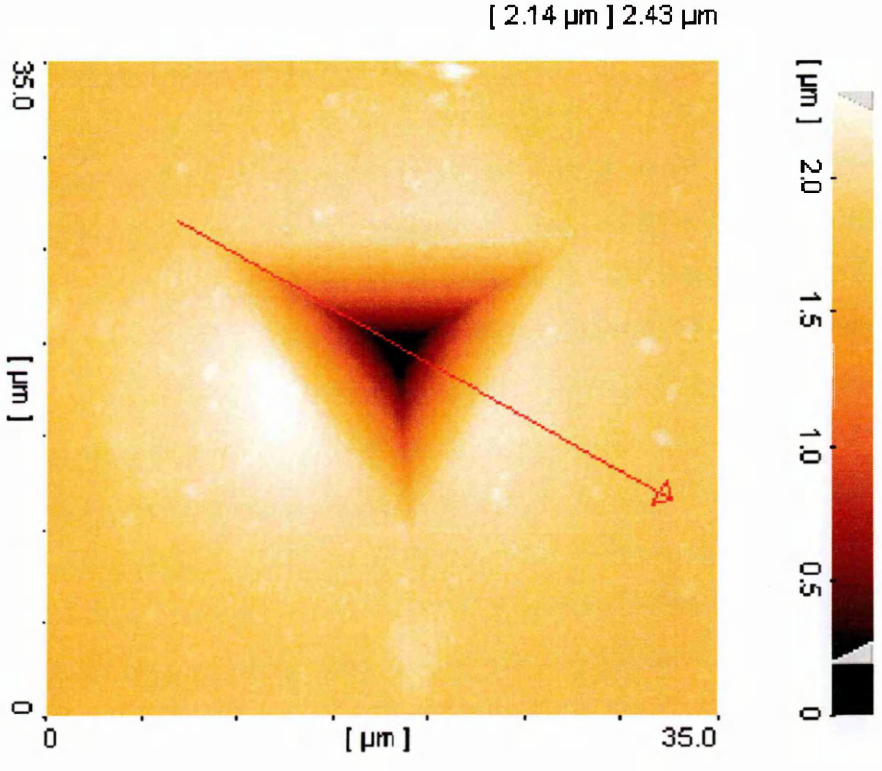
[2.14 µm] 2.43 µm
35.0
[µm]
0
0
[µm]
35.0
[µm]
2.0
1.5
1.0
0.5
0

(b)

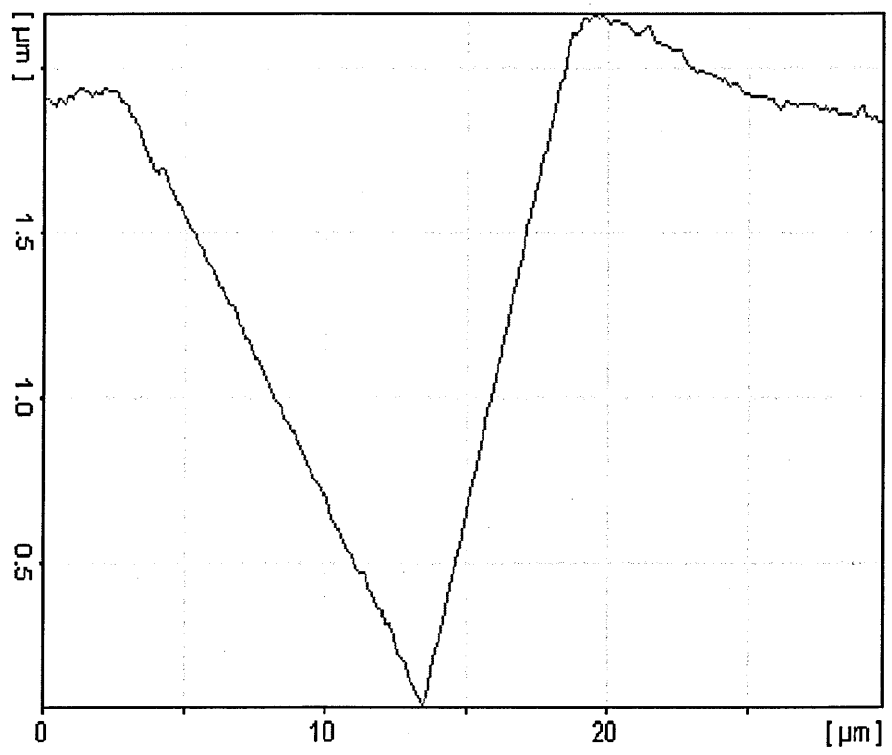

(c)

Fig. 3.10 - AFM image of an indent in Al-cladding at 60mN load, (a) 3D profile (b) showing the line profile (c) height profile along the line shown in figure 3.10b, showing pile up on the indent edge

3.4.3 Calculation of Area

The area of pile-up in Fig.3.11 forms a semi-ellipse. Thus, following Kese [3, 6, 9], the area of pile-up was calculated from the measurements as illustrated in Fig.3.11. The point T on Fig.3.11 marks the perimeter of the contact when viewed in profile; its horizontal displacement from the edge L of the nanoindentation is measured to be a_i (i =1, 2, 3 for the three pile-up lobes).

The pileup contact perimeter is obtained by projecting a semi-ellipse of major axis b and minor axis a_i, so that the length of the side of the projected triangular area is b, calculated at the contact depth h_c, while a_i is measured on the indent profile image as the horizontal distance of the pileup contact perimeter T from the edge L of the indentation.

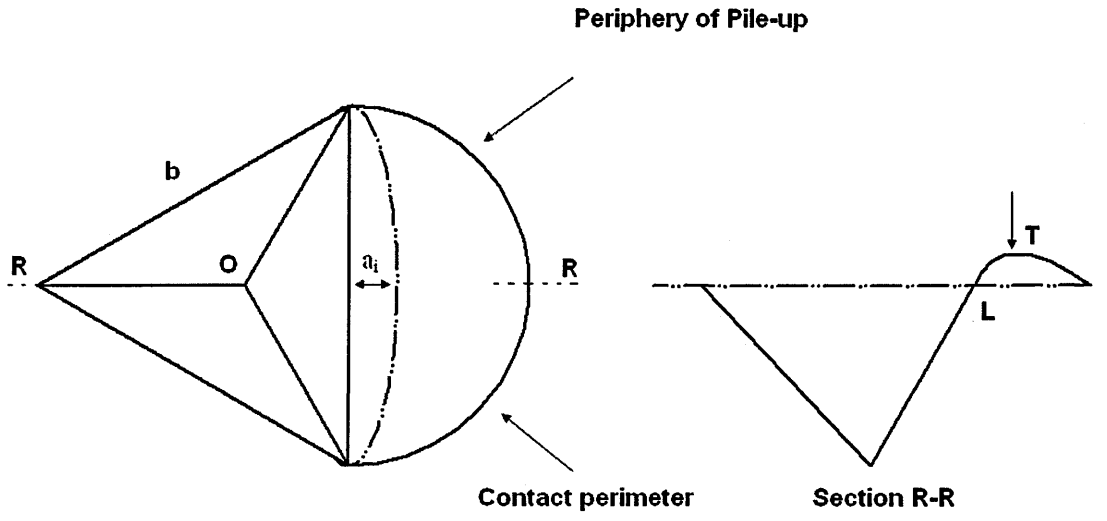

Fig. 3.11 - Analysis of the pile-up profile around the periphery of an indent

The triangular indentation area can be calculated as:

$$A_{O\text{-}P} = 0.433\, b^2 \qquad (3.19)$$

The indentation area as a function of contact depth for a perfect Berkovich tip is given by:

$$A_c = 24.56\, h_c^{\,2} \qquad (3.20)$$

From equations 3.19 and 3.20:

$$b = 7.531\, h_c^{\,2} \qquad (3.21)$$

The total pile-up area of the three semi-elliptical lobes around each side of the indent triangle, which may differ from each other, will be

$$A_{PU} = \frac{\pi b}{4} \Sigma a_i \qquad (3.22)$$

a_i can be obtained by measuring the horizontal displacement around each of the three sides of the indent

$$A_{PU} = 5.913 h_c (a_1 + a_2 + a_3) \qquad (3.23)$$

The total indentation area A can be calculated by adding this pile-up area to the area determined from eq.3.19.

The amount of pileup area in terms of the percentage of triangular area of indent calculated from the Oliver-Pharr Model is shown in Fig.3.12. The pile-up was measured for indentations made to different penetration depths and found to increase with penetration depth for both Al2024-T351 and the cladding; but for the Al-cladding, owing to its higher E/σ_Y ratio, more pile-up was observed at indentation depths of 1μm or greater.

The E/σ_Y ratios for both Al-cladding and Al2024-T351 are given in table 3.1. It can be seen that the E/σ_Y ratio is lower for Al2024 than the Al-cladding. If E/σ_Y =0, contact is strictly elastic and dominated by sink-in, if $E/\sigma_Y = \infty$, there is predominantly plastic deformation, and extensive pile-up occurs. The differences in the percentage pile-up seen in Fig.3.12 can thus be accounted for by the higher E/σ_Y ratio of the Al-cladding.

A tensile test was performed on Al2024-T351 to determine the strain-hardening exponent for Al2024-T351. This was calculated to be 0.1 which is small and this combined with the relatively high E/σ_Y ratio would predict that significant pile-up would be expected (as is observed here). Tensile testing of Al-cladding was not possible as it was present in the form of protective coating of thickness 100μm but nanoindentation reverse analysis were used to extract its yield stress and strain hardening exponent and was found as 120MPa and 0.1 respectively. Detail of reverse analysis is given in a chapter later in this thesis.

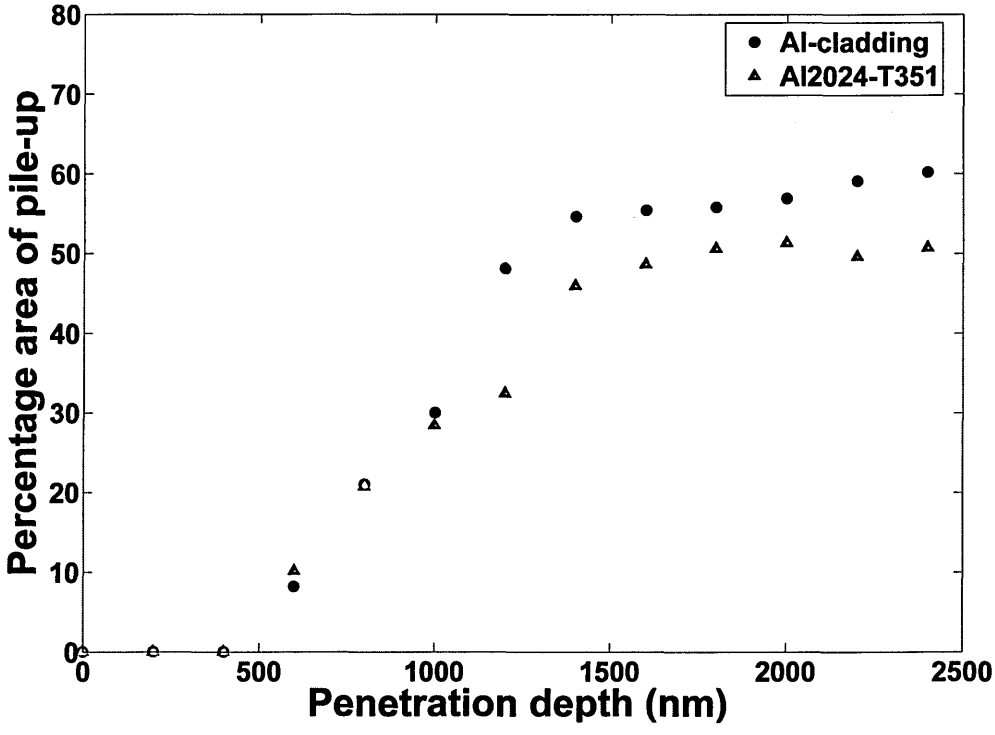

Fig. 3.12 - Percentage amount of pile-up for Al-clad and Al 2024-T351 at different depths

It can be seen that pile-up for both of the materials increased with penetration depth and was lower below 600nm depth. Keeping in view of indentation size effect up to 400nm depth and the continuous increase in pile-up beyond 600nm depth, the optimized depth obtained was 600nm which showed a good compromise being away from ISE region and exhibition of minimum pile-up.

3.4.4 Difference in Elastic Recovery of Al-Clad and Al2024-T351

The Al-clad material has a much lower hardness than the Al2024-T351. Nanoindentation tests at the same load give a greater indentation depth in the Al-clad compared to Al2024-T351, as shown in Fig.3.13 (a). The Al-cladding shows less elastic recovery of the displacement on unloading as compared to Al 2024-T351. The percentage elastic recovery W_e for the Al-cladding is only 3–4% of the total work W_t, as compared to Al2024-T351 for which the elastic recovery is 10–12% as shown in Fig.3.13 (b).

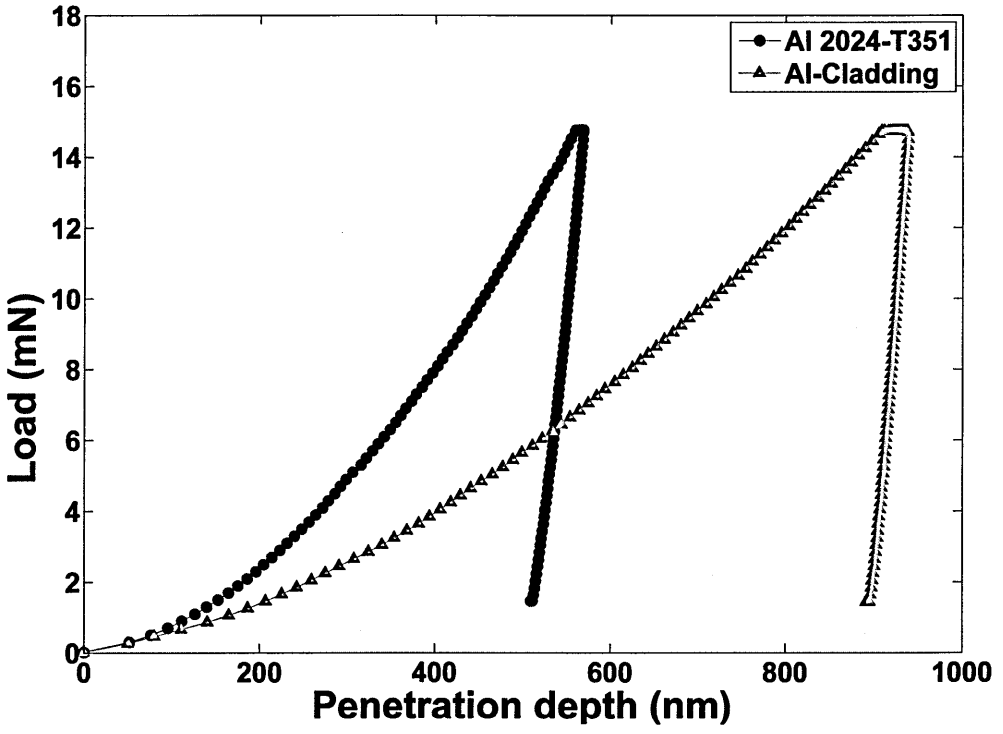

Fig. 3.13 (a) - Load-displacement curves at a load of 15mN.

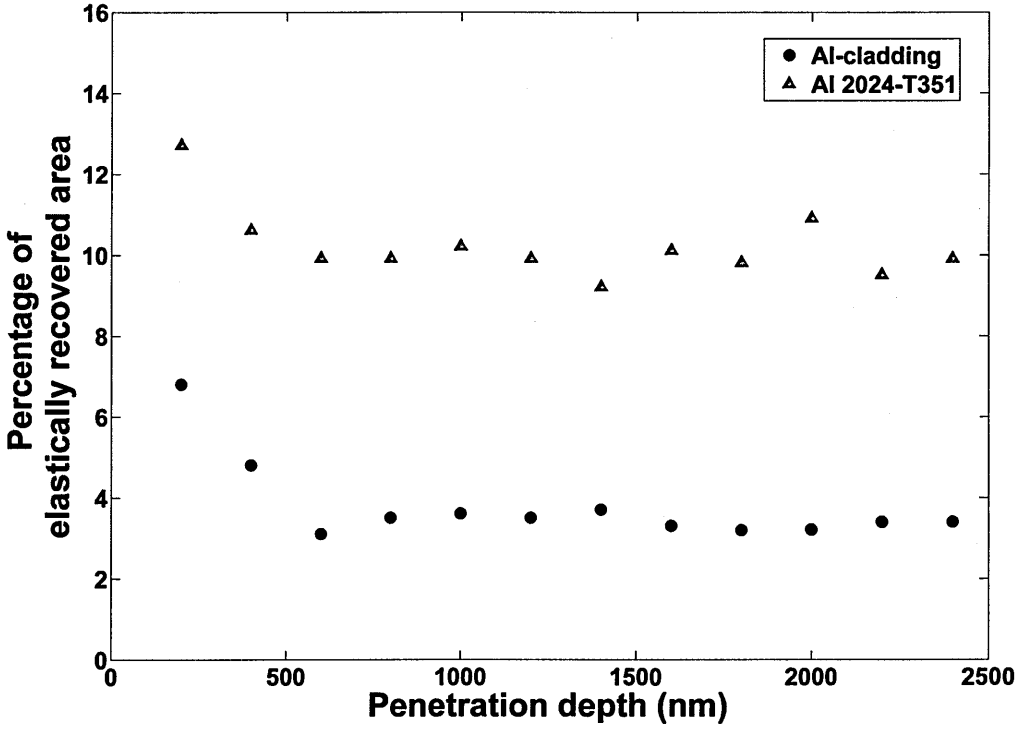

Fig. 3.13 (b) - Elastic recovery for Al-cladding and Al2024-T351

3.4.5 Anisotropy and Texture

One aim of this project was to calculate residual stresses from nanoindentation response. This would require indentation at low loads to study the deformation response of local regions near scribe roots. One concern of indenting at low loads which may indent single grains is the degree of variation of load-displacement curve between different grains. To extract residual stresses from nanoindentation this aspect has to be considered, as whenever there is some variation obtained from load-displacement curve it does not necessarily mean that this difference is due to residual stress but it could be due to grains of different orientation. Hence a grain orientation map was determined using EBSD to observe the different responses of differently oriented grains.

The crystallographic texture of various common diffracting planes was measured by electron backscatter diffraction (EBSD). In this study the texture pattern was determined and represented in terms of pole figures. The electron backscatter diffraction technique reveals the micro-texture pattern with high spatial resolution. In the experiments to determine the texture pattern in Al 2024-T351 and Al-cladding, a step size of 20 μm over a grid of 3mm × 3mm was used to ensure that information on the crystallographic texture pattern was obtained from a large number of grains. Two sample pieces designated as 1 & 2 were trimmed from a large plate as shown in Fig.3.14.

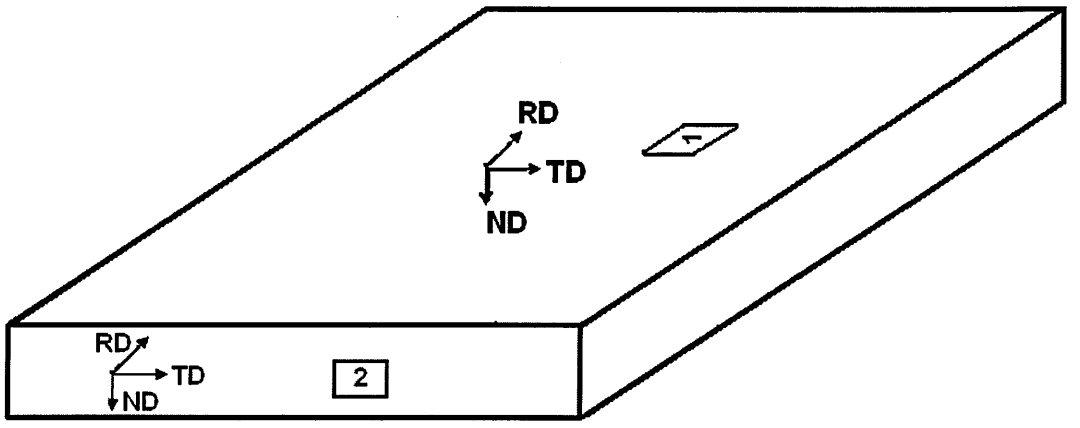

Fig. 3.14 - Al 2024-T351 plate for extraction of texture samples

Electron back scatter maps and pole figures for both of the pieces are shown in Fig. 3.15 and 3.16. It can be seen that there was difference in grain size distribution for sample 1 and 2. Grains were elongated for sample 2 in the normal direction and grain size for some of the grains reached to as large as ~100 μm. It can be seen that in the rolling direction of the plate a weak texture was present in which the intensity reached to ~5. This could be considered as a relatively weak texture as compared to other processing induced textures, like in welding this intensity can reached to ~40 which represents strong texture.

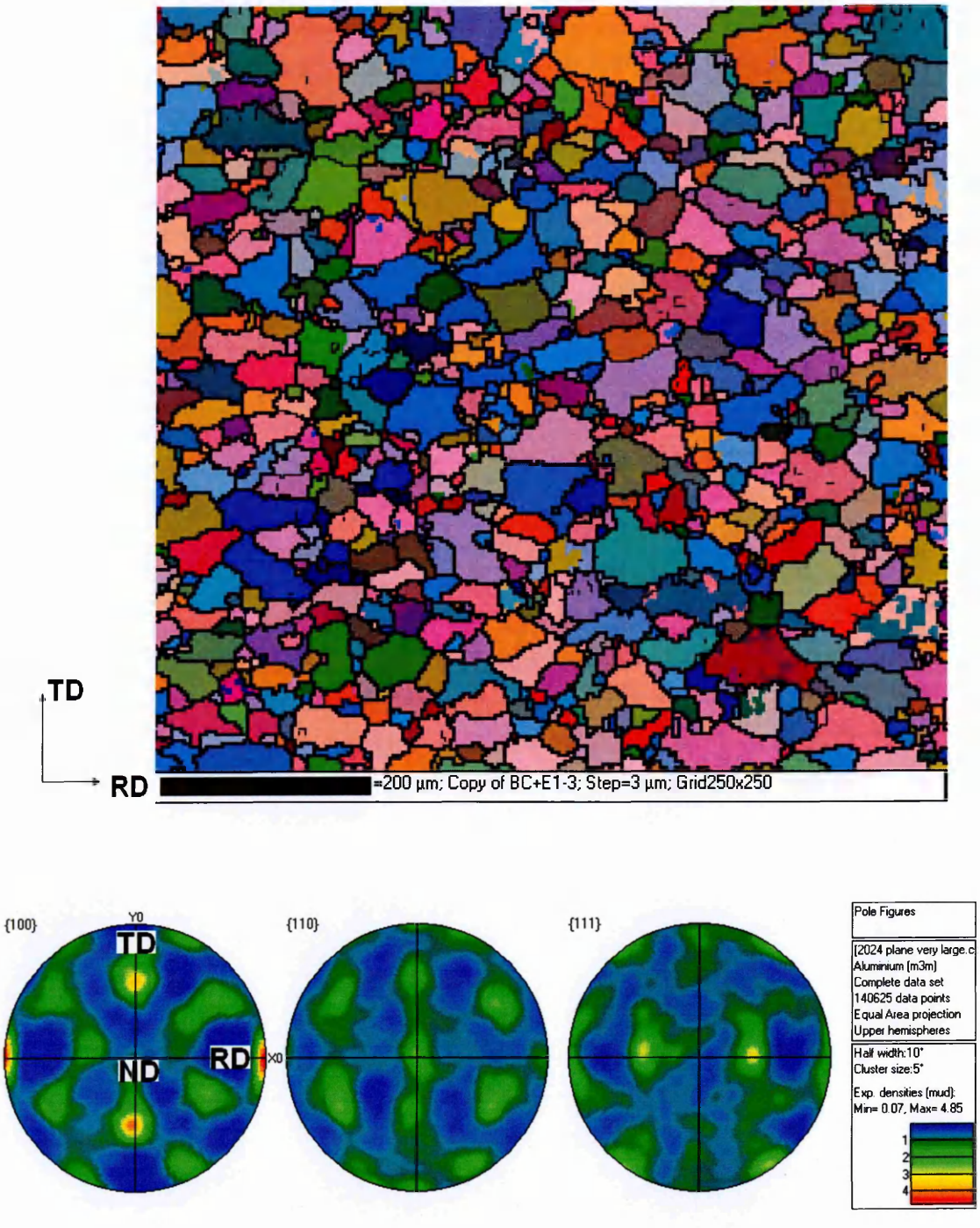

Fig. 3.15 - EBSD map and pole figure for Al 2024-T351 for sample #1

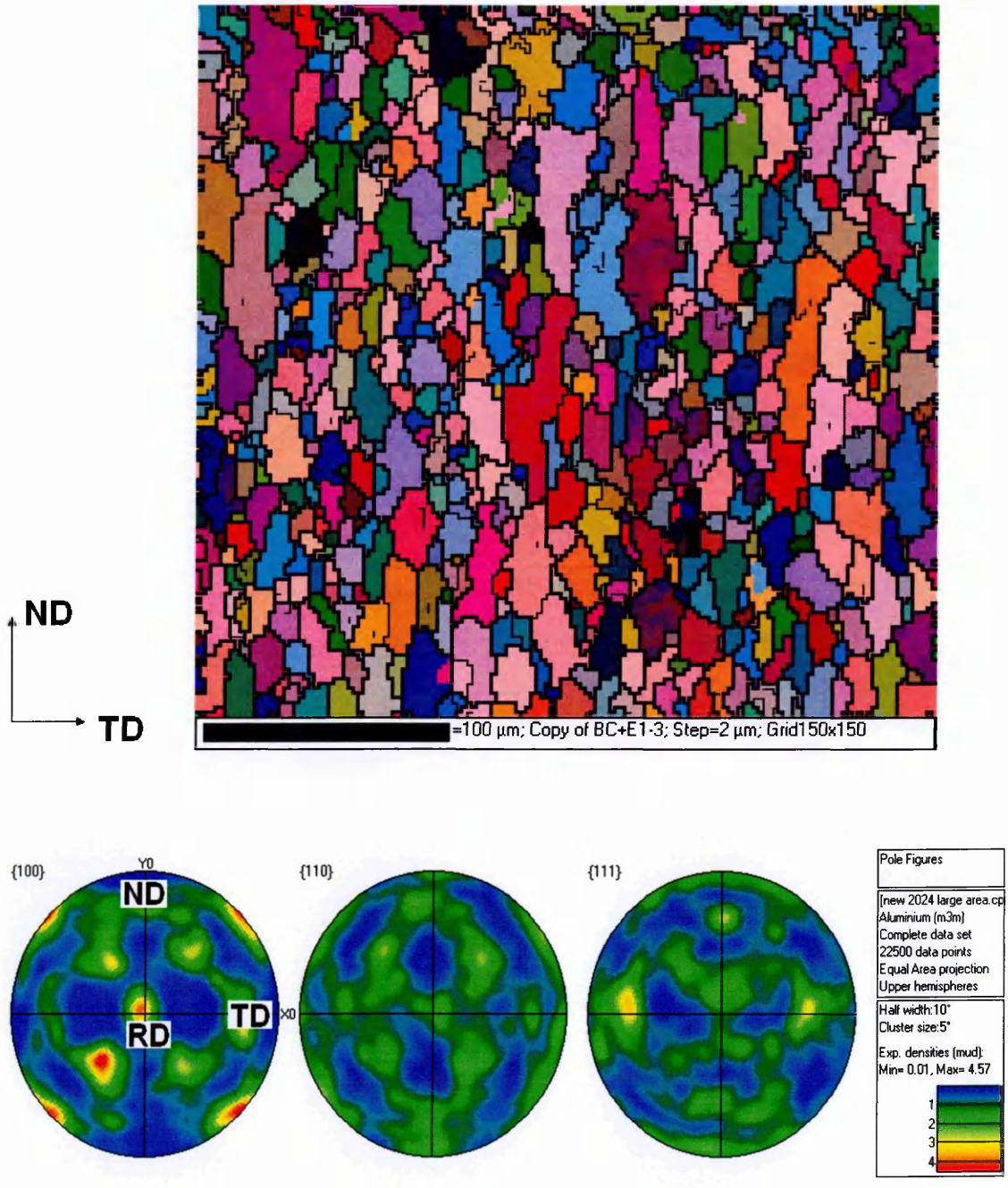

Fig. 3.16 - EBSD map and pole figure for Al 2024-T351 for sample #2

Sample preparation of EBSD required grinding and polishing of samples up to 1 µm finish. Due to softness of cladding and its presence in the thickness of only 100 µm, preparation of metallographic samples was not possible. Only section of the clad Al 2024-T351 could be tested and very similar results were found (shown in Fig.3.17) for pole figure of cladding as was obtained for Al 2024-T351.

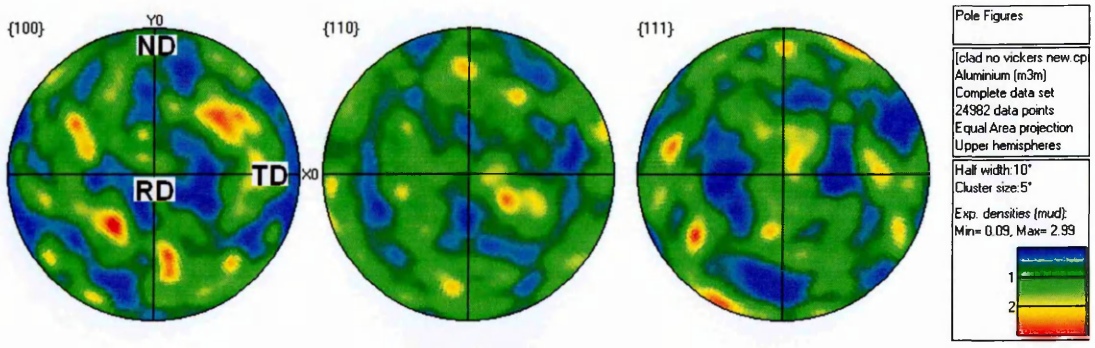

Fig. 3.17 - Pole figure for Al-cladding for piece #2

Though, it was clear from the EBSD maps and pole figures that there was random distribution of the grains, nanoindentation was used to study the hardness of these individual grains. First some Vickers indenter marks were produced in the Al 2024-T351 as shown in Fig.3.18. EBSD was carried out around these Vickers marks and EBSD maps so obtained are shown in Fig.3.19.

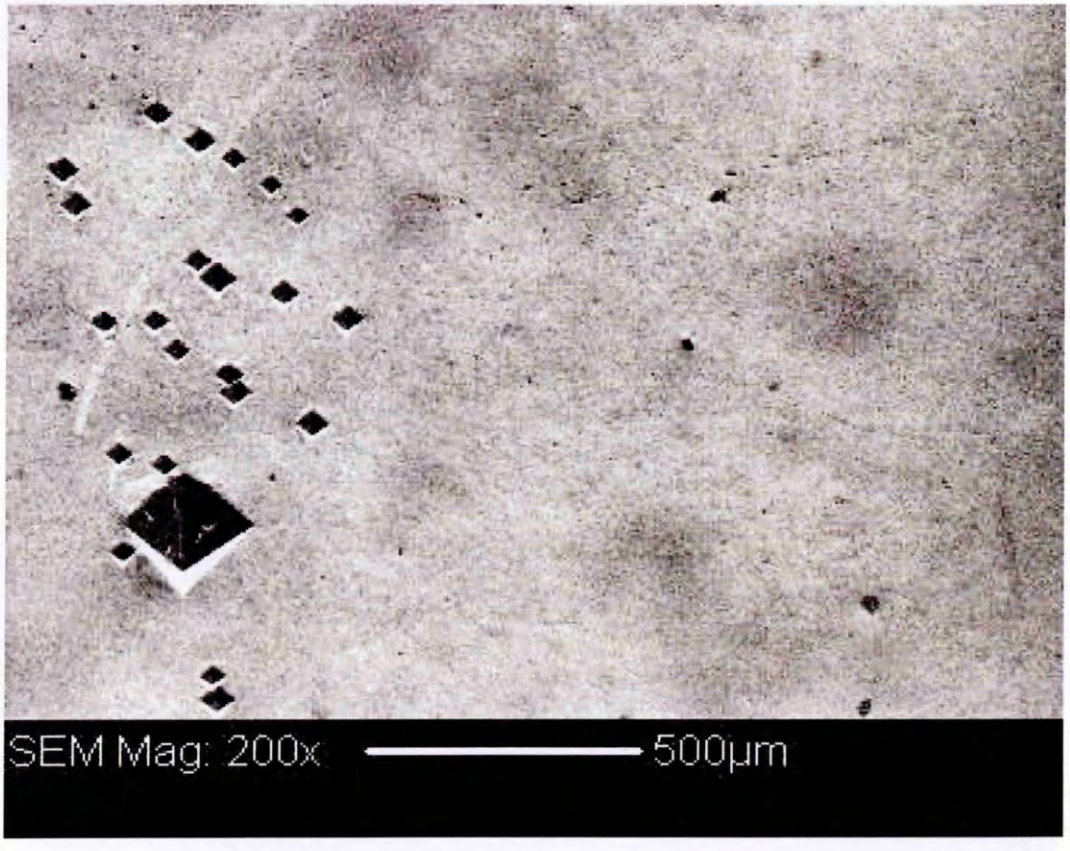

Fig. 3.18 - Vickers mark on Al2024-T351 sample

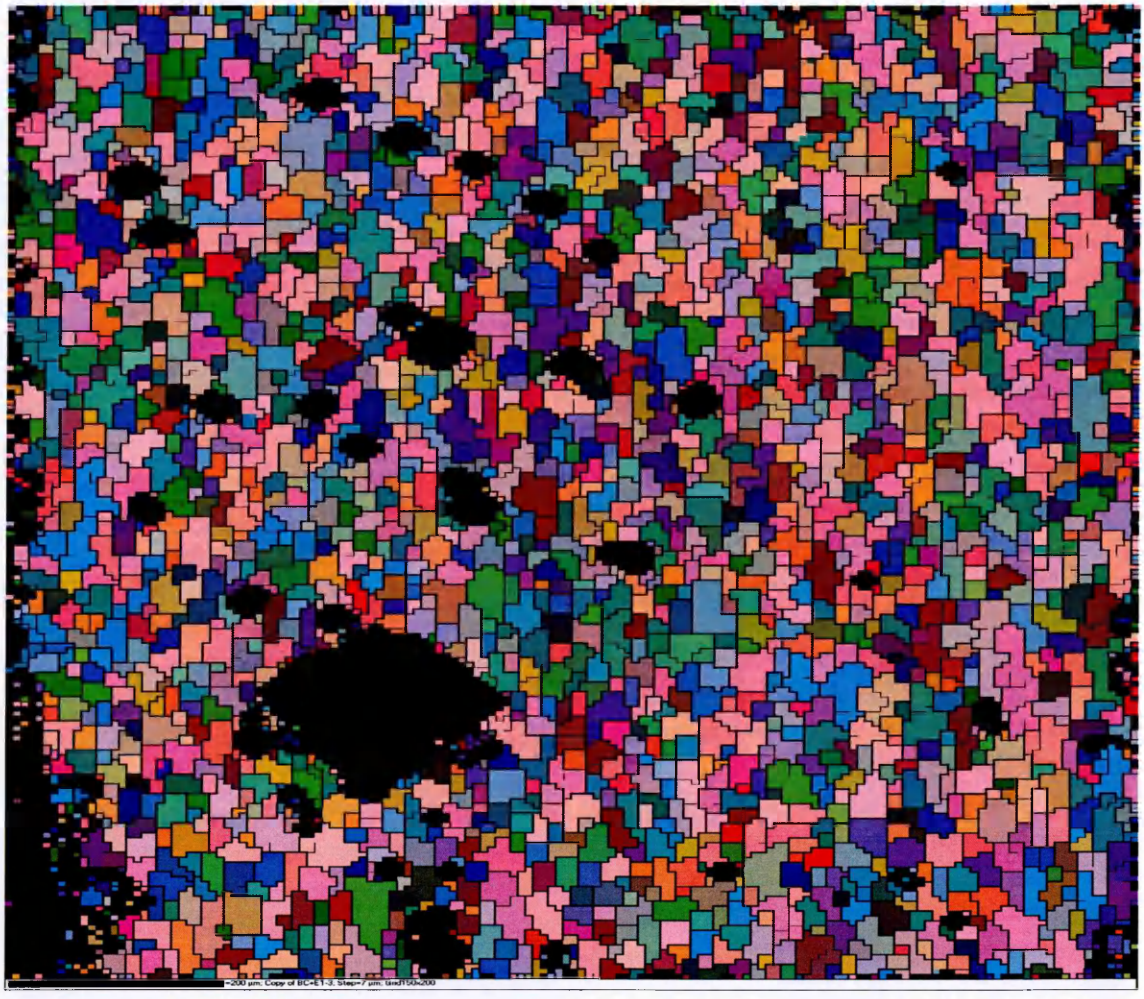

Fig. 3.19 - EBSD map around vickers marks before placement of nanoindents

Vickers marks which were produced before EBSD mapping worked as identification marks for nanoindentation testing. Nanoindentations at 600nm were carried out near to these Vickers marks to make sure that individual grains and orientations are being targeted. Great care was taken to target individual grains and Fig.3.20 (a) shows load-displacement curves of those grains for which it was sure that indentation was well inside a grain. It can be seen that there is some difference in terms of the load-displacement response of individual grains. It can be seen that there is difference in hardness and modulus between individual grains and grains of different orientation showed difference in hardness and modulus. Due to difference in hardness for grains, different loads were required to penetrate same depth of 600nm and hence showed difference in load-displacement curve.

Hardness and modulus of these grains are plotted as shown in Fig. 3.20 (b) and (c). This revealed that nanoindentation load-displacement curves do vary whenever responses of different grains are obtained for Al 2024-T351.

This degree of variation in hardness and modulus among grains showed that for residual stress regions, whenever there is some variation obtained from load-displacement curve it does not necessarily mean that this difference is due to residual stress but it could be due to grains of different orientation. Fortunately it is very clear that anisotropy among grains was not high and any change in response above the level of change we have seen here would definitely imply the effects of residual stresses.

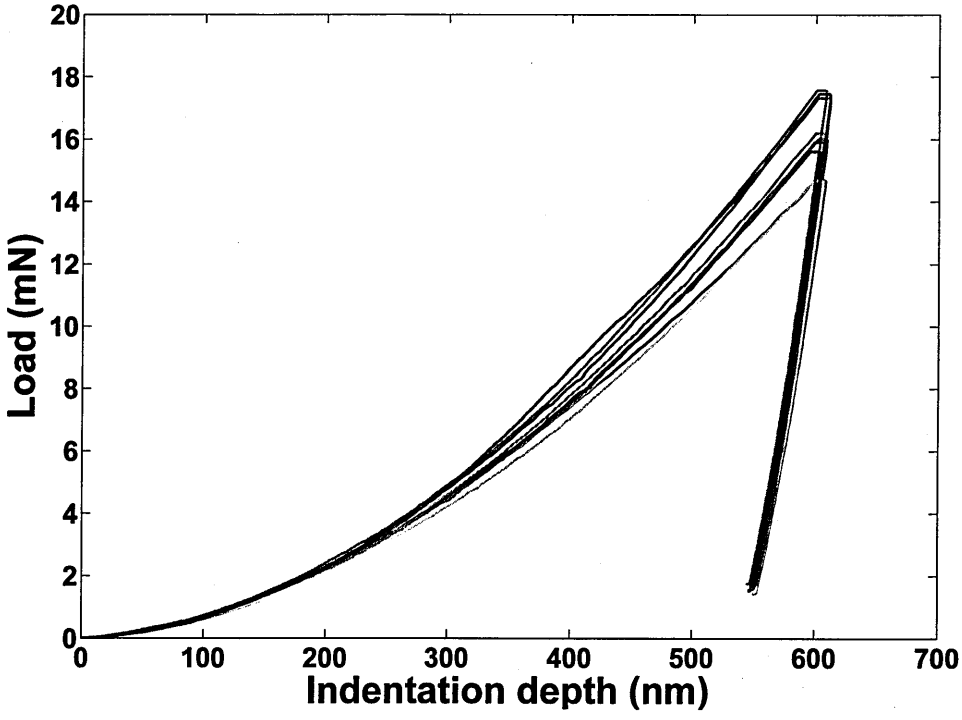

(a)

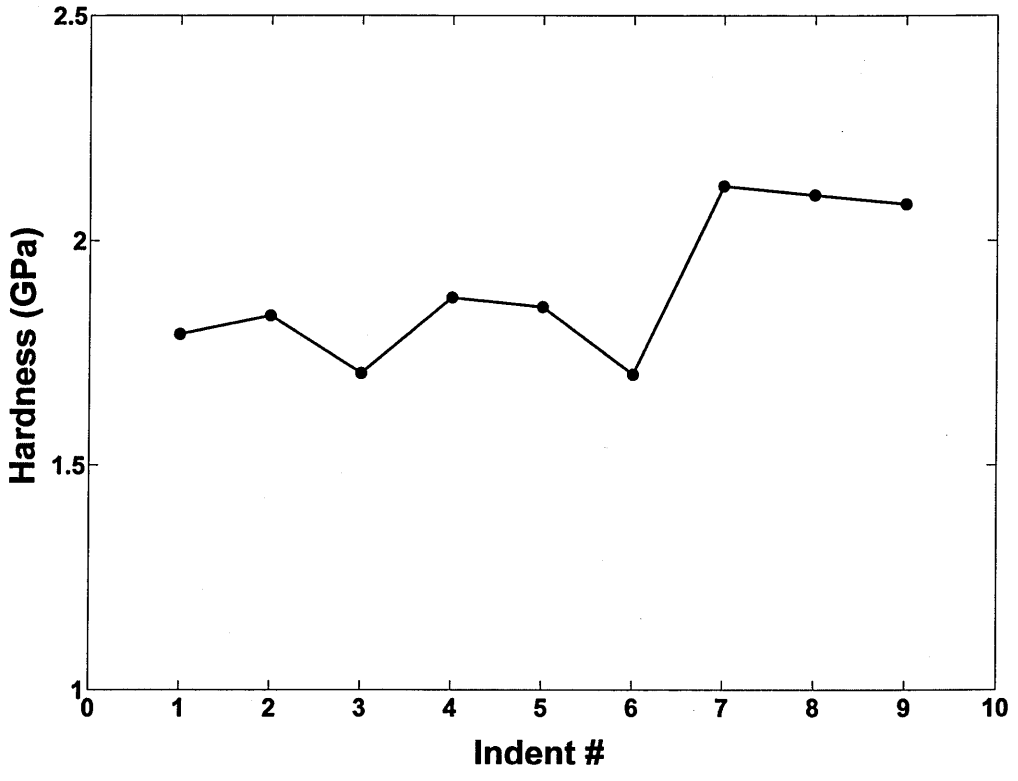

(b)

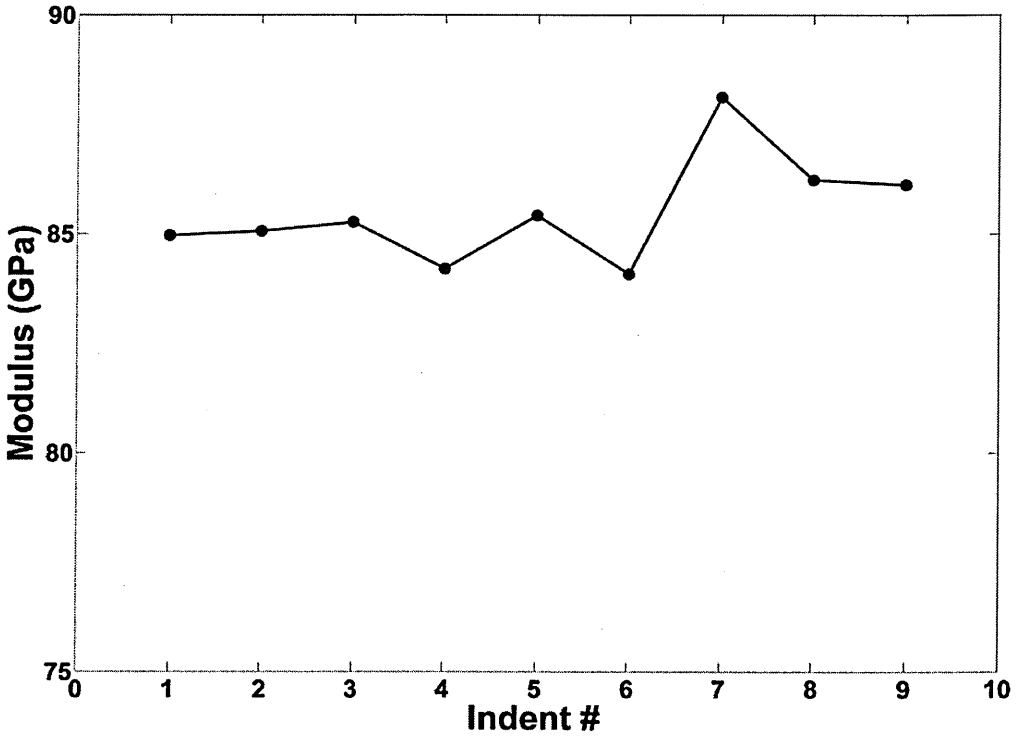

(c)

Fig. 3.20 - Response for indentation at different grains
(a) Load-displacement curve (b) Hardness (c) Modulus

3.5 Hardness Comparison from Different Approaches

Eqs. (3.23) and (3.24) were used to calculate hardness from the total work and plastic work approaches. The main advantage of these techniques is that there is no need to calculate the area of the indentation, which thus removes the difficulties caused by underestimating the contact area. The values of hardness as a function of penetration depth for the four different methods of calculation are shown in Fig.3.21 for the Al-clad and in Fig.3.22 for the Al2024-T351.

Fig.3.21 shows that three methods, the O-P model, the total work and plastic work methods, result in hardness values that are very close to each other and the quoted literature values of hardness for the Al-Clad. The hardness values obtained using correction for the area from the AFM measured areas are well below the other three methods [2, 8] (apart from the indentations to displacements of 200 and 400nm where the O-P and AFM values were found to be equal as no pile-up was observed at these depths). As we have discussed above, the AFM measured residual depths were less than the nanoindentation measured depths owing to relaxation of the material between indentation and AFM scanning, and tip convolution effects. AFM is also less accurate when estimating distances in the z-direction. If we consider the hardness values calculated from the work of indentation methods, at low penetration depths (200 and 400 nm) the hardness calculated from plastic work gives the highest value of hardness, followed by the O-P method and then the hardness calculated from the total work. No pile-up was measured on these indentations using the AFM, and the AFM calculated hardness values and hardness values from the O-P method are coincident. At larger penetration depths, the AFM corrected hardness values are low as discussed above whilst the three other methods show very little differences in the values obtained. Of the methods used, the hardness calculated from the total work using the work of indentation gave values of hardness very close to quoted literature values [25] of hardness in the range of 0.45-0.52 GPa. It should be noted that the hardness values

calculated from the work of indentation approach rise more steeply at lower penetration depths than the hardness values calculated by the O-P method. This is likely to be because the method of Tuck [2] makes no allowance for changes in tip geometry at lower indentation depths, where the tip geometry can significantly influence the calculated values, whilst tip geometry effects are allowed for in the O-P calculations.

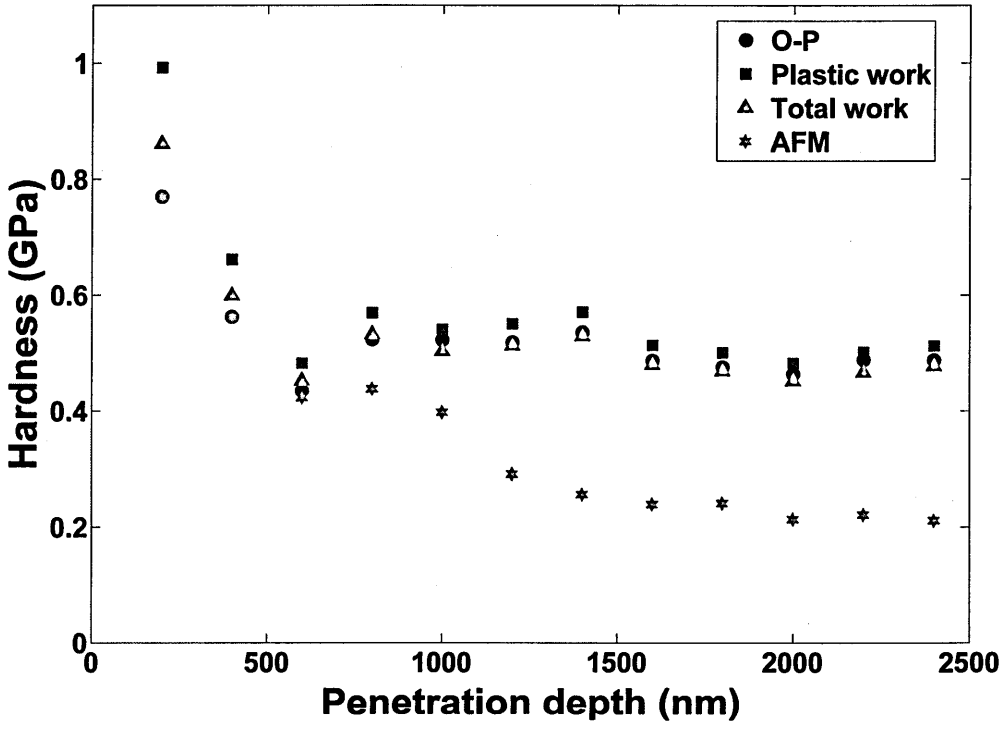

Fig. 3.21 - Hardness calculated using the four different methods for the Al-Clad

Fig.3.22 shows that the hardness values for the Al2024-T351 calculated from the O-P model, and work of indentation using the total work and plastic work approaches, are again close to each other, as well as to the literature values [25] of the hardness for Al2024-T351. The difference in the values of the hardness calculated by these three methods is greater than for the Al-Clad which corresponds to findings by other researchers [2, 4, 8, 12], and can be attributed to the higher hardness of the Al2024. The hardness values calculated using the plastic work of indentation are again highest at around 1.81-2.2 GPa and the O-P model values are also higher than those hardness values calculated using the total work of indentation. The greater differences between the total work of indentation approach and the

plastic indentation approach are to be expected owing to the greater elastic recovery for indentations into Al 2024-T351 (see Fig.3.13 (b) for example). Hardness values calculated from the total work values of indentation were found to be very close to literature values [25] of hardness in the range of 1.51-1.76 GPa.

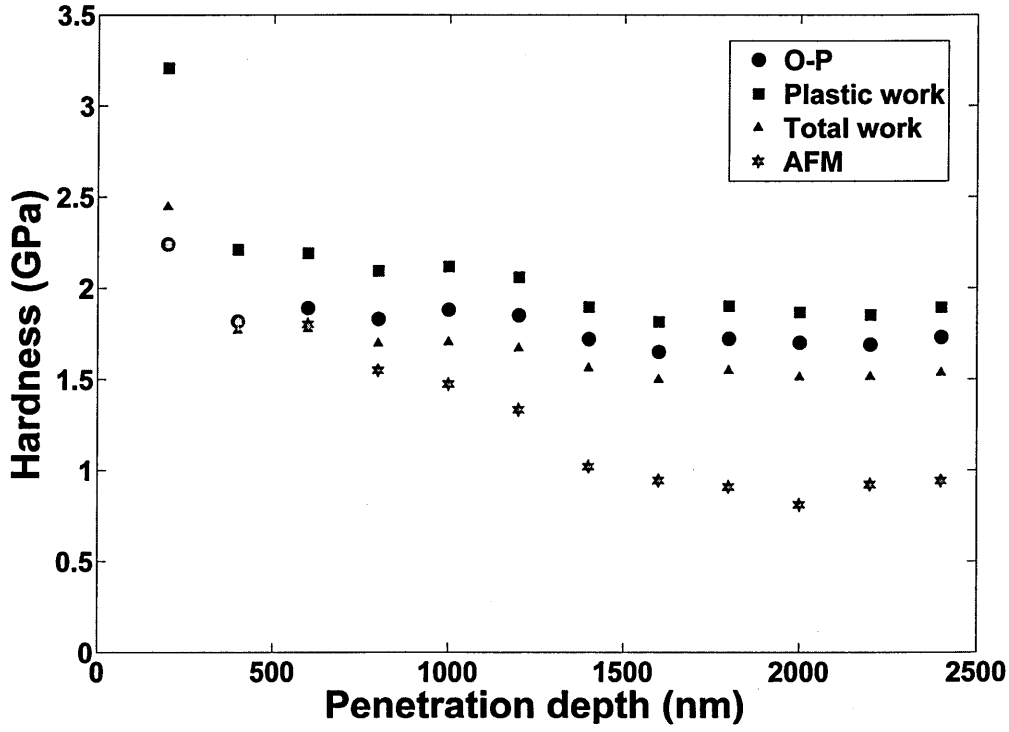

Fig. 3.22 - Hardness calculated using the four different methods for the Al 2024-T351

Thus, for a soft material such as the Al-cladding, where very little elastic recovery of the indentation occurs, both the total work and plastic work of indentation approaches were found to give results in good agreement with the literature. The O-P method, despite being influenced by pile-up also gives hardness values that are in reasonable agreement with the literature.

For the Al 2024, the total work of indentation approach gave the best agreement with the literature values. This is in agreement with the findings of Tuck [2], who found that for ductile materials where significant pile-up occurs, the total work of indentation approach always gave good results as compared to the plastic work of indentation technique. Tuck [2] did not fully explain why the total work of indentation approach gives better results

than using the plastic work alone, but it may be owing to the subtleties of the fact that elastic recovery tends to affect recovery of indentation depth rather than indentation area, and thus the total work is more representative of the work necessary create the indentation. This would make hardness calculated from total work of indentation more directly analogous to hardness values calculated by microhardness or macro-hardness tests.

3.6. Conclusions

Al-clad and Al2024-T351 materials have been characterized by nanoindentation. The nanoindentation load-displacement curves have been analysed to determine the hardnesses and Young's moduli of the samples. Owing to the relatively high E/σ_y ratio and low strain-hardening exponent of aluminium, pile-up occurred at the edges of the indentations. The widely-used Oliver and Pharr model does not account for pile-up and consequently overestimates hardness and modulus for the Al2024-T351. AFM imaging was performed to calculate the pile-up area, which was found to increase with indentation depth for both Al-Clad and Al2024-T351. The AFM measured pileup area was found to be overestimated owing to relaxation of the material between indentation and imaging, leading to underestimated hardness values. To minimize the effect on hardness and modulus values, further testing for residual stress measurement will be carried out at 600nm as we observed that this depth of penetration shows very nominal pile-up.

Work of indentation techniques do not require any calculation of the indentation area and are therefore useful for characterization of soft materials. Hardness values calculated from the total work and plastic work of indentation show good agreement with literature values of the hardness for these materials.

For the soft Al-cladding, where very little elastic recovery is observed, both the total work of indentation and plastic work of indentation methods were found to be effective. For the

slightly harder Al 2024-T351 where the material elastically recovers in unloading stage, the total work of indentation technique gave better agreement with literature values.

Anisotropy among grains was found and care has to be taken whenever these materials are indented to make sure of the exact reason for any change in response of load-displacement curves. To be precisely sure about variation in load-displacement curves due to residual stresses, the variation should be greater than the variation we studied here for different grains.

3.7 References

[1] W.C. Oliver and G.M. Pharr. An Improved Technique for determining hardness and elastic modulus using load and displacement sensing indentation experiments. J. Material Research. 7, 1992, pp 1564.

[2] J.R. Tuck, A.M. Korsunsky, S. J. Bull and R. I. Davidson. On the application of work of indentation to depth sensing indentation. Surface and Coatings Technology. 137, 2001. pp 217.

[3] K. O. Kese, Z.C. Li and B. Bergman. Influence of residual stress on elastic modulus and hardness of soda-lime glass measured by nanoindentation. Journal of Material Research, Vol. 19, No. 10, 2004. pp 3109.

[4] D. Beegan, S. Chowdhury and M.T. Laugier. Work of indentation methods for determining copper film hardness. Surface and Coatings Technology. 192, 2005, pp 57.

[5] A. Bolshakov and G. M. Pharr. Influences of pileup on the measurement of mechanical properties by load and depth sensing indentation techniques. Journal of Material Research, Vol. 13, No. 4, 1998, pp 1049.

[6] K. O. Kese, Z. C Li and B. Bergman. Method to account for true contact area in soda-lime glass during nanoindentation with the Berkovich tip. Material Science and Engineering A, 404, 2005. pp 1.

[7] B. Taljat and G. M. Pharr. Development of pile-up during spherical indentation of elastic-plastic solids. International Journal of Solids and Structures. 41, 2004, pp 3891.

[8] D. Beegan, S. Chowdhury and M.T. Laugier. A nanoindentation study of copper films on oxidised silicon substrates. Surface Coatings and Technology. 176, 2003, pp 124.

[9] K. Kese and Z.C Li. Semi-ellipse method for accounting for the pile-up contact area during nanoindentation with the Berkovich indenter. Scripta Materilia. 55, 2006. pp 699.

[10] R. Saha and W.D. Nix. Soft films on hard substrates-nanoindentation of tungsten films on sapphire substrates. Material Science and Engineering., 2001, pp 898.

[11] C. Tang ,Y. Li and K. Zeng. Characterization of mechanical properties of a Zr-based metallic glass by indentation techniques. Material Science and Engineering A, 384, 2004, pp 215.

[12] D. Beegan, S. Chowdhury and M.T. Laugier. The nanoindentation behaviour of hard and soft films on silicon substrates. Thin Soild Films, 466, 2004, pp 167.

[13] Khan, M. K., S. V. Hainsworth, M. E. Fitzpatrick and L. Edwards. Application of the work of indentation approach for the characterization of aluminium 2024-T351 and Al cladding by nanoindentation. Journal of Materials Science, 44(4), 2009, pp 1006-1015.

[14] R. M. Pothapragada, R. A. Mirshams and S. Vadlakonda. Effect of Pile-up in Nanoindentation of Micro and Nano crystalline Ni using FEM. Material Research Society Symposium. Proceedings. Vol. 880E, 2005, BB7.9.1.

[15] N. A Stillwell and D. Tabor. Elastic Recovery of Conical Indentations. Proceedings of Physical Society of London. 1961. pp 169.

[16] W. J. Poole, M. F. Ashby and N. A. Fleck. Micro-hardness of annealed and work-hardened copper polycrystals. Scripta Materilia., Vol. 34, No. 4, 1996, pp 559.

[17] L. Zhou and Y. Yao. Single crystal bulk material micro/nano indentation hardness testing by nanoindentation instrument and AFM. Material Science and Engineering A. 460-461, 2007, pp 95.

[18] J. R. Tuck, A. M. Korunsky, R. I. Davidson, S.J. Bull and D. M. Elliott. Modelling of the hardness of electroplated nickel coatings on copper substrates. Surface Coatings and Technology. 127, 2000. pp 1.

[19] T. Zhang, W. Xu. Surface effects on nanoindentation. Journal of Materials Research., Vol. 17, No. 7, 2002, pp 1715.

[20] I. N. Sneddon. The relation between load and penetration in the axisymmetric boussinesq problem for a punch of arbitrary profile. International Journal of Science,3, 47, 1965.

[21] G. M. Pharr, A. Bolshakov. Understanding nanoindentation unloading curves. Journal of Materials Research, Vol17, No. 10, 2002, p. 2660.

[22] Yu, N., A. A. Polycarpou and T. F, Conry. Tip-radius effect in finite element modeling of sub-50 nm shallow nanoindentation." Thin Solid Films 450(2), 2004, pp 295-303.

[23] J. Y. Kim, B. W. Lee, D. T. Read and D. Kwon. Influence of tip bluntness on the size-dependent nanoindentation hardness. Scripta Materialia 52(5), 2005, pp 353-358.

[24] Y. Choi, H. S. Lee and D. Kwon. Analysis of sharp-tip-indentation load-depth curve for contact area determination taking into account pile-up and sink-in effects. Journal of Materials Research 19(11), 2004. pp 3307-3315.

[25] Materials Handbook, 9th edition, Vol. 2, Properties and selection: Nonferrous Alloys and Pure Metal, 1979, American Society for Metals, Metal Park, Ohio 44073.

Chapter 4: Local Hardness around Scribe Marks of Different Root Radii Produced from Different Tools

4.1 Introduction

The morphology of a scribe will vary depending upon the mechanism of scribe formation, the forces involved, and the geometry of the tool which produced the scribe. Fatigue cracks can grow and propagate from the base of a scribe, and the resultant fatigue life is highly influenced by the manner in which the scribe was produced. Not only the geometry of the scribes, in terms of depth and root radius, play an important role to initiate and propagate cracks, but different tools while producing a scribe of the same depth and root radius may generate different levels of residual stress around the scribe root. The magnitude and extent of the residual stress field influences the way in which cracks from the root propagate in fatigue. Additionally the local damage induced during scribing results in different levels of plastic deformation around scribe root.

Scratching or scribing consists of cutting, ploughing and wedge formation. In ploughing pile-up pads are formed on both sides of scribe, and in cutting material is displaced away from scribe track. These wear mechanisms produce different levels of work hardening around scribes. Mezlini et al. [3, 5] indicated that two different behaviours and wear resistances can be induced by changing the geometry of the tool. He compared the level of plastic deformation while scratching using conical and spherical indenters and found that more severe plastic deformation can be generated from a conical indenter as compared to a spherical indenter. Tkaya et al. [4] and Mezlini et al. [5] observed wear mechanisms for different attack angles from 5-60° and found that for a 30° attack angle material was pushed to the side of scratches and for a 60° attack angle this wear mechanism changed to cutting. Kato [9] found that the wear mode during repeated sliding processes changes form cutting to wedge formation and then to ploughing. Subramanian [10] showed that the abrasive wear pattern depends on sliding velocity and pressure during scratching.

This chapter presents an investigation of local hardness, wear mechanism and plastic deformation around scribe marks of different depths and root radii produced from different tools. Nanoindentation has been used to study the hardness changes produced by scribing of Al 2024-T351 with and without cladding whilst scanning electron microscopy was used to characterise wear around scribes. Scribes or scratches are usually characterized in terms of depth, root radius and included angle. To study the effect of these parameters on wear, scribes of root radii 5 μm, 25 μm and 50 μm with different depths have been produced. Additionally, to study the effect of the tool on wear in production of a similar configuration scribe, two tools designated as A and B, were used to produce scribes. Overall, the local hardness environment and wear around scribes were investigated with respect to different scribe depth, root radius and the tools by which the scribes were produced.

The effect of fatigue cycling on work hardening around scribe root was investigated in four point bending and tension-tension fatigue loading. The local hardness around scribes was investigated before and after fatigue to observe any relaxation in plastic deformation around the scribe roots.

4.2 Materials and Experimental Details

4.2.1 Material Details

The materials used were Al2024-T351 of 2mm total thickness, with and without aluminium cladding of 100μm on both faces as discussed in chapter 3.

4.2.2 Introduction of Scribes

It was difficult to produce service scribes which are found on the fuselage of in-service aircrafts. To simulate the service scribes, scribe marks were created on a specially set up milling machine using a diamond-tipped tool. Kyle and Irving [25] in a previous study concluded that a stress concentration factor K_t of at least 3 and 4 was necessary, but not sufficient, criteria for fatigue cracking to initiate. They obtained this value of K_t while

creating scribes of different depths with 5 μm root radius. Hence, in this study to obtain the same Kt, two diamond-tip cutting tools designated as 'A' and 'B' with a nominal tip radius of 5μm as used in previous study [24] was used for the actual marking of scribes. These two tools had been found, by chance, to give very different fatigue lives despite having the same nominal specifications. So part of this study was to investigate reasons for this difference. In addition to observe the effect of increase in root radius, two other tools 'C' and 'D', of radius 25 and 50 μm radius were also used to create scribes.

A schematic of typical scribe geometry is shown in Fig.4.1. The scribe has a notch depth d, width w, root radius ρ, and a notch angle of 2θ.

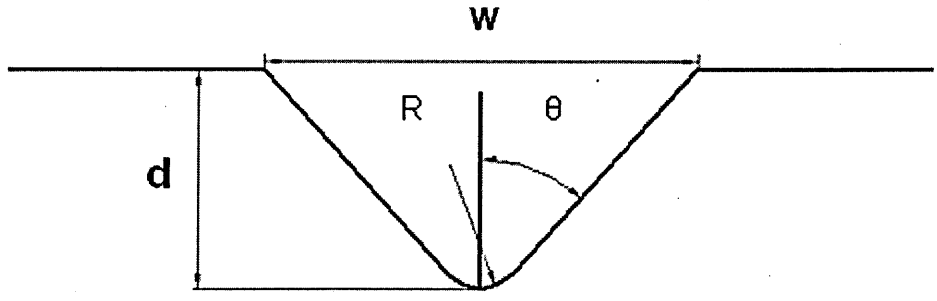

Fig. 4.1 - Scribe geometry

An example of the different scribe profiles generated by tool A and B for 5 μm root radius is shown in Fig.4.2. Scribes made by both tools resulted in a scribe root radius of 5μm but tool A generated scribes with a non-symmetric cross-section (Fig. 4.2a), which was seen on all scribes made with this tool and which was caused by a flaw on the tool. Scribes were made to controlled depths, but elastic recovery of the scribes after the load was removed, and the different forces required for the two tools, meant that in practice for an initial set depth the residual scribes from tool A were 10% deeper than scribes made with tool B.

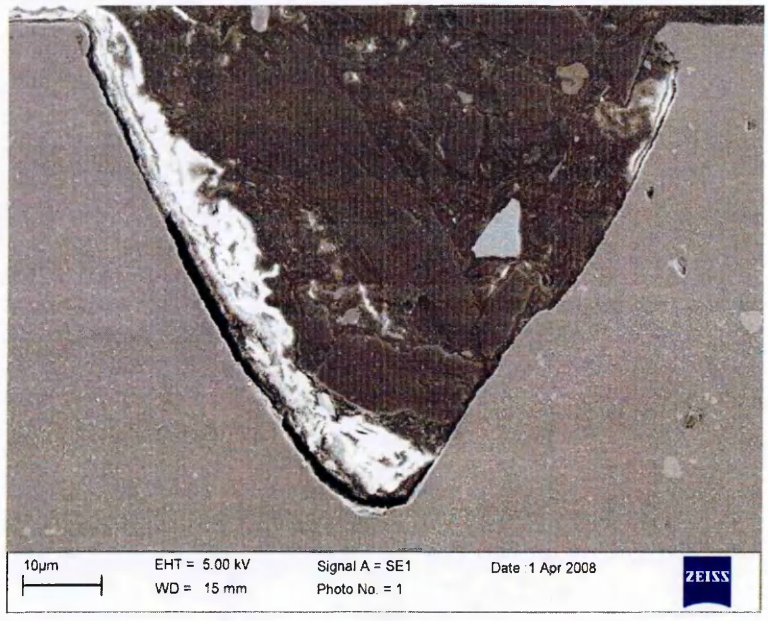

(a)

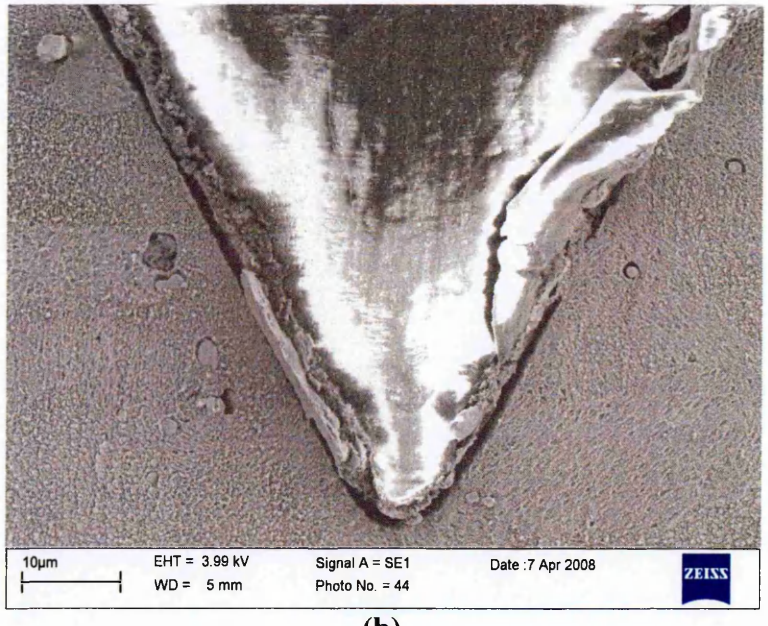

(b)

Fig. 4.2 - SEM pictures of cross-section of scribes (a) 50 µm deep from tool A (b) 100 µm deep from tool B

Scribes were produced in clad and unclad Al 2024-T351. Owing to differences in the work hardening exponents and E/σ_Y ratios for the pure aluminium cladding and the Al 2024-T351, different extents of plastic deformation were obtained around the resultant scribe tracks. This plastic deformation plays an important role in fatigue crack initiation and propagation from the roots of these scribes.

After the scribes were made, the coupons were cross-sectioned and polished and etched to reveal the extent of the plastic deformation, and for nanoindentation testing. To observe the behaviour of the cladding, scribes were made to two different depths: scribes with a depth of 50μm (less than the clad thickness) and scribes with a depth of 100 μm (equal to the clad thickness). Scribes were also made into unclad Al2024-T351 to depths of 50, 75, 100, 125 and 150 μm.

4.2.3 Nanoindentation Testing

Nanoindentation was carried out to 600nm depth [1] with the same experimental procedure as discussed in chapter 3. Indentations were made in an array around the scratch cross-section with 20μm spacing between the indentations. Load-displacement data was obtained for each indentation. Fig.4.3 shows the arrangement of indentations in greater detail.

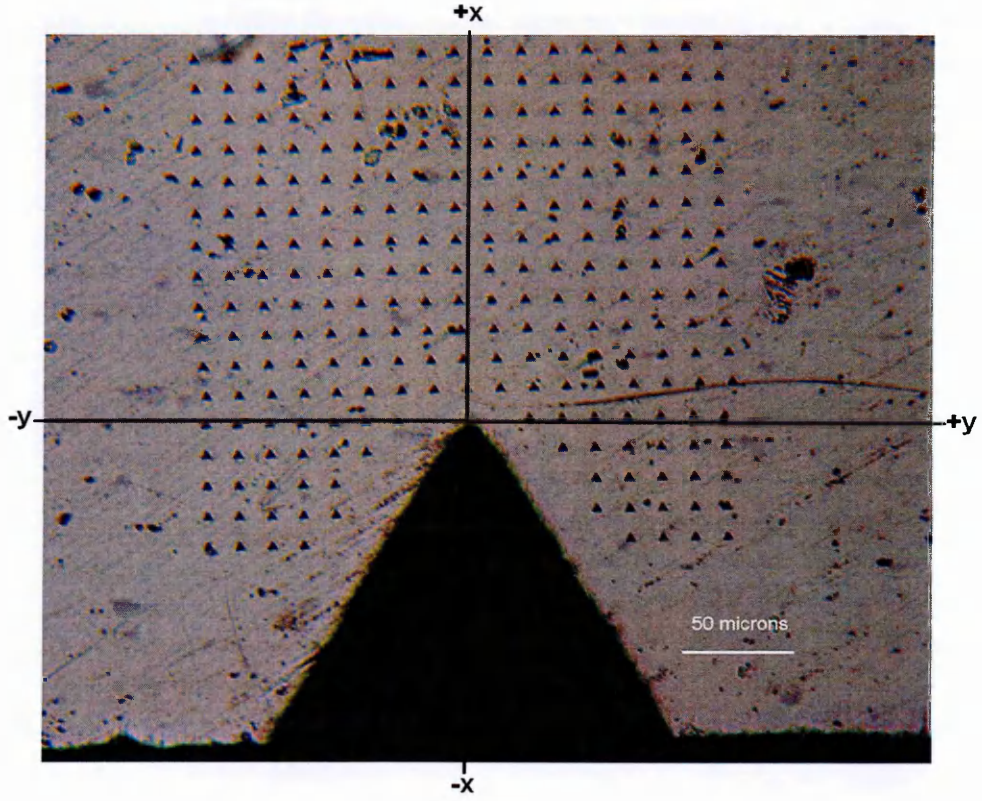

Fig. 4.3 – Indentation array

4.2.4 Fatigue Testing

Four-point bend samples were prepared of size 50 mm x 210 mm x 2mm for the clad Al 2024-T351 and 50 mm x 210 mm x 1.8 mm for the unclad Al2024-T351 (after removal of 100 μm cladding from both sides). Samples were tested in an MTS servo-hydraulic test system at a maximum stress of 200MPa and constant load ratio 'R' of 0.1. All tests were of constant amplitude for consistency in the results and were conducted at a frequency of 5 Hz. For accurate calculation of fatigue cycles, tests were carried out in load control environment. Span length between top and bottom rollers was 35 and 70mm respectively. The assumption was then made that the deformation would be entirely elastic because of the low optimal stress when compared to the yield strength of Al 2024-T351, and therefore using the maximum stress value, the force necessary to apply to achieve the correct stresses was calculated. Maximum force of 617N was used for unclad samples and 761N for clad samples.

In total 11 different samples of Al 2024-T351 with and without clad were fatigue tested. Nine samples were tested to failure and two further samples, with scribes made by tool A, were fatigued to 250000 and 500000 cycles in the unclad Al2024-T351 samples. These cycles were well below the fatigue life (~1000000 cycles) of those particular samples, to observe the effect of cyclic loading on the hardness at the scribe root.

After cycling, hardness mapping tests were conducted around the scribe roots in the same way as for the un-fatigued samples.

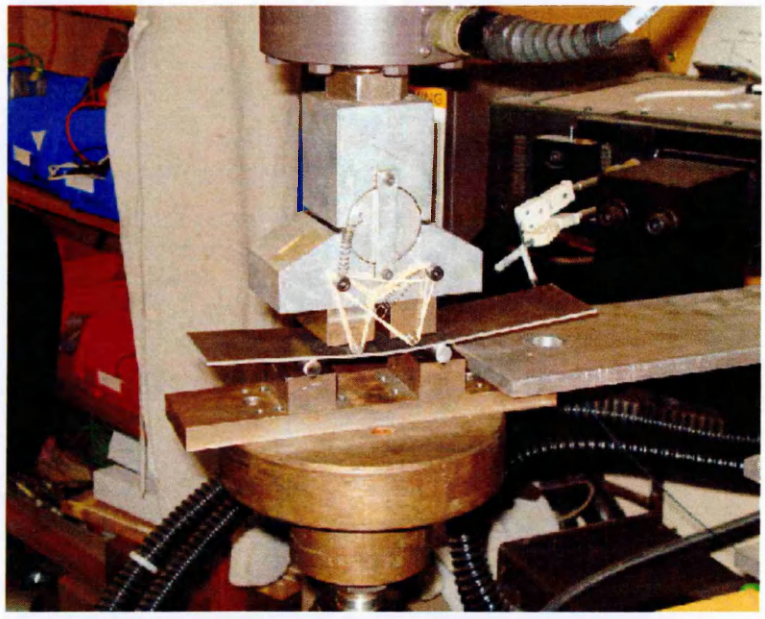

Fig. 4.4 - Four point bend fatigue testing

4.3 Results and Discussion

4.3.1 Profiles of 5 µm Root Radius Scribes

For 5 µm root radius, scribes were produced from two tools designated as tool A and B. For tool A scribe cross-section was not symmetric and there was an abrupt change in scribe profile on one side of scribe track. Another important aspect of scribes from tool A was that all of the scribes were 10% more deep as compare to tool B scribes as shown in Table 4.1. Fig.4.5 shows 50 µm deep scribes in clad Al2024-T351 from both tools and it is clear that the tool A scribe has penetrated the clad layer (For some samples clad layer was 80 µm). For tool B the scribe cross-section was axisymmetric, and no irregularity in morphology was present, as shown in Fig.4.2 and 4.5.

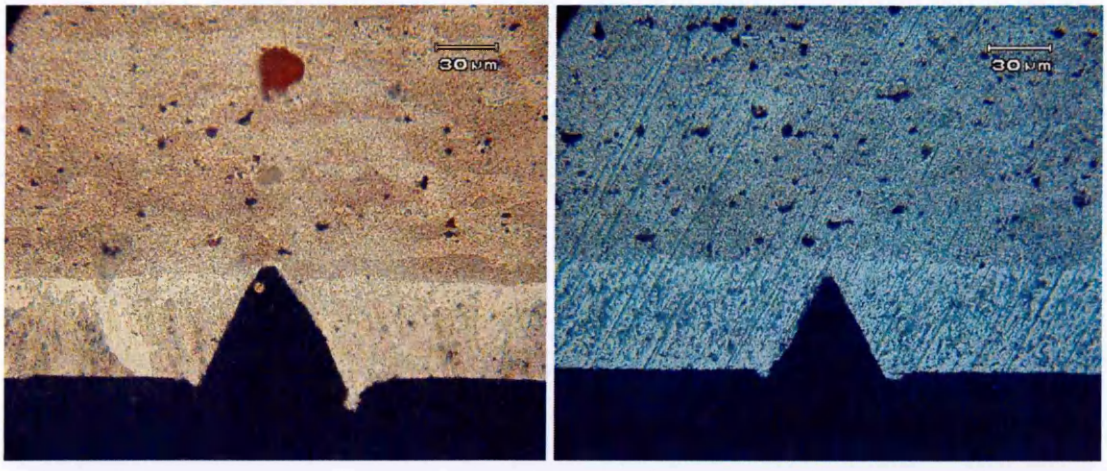

Fig. 4.5 - Etched cross-section of 50 µm deep scribes in clad Al 2024-T351 from tool (a) A (b) B

Because of the need to ensure accuracy of the depth of the scratches and the limits of the machine used, only 10μm in depth could be removed with each pass of the cutting tool. Therefore multiple passes were necessary to achieve the required nominal depth on the test samples, and the process was made even more difficult by the fact that the samples themselves possessed manufacturing defects and were not flat to within 10μm, so some variation in depth was to be expected. The profiles of the scribes obtained from two tools and difference in scribes depth after same number of passes suggested that there is some difference between the two tools and tool A removes 2~4 μm more material in each pass as compared to tool B, hence achieve more depth of scribe. This is possibly a consequence of the 'blunt' tool profile, requiring a greater force to be applied, and the depth control for the tool being relatively coarse.

For both tools, pile-up of material was observed around the scribe track. For tool A the pile-up was more severe as compared to tool B (Fig.4.6). Due to the irregular shape of tool A, the pile-up was not symmetric, with more pile-up on the side of the scribe which showed irregularity in profile as shown in Fig.4.6 (a) and 4.7 (a). For tool A, the extent of material displaced around the scribe track was greater. A 'rough' scribe track, with deformed material or debris around scribe was seen. The scribing of the surface had clearly been associated with a large amount of plastic deformation and displacement of material, rather than a cutting action by which material is simply removed. This phenomenon, in which material is deposited around the edges of a scribe in the form of plastic pads, is known as 'ploughing'.

In contrast, a very smooth scribe track was obtained for tool B, with very little deformed material around the scribe (Fig.4.6 (b) and 4.7 (b)). Very little debris was found around the scribe track, which revealed that this tool was clearly removing material by a cutting action, rather than by plastic deformation and displacement of material, by the tool.

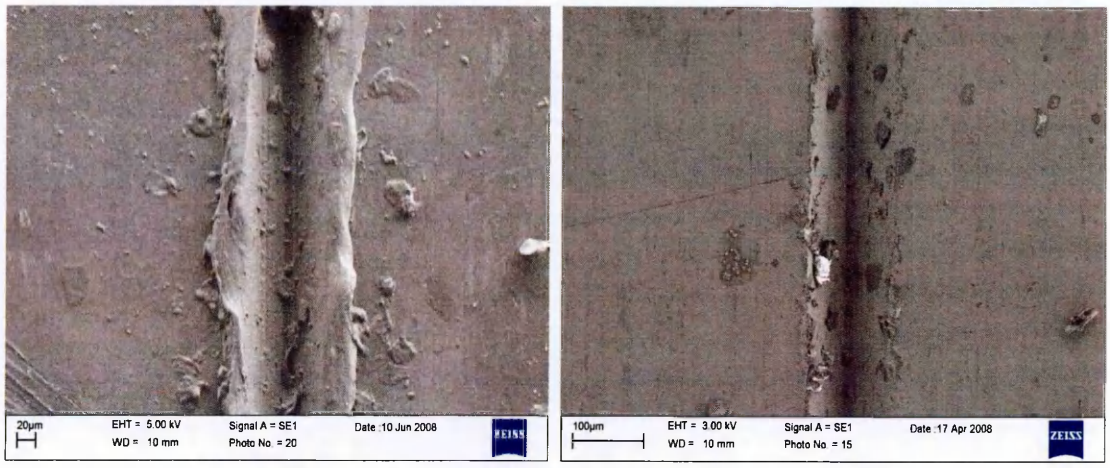

(a) (b)

Fig. 4.6 - Surface profile of scribes in clad Al2024-T351
(a) 50 µm deep from tool A (b) 50 µm deep from tool B

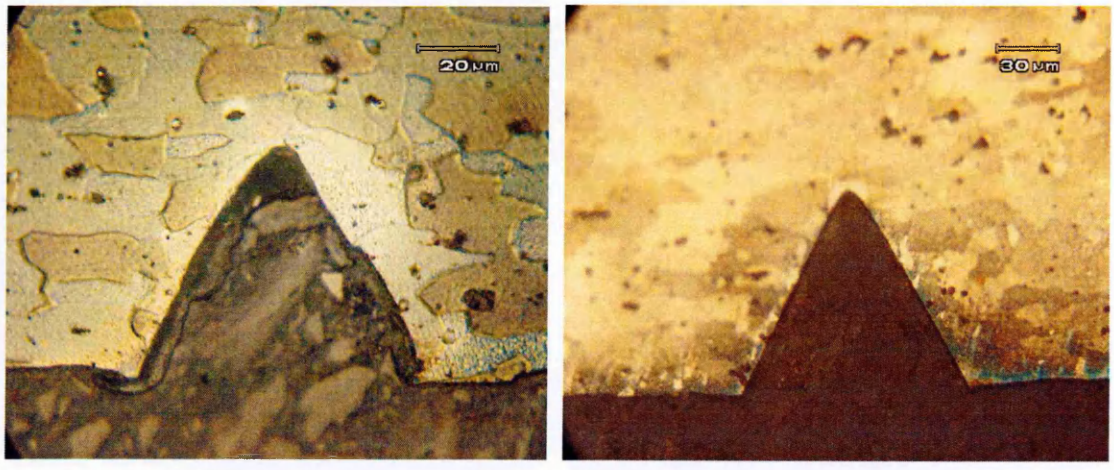

(a) (b)

Fig. 4.7 - Etched cross-section of scribes in Al2024-T351
(a) 50 µm deep from tool A (b) 100 µm deep from tool B

S. No	Tool	Material	Required depth (μm)	Scribe depth *d* (μm)	Scribe width *w* (μm)
1	A	Cladding-Al2024-T351	100	110	124
2	A	Al2024-T351	100	110	124
3	A	Al2024-T351	50	56	68
4	A	Al2024-T351	75	80	104
5	A	Cladding	50	56	72
6	B	Cladding	50	50	64
7	B	Cladding-Al2024-T351	100	106	104
8	B	Al2024-T351	50	50	64
9	B	Al2024-T351	100	100	110

Table 4.1 - Depth and width of scribes generated from tool A and B

The difference in terms of the depth and width, and the irregular profile of scribe cross-section, demonstrates that these two tools are different from each other when scribing. It has been reported that the shape of the tool, and in particular the 'attack angle' between the leading edge of the tool and the workpiece, along with the shear strength at the interface between the cutting tool and the surface, have a significant effect on deformation behaviour around scribes. Mezlini [17], Kato [9] and Subramanian [10] showed that abrasive wear mechanisms depend on the tool shape, attack angle, and test parameters. Tkaya [4] observed the effect of tool attack angle on the wear mechanism. He found that for a 30° attack angle a transition of wear mechanism from ploughing to cutting, with chips in front of the indenter, was observed. Here the two tools produced different morphologies of scribes and different levels of deformation around the scribes. From Fig.4.2 it can be seen that the tool profiles are significantly different, and although the images do not give information directly about the attack angle, the tool profile suggest that tool A has an attack angle (angle between leading edge of the tool and workpiece) of ~40° whilst for tool B the

figure is closer to 30°. Analysis of the cutting tracks indicates that tool A is tending towards a ploughing action, while tool B is just cutting the material during scribing.

4.3.2 Scribes with 25 & 50 µm Root Radius

Fig.4.8 shows cross-sections of 25 µm and 50 µm root radius scribes. For 25 µm and 50 µm root radius scribes, like tool B of 5 µm radius scribes, a very smooth scribe track with very little deformed material around the scribe was obtained as shown in Fig.4.9. However, there was some debris found for scribes in clad material, but less than that obtained for 5 µm radius scribe from tool A. This revealed that these tools were also removing the material by a cutting action like tool B, rather than by plastic deformation and displacement of material by the tool.

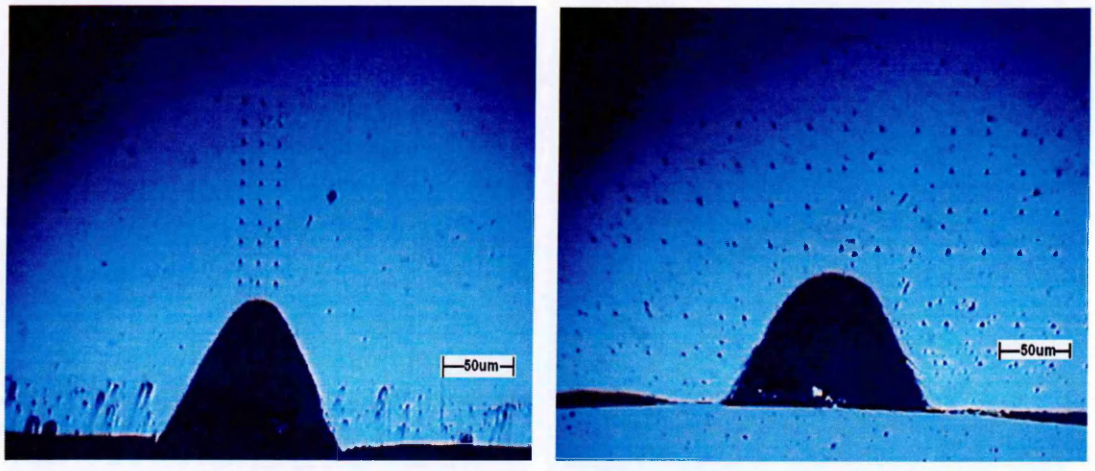

Fig. 4.8 - Scribe cross-sections for 100 µm deep scribes
(a) 25 µm radius (b) 50 µm radius

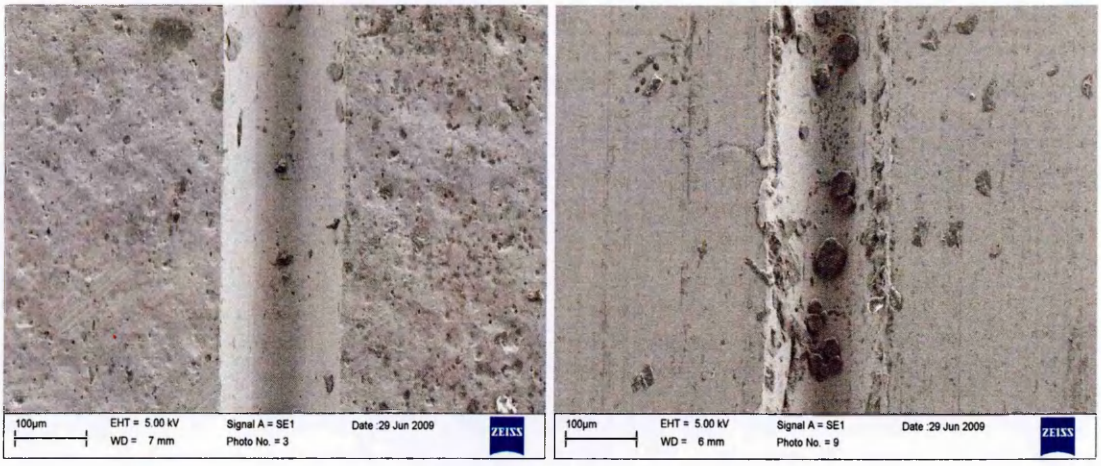

Fig. 4.9 - Surface Profile of scribes of 100 µm depth and 50 µm radius in (a) Al 2024-T351 (b) Al-cladding

4.3.3 Hardness Maps around Scribes of 5 µm Root Radius

The hardness environments around scribes with different depths produced from different tools were investigated. Indentations were made around each scribe according to scheme shown in Fig.4.3.

Fig.4.10 and 4.11 shows hardness maps around scribes of 50 and 100 µm deep scribes produced from tool A and B respectively. It can be seen that the hardness around the scribe root is totally dependent upon the tool by which these scribes were produced and irrespective of the depth of the scribes.

Fig. 4.12 (a) (b) shows hardness maps obtained for 100 µm deep scribe produced from tool A and B respectively in clad Al 2024-T351. It can be seen that there is no such difference in the hardness maps for scribes in clad Al 2024-T351 especially around scribe root. Lower hardness values were found for clad material as discussed in chapter 3.

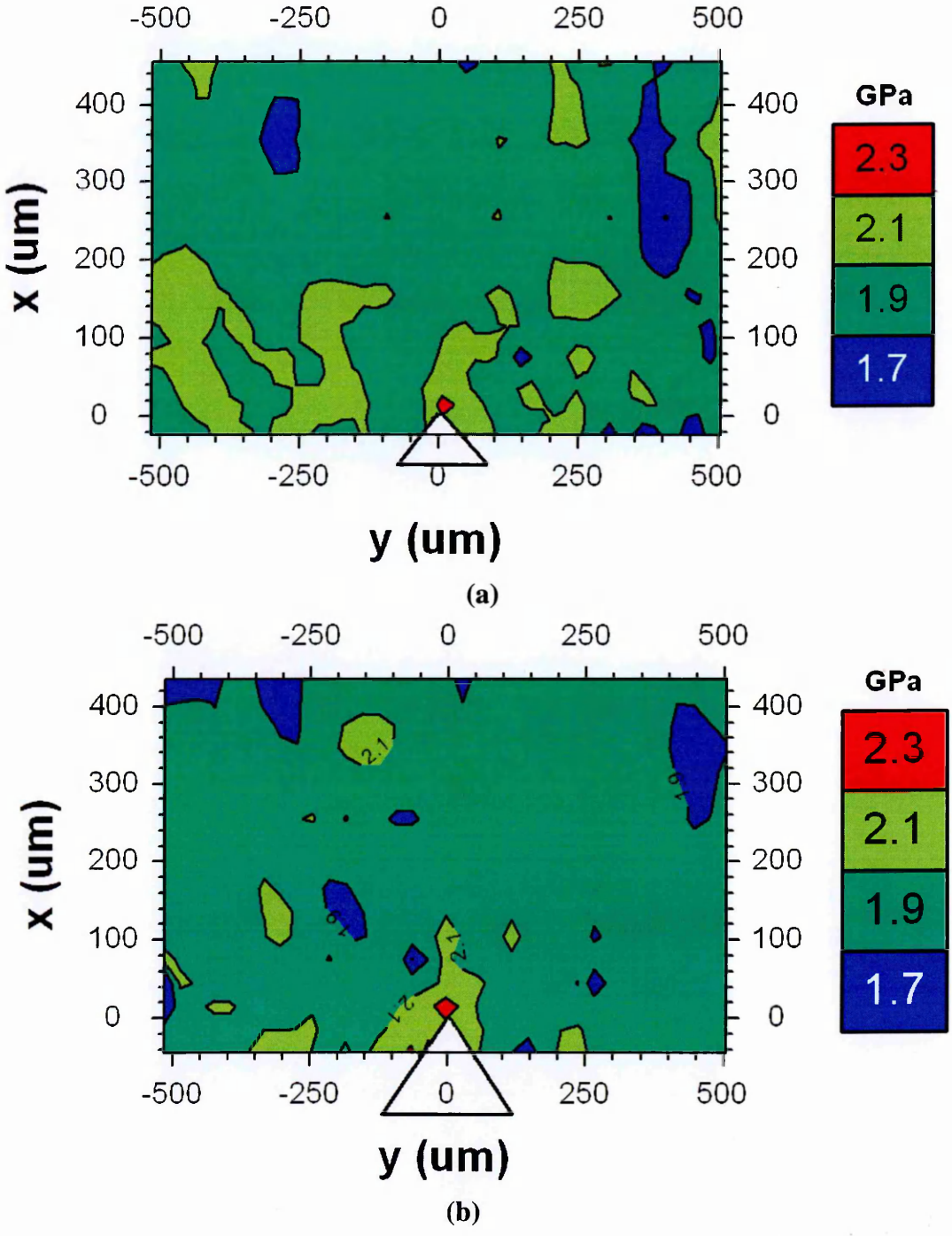

Fig. 4.10 - Hardness maps around tool A scribes of depth (a) 50 µm (b) 100 µm

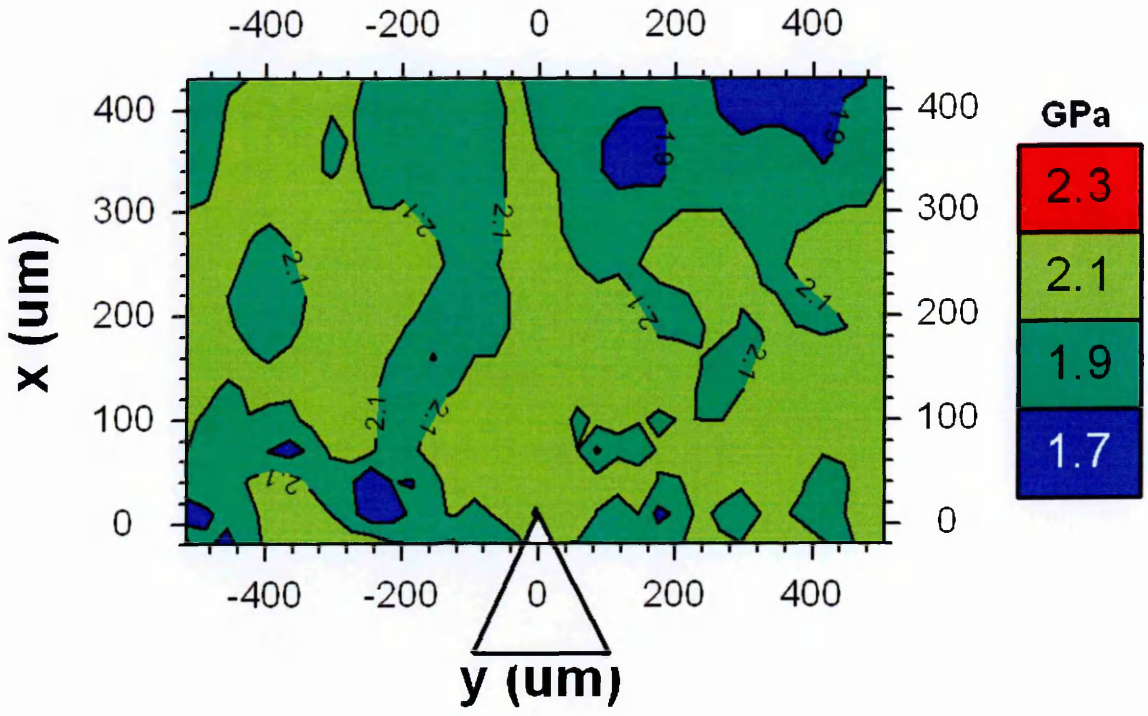

(a)

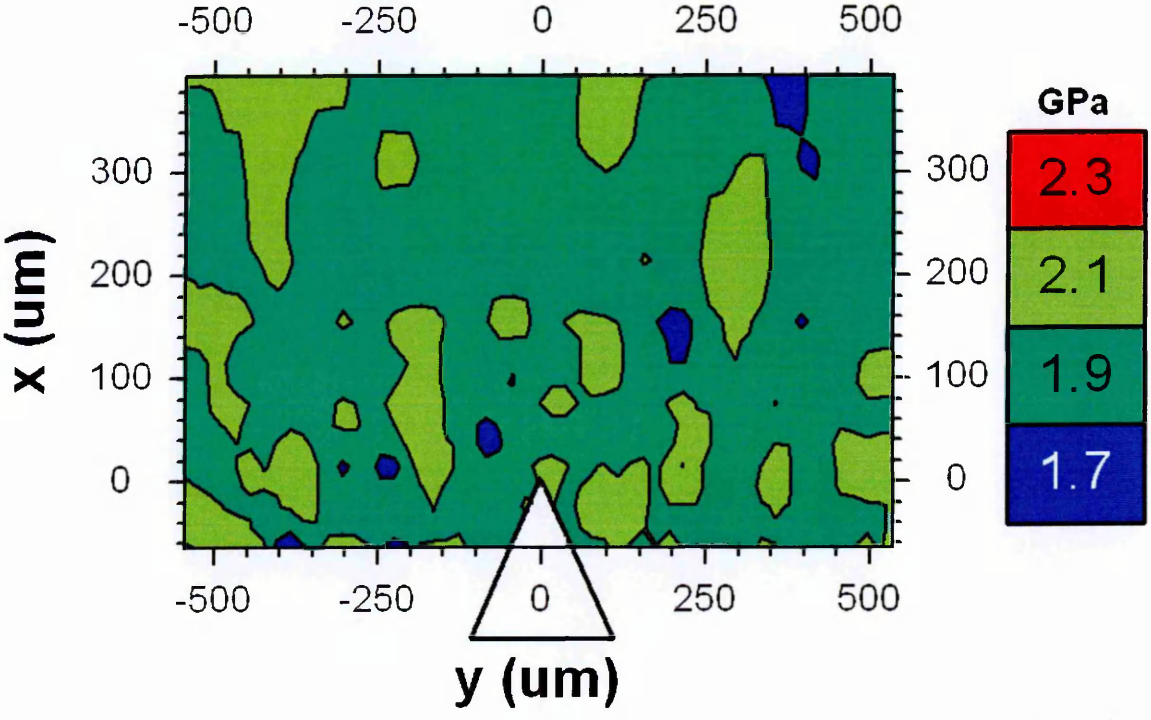

(b)

Fig. 4.11 - Hardness maps around tool B scribes of depth (a) 50 µm (b) 100 µm

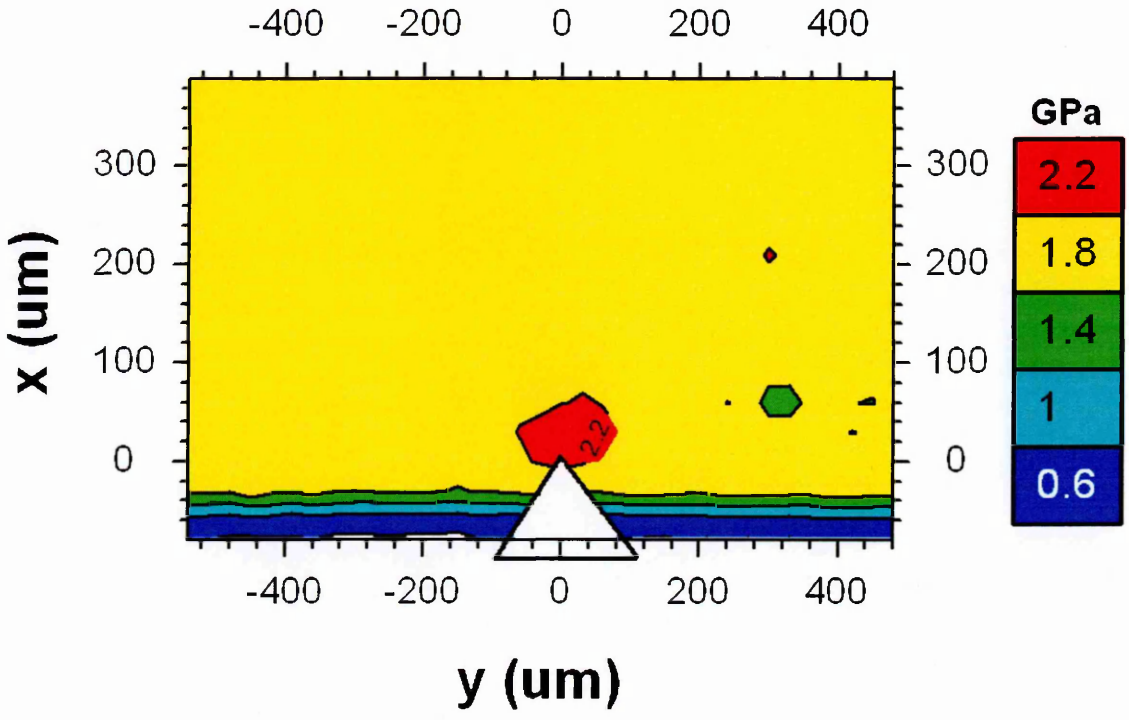

(a)

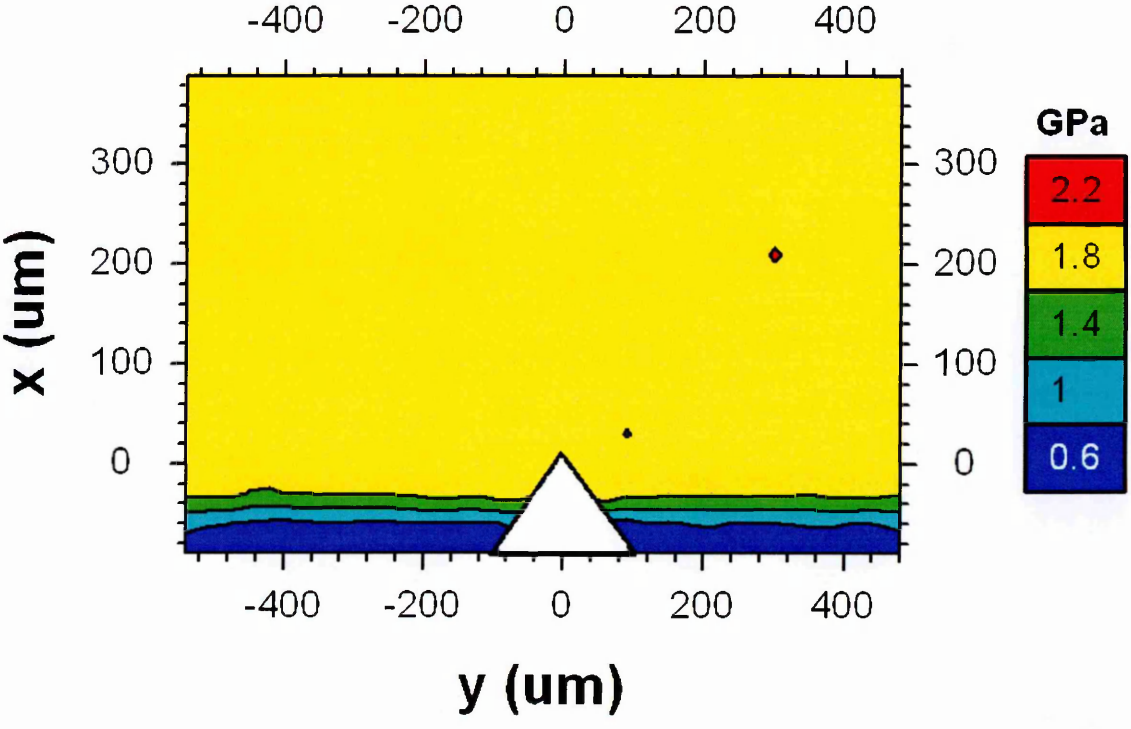

(b)

Fig. 4.12 - Hardness maps around 100 µm deep scribe in clad Al 2024-T351 from (a) Tool A (b) Tool B

The hardness profiles measured for 25 μm and 50 μm root radii scribes revealed that there was no such effect of increased hardness below scribe root. Fig.4.13 shows hardness maps for 50 μm and 100 μm deep scribes of 50 μm root radius. Similar to the scribe profiles, hardness environment was also the same as for tool B. No local hardening effect below the root of the scribe was obtained. This could be attributed to the cutting mechanism of removing material which did not cause significant plastic work hardening around the scribe root.

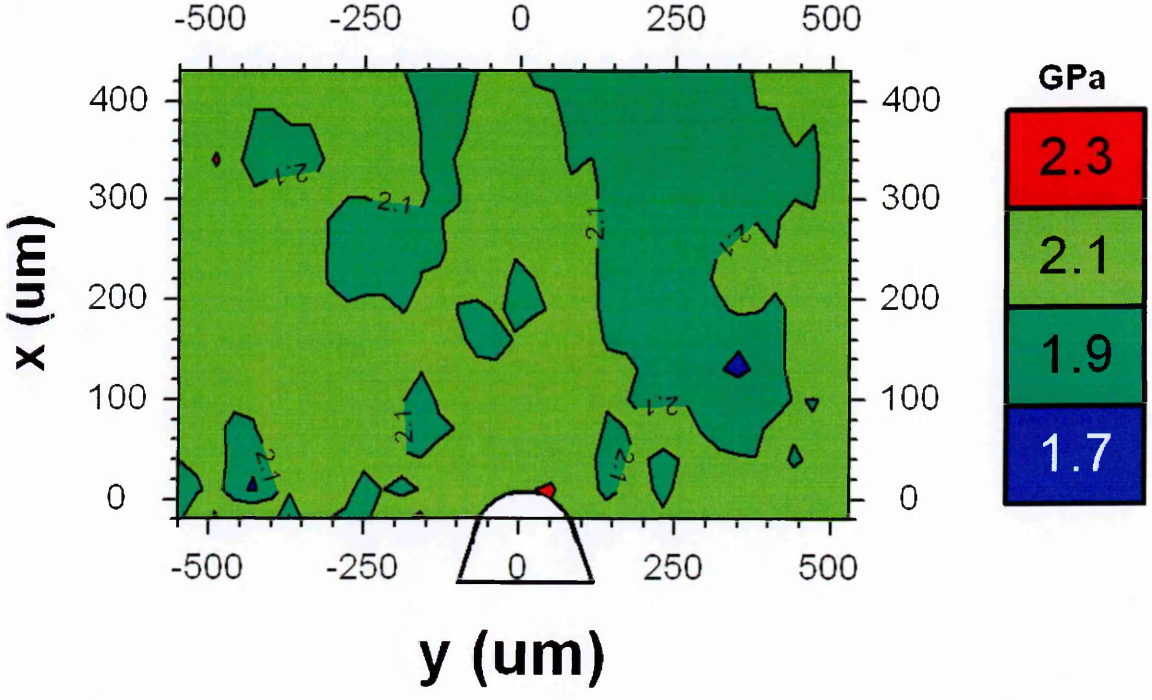

(a)

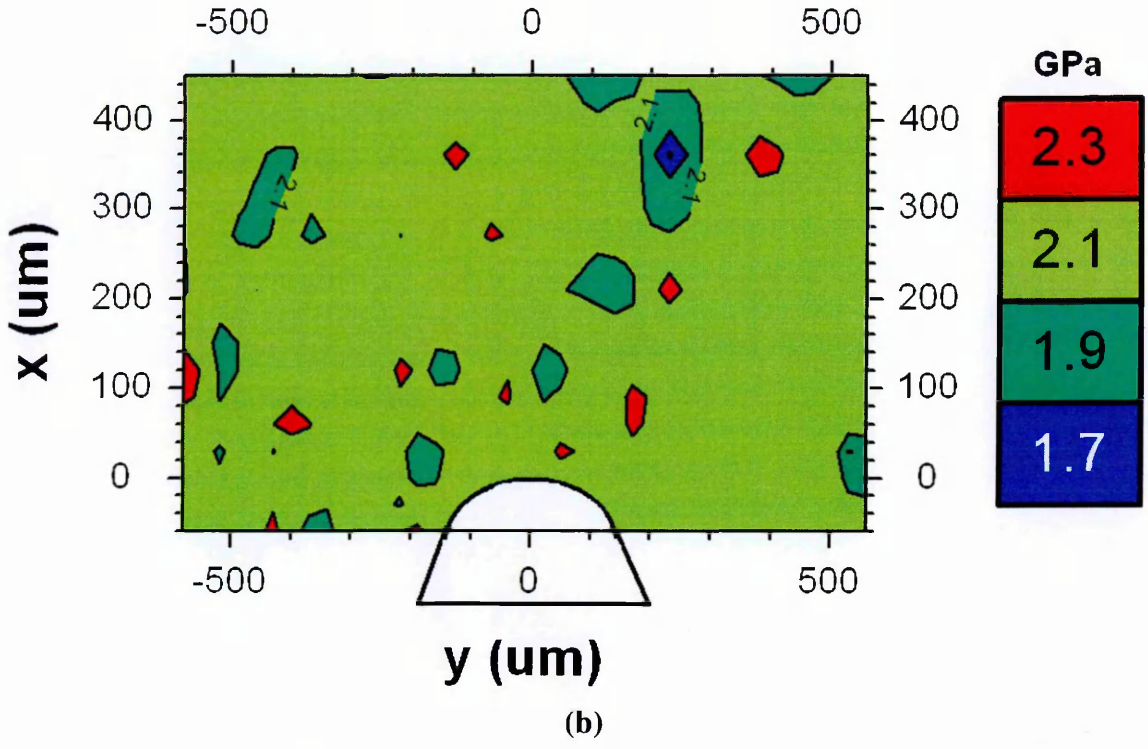

(b)

Fig. 4.13 - Hardness maps around 50 µm root radius scribes of depth (a) 50 µm (b) 100 µm

4.3.4 Hardness Profiles around Scribes of 5 µm Root Radius

The hardness results were found to be independent of the scribe depth, so here initially results of only the 75 µm deep scribe from tool A and the 100 µm deep scribe from tool B are presented. Later in the chapter hardness maps of the scribes are given.

For scribes from tool A, hardness values were constant in the first two rows of indentations from the surface, which indicated there was no localized hardening effect in this region. The first row of indents was actually slightly too close to the surface, giving hardness measurements that were lower by 5-8% [14].

For the next three rows of indentations a distinct localized hardening effect was seen close to the scribe as observed by Mezlini et al. [17]. The effect of this localized deformation extended up to ~100-150 µm from the scribe center as shown in Fig.4.14 (b). The effect of increased hardness was present on both sides of the scribe, although the hardening was not symmetric. The hardness was higher beneath the irregular feature on the tool, where the

hardness increased as much as 35% and reached up to 2.4GPa. For other side the hardness increase was around 25%. This showed that there was stronger deformed layer below this feature.

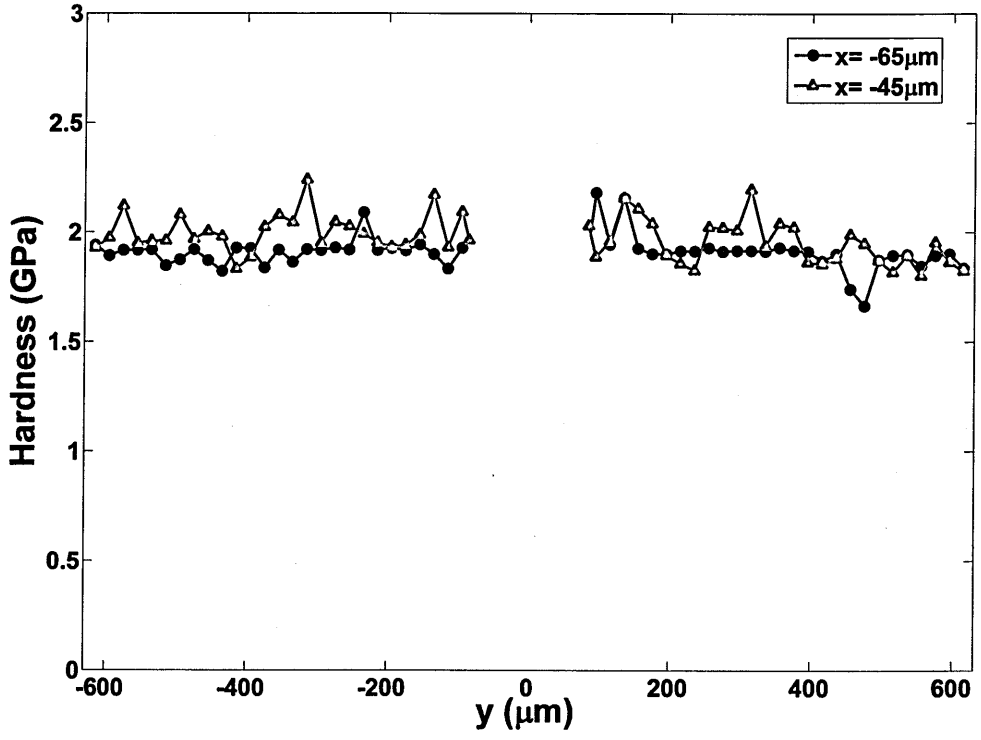

Fig. 4.14(a) - Hardness values for first two rows of indents (near to surface) in unclad Al 2024-T351 around 75 μm deep scribe from tool A

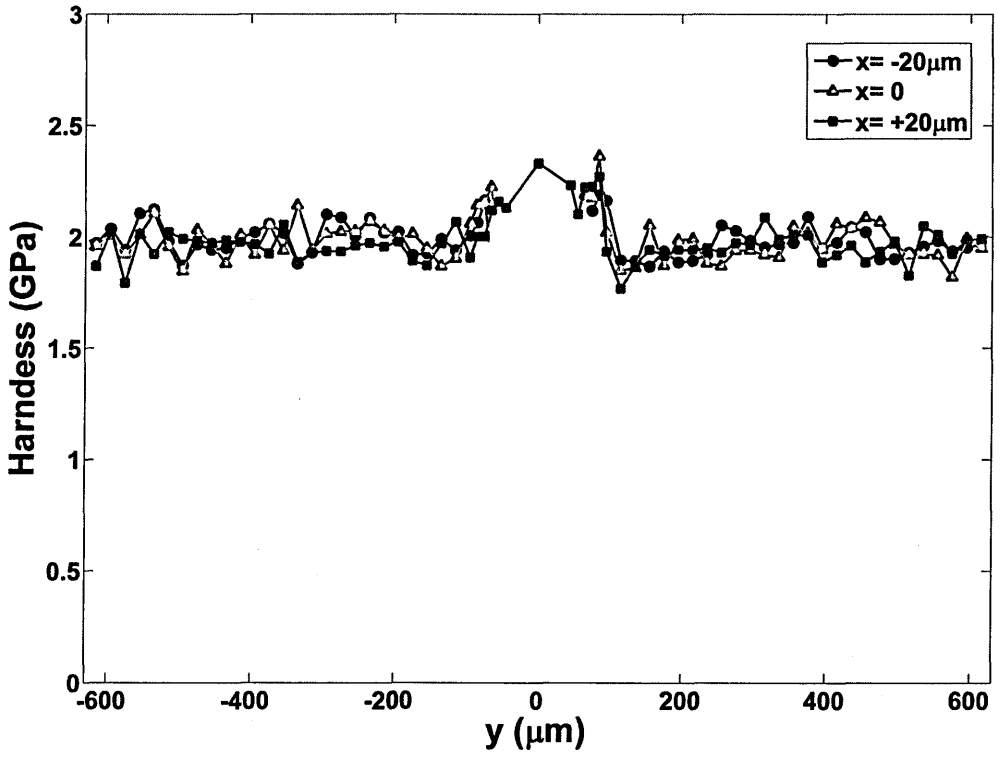

Fig. 4.14(b) - Hardness values for next three rows of indents in unclad Al 2024-T351 around a 75 μm deep scribe from tool A

For the 100 μm deep scribe from tool B, the hardness values remained constant for all the rows of indentations as shown in Fig.4.15 indicating that there is no localized work hardening effect (the first row of indentations 10μm from the surface had a slightly lower hardness but these were indents were too close to the surface). This result is in agreement with Figs.4.6 and 4.7: it was evident that no localized deformation or work hardening layer was present around the scribe and all material had been removed rather than displaced during cutting.

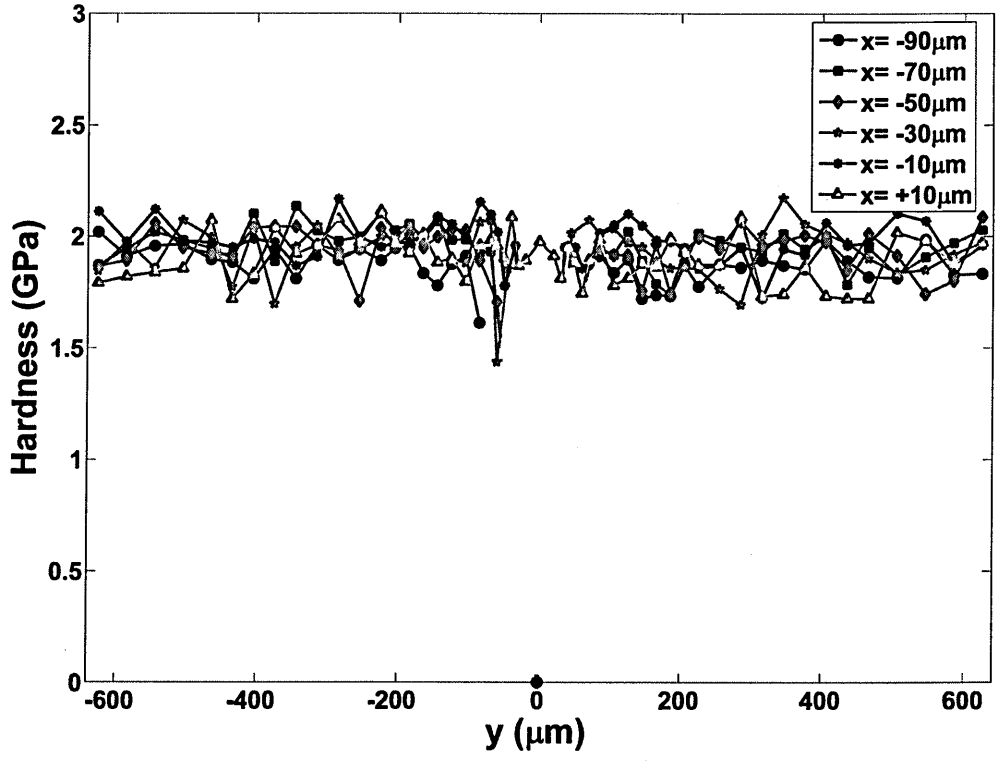

Fig. 4.15 - Hardness around 100 μm scribe in unclad Al 2024-T351 from Tool B

Hardness profiles below the scribe roots were also measured (Fig.4.16 and 4.17). For tool A scribes, a hardened region extending 100 μm was present below the scribe root. This layer was constant for every scribe and it did not change with the depth of the scribe, as shown in Fig.4.16. The hardness was a maximum at the scribe root, and decreased continuously up to ~100μm distance. This hardening can be attributed to the plastic deformation ahead of the scribe root, and this plastic deformation and the associated hardening plays a positive role in terms of the final fatigue life.

For tool B scribes, there was little evidence of any hardening at all below the scribe root, with perhaps a small hardness increase in the first 25μm (Fig.4.17). The conclusion for tool B was that it removed material through a cutting mechanism that did not cause significant plastic work hardening around the tool flanks or below the root of the scribe it produced.

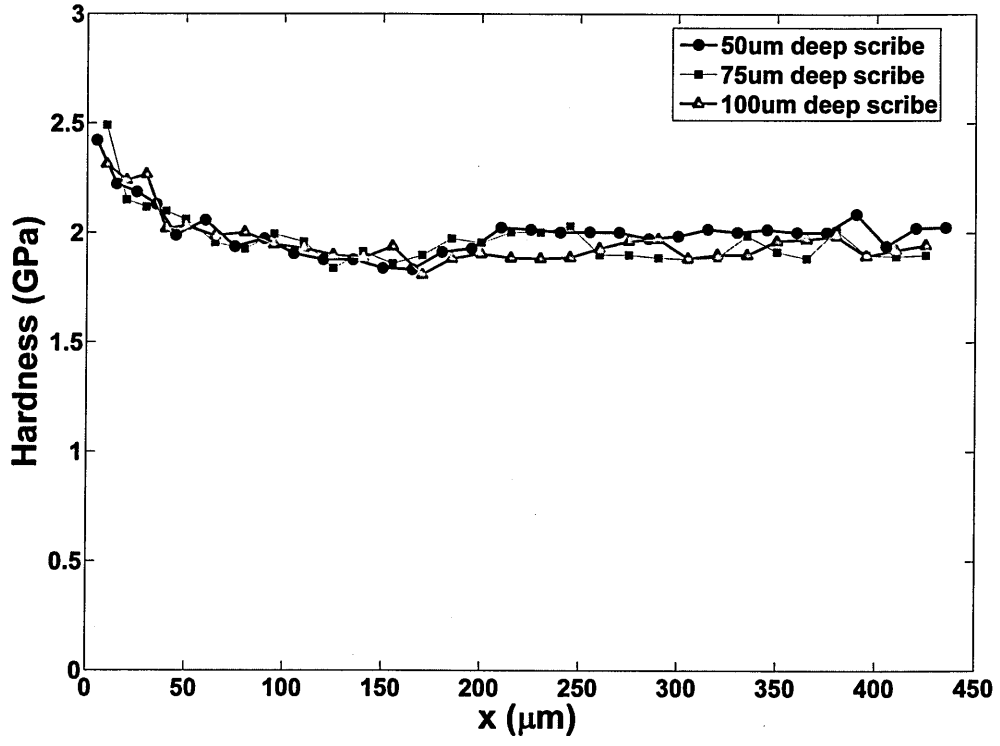

Fig. 4.16 - Root hardness for scribes produced in Al 2024-T351 from tool A

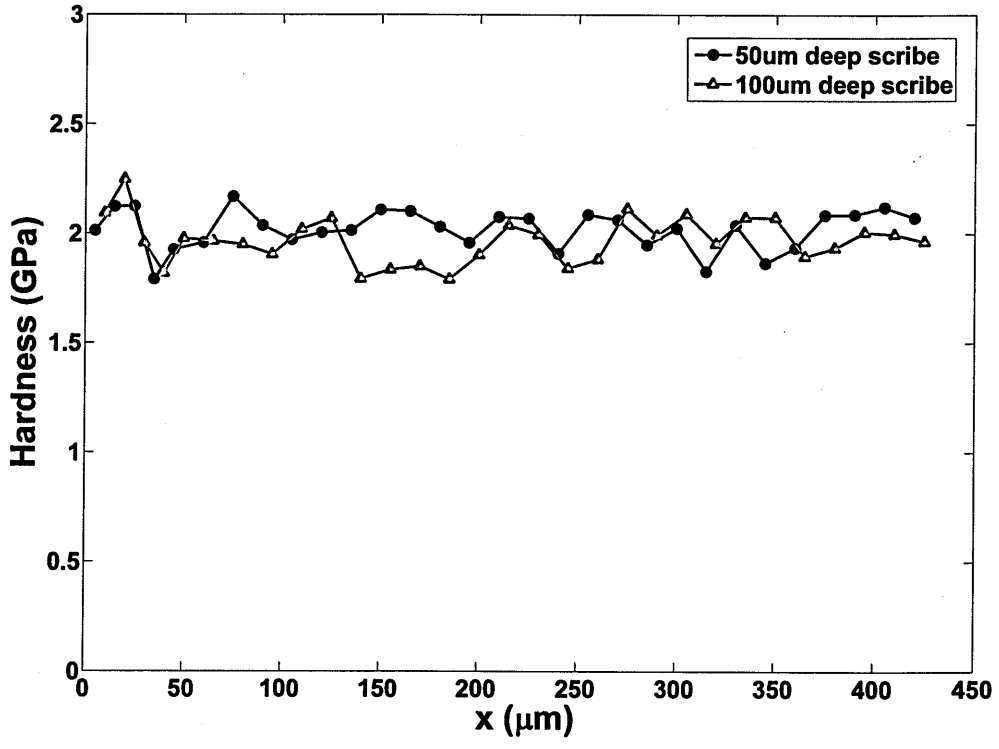

Fig. 4.17 - Root hardness for scribes produced in Al 2024-T351 from tool B

The hardness results obtained for the clad samples were also independent of the scribe depth, so results of only the 100μm deep scribes are presented here. A similar scheme of indentations was performed as for the unclad Al 2024-T351. For tool A, the hardness values increased overall as the distance from the surface increased (Fig.4.18). Although the cladding has a thickness of 100μm but the effect of the substrate (Al 2024-T351) which has a higher hardness starts to occur as indentations reach towards substrate. Hence on the cross-section of the sample when distance increase towards the substrate, effect of increased hardness starts to occur till the hardness value reached to bulk hardness value of Al 2024-T351. The first row was again slightly too close to the surface for complete validity, and the third row of indentations showed that effect of substrate hardness has started (due to increase in hardness) at 50μm and an intermediate value of hardness was obtained. The final rows of indentations were located in the 2024 substrate region and these rows of indentations revealed similar hardness behaviour as for the unclad sample, indicating a localized hardening.

For tool B, no localized hardening effect was found near the scribes (Fig.4.19). For tool A, as for the scribes in the unclad material, a 100μm layer was found in which the hardness was increased as much as 35% (Fig.4.18). The hardness then decreased continuously until it reached the parent material hardness after ~100μm. For the tool B scribe, there was no hardening effect at the scribe root.

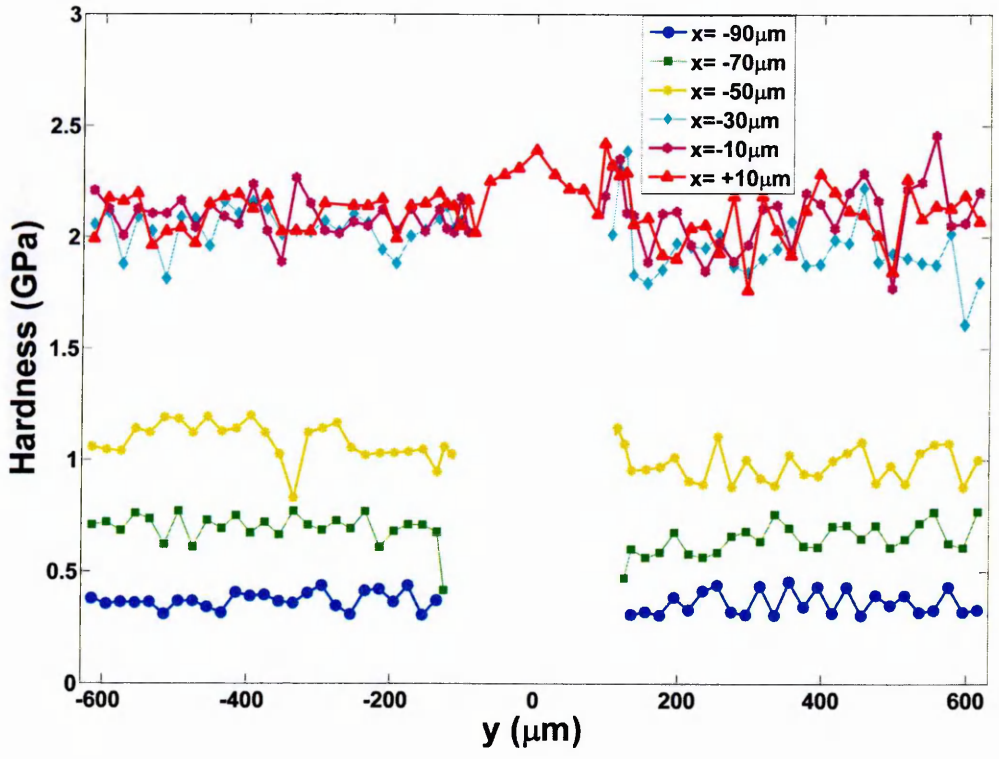

Fig. 4.18 - Hardness environment around 100 μm deep scribe in clad Al2024-T351 from tool A

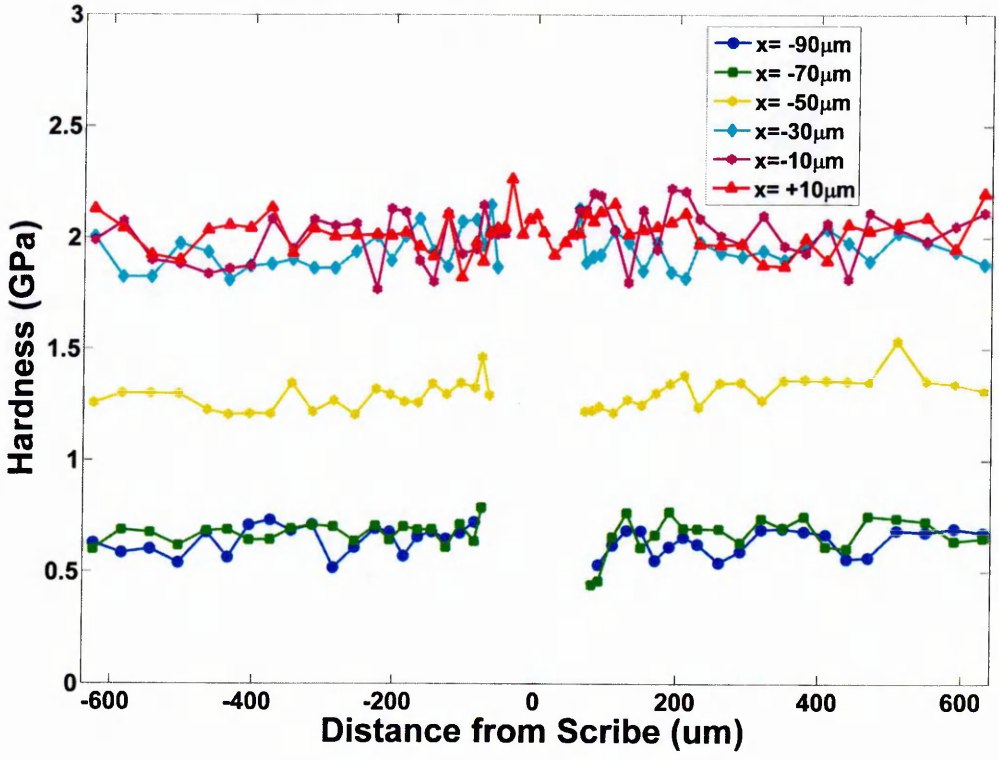

Fig. 4.19 - Hardness environment around 100 μm deep scribe in clad Al2024-T351 from tool B.

4.3.5 Effect of Fatigue on Hardness Environment

Scribes of 5 μm root radius were fatigued to observe the difference in fatigue lives with the change in tools and subsequently the effect on hardness environment on fatigue loading. Fatigue lives of the different samples with varying scribe depths are given in Table 4.2 and shown in Fig. 4.20 (a). It can be seen that there fatigue life of scribes are dependent upon the depth of the scribe. Fatigue life was decreased with increase in depth of the scribe for unclad Al 2024-T351 while opposite effect was observed for clad Al2024-T351. More fatigue life was obtained for deeper scribes for clad Al 2024-T351 In general, the fatigue life of the samples with scribes made with tool A are substantially higher than the fatigue life when using tool B. The higher fatigue life for tool A is attributed to the extensive plastic deformation and hardening associated with scribes made with this tool.

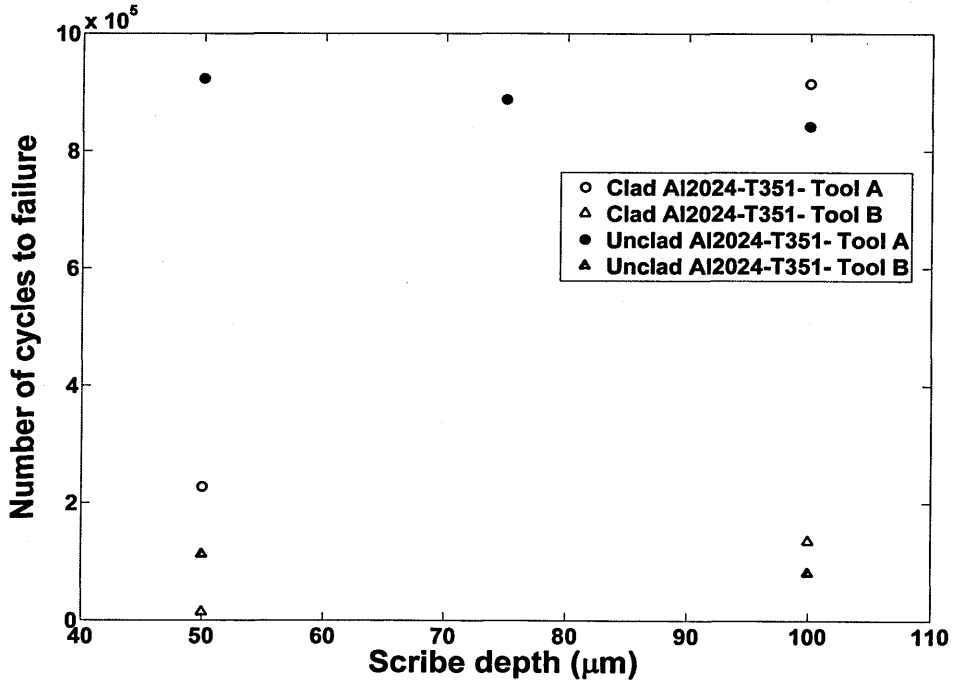

Fig. 4.20 (a) - Fatigue lives of scribes in Al2024-T351 with and without cladding

Fatigue cracks were initiated at the scribe root and propagate directly through the plate. Fig. 4.20 (b) shows a crack emanating from a scratch from a 75 μm deep scribe in clad Al2024-T351. More detail about crack initiation and propagation from these scribes produced from the same tools as in this study is available in another PhD program at Cranfield University [26].

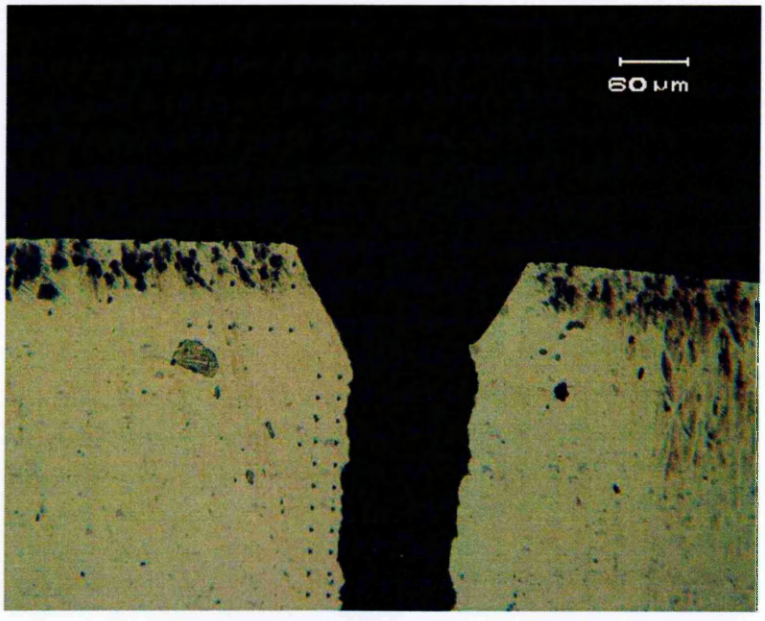

Fig. 4.20 (b) – Crack emanating from a scribe in clad Al 2024-T351

Several samples were fatigue loaded without being taken to failure (no fatigue crack was found), in order to observe the effects of cyclic loading on the hardness at the scribe tip. Fig.4.21 shows typical results that were obtained. No change in the hardness at the scribe root was seen in either clad or unclad material, for scribes produced with either tool. Few samples which were used in tension-tension fatigue loading in a previous study [24] used to observe effect of a different mode of fatigue loading on hardness environment. Similar effects were observed as in four point bending fatigue loading and no difference in hardness environment was obtained before and after loading.

It is therefore likely that the initial state of the material after the scribe is produced, in terms of the local hardness and residual stress, is not further affected by fatigue loading to a significant degree.

Serial #	Clad/Unclad	Tool	Depth d (μm)	Radius ρ (μm)	FPB Fatigue Life (No. of cycles)
1	U	A	50	5	923338
2	U	A	75	5	887359
3	U	A	100	5	841586
4	U	B	50	5	112140
5	U	B	100	5	80851
6	C	A	50	5	227747
7	C	B	50	5	13700
8	C	B	100	5	135028
9	C	A	100	5	914563

Table 4.2 - Fatigue life of scribes in four point bending

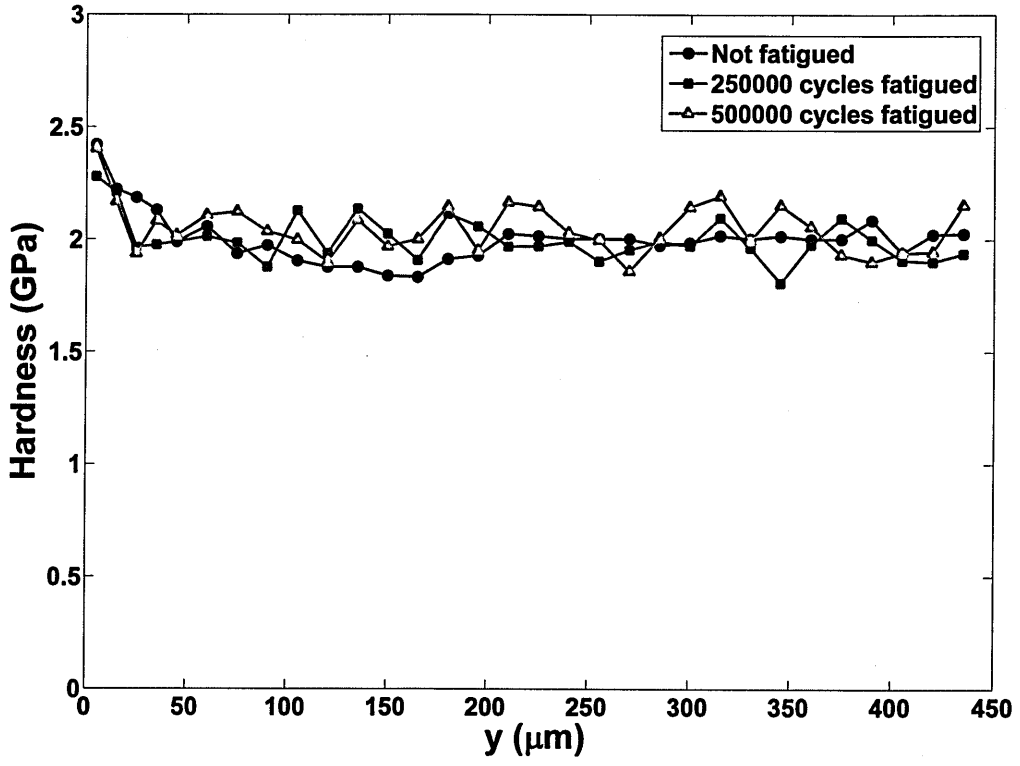

(a)

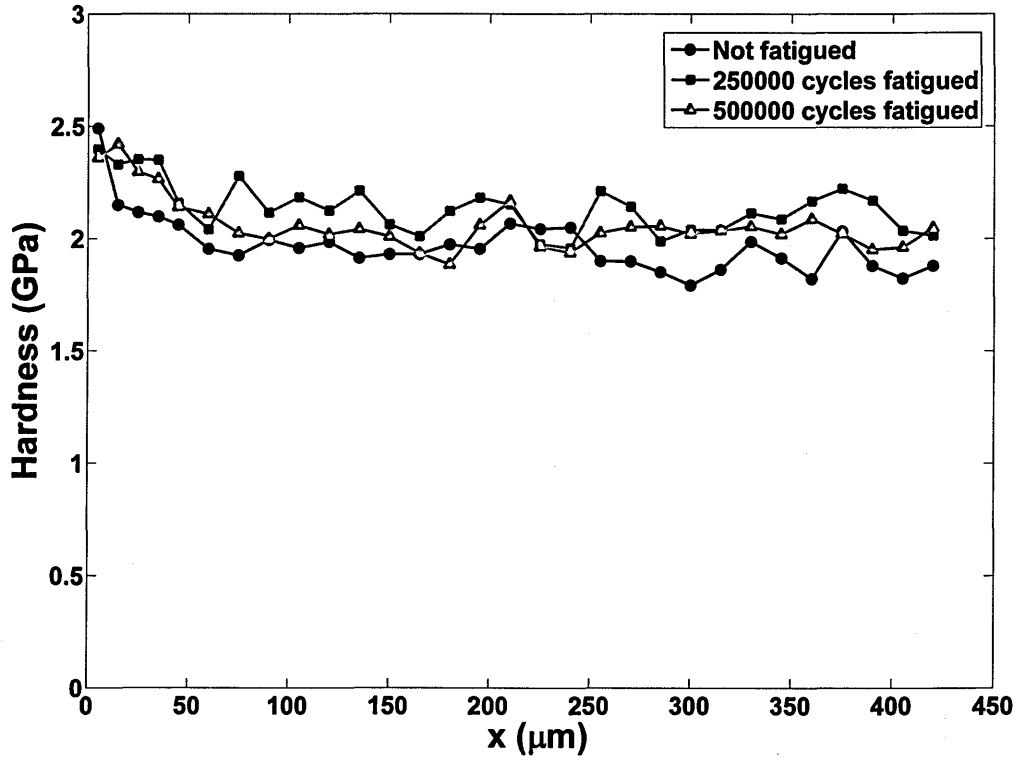

(b)

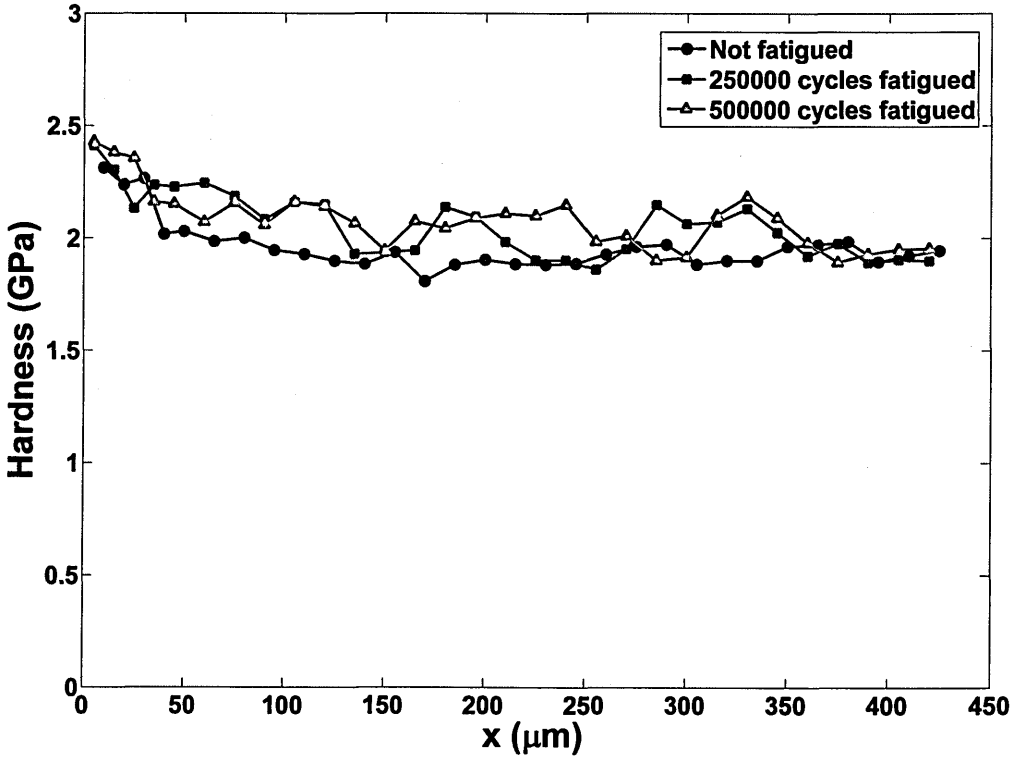

(c)

Fig. 4.21 - Root hardness after fatigued cycles in unclad Al2024-T351 from tool A in scribe of depth (a) 50 μm (b) 75 μm (c) 100 μm

It can be seen in Fig. 4.21 that hardness along the root of the scribe depends upon the depth of the scribe. With an increase in depth of the scribe, it seems that extent of the deformed region has increased. Scribes of 50 μm showed an increase in hardness in a smaller region compared to 75 and 100 μm deep scribes for which the hard deformed region had a greater extent. This is probably because in creating the larger depth scribes more material was ploughed and hence developed increase in hardness in a large region owing to the greater plastic deformation.

For clad samples, 100 μm deep scribes were tested from both tools. A similar trend was found and there was no effect on work hardening layers for either tool after fatigue cycling as shown in Fig.4.22. As the fatigue life for this scribe from tool B was considerably higher as shown in table 4.2, so this time it was hardness tested after 100000 fatigue cycles and the results are shown in Fig.4.22.

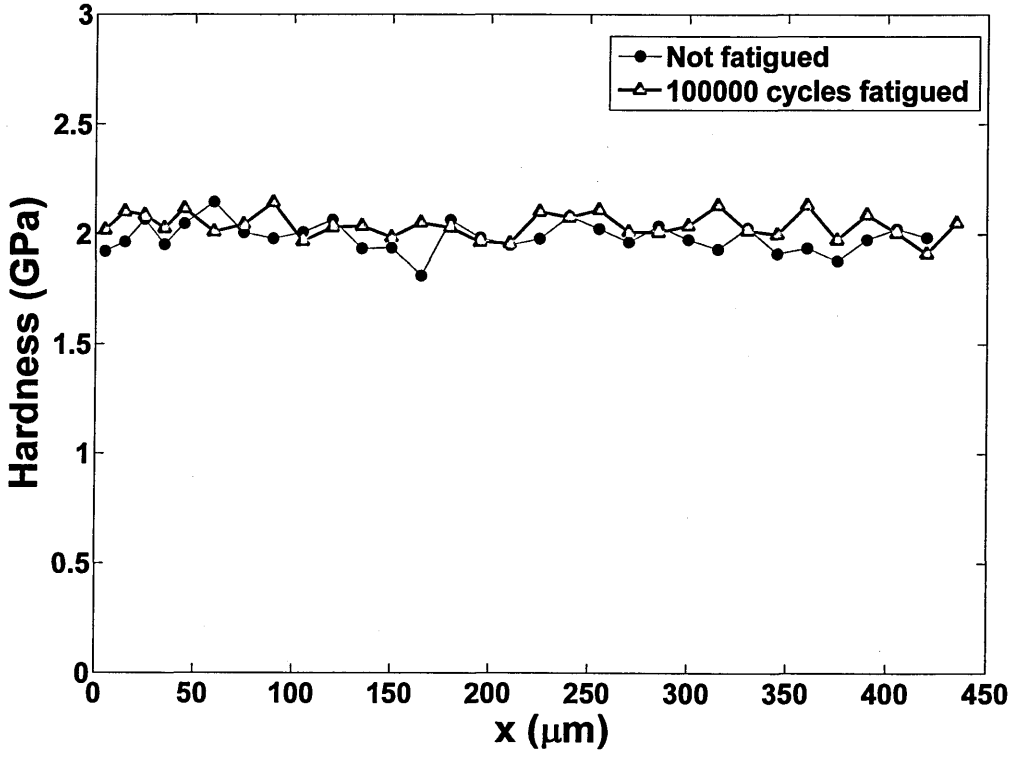

(b)

Fig. 4.22 - Root hardness after fatigued cycles in clad Al2024-T351 in 100 μm deep scribe from tool (a) A (b) B

4.4 Conclusions

Nanoindentation has been used to map the hardness around scribes in clad and unclad 2024 aluminium alloy, for scribes produced with two different tools. The hardening around such features is extremely localized and a method is required with a very high spatial resolution in order to be able to discern the small-scale changes that are induced.

Two tools capable of producing 5 μm root radius and one tool for 25 and one for 50 μm radius scribes were studied. Two tools, A and B, which produced scribes of 5 μm root radius, produced very different scribe profiles. Tool A was less 'sharp', and appeared to have some damage on the tool profile. Tool A produced a scribe by a ploughing rather than a cutting mechanism, and examination of the scribes it produced indicated that its attack angle was probably greater than for tool B. A higher attack angle is expected to tend towards ploughing during the production of a scribe. Tool A showed significant hardening around the scribe, which was not seen for the sharper tool B.

The tools used to produce 25 and 50 μm root radius scribes were very similar in wear mechanism to tool B of 5 μm root radius. These tools cut the material away and no debris around the scribe tracks was observed.

The effect of fatigue loading was investigated on the local hardness environment around the scribes. It was concluded that there was no change in the local hardness around the scribes was observed with fatigue loading of samples containing scribes. The results were the same for different modes of fatigue loading as well.

4.5 References

[1] Khan, M. K., S. V. Hainsworth, M. E. Fitzpatrick and L. Edwards. Application of the work of indentation approach for the characterization of aluminium 2024-T351 and Al cladding by nanoindentation. Journal of Materials Science 44(4), 2009, pp 1006-1015.

[2] Lee, Y.-H. and D. Kwon. Measurement of residual-stress effect by nanoindentation on elastically strained (1 0 0) W. Scripta Materialia 49(5), 2003, pp 459-465.

[3] S. Mezlini, P. Kapsa, J. P. Abry, C. Henon and J. Guillemenetet. Effect of indenter geometry and relationship between abrasive wear and hardness in early stage of repetitive sliding. Wear 260(4-5), 2006, pp 412-421.

[4] Ben Tkaya, M., M. Zidi, S. Mezlini, H. Zahouani, P. Kapsa. Influence of the attack angle on the scribe testing of an aluminium alloy by cones: Experimental and numerical studies. Materials & Design 29(1), 2008, pp 98-104.

[5] S. Mezlini, M. Zidi, H. Arfa, Ben Tkaya, M and P. Kapsa. Experimental, numerical and analytical studies of abrasive wear: correlation between wear mechanisms and friction coefficient. Comptes Rendus Mécanique 333(11), 2005, pp 830-837.

[6] Chen, Y. M., L. K. Ives, J. W. Dally. Numerical simulation of sliding contact over a half-plane. Wear 185(1-2), 1995, pp 83-91.

[7] Lee, J. H., G. H. Xu, H. Liang. Experimental and numerical analysis of friction and wear behaviour of polycarbonate.Wear 251(1-12), 2001, pp 1541-1556.

[8] Barge, M., G. Kermouche, P. Gilles, J. M. Bergheau. Experimental and numerical study of the ploughing part of abrasive wear. Wear 255(1-6), 2003, pp 30-37.

[9] K. Kato, "Micromechanics of wear-wear modes", Wear. 153, 1992, pp 277-295

[10] C. Subramanian. Some considerations towards the design of a wear resistant aluminium alloy. Wear 155, 1992, pp 193-205.

[11] Johnson, K. L. Contact mechanics and the wear of metals. Wear 190(2), 1995, pp 162-170.

[12] Kapoor, A. Wear by plastic ratchetting. Wear 212(1), 1997, pp 119-130.

[13] Kitsunai, H. and K. Hokkirigawa. Transitions of microscopic wear mode of silicon carbide coatings by chemical vapor deposition during repeated sliding observed in a scanning electron microscope tribosystem. Wear 185(1-2), 1995, pp 9-15.

[14] Ann Sundstrom , Jose Rendon, M. Olsson. Wear behaviour of some low alloyed steels under combined impact/abrasion contact conditions. Wear250, 2001, pp 744-754.

[15] P. Larsson and F. Wredenberg. On indentation and scratching of thin films on hard substrates. 3rd International Indentation Workshop, Cambridge, England, Journal of Physics D 41, 2008, 074022, pp 1-9

[16] Liu, Z., J. Sun and W. Shen. Study of ploughing and friction at the surfaces of plastic deformed metals. Tribology International 35(8), 2002, pp 511-522.

[17] Mezlini, S., P. Kapsa, C. Henon and J. Guillemenet. Abrasion of aluminium alloy: effect of subsurface hardness and scribe interaction simulation. Wear 257(9-10), 2004, pp 892-900.

[18] Saha, R. and W. D. Nix. Effects of the substrate on the determination of thin film mechanical properties by nanoindentation. Acta Materialia 50(1), 2002. pp 23-38.

[19] Bucaille, J. L., C. Gauthier, E. Felder and R. Schirrer, The influence of strain hardening of polymers on the piling-up phenomenon in scribe tests: Experiments and numerical modelling. Wear 260(7-8), 2006, pp 803-814.

[20] Gauthier, C., S. Lafaye, R. Schirrer. 2001. Elastic recovery of a scribe in a polymeric surface: experiments and analysis. Tribology International 34(7), 2001, pp 469-479.

[21] Gore, G. J. and J. D. Gates. Effect of hardness on three very different forms of wear. Wear 203-204, 1997, pp 544-563.

[22] Sauger, E., S. Fouvry, L. Ponsonnet, P. Kapsa, J. M. Martin, L. Vincent. Tribologically transformed structure in fretting. Wear 245(1-2), 1998, pp 39-52.

[23] M. E. Fitzpatrick, M. T. Hutchings and P. J. Withers. Separation of Measured Fatigue Crack Stress Fields in a Metal Matrix Composite Material, Acta Mater. 47 (1999) 585-593.

[24] Morency, R. Fatigue Crack Initiation and Growth from Scratches in 2024-T351 Aluminium. 2006, Cranfield University MSc Thesis.

[25] Kyle, C. Investigation of the transformation of defects in aircraft structures into cracks. Cranfield University MSc Thesis, 2005.

[26] Cini, A. Scribe Marks at Fuselage Joints- Initiation and propagation of cracks from mechanical defects in aluminium alloys. PhD Thesis, Cranfield University, 2009.

Chapter: 5 Finite Element Analysis of Nanoindentation Properties of Al 2024-T351 and Al-cladding

5.1 Introduction

In chapter 3 it was discussed that accurate determination of hardness and modulus is not straight forward for soft materials like aluminium alloys due to piling-up of material around the indenter. It was concluded that the work of indentation technique is most accurate technique for characterisation of soft material like aluminium alloys as it does not require the calculation of area to calculate hardness. However, to extract residual stresses from the load-displacement curve, area calculation is a must ($\sigma = Force / Area$).

Whilst all of the techniques e.g. the Oliver-Pharr model, AFM correction, etc. have their limitations to determine area of contact accurately, FEA based simulation has been proved very successful in earlier studies [1-6]. FE simulation of the indentation process can be used to study the response of the material under residual stresses, and in addition it gives insight into the mechanical behaviour of the surface during loading and unloading so accurate calculation of the area of contact is possible. This chapter discusses the development of a finite element model of the nanoindentation process using the commercial finite element package ABAQUS, and comparison of nanoindentation properties obtained from experimental nanoindentation with FE modelling.

Numerical simulation of the nanoindentation process from FEM has been widely performed by many researchers [1-6]. Elastic-plastic properties obtained from tensile testing were used successfully to simulate nanoindentation load-displacement curves. Comparison of experimental and simulated results was first presented by Bhattacharya and Nix [1] who compared the load-displacement curve obtained from simulation and experimental nanoindentation process. Pelletier [2] concluded that different pairs of yield strength and elastic modulus can produce a good fit to the experimental results of load

versus displacement. Lichinchi et al. [3] have simulated nanoindentation of TiN film by a Berkovich indenter with axisymmetric and 3D models and concluded that both models were similar and provided the same results. Bolshakov et al. [4] simulated the nanoindentation process and studied pile-up behaviour with different elastic-plastic material properties. They compared area of contact with standard analytical procedures and direct observation of contact profiles from simulation. Taljat et al. [5] in their FE study of nanoindentation showed that pile-up at full load and after unloading changes significantly, especially for materials with greater elastic recovery. They concluded that pile-up is a function of the E/σ_Y ratio and strain hardening exponent of the material.

In this study, to simulate the nanoindentation process on Al 2024-T351 and cladding, different strategies were adopted. For Al 2024-T351, elastic-plastic properties were obtained from tensile testing and used in a FE model to simulate load-displacement curves. This aspect of nanoindentation is called 'forward analysis', in which elastic-plastic properties are used to simulate nanoindentation load-displacement curves. A different strategy was adopted for the simulation of nanoindentation response of cladding for which elastic-plastic properties were not known due to its presence in a very small thickness ($100\,\mu m$ on both sides of Al 2024-T351 plate). In this case, the experimental load-displacement curves were used to approximate the elastic-plastic properties of the cladding. This is called 'reverse analysis'.

Simulations were performed using the commercial finite element package ABAQUS. For Al 2024-T351 and Al-cladding, load-displacement curves of experimental nanoindentation were compared with simulated load-displacement curves. Nanoindentation properties like maximum load P_{max}, contact depth h_c, area of contact A_c, stiffness S and pile-up around indents were compared from experiments and simulation. Excellent agreement was found for nanoindentation properties obtained from forward and reverse analysis with experimental results.

5.2 Material Properties and Finite Element Simulation Procedure

5.2.1 Materials Properties

For forward analysis of Al 2024-T351, material properties used in the FE model were obtained from tensile testing according to ASTM standard E 8/E 8M-08 [28]. Mechanical properties and stress strain curve of Al 2024-T351 are given in chapter 3.

For Al-cladding reverse analysis was performed for which the constitutive law used was obtained from a detailed exercise which will be discussed later in this chapter. Experimental nanoindentation was performed on Al 2024-T351 and Al-cladding using an MTS nanoindenter with similar experimental parameters as discussed in chapter 3. Ten indents were made at each indentation depth to avoid any abnormality in the test results and average values have been considered as representative values.

5.2.2 Finite Element Simulation Procedure

The Berkovich indenter is a triangular-base pyramid having a six-fold symmetry. When the indenter has an axisymmetric form (cones, spheres, etc.), an axisymmetric finite element model remains sufficient [1-6]. An axisymmetric model can also be used to simulate a Berkovich indenter [4-5] as it not only saves the computation time and cost but provides similar contact area as a Berkovich indenter. Lichinchi et al. [3] simulated the nanoindentation response with axisymmetric model and validated their results with a 3D model. They concluded that there was no difference in results if axisymmetric model is used instead of 3D models. Hence in this study an axisymmetric finite element model has been used for simulation of nanoindentation response.

Al 2024-T351 and cladding were modelled with consideration of different mechanical properties. Simulations were performed using a deformable axisymmetric material and a rigid indenter. Model size of 2mm x 2mm was constructed in two parts: an indenter and test material, with axisymmetric geometries. The material was modelled using four node

axisymmetric reduced integration element 'CAX4R' while the indenter was modelled as a 'rigid element'. The Von-Mises yield criterion was applied for determination of plastic deformation. The indentation region was very small as compared to the size of the model so due to more straining around the indenting region, a fine mesh size was used around near contact regions. The total number of elements was 8500. The indenter was considered as a perfect rigid cone with the same area-depth function as a Berkovich indenter, as cone of 70.3° gives the same area-depth function as a Berkovich indenter [4]. Schematic representation of the model is given in Fig.5.1.

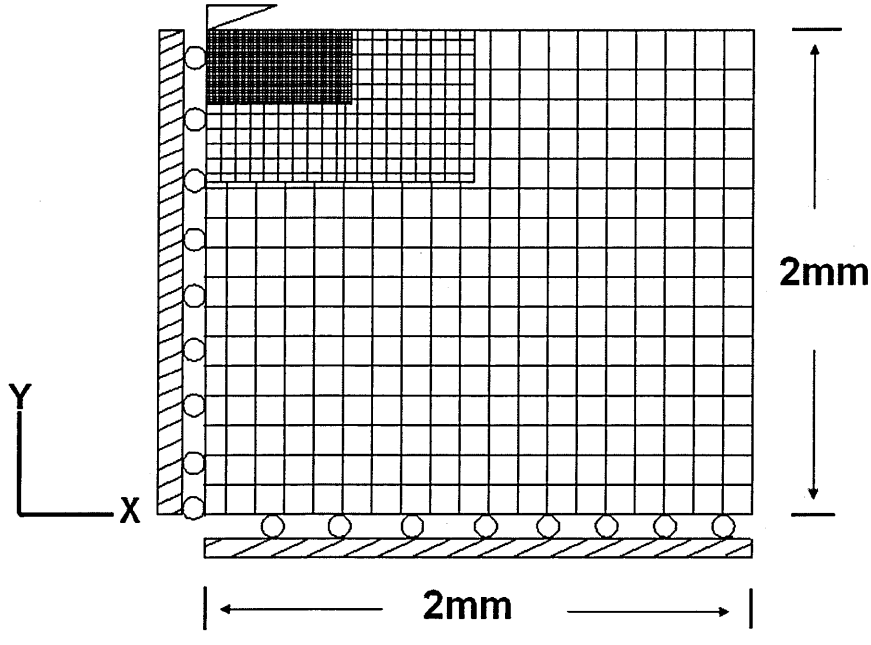

Fig. 5.1 - Schematic of finite element model

In experimental nanoindentation, an indenter is pressed against the material and load applied on the indenter, and the indentation depth is recorded by two sensors above the indenter. Similarly in simulation, for contact elements, constraint was enforced by the definition of indenter as 'master' and the sample as 'slave' surfaces. Only the master surface was allowed to penetrate into the slave surface and the contact direction was always taken as being normal to the master surface. The indenter surface was chosen as the master surface due to the larger stiffness of the indenter with respect to the specimen.

Roller boundary conditions were applied on the bottom surface of the model in which material was free to move in x- direction but other two degrees of freedom were constrained. The coefficient of friction between the indenter tip and the specimen surface was assumed as zero which doesn't have any significant effect on nanoindentation load-displacement response [2]. The simple strategy "Interaction = Frictionless" for contact elements was chosen. "Surface to Surface Contact" was defined between indenter and material's surface in order to avoid any kind of separation during loading stage. For each displacement of the indenter, the subsequent reaction force was recorded on the reference point at the top surface of rigid indenter. Loading and unloading stages were simulated in two different steps in which during loading, the rigid indenter penetrated the sample up to the maximum depth while during unloading the indenter tip returned to the initial position. An ideal Berkovich indenter is assumed to have no roundness at its tip. But tip bluntness occurs in every indenter due to machining limits during manufacturing. This tip blunting effect is more significant for shallow indents of the same depth as the order of roundness of the tip, as up to this range of depth a Berkovich indenter behaves like a spherical indenter. The O-P model calibrates the area to compensate for the tip roundness effect with a polynomial area function as discussed in chapter 3 according to eq. 3.7, therefore for comparison of results from experimental and simulated nanoindentation, the FE model should take account of this effect. Tip blunting effects can be obtained by fitting the square root of load and depth curve [6, 24-26]. Tip roundness effects can be observed only at shallow indents which have indentation depths in the order of 100-200 nm. No account for tip blunting effect was taken here in current model as the depths of indentations were not that shallow.

5.3 Results and Discussion

5.3.1 Forward Analysis on Al 2024-T351

Elastic-plastic data obtained from tensile testing has been fed into ABAQUS to simulate the indentation process. Simulations of indentations were performed at different depths similar to experimental nanoindentation depths [8]. Load-displacement curves obtained from simulations were compared with experiment and agreed well with each other as shown in Fig.5.2. The curve showed a small deviation especially in the unloading curve due to the differences in the assumed friction coefficient, tip blunting effect and strain rate during simulations which were not considered here [2-3]. Due to the relative softness of Al 2024-T351, although we performed experimental indentation at zero hold time, maximum depth of the indentation increased 5-10nm further due to creep. This difference in maximum depth caused some difference as well in unloading curves between experiments and simulation.

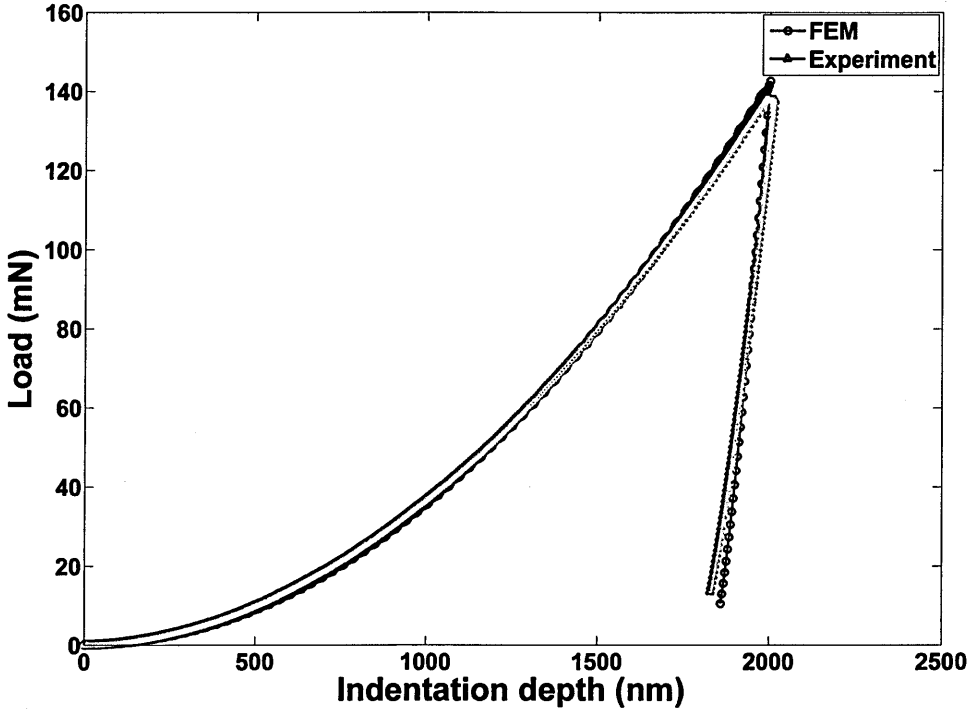

Fig. 5.2 - Comparison of load-displacement curves from FEM and experimental nanoindentation at 2000nm.

5.3.1.1 Comparison of Nanoindentation Properties

For every indentation depth, the maximum load of indentation P_{max}, the indentation contact depth h_c at full load, and the contact area of indentation A_c were calculated using the procedure given in chapter 3. For simulation, the area was calculated using $A_c = 24.5h_c^2$ without any tip bluntness effect as this effect was not considered here in the model. P_{max}, h_c and A_c calculated from FEM and experimental nanoindentation agreed extremely well with experimental results as shown in Fig.5.3.

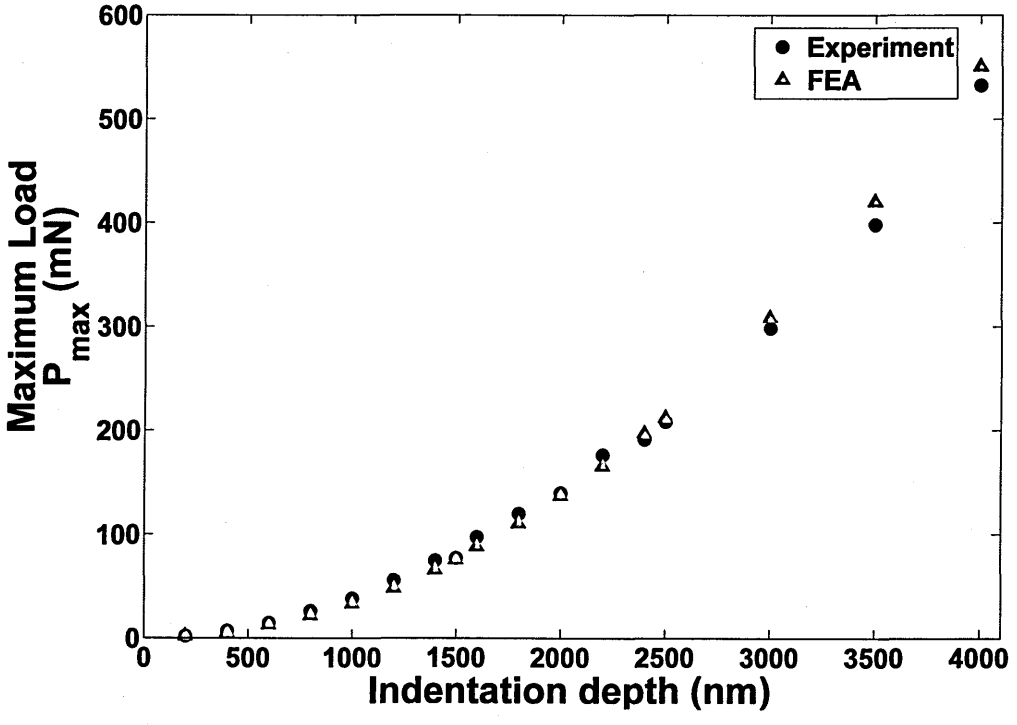

(a)

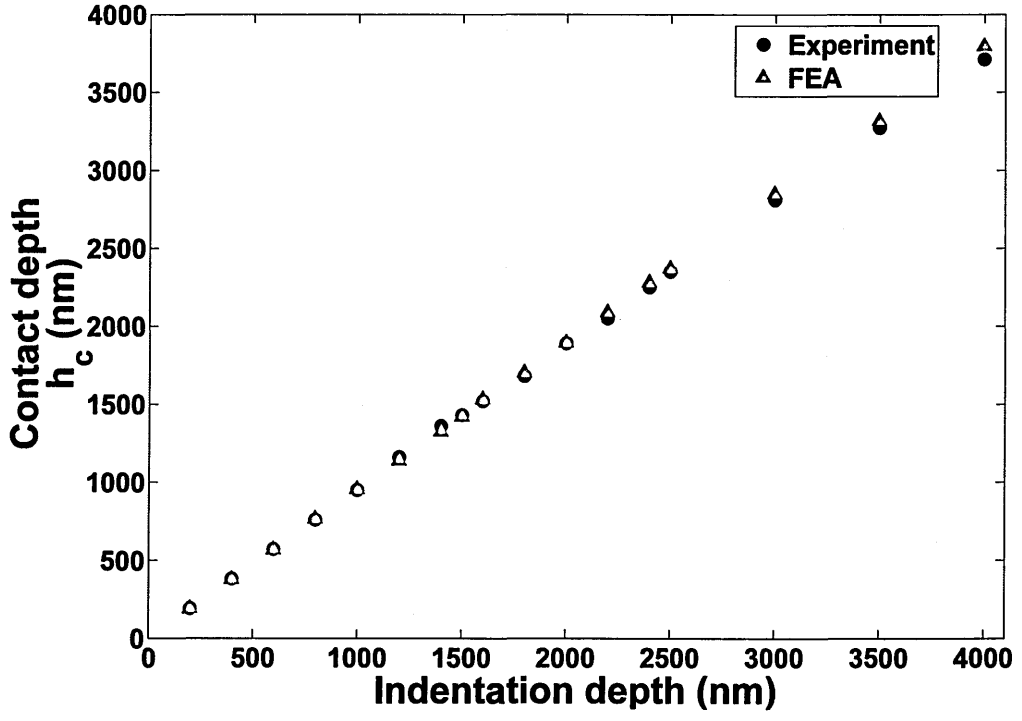

(b)

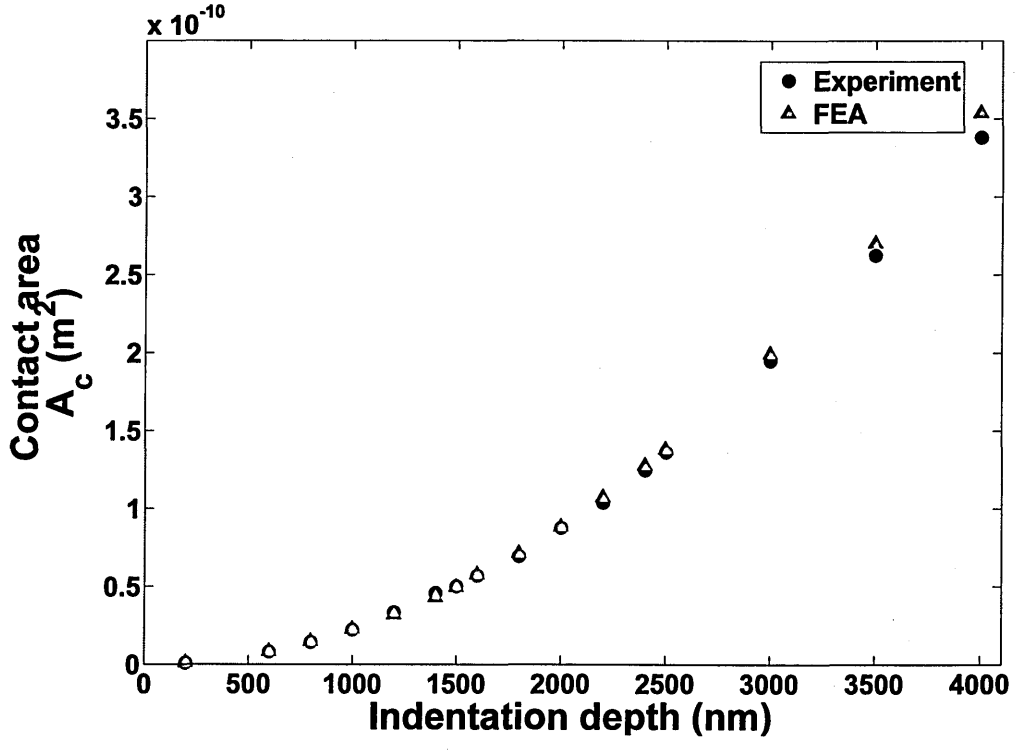

(c)

Fig. 5.3 - Nanoindentation properties from FEM and experimental nanoindentation (a) Maximum load (b) Contact depth (c) Contact area

5.3.1.2 Pile-up Characterization

It has already been discussed in chapter 3 that while indenting aluminium alloys, due to their low hardness and small strain hardening exponents, pile-up around indents starts to occur even at low loads [8]. For experimental nanoindentation, quantification of pile-up was characterized using Atomic force microscopy (AFM) [8]. It was observed that pile-up occurred in the form of three lobes around three edges of the triangular indent, and was not necessarily of equal length and height around all three edges of indentation.

With a very low work hardening exponent of 0.1 and E/σ_Y ratio of 188, as shown in in chapter 3, pile-up was expected for Al 2024-T351. These two parameters lead to very small elastic recovery of the materials during the unloading phase of indentation. The ratio of final depth of indentation to maximum depth of indentation, h_f/h_{max}, gives an indication of elastic recovery for any material. The value of this ratio can be from 0 to 1. For Al 2024-T351, the final depth h_f obtained after unloading returned a value very close to 1 for the ratio of these two depths i.e. $h_f/h_{\max}$. Bolshakov et al. [4] showed that significant pile-up forms for materials which exhibit this ratio close to 1 and this piling-up of material starts from a value of 0.7, while Lee et al. [6] stated it as 0.88. The ratio h_f/h_{max}, which can be used as indicator for pile-up, was calculated for Al 2024-T351 from experimental and simulated load-displacement curves at different depths and was found as 0.91-0.92 as shown in Fig.5.4 (b).

To compare the accuracy of FEM in simulating nanoindentation, contact profiles were used to obtain the amount of pile-up at each depth and were compared with experimental results. The extent of pile-up will not necessarily be symmetric but the axisymmetric model had the limitation that it will always predict symmetric pile-up behaviour. A comparison of pile-up height showed excellent agreement as shown in Fig.5.4 (a) and the extent of pile-up in terms of horizontal distance agreed reasonably well. The differences could be attributed to the true friction coefficient between indenter and indented material

(which was assumed zero), and the tip convolution effect of the real Berkovich indenter [13]. This is the limitation of the axisymmetric model which cannot calculate the three dimensional periphery of the pile-up. Another important factor is that the real Berkovich indenter has a tip blunting effect which generates pile-up that may not be of equal length and height around all three edges of indentation due to a variable radius of tip blunting. Hence, even a 3D finite element model with consideration of tip roundness effect cannot predict accurately asymmetric behaviour of pile-up.

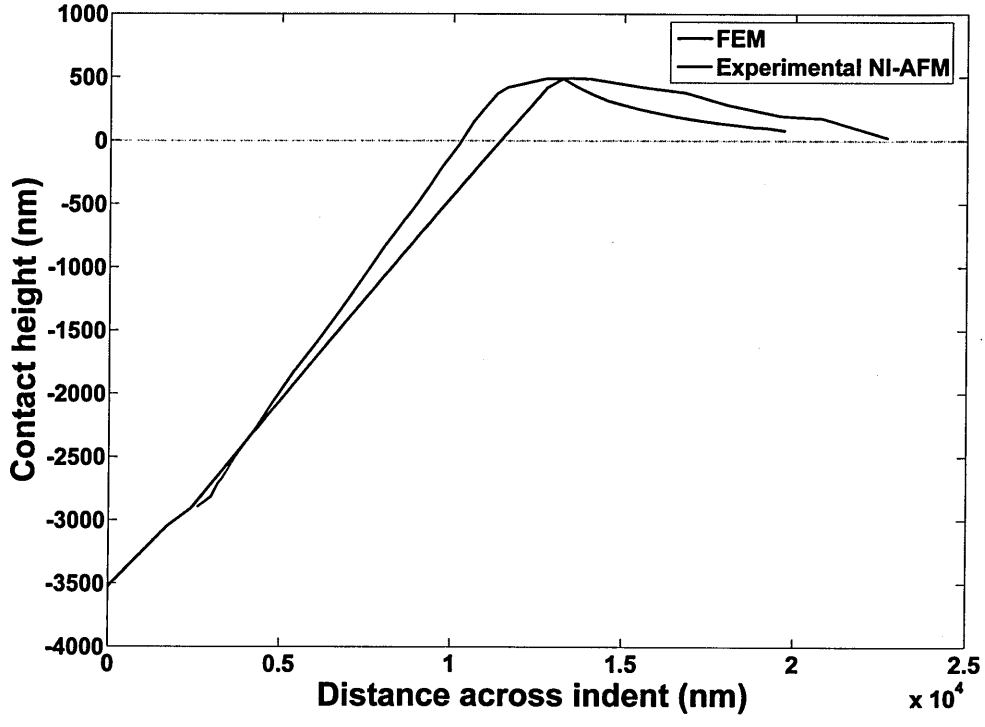

(a)

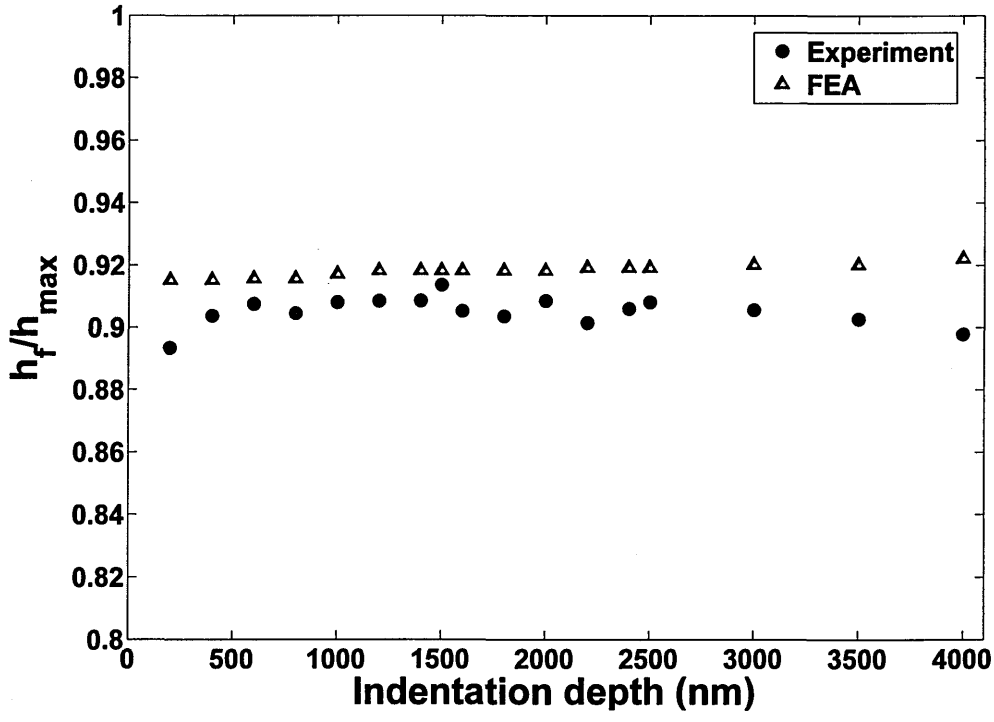

(b)

Fig. 5.4 - Pile-up properties comparison (a) Cross-section of indent from AFM and FEM for an indent at 400nm depth (b) ratio h_f/h_{max} which explains existence of pile-up

5.3.2 - Reverse Analysis on Al-cladding

The cladding of pure aluminium has a thickness of only 100μm. Due to this form of cladding, tensile testing was not possible and consequently without elastic-plastic properties, simulation of the load-displacement curve was not possible.

It has been discussed in earlier sections of this chapter that for Al 2024-T351, elastic-plastic properties can be used to simulate the load-displacement curve with FEM. A unique set of elastic-properties results in a unique load-displacement curve. This process of getting nanoindentation properties from elastic-plastic properties is termed forward analysis. If elastic plastic properties are unknown a priori, experimental load displacement curves are used to back calculate elastic-plastic properties; this process is termed reverse analysis and in this process different dimensionless functions are used to approximate elastic-plastic properties and constitutive laws from a single experimental indentation test [9-18].

Hainsworth et al. [9] showed that every load-displacement curve is a unique outcome of specific elastic-plastic properties. Tabor [19] in his work used yield stress at 8-10% plastic strain to define hardness for ductile materials i.e. $H=3\sigma_{Y8-10\%}$. Based on Tabor's work, different studies have been carried out describing different functions to approximate the elastic-plastic properties from load-displacement curve. In these studies, different values of yield stress have been used to determine the level of the plastic strain at which yield stress best normalizes the dimensionless functions. Cheng et al. [10-13] used the yield stress at 10%, Giannkapolous et al. [15] used 29%, Dao et al. [14] used 3.3%, Osgawara et al. [17] used 1.15%, and Chollacoop et al. [23] with dual indenters used 3.3% and 5.7%. These different definitions of yield stress (i.e at different strain levels) are due to differences in terms of functional definitions of their dimensionless functions and have nothing to do with the mechanical behaviour of the material. All of these different studies have different conclusions about the effectiveness of using the load-displacement curve for extraction of elastic-plastic properties [9, 14, 20, and 23]. Alkorta et al. [20] showed that no unique relationship exists between load-displacement curve and elastic-plastic properties, and different combinations of these properties can generate similar load-displacement curve.

In this study, Tabor's work is used to define the yield stress used in the simulations and 10% plastic strain has been used. No specific dimensionless function was used here, and instead, all four basic parameters were obtained from the load-displacement curve and minimized the difference between these parameters from simulation and experiment. The work presented here does not challenge any of the conclusions which have been made in earlier research but this was an attempt to characterize the elastic-plastic properties of the cladding which were required for further work in terms of the response of load-displacement curves in existence of residual stresses.

5.3.2.1 - Indentation Load-displacement Curve

The load-displacement curve for a typical experimental nanoindentation consists of loading and unloading sections. The loading curve behaves according to a power law and can completely be described by its curvature C and maximum load P_{max}. On the other hand, the unloading curve can be fully described by the gradient of the initial part of the loading curve, which is known as stiffness S, and upon the elastically recovered depth h_f. Based on the maximum depth of penetration h_{max} and the depth at the end of unloading h_f, the elastic, plastic and total work of indentation can be determined as discussed in chapter 3.

These four parameters i.e. $C, P_{\max}$, S and $h_f/h_{\max}$ (or W_p/W_t) had been used in different dimensionless functions in earlier studies to obtain elastic-plastic properties from the load displacement curve [10-18].

Characteristically, the indentation load-displacement curve for an elastic-plastic work hardening solid is a function of indentation depth h, elastic modulus E, initial yield stress σ_Y, indenter half angle θ, work hardening exponent n and Poisson's ratio v. With the assumption of certain parameters, the number of variables can be reduced. All of the simulations were carried out with a cone of semi apex angle $\theta = 70.3°$ to an indentation depth of 1000nm. Considering that there is almost no effect of Poisson's ratio on the load-displacement curve, and for most of aluminium alloys this ratio is 0.33 [27], it was assumed constant in this study. The elastic modulus E for pure aluminium may lie in range of 65-70GPa [27], so 67GPa was chosen as the value of modulus to make reverse analysis much more simplistic.

These assumptions reduced the number of variables to only two i.e. the initial yield stress σ_Y and work hardening exponent n and all of the simulations performed were described by only these two parameters.

5.3.2.2 - Error Analysis

Experimental indentation tests were performed on the cladding and the four parameters C, S, P_{max} and W_p/W_t were calculated from each indentation. The elastic-plastic properties of many engineering metals under loading can be described by a true stress-strain curve as shown in Fig.5.5. According to this, a set of $E, \nu, \sigma_y, and\ n$ are required to describe the constitutive behaviour of any material. For simulation of nanoindentation, one particular material constitutive law generates its own distinct set of four indentation parameters as discussed above. As we have concluded that Poisson's ratio and elastic modulus are 0.33 and 67GPa for cladding so only initial yield stress σ_Y and strain hardening exponent n were required for definition of the elastic-plastic properties in simulation.

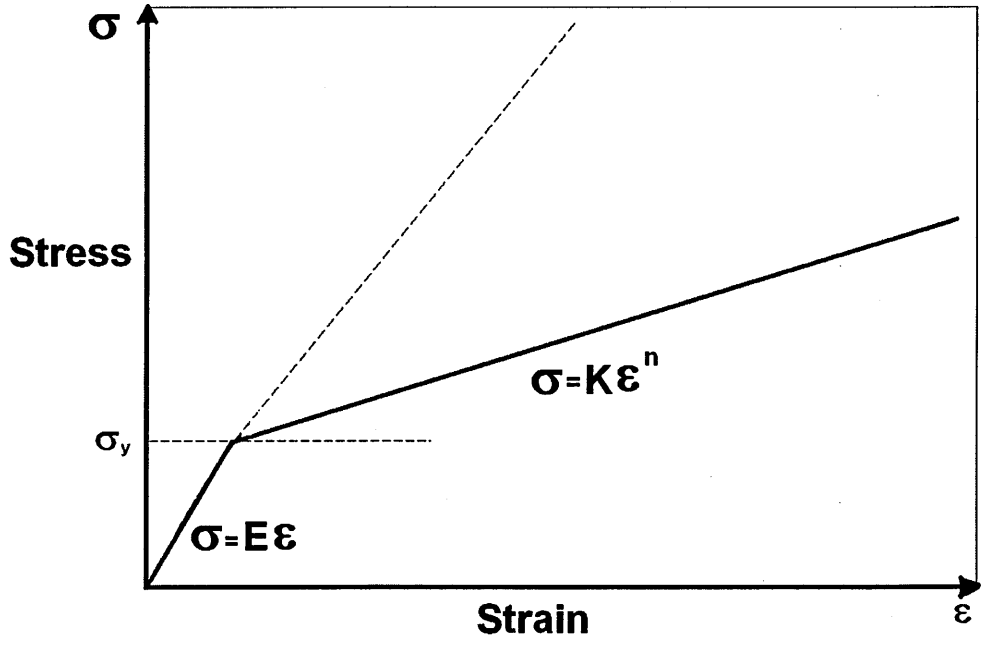

Fig. 5.5 - Constitutive law used to define elastic-plastic properties for FEM

The initial yield stress and work hardening exponent were chosen carefully. According to Tabor's relation, the hardness of any elastic-plastic material can be expressed as $H=3\,\sigma_{Y8\text{-}10\%}$. In chapter 3, the hardness of Al-cladding was found as 0.45GPa. This value of hardness leads to a yield stress of 150MPa at 8-10% of plastic strain. This implies that the initial yield stress at 0% plastic strain may lie in a range of 90 to 130 MPa

approximately. The clad consisted 99.5% Aluminium and pure aluminium is considered as elastic-fully plastic having no or very low work hardening exponent. So in reverse analysis range of yield stress from 40MPa to 160MPa in a step of 10MPa was used which lead to 13 values of initial yield stress and work hardening from 0 to 0.2 in a step of 0.025 was used which lead to 9 values of strain hardening exponent. In total this made 108 sets of σ_Y and n. For all these 108 sets simulations were performed to obtain load-displacement curves and subsequently $C, S, P_{\max}$ and W_p/W_t. Distributions of these four parameters for all values of σ_Y and n are shown in Fig. 5.6.

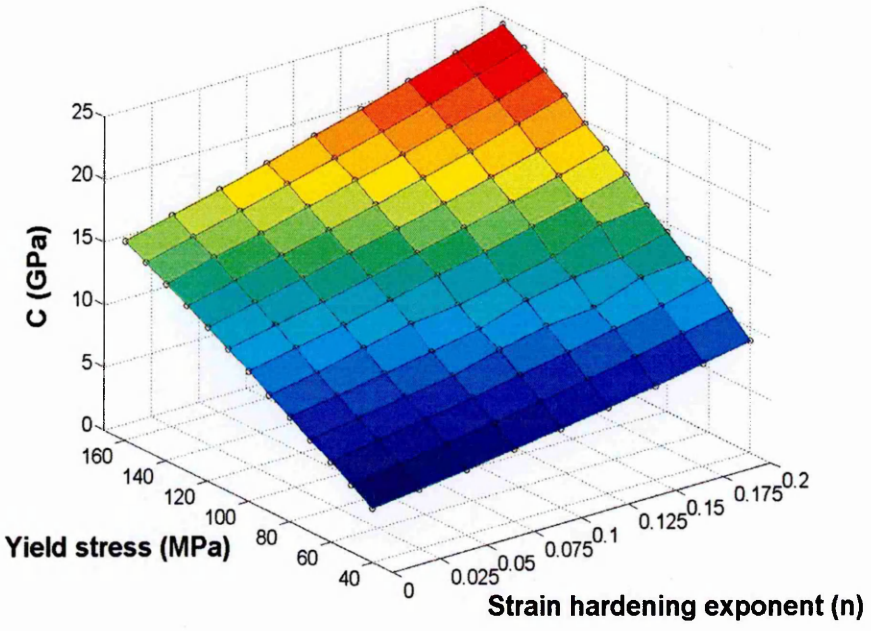

(a)

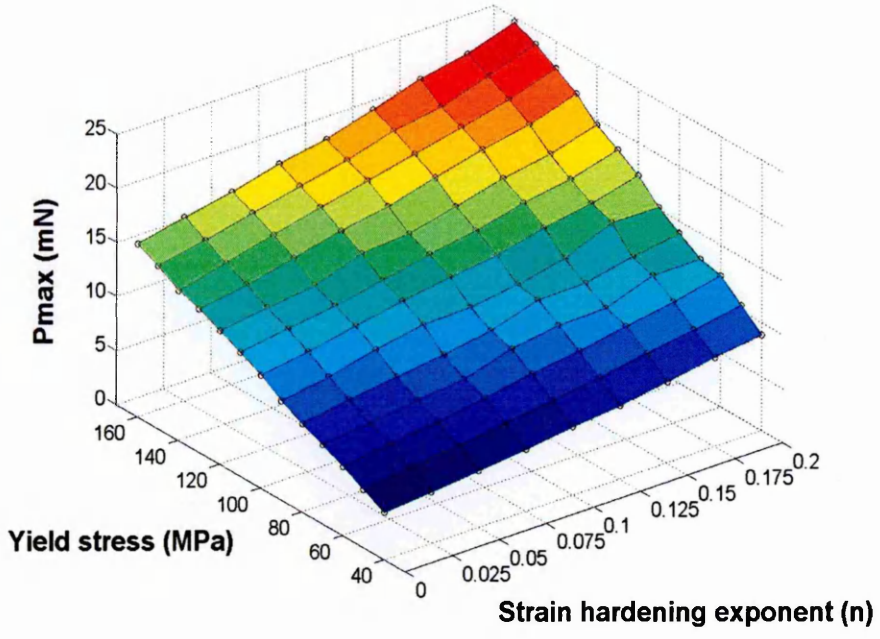
Pmax (mN)
25
20
15
10
5
0
160
140
120
100
80
60
40
Yield stress (MPa)
0
0.025
0.05
0.075
0.1
0.125
0.15
0.175
0.2
Strain hardening exponent (n)

(b)

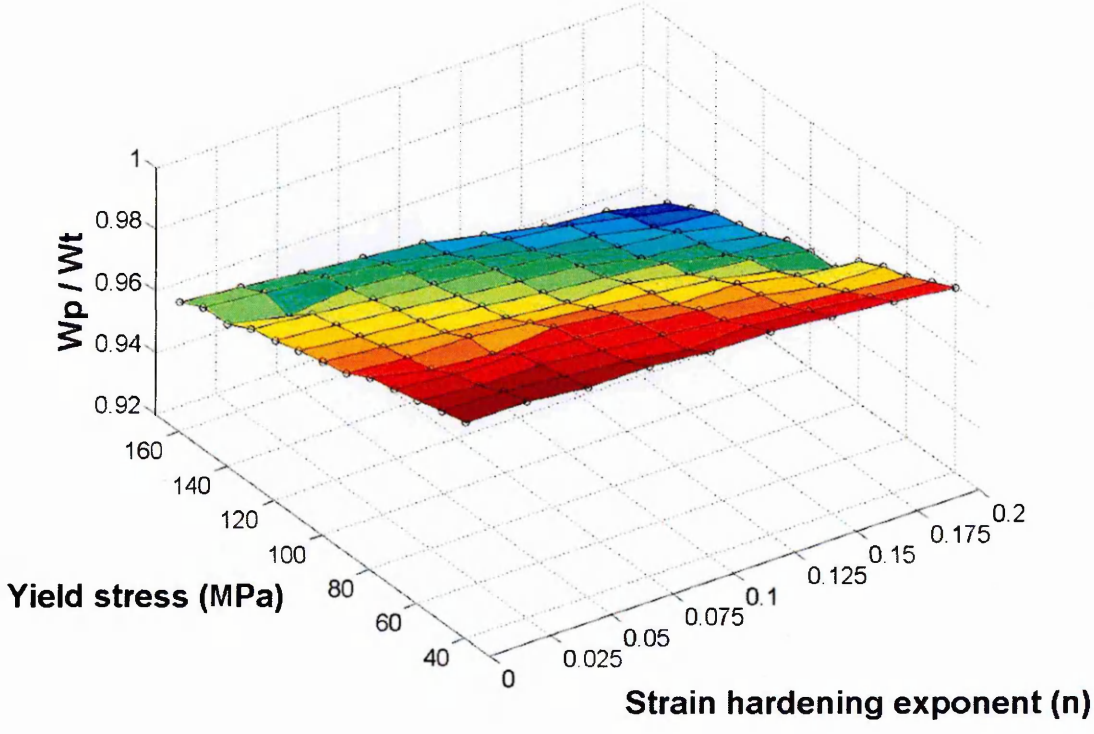
Wp / Wt
1
0.98
0.96
0.94
0.92
160
140
120
100
80
60
40
Yield stress (MPa)
0
0.025
0.05
0.075
0.1
0.125
0.15
0.175
0.2
Strain hardening exponent (n)

(c)

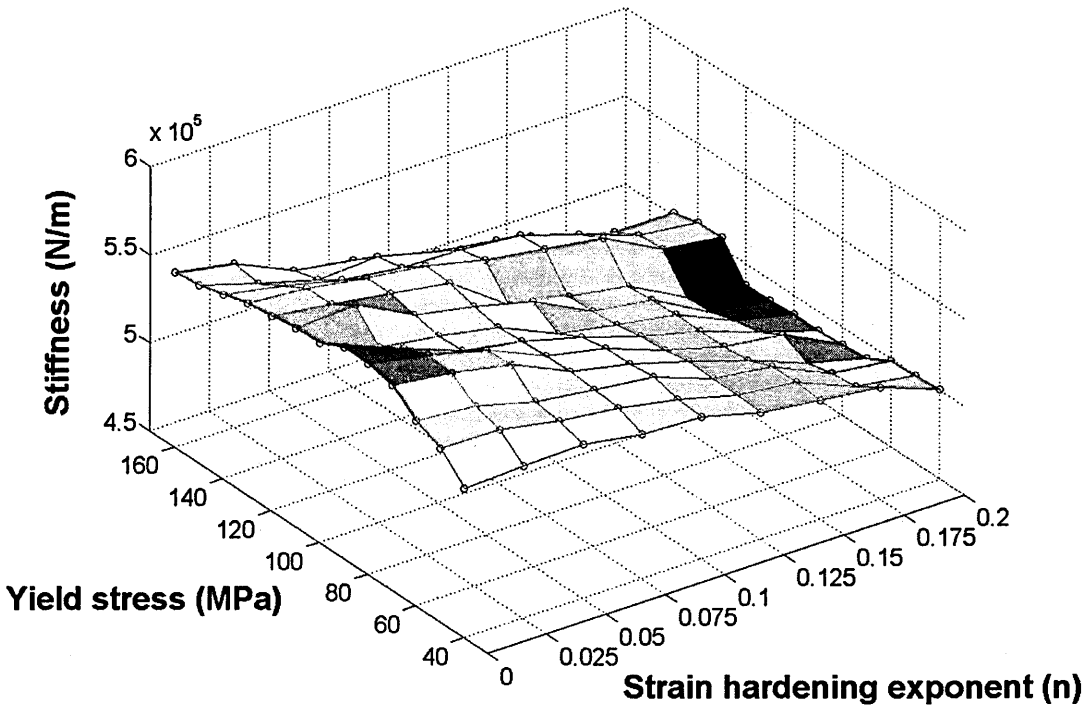

(d)

Fig. 5.6 - Surfaces describing distribution of (a) Curvature of loading curve (b) Maximum load (c) W_p/W_t (d) Stiffness ; for different sets of σ_Y and n

These four parameters for each simulation were compared with the experimentally obtained values of these parameters. Error values e_1, e_2, e_3 and e_4 were calculated for each parameter between the simulated and experimental value for each parameter and then the total cumulative error e was calculated. For every single indentation test, a set of σ_Y and n was found which generated least percentage of total error. The scheme of this reverse analysis is shown in Fig.5.7 (a) while the error variation for different combinations of σ_Y and n is shown in Fig.5.7 (b). It is clear that the least error occurs in a region 90 to 140 MPa in terms of initial yield stress.

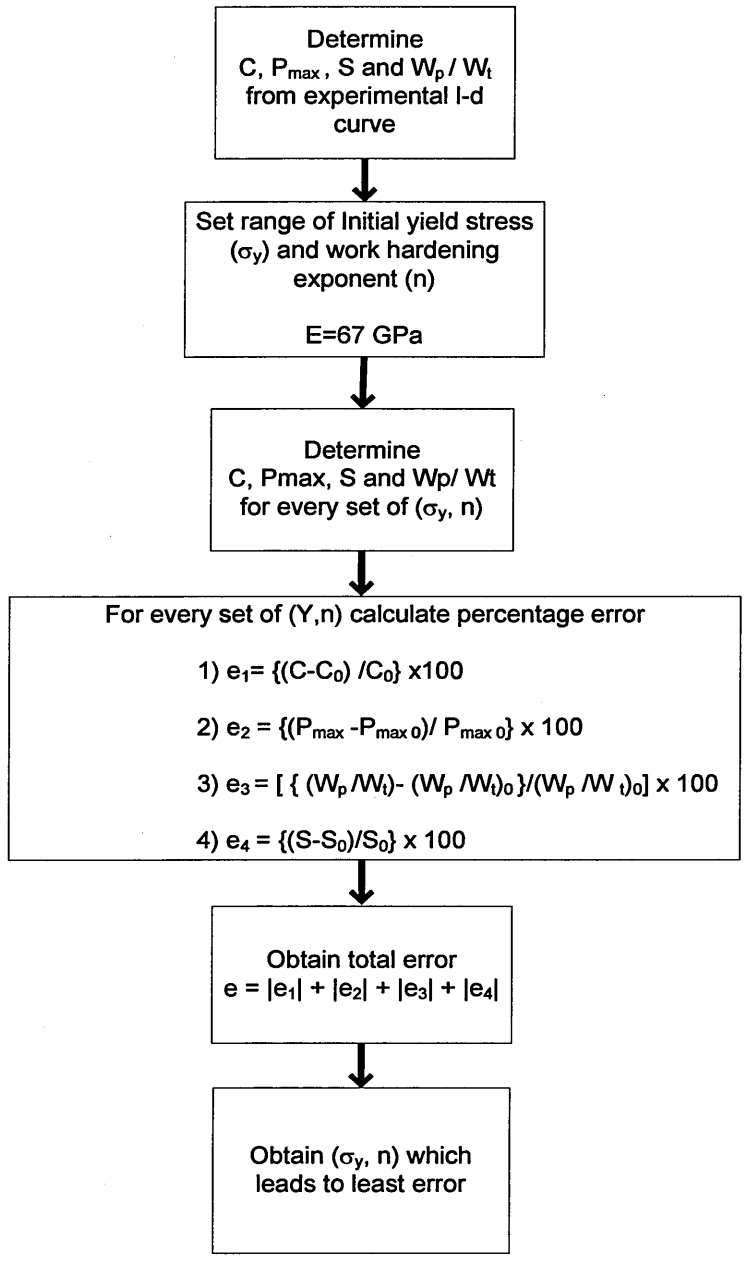
Determine
C, P_{max}, S and W_p / W_t from experimental l-d curve
Set range of Initial yield stress (σ_y) and work hardening exponent (n)
E=67 GPa
Determine
C, Pmax, S and Wp/ Wt for every set of (σ_y, n)
For every set of (Y,n) calculate percentage error
1) $e_1 = \{(C-C_0)/C_0\} \times 100$
2) $e_2 = \{(P_{max} - P_{max\,0})/ P_{max\,0}\} \times 100$
3) $e_3 = [\{(W_p/W_t) - (W_p/W_t)_0\}/(W_p/W_t)_0] \times 100$
4) $e_4 = \{(S-S_0)/S_0\} \times 100$
Obtain total error
$e = |e_1| + |e_2| + |e_3| + |e_4|$
Obtain (σ_y, n) which leads to least error

(a)

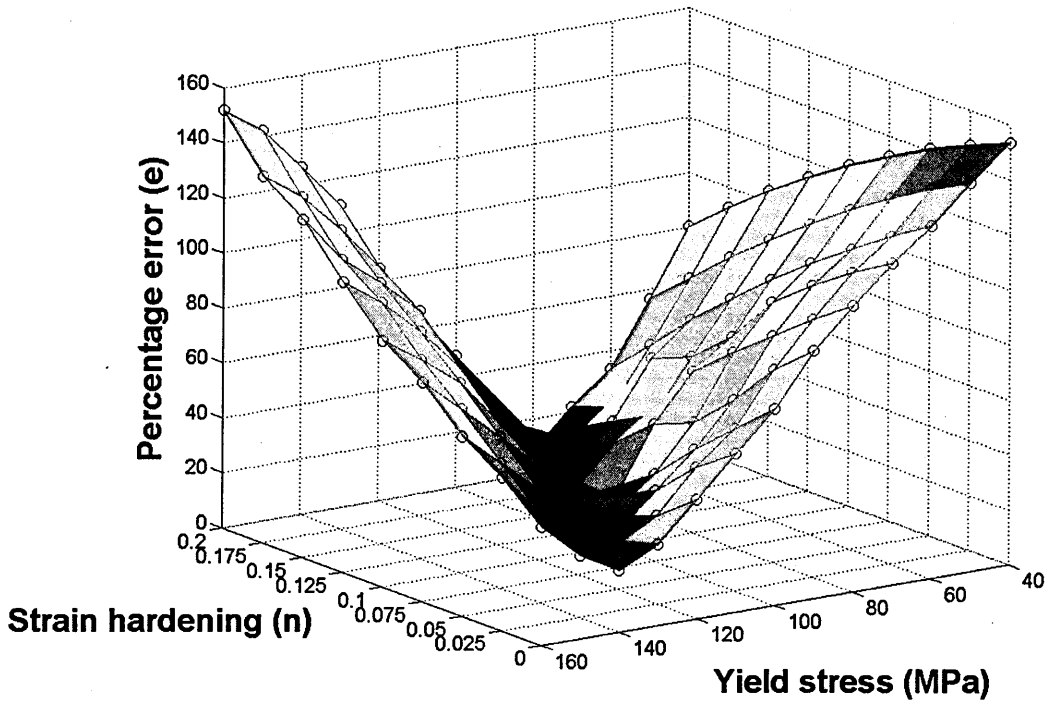

(b)

Fig. 5.7 - (a) Scheme of reverse analysis (b) Percentage total error

Table 5.1 shows all parameters obtained from five lowest error sets of σ_Y and n for four different indentation experiments. The main source of the error was the stiffness which was obtained by slope of initial part of the unloading curve. Experimental indentations were made at a maximum depth of 1000nm but due to the softness of cladding, even for experiments at 0 sec hold time, the clad starts to creep. This results in slightly higher depth of h_{max} up to 1010-1020nm which gives a slightly different stiffness as compared to simulation. The rest of the parameters yielded nominal errors up to 0.05%. From table 5.1, it is clear that a yield stress of 100 to 120 MPa with a strain hardening coefficient 0.05 to 0.1 are the possible values for the clad. Fig.5.8 (a) shows a comparison of load-displacement curves for test # 1, between experimental and simulated load-displacement curves; which agreed well with each other. Fig.5.8 (b) shows the stress-strain curve

obtained for these sets of σ_Y and n, and it can be seen that there is not a significant difference in curves.

Test No.	Total Error (%)	Yield Stress (MPa)	Strain Hardening n	Curvature C (GPa)		Load P_{max} (mN)		Stiffness S (N/m)		W_p/W_t	
				Exp.	FEA	Exp.	FEA	Exp.	FEA	Exp.	FEA
1	8.02	120	0.050	14.07	13.93	13.18	13.51	584130	560000	0.964	0.968
	10.65	130	0.050		15.86		15.99		550800		0.964
	12.05	120	0.025		13.07		12.96		568400		0.97
	13.66	110	0.075		13.71		13.59		532300		0.968
	17.36	100	0.100		13.59		13.53		520770		0.968
2	12.43	90	0.15	13.74	13.72	12.89	13.39	430460	509400	0.964	0.968
	16.81	100	0.100		13.59		13.53		520770		0.968
	19.41	90	0.125		14.37		14.09		516200		0.968
	20.48	110	0.075		13.71		13.59		532300		0.968
	21.37	100	0.075		12.72		12.81		531980		0.97
3	14.23	90	0.150	19.51	13.72	12.80	13.39	414210	509400	0.965	0.968
	14.56	100	0.125		14.37		14.09		516200		0.968
	16.74	100	0.100		13.59		13.53		520770		0.968
	18.90	110	0.100		14.58		14.49		525050		0.966
	20.39	110	0.075		13.71		13.59		532300		0.968
4	11.57	90	0.150	14.58	13.72	13.51	13.39	475770	509400	0.964	0.968
	15.89	100	0.100		13.59		13.53		520770		0.968
	17.03	90	0.125		14.37		14.09		516200		0.968
	19.01	100	0.075		12.72		12.81		531980		0.97
	19.45	110	0.075		13.71		13.59		532300		0.968

Table 5.1 - Reverse analysis for Al cladding for first five least error generated set of σ_Y and n

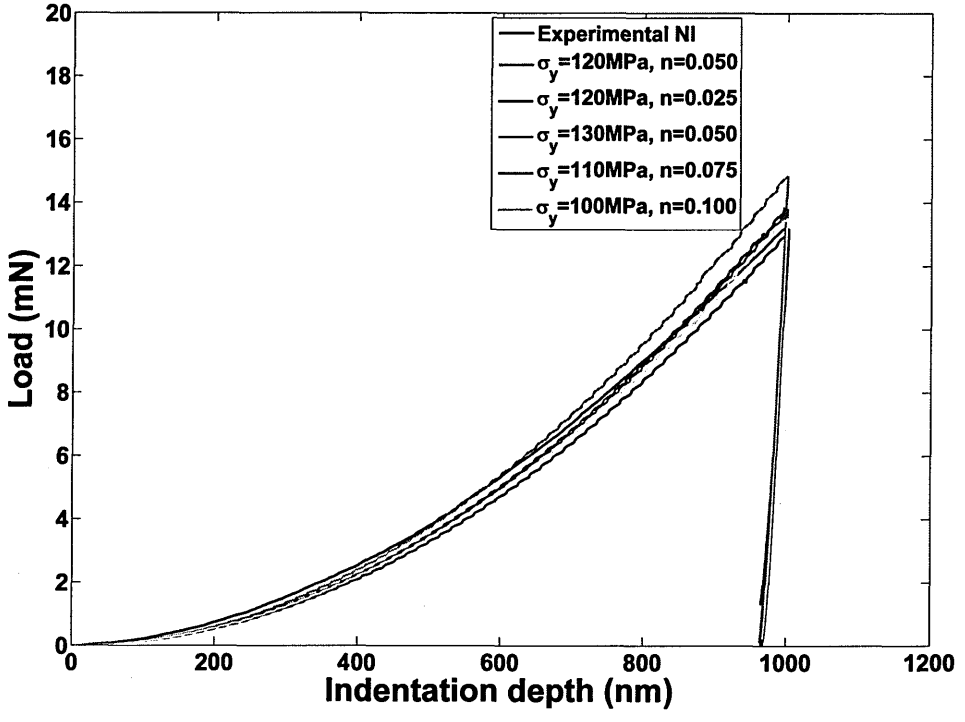

(a)

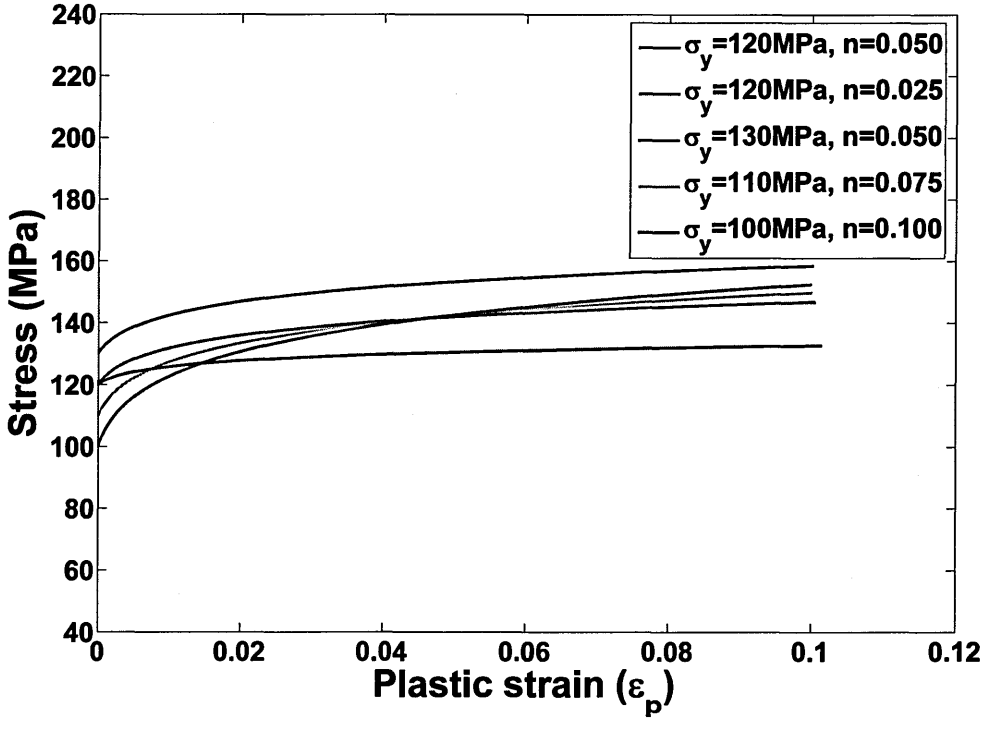

(b)

Fig. 5.8 - Error analysis results for Test #1
(a) Load-displacement curves (b) Plastic part of constitutive law

Further refinement towards an accurate set of σ_Y and n was made by examining pile-up height for these simulations. As discussed earlier, pile-up is a function of E/σ_Y and n, so to confirm that the reverse analysis gave values of σ_Y and n that produce similar pile-up to experiment, the height of pile-up was plotted the five lowest error sets of σ_Y and n for test #1, and compared with the AFM measured pile-up for experimental nanoindentation as shown in Fig.5.9 (b). Fig.5.9 (a) shows an AFM scanned image of an indent in the clad and it can be seen clearly that the extent of the pile-up is not symmetric. Although the axisymmetric model does not accurately characterize the 3D morphology of pile-up, the vertical height of the pile-up obtained from simulation and AFM agreed well with each other as shown in Fig.5.9 (b).

Due to the absence of true friction coefficient, the tip bluntness effect in the model and limitation of the axisymmetric model to predict actual 3D morphology of pile-up, it was decided that accurate characterization of pile-up was not feasible and hence in this study more emphasis was given to other indentation parameters which were easier to obtain from the axisymmetric model. These indentation parameters will be used to approximate the elastic-plastic properties of clad.

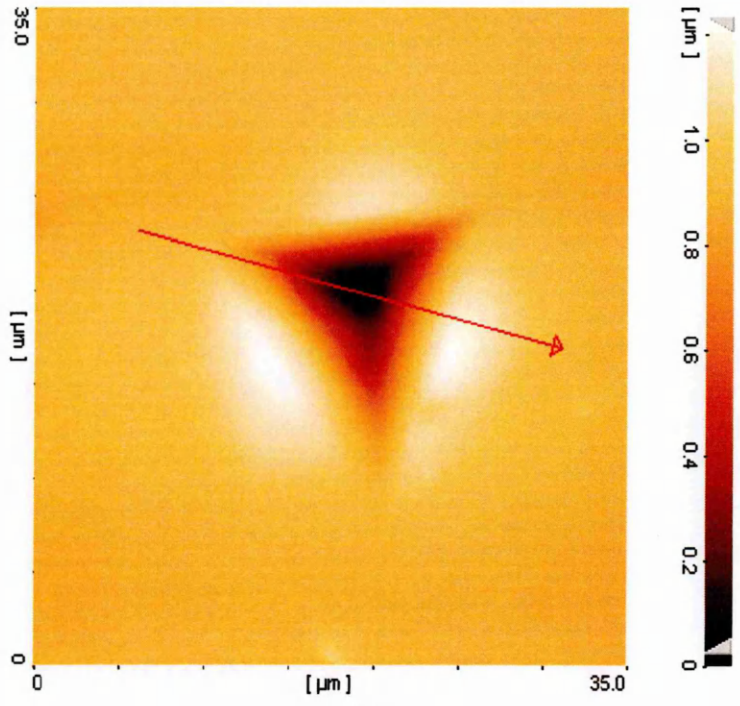

(a)

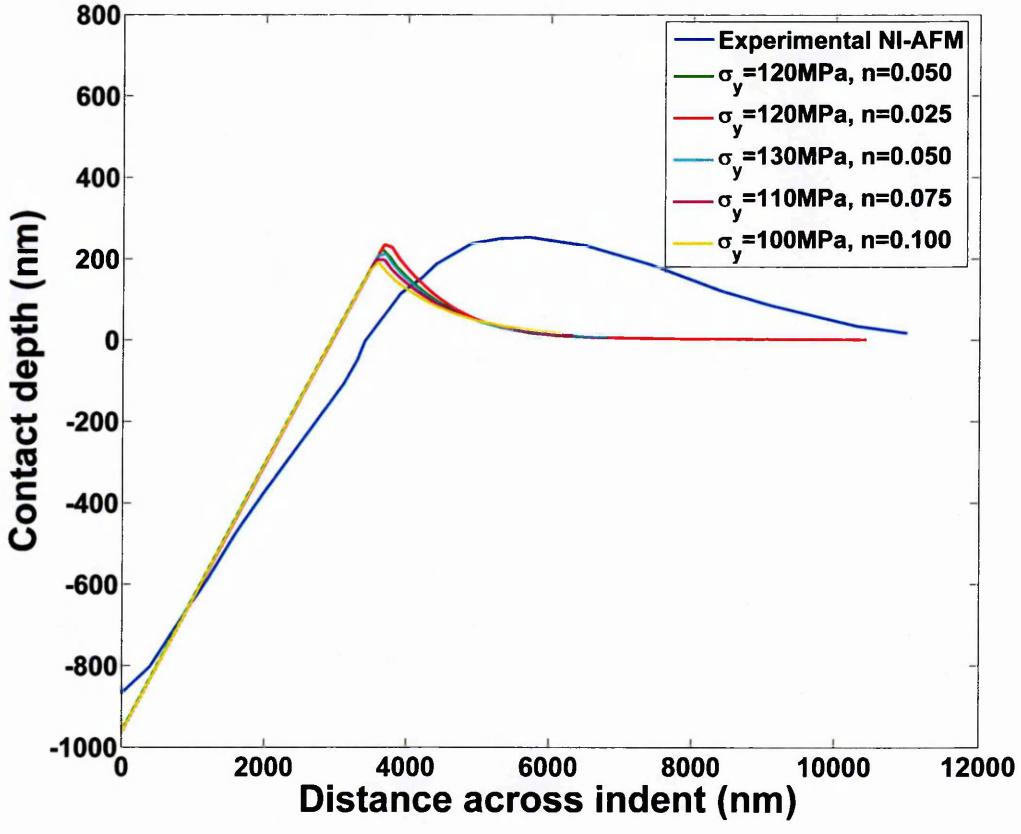

(b)

Fig. 5.9 - Pile-up comparison for cladding (a) AFM scanning of experimental indentation shows unequal distribution of pile-up; line across indent shows indent edge for which pile-up was represented in part b of fig (b) Comparison of vertical height of pile-up from AFM for experimental nanoindentation and FEM for simulation.

With very little difference in the load-displacement curves and pile-up height for the five lowest error sets of σ_Y and n, it was very difficult to find the best suitable values. In Fig.5.8 (a), set $(130,0.05)$ was rejected as it deviated most from the experimental load-displacement curve. Information about the hardness of clad in chapter 3 showed high values as compared to pure aluminium, so this implied that work hardening was a factor for significant increase in hardness. Pure aluminium has very low hardness and work hardening but due to relatively higher hardness as obtained in this study (chapter 3), it was anticipated that there is some work hardening in clad and 0.075 was chosen as approximate work hardening of cladding. Consequently 110MPa was taken as the initial yield stress of the clad. In confirmation of these parameters, nanoindentation properties were calculated from simulation at $(110, 0.075)$ and compared with experimental results of P_{max}, h_c and A_c. Excellent agreement was found as shown in Fig.5.10.

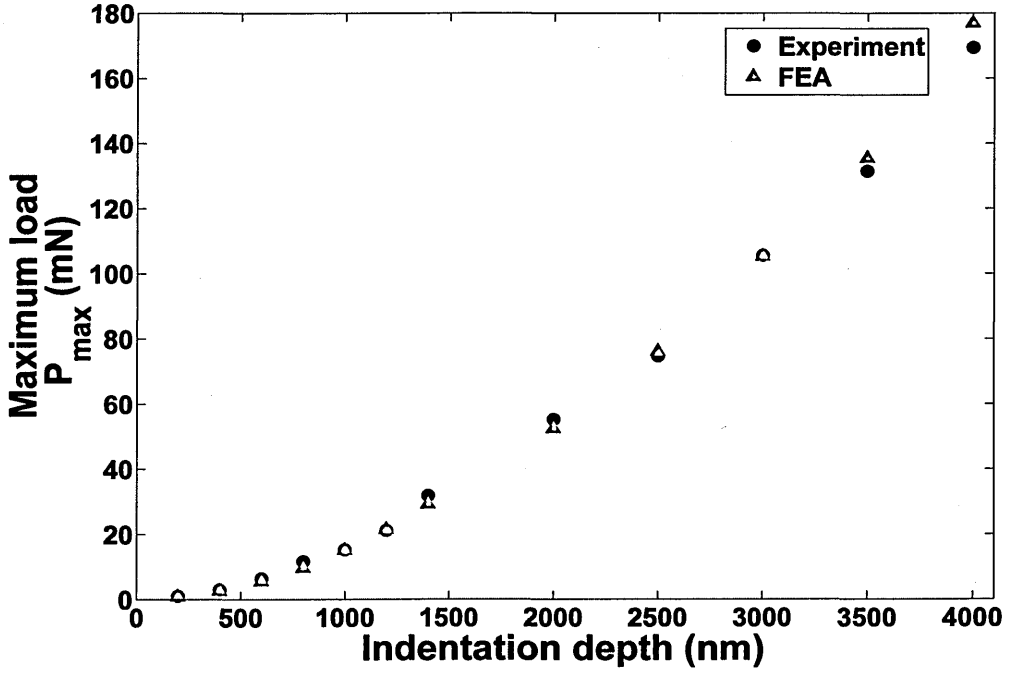

(a)

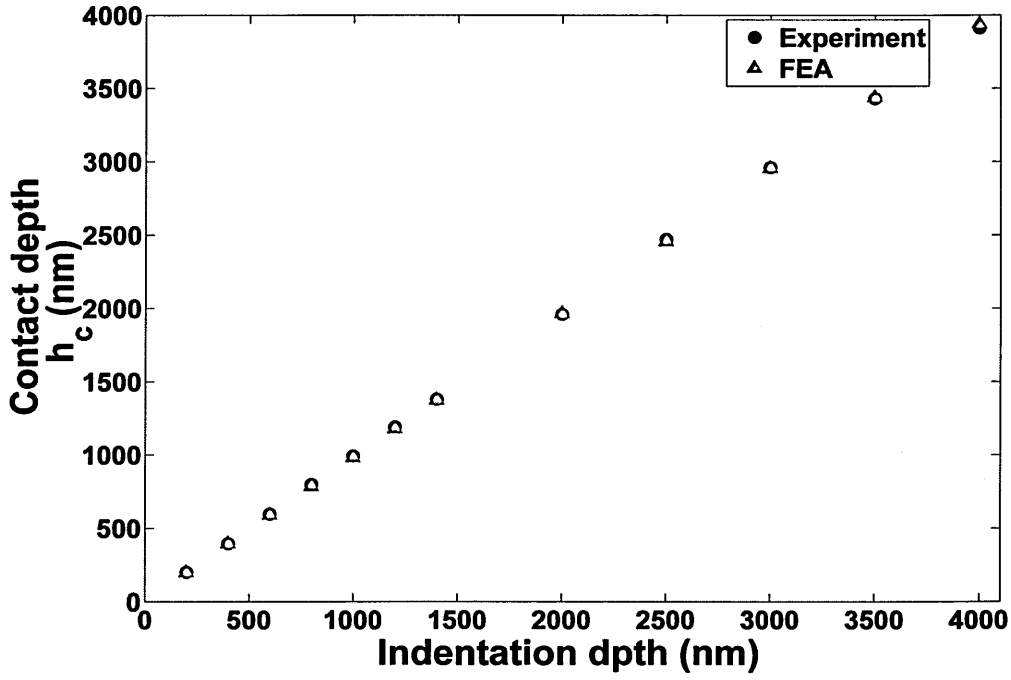

(b)

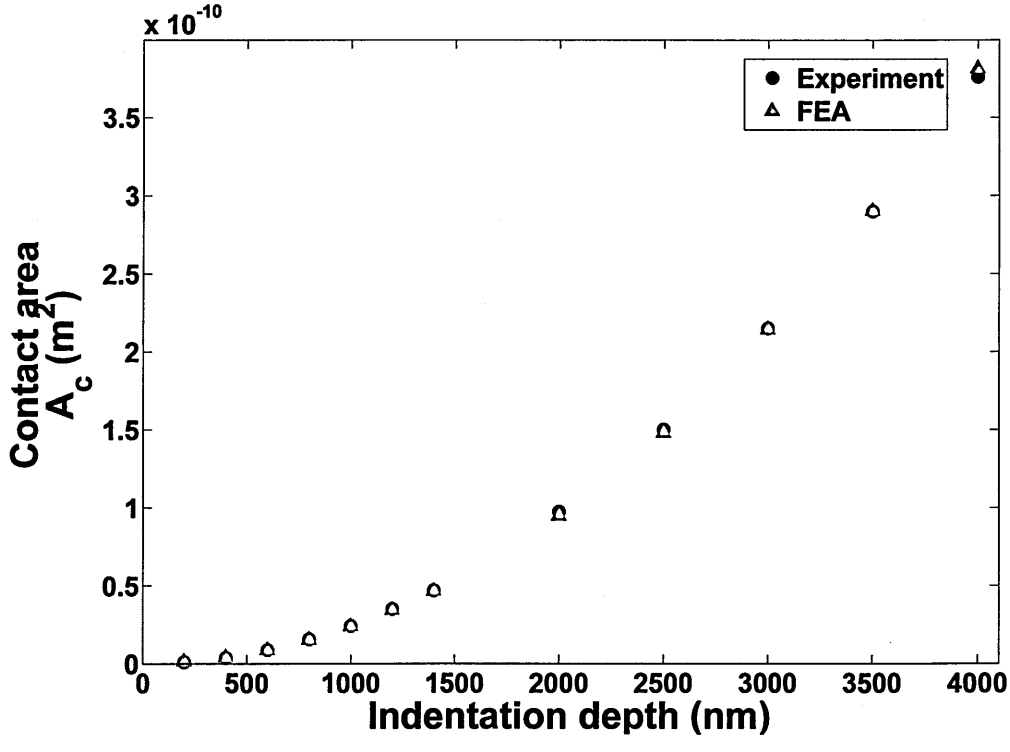

(c)

Fig. 5.10 - Nanoindentation properties from reverse analysis generated plastic properties and experimental nanoindentation.
(a) Maximum load (b) Contact depth c) Contact area

So it was concluded that there are different set of yield stress and work hardening which can yield similar load-displacement curves from simulation as of experiment. Reverse analysis is an effective approach to approximate elastic-plastic properties and can work well if the number of parameters can be reduced based on information about the material.

5.4 Conclusions

Finite element simulations have been performed to obtain load-displacement curves in comparison with experiments. With this simulated study of the nanoindentation process, the accurate determination of area is possible which is a necessary calculation for residual stresses. In forward analysis, the material properties of Al 2024-T351 were obtained from tensile testing and were used to simulate the nanoindentation process. Excellent agreement was obtained between experimental and simulated nanoindentation properties. Pile-up characterization was performed with the help of simulation and it was found that elastic-plastic properties obtained from tensile testing provide similar information of pile-up as compared to experimental information obtained from AFM.

For cladding, due to the absence of elastic-plastic properties, reverse analysis was performed from indentation load-displacement curve for curvature, maximum load stiffness and ratio of plastic to total work of indentation. Initial yield stress and work hardening exponent, obtained from reverse analysis, did simulate load-displacement curve excellently. With due consideration of different aspects, a yield stress of 110-120MPa and 0.075-0.1 as work hardening was obtained for Al cladding.

Forward analysis and reverse analysis applied effectively on two parts of clad Al 2024-T351. With different known parameters in both of the analyses, simulation of nanoindentation process was performed successfully.

5.5 References

[1] Bhattacharya, A. K. and W. D. Nix. Finite element simulation of indentation experiments. International Journal of Solids and Structures 24(9), 1988, pp 881-891.

[2] Pelletier, H., J. Krier, A. Cornet and P. Mille. Limits of using bilinear stress-strain curve for finite element modeling of nanoindentation response on bulk materials. Thin Solid Films 379(1-2), 2000, pp 147-155.

[3] Lichinchi, M., C. Lenardi, J. Haupt and R. Vitali. Simulation of Berkovich nanoindentation experiments on thin films using finite element method. Thin Solid Films 312(1-2), 1998, pp 240-248.

[4] Bolshakov, A. and G. M. Pharr. Influences of pileup on the measurement of mechanical properties by load and depth sensing indentation techniques. Journal of Materials Research 13(4), 1998, pp 1049-1058.

[5] Taljat, B. and G. M. Pharr. Development of pile-up during spherical indentation of elastic-plastic solids. International Journal of Solids and Structures 41(14), 2004, pp 3891-3904.

[6] Choi, Y., B. W. Lee, H. S. Lee and D. Kwon. Indentation curve analysis for pile-up, sink-in and tip-blunting effects in sharp indentations. Symposium on Thin Films - Stresses and Mechanical Properties X held at the 2003 MRS Fall Meeting, 2003, Boston, MA, Materials Research Society.

[7] Oliver, W. C. and G. M. Pharr. An Improved Technique for determining hardness and elastic modulus using load and displacement senssing indentation experiments. Journal of Materials Research 7(6), 1992, pp 1564-1583.

[8] Khan, M. K., S. V. Hainsworth, M. E. Fitzpatrick and L.Edwards. Application of the work of indentation approach for the characterization of aluminium 2024-T351 and Al cladding by nanoindentation. Journal of Materials Science 44(4), 2009, pp 1006-1015.

[9] Hainsworth, S. V., H. W. Chandler and T. F. Page. Analysis of nanoindentation load-displacement loading curves. Journal of Materials Research 11(8), 1996, pp 1987-1995.

[10] Cheng, Y. T. and C. M. Cheng. Scaling relationships in conical indentation in elastic-plastic solids with work-hardening. Materials-Research-Society Symposium on Fundamentals of Nanoindentation and Nanotribology, 1998, San Francisco, Ca, Materials Research Society, pp 91-149.

[11] Cheng, Y. T. and C. M. Cheng. Scaling, dimensional analysis, and indentation measurements. Materials Science & Engineering R-Reports 44(4-5) 2004, pp 91-149.

[12] Cheng, Y. T., Z. Y. Li and C. M. Cheng. Scaling, relationships for indentation measurements. 2nd International Indentation Workshop, 2001, Cambridge, England, Taylor & Francis Ltd.

[13] Cheng, Y. T. and C. M. Cheng. Further analysis of indentation loading curves: Effects of tip rounding on mechanical property measurements. Journal of Materials Research 13(4): 1998, pp 1059-1064

[14] Dao, M., N. Chollacoop, K. J. Van Vliet, T. A. Venkatesh and S. Suresh. Computational modeling of the forward and reverse problems in instrumented sharp indentation. Acta Materialia 49(19), 2001, pp 3899-3918

[15] Giannakopoulos, A. E. and S. Suresh. Determination of elastoplastic properties by instrumented sharp indentation. Scripta Materialia 40(10), 1999, pp 1191-1198.

[16] Tho, K. K., S. Swaddiwudhipong, Z. S. Liu and K. Zeng. Simulation of instrumented indentation and material characterization. Materials Science and Engineering a-Structural Materials Properties Microstructure and Processing 390(1-2), 2005, pp 202-209.

[17] Ogasawara, N., N. Chiba and X. Chen. Measuring the plastic properties of bulk materials by single indentation test. Scripta Materialia 54(1), 2006, pp 65-70.

[18] Zhao, M. H., X. Chen, N. Ogasawara, A. C. Razvan, N. Chiba, D. Lee and Y. X. Gan. New sharp indentation method of measuring the elastic-plastic properties of compliant and soft materials using the substrate effect. Journal of Materials Research 21(12), 2006, pp 3134-3151.

[19] Tabor, D. A Simple theory of static and dynamic hardness. Proceedings of the Royal Society of London Series a-Mathematical and Physical Sciences 192(1029), 1948, pp 247-274.

[20] Alkorta, J., J. M. Martinez-Esnaola and J. G. Sevillano, Absence of one-to-one correspondence between elastoplastic properties and sharp-indentation load-penetration data." Journal of Materials Research 20(2), 2005, pp 432-437.

[21] Stilwell, N. A. and D. Tabor. Elastic recovery of conical indentations. Proceedings of the Physical Society of London 78(500), 1961, pp 169.

[22] M. K. Khan, M. E. Fitzpatrick, S. V. Hainsworth and L. Edwards. Effect of Tool Profile and Fatigue Loading on the Local Hardness Around Scratches in Clad and Unclad Aluminium Alloy. Materials Science & Engineering A, Volume 527, Issues 1-2, 2009, pp 297-304.

[23] Chollacoop, N., M. Dao and S. Suresh. Depth-sensing instrumented indentation with dual sharp indenters. Acta Materialia 51(13), 2003, pp 3713-3729.

[24] Yu, N., A. A. Polycarpou and T. F. Conry. Tip-radius effect in finite element modeling of sub-50 nm shallow nanoindentation. Thin Solid Films 450(2), 2004, pp 295-303.

[25] Kim, J. Y., B. W. Lee, D. T. Read and D. Kwon. Influence of tip bluntness on the size-dependent nanoindentation hardness. Scripta Materialia 52(5), 2005, pp 353-358.

[26] Choi, Y., H. S. Lee and D. Kwon. Analysis of sharp-tip-indentation load-depth curve for contact area determination taking into account pile-up and sink-in effects. Journal of Materials Research 19(11), 2004, pp 3307-3315.

[27] Materials Handbook, 9th edition, Vol. 2, Properties and selection: Nonferrous Alloys and Pure Metal, 1979, American Society for Metals, Metal Park, Ohio 44073.

[28] Standard Test Methods for Tension Testing of Metallic Materials. ASTME-E 8/E 8M-08. ASTM International, West Conshohocken, PA, 2003.

Chapter 6: Effect of Residual Stress on Nanoindentation Response of Al-cladding and Al 2024-T351

6.1 Introduction

Experimental and finite element simulations have been used to study the effect of uniaxial and biaxial residual stresses on nanoindentation response. The results were used to develop a methodology which could be applied to residual stress measurement around scribe marks. Tensile and compressive residual stresses lead to changes in the nanoindentation response. Loading and unloading curves were studied to observe the effect of residual stresses. Maximum load of indentation, curvature of the loading curve, elastically recovered depth, work of indentation, pile-up and contact area were measured and found to have a linear relationship with residual stress. To calculate residual stress from load-displacement curve, it was concluded that pile-up should be measured carefully.

The influence of residual stress on load-displacement curves has been investigated in earlier studies both experimentally and with Finite Element modelling [9-18]. Different parameters, includes hardness [9], loading behaviour [12-14], maximum indentation depth, contact area [11], pile-up [15] and unloading behaviour [16-18] can be compared to estimate the effect of residual stresses. There are a few models available also to extract residual stresses from nanoindentation load-displacement curves [10-15].

Numerical simulation of the nanoindentation process from FEM has been widely performed by many researchers [1-3]. Elastic-plastic properties obtained from tensile testing have been used successfully to simulate nanoindentation load-displacement curves which give an insight into the mechanical behaviour of the surface during loading and unloading. These FEA based simulations of the indentation process can be used to study the response of the material under residual stresses [11, 16-18]. Experimental and finite element based studies have shown that the nanoindentation load-displacement curve

changes in the presence of residual stresses. However, the nanoindentation parameters obtained from load-displacement curves are also affected by material properties such as E/σ_Y ratio, work hardening exponent. Based on these mechanical properties slope of variation of these parameters changes as well [16-17].

This chapter presents results of experimental and finite element simulations for the effect of residual stresses on nanoindentation properties. Experimental indentations were performed with uniaxial and biaxial loading apparatuses (used for simulation of residual stresses) and load-displacement curves were studied thoroughly. Finite element simulations were used to observe the effect of residual stresses on nanoindentation response for Al-cladding and Al 2024-T351. From experimental and simulations results, it was observed that the load-displacement curve changed as compared to the stress free condition when residual stress was present prior to indentation. The loading as well as the unloading part of the load-displacement curves were affected by residual stress. For both Al 2024-T351 and Al-cladding, the curvature of loading curve increased and yielded a higher value of maximum load of indentation. Similarly, the unloading curve started to shift towards the loading curve for compressive residual stress and moved away for tensile residual stress. Due to this shift in load-displacement curve, the nanoindentation properties so obtained changed as well.

Based on the results obtained from experiments and simulations, a methodology was developed from which equi-biaxial residual stress can be extracted from indentation load-displacement curves. This developed methodology will be applied to scribe marks to extract residual stresses from the load-displacement data.

6.2 Materials, Experimental and Finite Element Simulation Details

6.2.1 Materials Details

The materials studied were Al-cladding and Al 2024-T351. Mechanical properties have already discussed in chapter 3.

6.2.2 Experimental Details

A rectangular plate was used as a sample for uniaxial loading and a cross shaped sample was used for biaxial loading. Fig.6.1 shows the uniaxial and biaxial samples mounted in their respective apparatuses. Biaxial strain gauges were used to measure the in-plane components of the strain i.e. ε_{xx} and ε_{yy}. Uniaxial and biaxial loading was applied and the effective stress field was calculated from biaxial stress-strain relations. As the cladding was in a very thin form of $100\,\mu m$ on both sides of the plate, it was not possible to get its response under loading from these apparatuses, hence, in this study only Al 2024-T351 plates were used for experimental investigations.

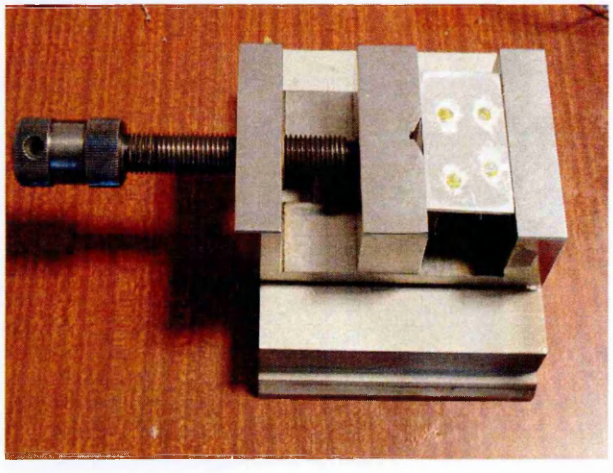

(a)

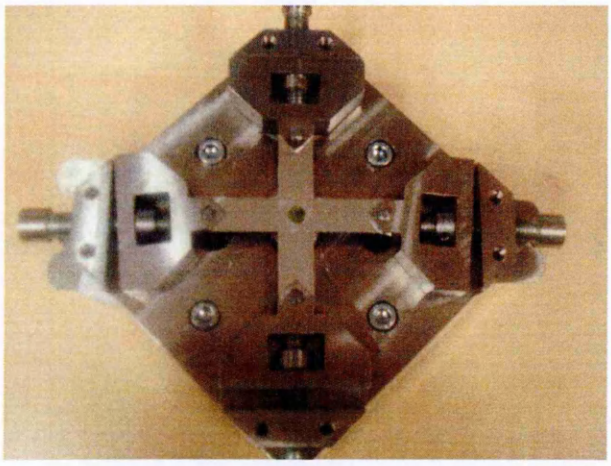

(b)

Fig. 6.1 - Apparatus for artificial stress (a) Uniaxial loading (b) Biaxial loading

Indentations were carried out very near to the strain gauges to avoid any effect of change in stress state, and load-displacement curves were obtained at different stress levels. All indentations were carried out to 600nm depth to get minimum pile-up with the similar procedure as discussed in chapter 3.

6.2.3 Finite Element Simulation Details

Simulations were performed for both Al-cladding and Al 2024-T351 in the FEM package ABAQUS using a deformable axisymmetric material and a rigid indenter. Model size of 2mm x 2mm was constructed in two parts: an indenter and the test material, with axisymmetric geometries. The test material was modelled with four node axisymmetric reduced integration element CAX4R while the indenter was modelled as a rigid element. The Von-Mises yield criterion was applied for determination of plastic deformation. The indentation region was very small as compared to the size of the model and because of the straining around the indented region, a fine mesh size was used around the near contact regions. The total number of elements was 8500. The indenter was considered as a perfect rigid cone of the same area-depth function as a Berkovich indenter, as a cone of 70.3° gives the same area-depth function as a Berkovich indenter [1-3].

The equibiaxial compressive or tensile stress was introduced into the model by prescribing an axial displacement prior to the indentation parallel to the top surface of the material. A different mesh scheme was used here compared to the finite element model used in chapter 5. This new mesh scheme allowed set-up of equibiaxial stresses whenever an axial displacement parallel to the top surface was applied prior to indentation. Whenever initial stresses prior to indentation were applied in mesh scheme used in chapter 5, due to the different mesh size and density used (finer near indentation region), a difference in the two components of the stress obtained. A typical example of assigning an initial stress with new mesh scheme is shown in Fig. 6.2 (b) and (c) and has been used earlier successfully [17]. A schematic representation of the model is given in Fig.6.2 (a). More in-depth details of the model have already been discussed earlier in chapter 5.

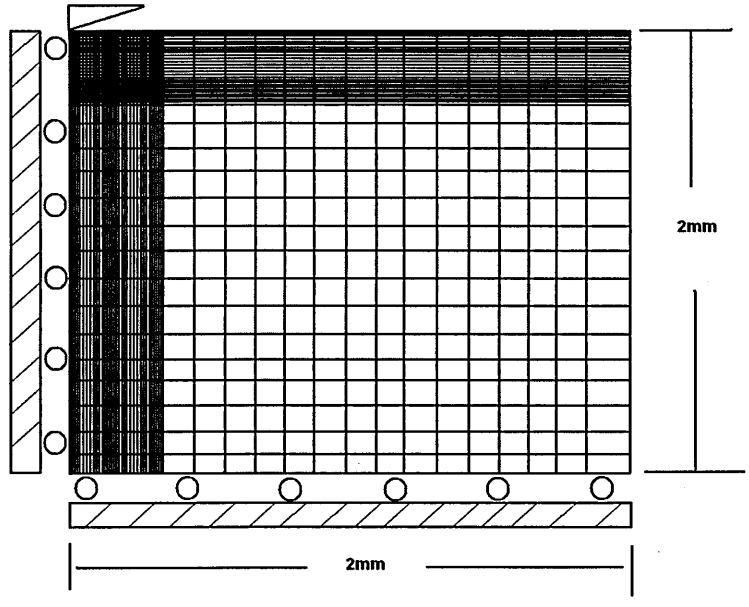

Fig. 6.2 (a) - Schematic of Finite Element Model

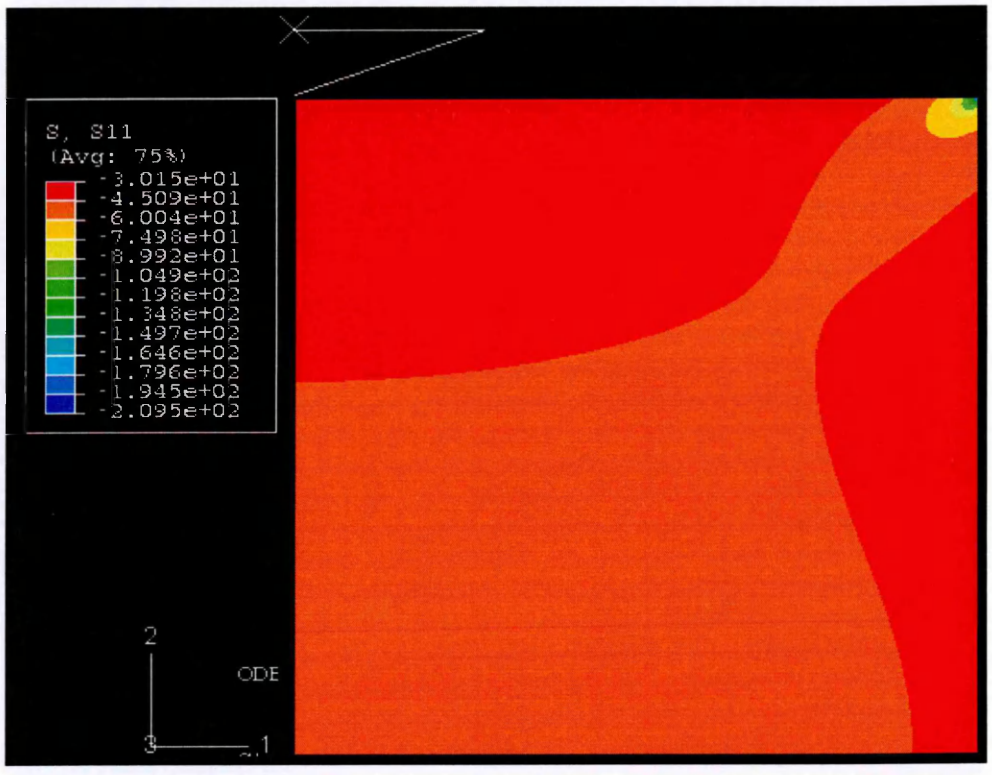

(b)

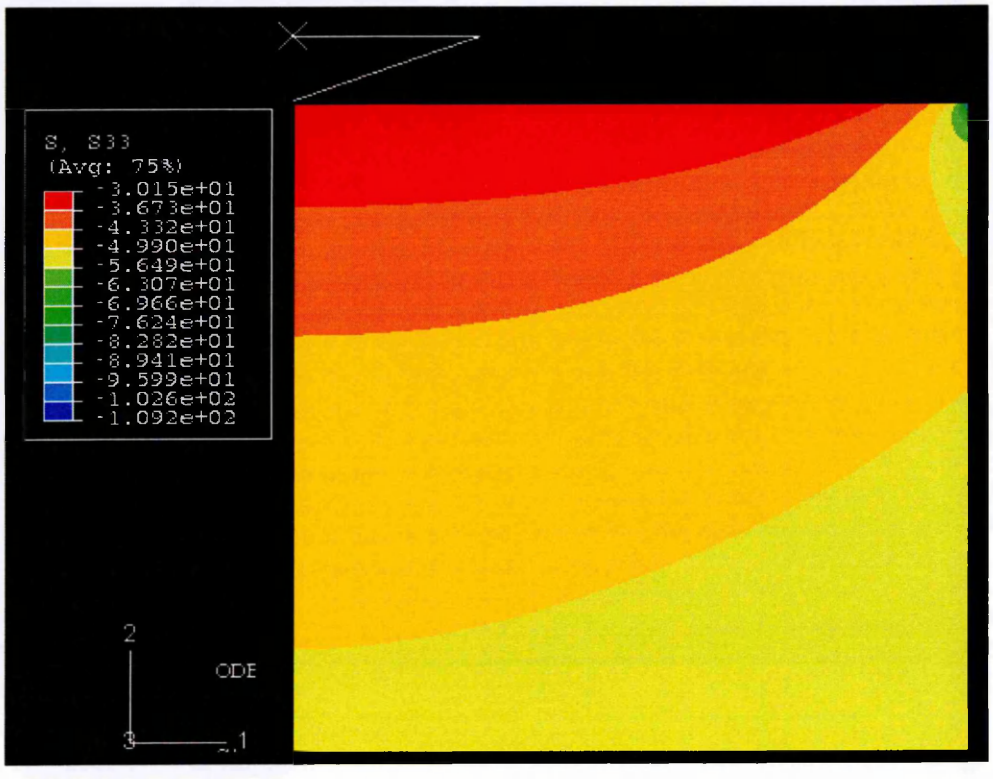

(c)

Fig. 6.2 (b) and (c)– Equibiaxial stress components of -30MPa below indenter (b) σ_{11} (c) σ_{33}

6.3 Results and Discussion

6.3.1 Experimental Investigation

6.3.1.1 Uniaxial Stresses

Fig.6.3 shows load-displacement curves obtained for different uniaxial stress states and it can be seen that as compared to the stress free loading curve, for compressive residual stress loading curve moved up and an opposite effect was obtained for tensile residual stress. With this change in loading curve path, the curvature and maximum load-of indentation changed as well.

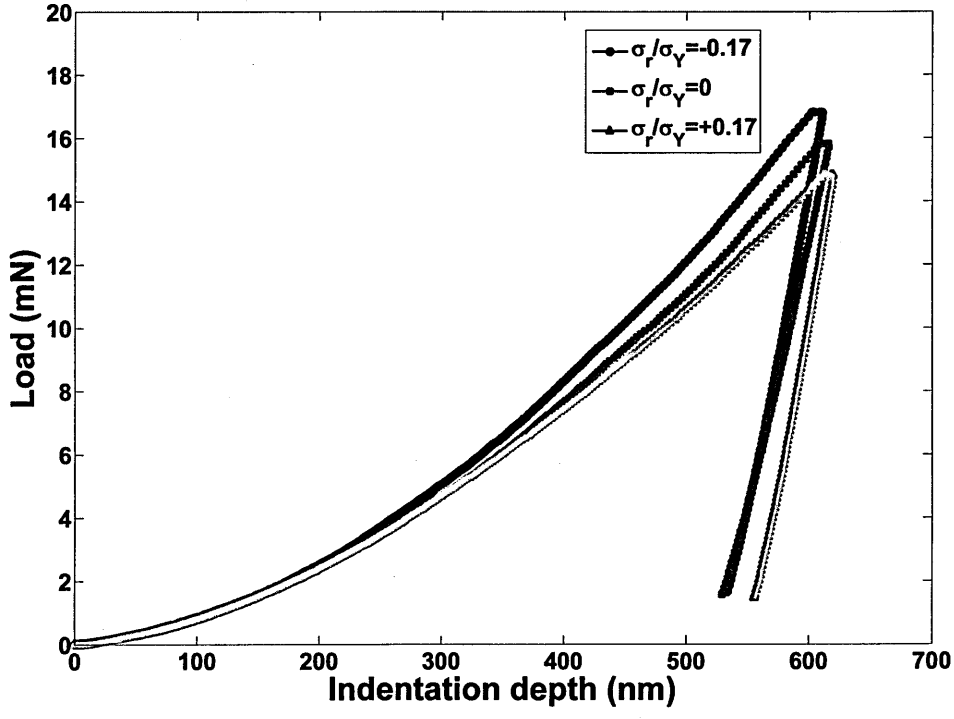

Fig. 6.3 - Load-displacement curves for uniaxial residual stresses

Fig.6.4 shows the variation of maximum load of indentation with respect to different residual stress levels for two different samples. Residual stress was normalized with respect to yield stress σ_Y of Al 2024-T351. It can be seen that for both of the samples a linear trend for variation of maximum load of indentation was obtained, though data was not present in a wide range in tensile region as compare to compressive region due to the limitations of the apparatus.

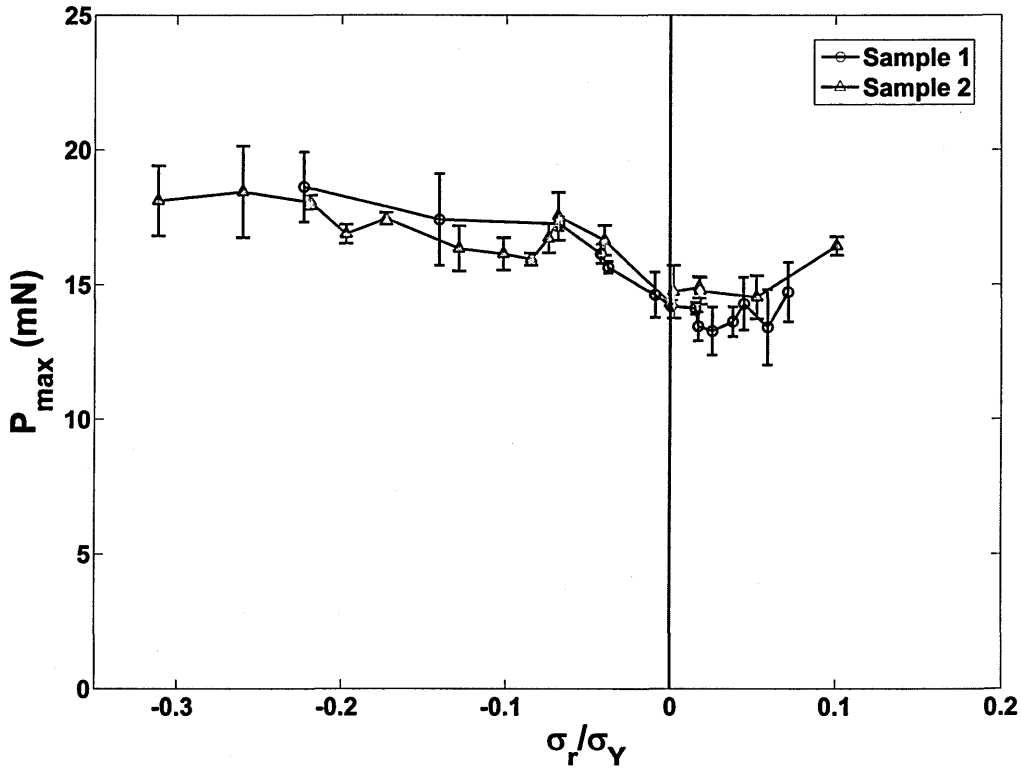

Fig. 6.4 - Variation of maximum load of indentation with uniaxial residual stresses

6.3.1.2 Biaxial Stresses

The sensitivity of nanoindentation load-displacement curves with respect to the individual components of the stress was examined from biaxial loading. Load-displacement curves obtained from biaxial loading produced twice the effect on indentation parameters as compared to uniaxial loading. Typical example of shifting of load-displacement curves are shown in Fig.6.5 (a).

The most significant effect of the biaxial loading was obtained for pure shear, in which no effect on the load-displacement curve was obtained. It is clear from Fig.6.5 (a) that those load-displacement curves of $\sigma_{xx}/\sigma_Y = +0.17, \sigma_{yy}/\sigma_Y = -0.17$ and the stress free conditions were almost the same. The effect of one component of the stress $\sigma_{xx}/\sigma_Y = +0.17$ had been cancelled by the other component $\sigma_{yy}/\sigma_Y = -0.17$, opposite in sign but equal in magnitude. This was consistent with the investigations of Lee et al. [14] where there was no effect of pure shear obtained on nanoindentation load-

displacement curves. This indicated that the stress ratio ($k=\sigma_{xx}/\sigma_{yy}$) which is ratio of the minimum stress component to maximum stress component, plays an important role and whenever they are same (k= positive) in terms of type (tensile or compressive) they support each other and produce a cumulative effect on the load-displacement curve. On the other hand when they are opposite in type (k= negative) they negate the effect of each other and produce no effect for the case of pure shear (k= -1).

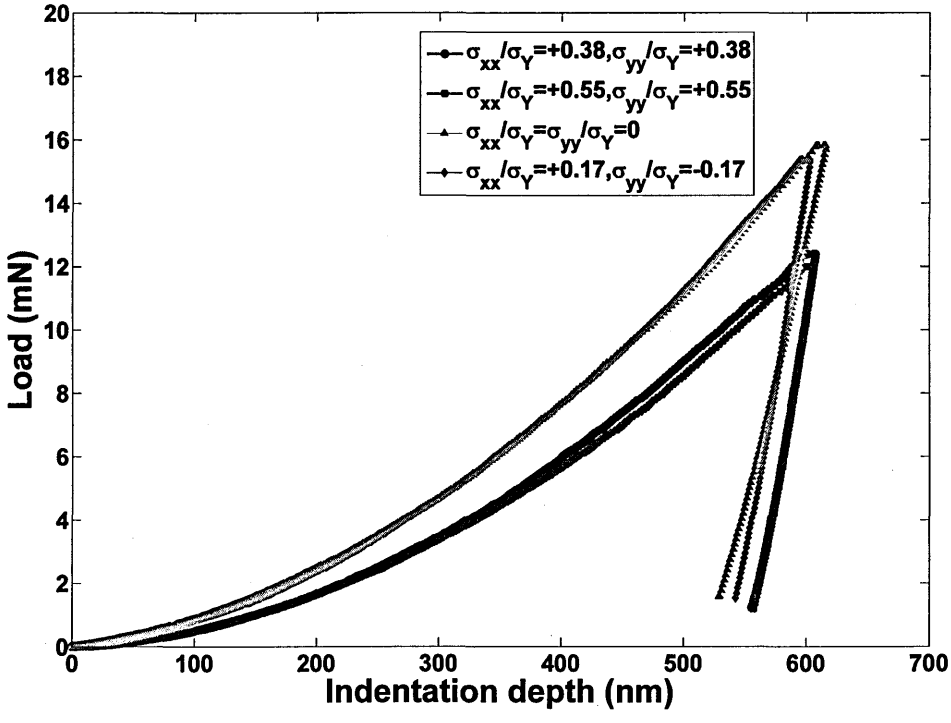

(a)

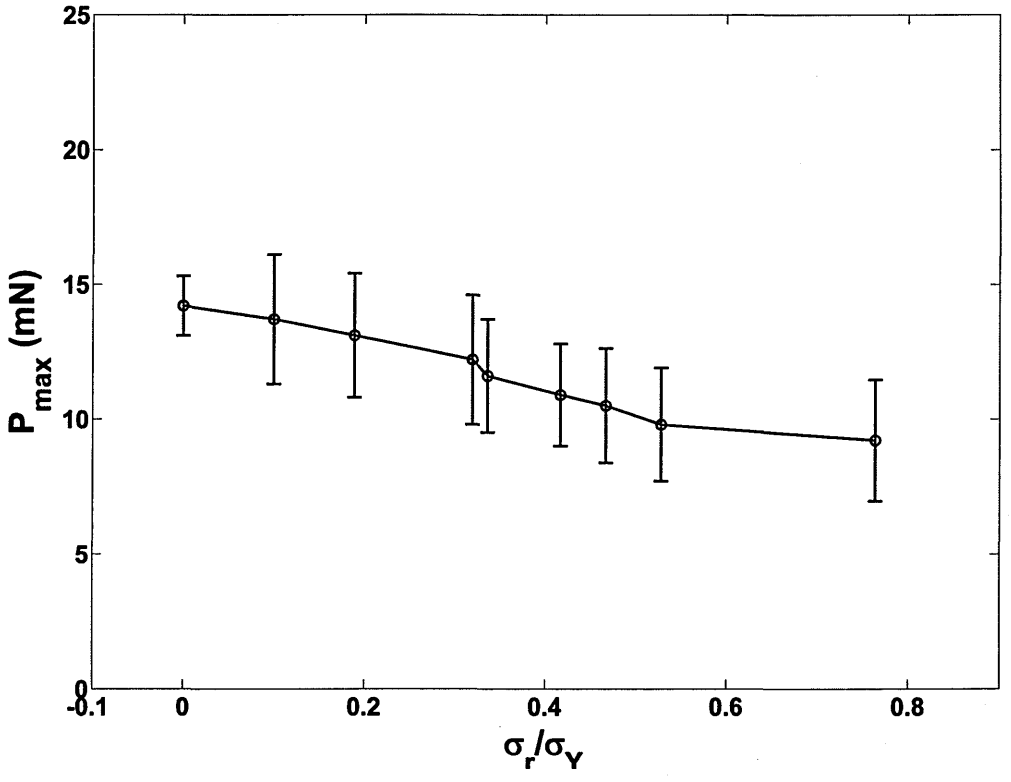

(b)

Fig. 6.5 - Variation of indentation response with biaxial residual stresses (a) Load-displacement curves (b) Maximum load variation

Due to the design of the apparatus, only tensile loading was possible. Compressive loading was tried but due to the very small thickness (2mm) of the sample, bending of the sample started to occur whenever compressive loading was applied. This bending results in a component of the strain perpendicular to the sample plane for which with biaxial strain gauges were not useful. Hence, the nanoindentation response with compressive loading was not obtained.

Another important issue during loading was change in compliance. Nanoindenter testing is recommended with a standard loading tray in which samples are mounted and is used robustly for material characterization. The loading apparatuses were designed and fabricated with due care to make sure that loading apparatus should be of same size and weight, yet some difference in weight occurred due to sample geometry (rectangular for

uniaxial stresses and cross shaped for biaxial stresses) and strain gauges mounted on the sample. Although, the MTS nanoindenter tries to correct compliance yet difference in nanoindentation response is obtained (especially in the slope of unloading curve as shown in Fig. 6.5 (a)) whenever the same sample was loaded with different stress condition. This difference in the nanoindentation response resulted in scatter in the data obtained for a given stress condition.

Hence, due to the limitation of the capabilities of the apparatuses to induce different level of all stress states, a more comprehensive study was carried out through finite element simulations. Due to the fact that aluminium alloys start to show pile-up even for stress free materials, and the level of pile-up is highly dependent on the magnitude and type of the residual stress, calculation of true contact area from the load-displacement curve based on Oliver-Pharr method was not possible. Atomic force microscopy was required for every state of the residual stress to calculate the true contact area which itself was a tedious task. So, instead of calculation of true contact area from experimental nanoindentation, again finite element simulations have been used to study the effect of residual stresses on load-displacement data.

6.3.2 Investigation through Finite Element Simulation

For every single indentation a load-displacement curve is obtained which gives information about the response of the deformation of the material. As discussed in chapter 5 section 5.3.2.1 curvature C is obtained by fitting the loading curve with a second order polynomial [4].

$$P = Ch^2 \qquad (6.1)$$

Contact depth h_c, area of contact A_c and stiffness S can be obtained using Oliver-Pharr model [5] from equations 6.2, 6.3 and 6.4 respectively which are given below.

$$h_c = h_{\max} - \varepsilon \frac{P_{\max}}{S} \qquad (6.2)$$

$$A = 24.5h_c^2 \quad (6.3)$$

$$S = \left(\frac{dP}{dh}\right)_{h=h_{max}} \quad (6.4)$$

Based on maximum depth of penetration h_{max} and depth at the end of unloading h_f, the elastic, plastic and total work of indentation can be determined as shown in eq. 6.5, 6.6 and 6.7. Details for these parameters have already been given in chapter 3.

$$W_t = P_{max}\ h_{max}/3 \quad (6.5)$$

$$W_p = h_f\ W_t / h_{max} \quad (6.6)$$

$$W_t = W_p + W_e \quad (6.7)$$

Parameters at a certain depth are considered as the response of a stress free material. The existence of residual stresses prior to indentation strongly affects the load-displacement curve. All of the above discussed parameters change with a change in the load-displacement curve. Simulations of indentation for a fixed depth of 600nm were carried out with normalized residual stress σ_r/σ_Y ranging from -0.63 to 0.63 prior to indentation. Loading and unloading curves both were affected by residual stresses and it was observed that curves move in different directions with respect to the stress free load-displacement curve depending upon the sign of σ_r/σ_Y .

6.3.2.1 Effect on Load-displacement Curve

Fig.6.6 shows load-displacement curves for compressive, stress free and tensile residual stress conditions for Al-cladding. It can be seen that both loading and unloading curves were affected by residual stress. As compared to the stress-free condition, the path of the loading curve changes and consequently shows variation in slopes with residual stresses. A similar behaviour was observed for the unloading curve which shifted towards the loading curve for compressive residual stress and away for tensile residual stress.

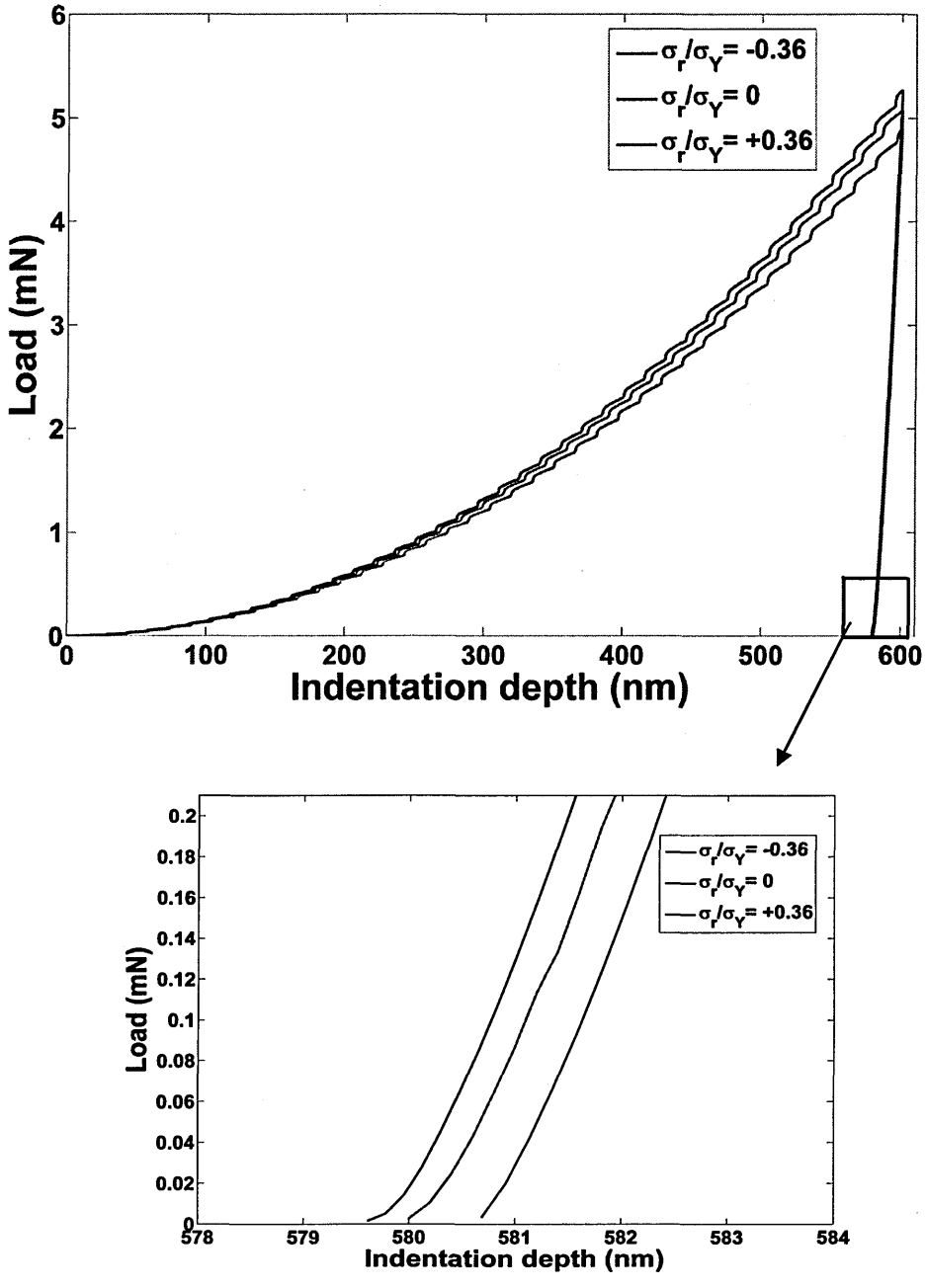

Fig. 6.6 - Effect of residual stress on load-displacement curve for Al-cladding

6.3.2.2 Effect on Loading Curve

As discussed earlier, the two parameters which are obtained from the loading curve are C and P_{max}. For compressive residual stresses, more force was required to penetrate to a specific depth, hence the maximum load P_{max} increased, and the opposite effect was observed for tensile residual stresses. To attain a high load in compression and less in

tension, the loading curve moved up and down for compressive and tensile residual stresses respectively, and consequently the curvature C of the loading curve was affected. Fig.6.7 (a) and (b) shows the behaviour of these two parameters and a direct relation was observed with residual stresses.

There was a significant difference in the maximum load and curvature for both of the materials for a specific residual stress. Owing to the higher yield stress of Al 2024-T351 as compared to the cladding, more force was required to penetrate to a depth of 600 nm. The maximum load P_{max} for Al 2024-T351 was from 14 to 10.5 mN in the compressive and tensile regions (-0.63 σ_Y to +0.63 σ_Y) respectively while this range remained from 5.3 to 4.6 mN for Al-cladding.

It can be seen that although there was direct relation between residual stress and change in P_{max} but the slope was higher in the case of Al 2024-T351. As both materials have almost the same elastic modulus and strain hardening exponent, this change in slope can be attributed in P_{max} was due to the higher yield stress of Al 2024-T351. A similar effect was observed for the curvature of the loading curve of these two materials as shown in Fig.6.7 (b). It was found that the slopes of $P_{\max}$ and C are directly related to the yield stress of the material, and a higher yield stress results in a higher slope of $P_{\max}$ and C.

Data for the variation in $P_{\max}$ and C for both of the materials can be described by equations given below;

$$P_{\max} = a\frac{\sigma_r}{\sigma_Y} + b \qquad (6.8)$$

$$C = a\frac{\sigma_r}{\sigma_Y} + b \qquad (6.9)$$

Values for the constants a and b for both materials are given in Table 6.1. It can be seen that there is significant difference between the slopes and intercept values for both materials, with smaller values for the Al-cladding as compare to Al 2024-T351.

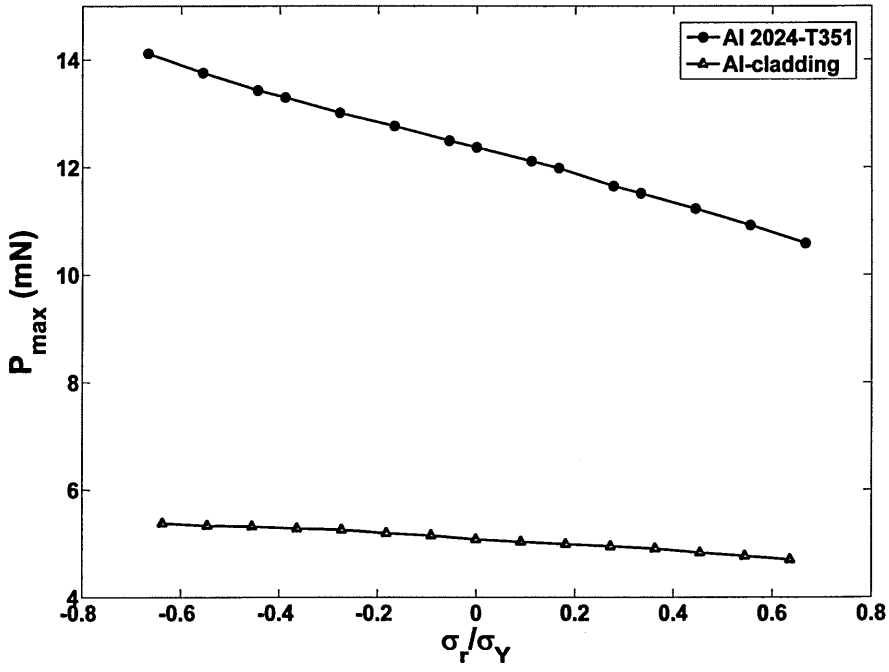

(a)

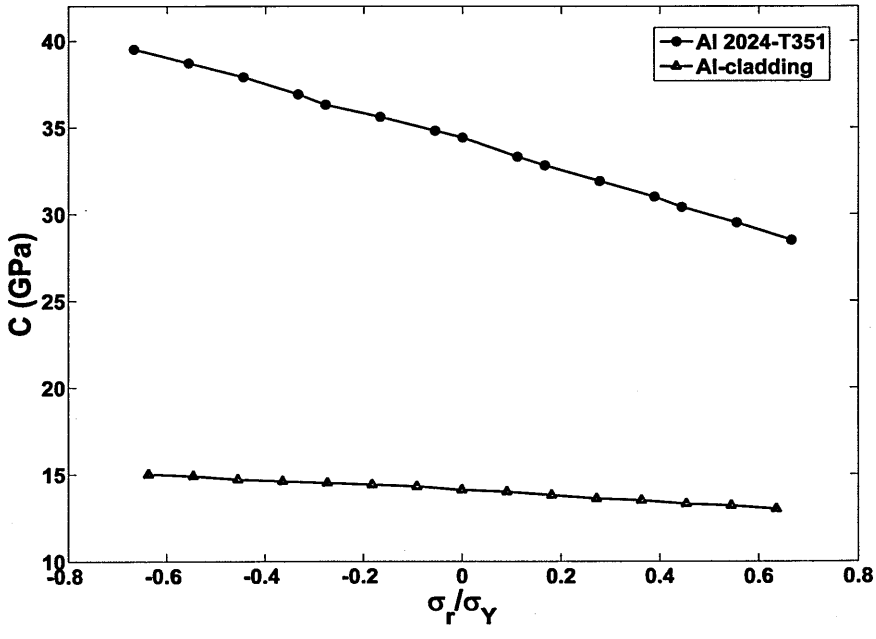

(b)

Fig. 6.7 - Effect of residual stress on the loading curve for Al 2024-T351 and Al cladding (a) Variation in maximum load (b) Variation in curvature of loading curve

6.3.2.3 Effect on Unloading Curve

For compressive residual stresses, material tried to move up more which resulted in more amount of material recovered from deformation while for tensile residual stresses material

behaved oppositely and less amount of material recovered elastically. In the FE simulation, due to this change in elastically recovered depth, the unloading curve moved towards the loading curve for compressive residual stress and away for tensile residual stress. This change in position of the unloading curve resulted in an increase in the elastically recovered depth h_e for compressive and a decrease for tensile residual stress. With an increase in elastically recovered depth for compressive residual stress, final depth h_f decreased and the ratio h_f/h_{max} decreased, and the opposite effect was observed for tensile residual stress. This ratio of final depth to maximum depth h_f/h_{max} is a parameter which gives information about the part of the deformation which was not recovered elastically and at the same time it is equivalent to the ratio of plastic work to total work W_p/W_t as can be obtained from eq. 6.5 and 6.6.

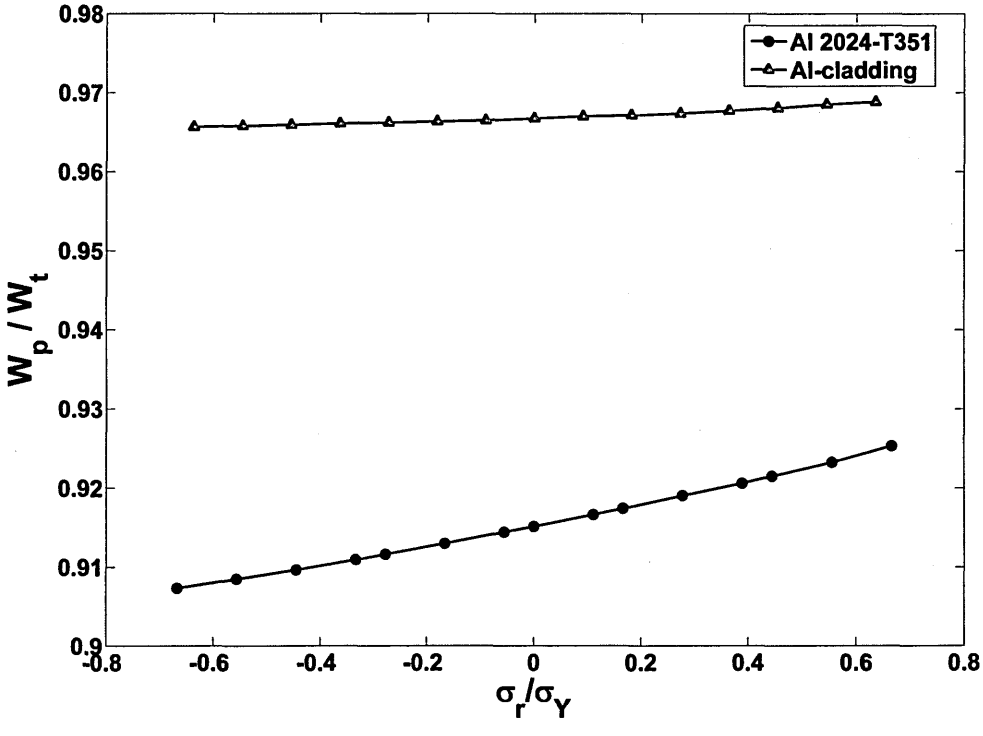

Fig. 6.8 - Effect of residual stress on W_p/W_t for Al 2024-T351 and Al-cladding.

Fig.6.8 shows that a direct relation for ratio W_p/W_t with residual stress and this ratio decreased for compressive residual stresses and increased for tensile residual stresses. W_p/W_t varied from 0.905 to 0.925 for Al 2024-T351 for stresses in the range -0.63σ_Y to +0.63σ_Y, and varied from 0.965 to 0.97 for the Al-cladding. As Al-cladding has a lower yield stress so it has less elastically recovered depth. This results in the area under the curve being more dominated by plastic deformation so W_p/W_t was higher for the Al-cladding as compared to Al 2024-T351.

Additionally, slope of change in W_p/W_t for Al-cladding was less as compare to Al 2024-T351. The same amount of residual stress produced a greater change in W_p/W_t for Al 2024-T351 as compared to the Al-cladding. As both materials have almost the same elastic modulus and strain hardening exponent, this difference can attributed to the lower yield stress of the Al-cladding. Xu et al. [16-17] showed in their study that the slope of W_p/W_t is independent of the strain hardening of the material and directly dependent on the E/σ_Y ratio of the material.

As there was a direct relation of residual stress with W_p/W_t so the data in Fig.6.8 can be described as similar to equation 6.8 and 6.9.

$$W_p/W_t = a\frac{\sigma_r}{\sigma_Y} + b \qquad (6.10)$$

The values for a and b for both materials are given in Table 6.1. Again it was clear that the slope and intercept values for Al-cladding were less as compared to Al 2024-T351.

6.3.2.4 Effect on Pile-up

For aluminium alloys, due to their low hardness and small strain hardening exponents, pile-up around indents start to occur even at low loads [8]. When residual stressed material was indented, pile-up started to change as compared to stress free condition. During

indentation of a compressive residual stress region, material was pushed-out to the indented surface, which resulted in more pile-up, and tensile residual stress pulled-in to the material surface which resulted in less pile-up. The surface profiles of indentation at the end of loading step for different residual stresses are shown in Fig.6.9.

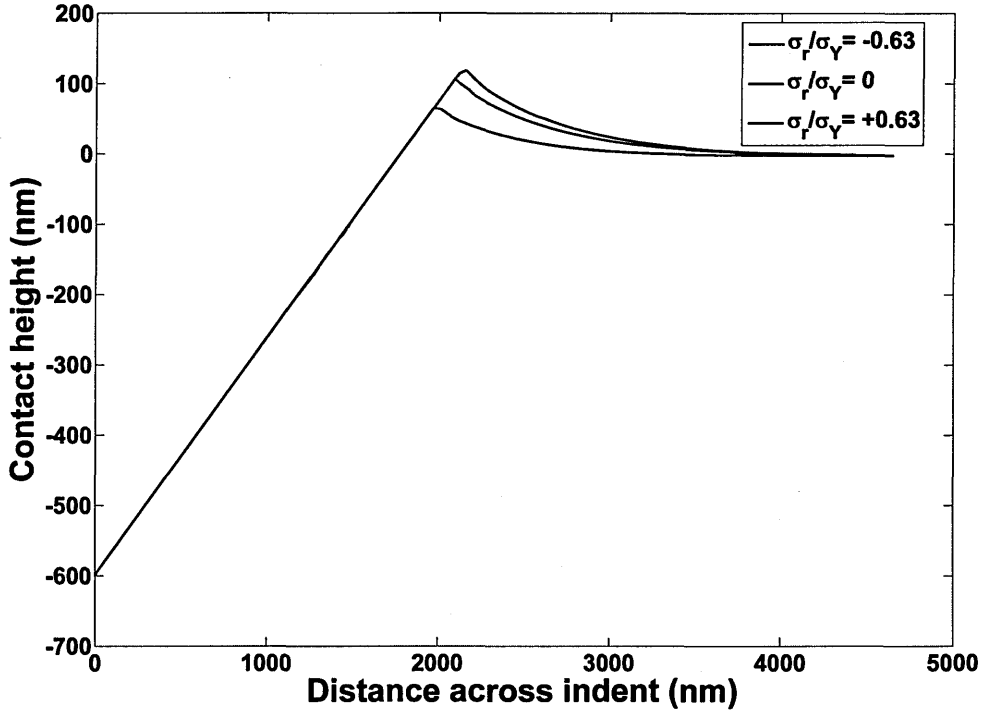

Fig. 6.9 - Effect of residual stress on surface profile of indentation from Al-cladding

From Fig.6.9 it is clear that pile-up height increased for compressive residual stress and decreased for tensile residual stresses. It can be observed even at zero stress condition that there was pile-up around the indents which showed that this effect of pile-up is not only due to the residual stress but is also a characteristic of the material which was indented.

It can be seen that the pile-up height was more affected in tension as compared to compression, and a similar amount of tensile residual stress produced more change in pile-up height as compared to compressive residual stress. This non-linearity was first reported by Tsui et al. [9] when reporting the hardness results in the presence of residual stresses.

6.3.2.5 Effect on Contact Area

The contact area of the indentation can be calculated from load-displacement data based on the method proposed by Oliver & Pharr [5] from eq. 6.3. The area of contact A_c, which O-P model calculates from the load-displacement curve, purely depends upon the part of the indenter which penetrates in to the material and doesn't take into account the amount of pile-up of material which comes out during indentation. As pile-up around the indenter depends upon the residual stress state, so the contact profile of each simulation was used to calculate accurate contact depth and consequently the corrected contact area $A_{c'}$. $A_{c'}/A_c$ was calculated, to normalize the area obtained from FEM with the area from O-P model from eq. 6.3.

Fig.6.10 shows the effect of residual stress on contact area for both materials. It is noteworthy that at zero stress, $A_{c'}/A_c$ was not equal to unity due to the fact even for a stress free material pile-up was obtained as discussed in chapter 3. It can be seen that residual stress produced a significant change on the area of contact and due to the lower yield stress of the Al-cladding; the residual area due to indentation was greater. So for the same depth and residual stress, a higher indentation area was obtained for the Al-cladding as compared to the Al 2024-T351, which had higher yield stress and greater hardness. The area ratio for Al-cladding was from 1.5 to 1.25 for stresses in the range $-0.63\,\sigma_Y$ to $+0.63\,\sigma_Y$, and varied from 1.4 to 1.1 for the Al 2024-T351. One thing which was notable that the slope for both materials remained almost the same, which showed that there was no effect of yield stress on slope of area. Xu et al. [16-17] reported that the slope of contact area was dependent on the work hardening exponent and remained independent for E/σ_Y ratio.

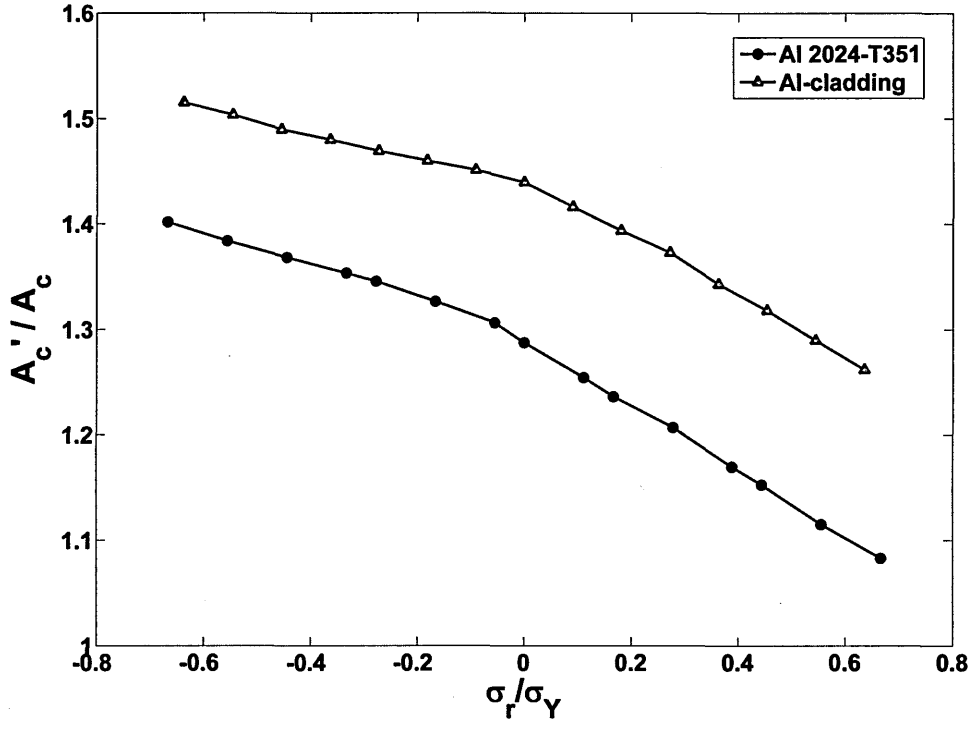

Fig. 6.10 - Effect of residual stress on contact area for Al 2024-T351 and Al-cladding.

It was observed that $A_{c'}/A_c$ had a linear relationship with residual stress: it increased for compressive residual stress and decreased with tensile residual stress as shown in Fig.6.10. Although the contact area varied with residual stresses, the slope of variation of this ratio was not the same for compressive and tensile residual stress. In the tensile region, the slope of $A_{c'}/A_c$ was higher, in agreement with the non-linearity first reported by Tsui et al. [9]. This was due to the fact that a same numerical value of tensile residual stress decreased pile-up more as compared to a compressive residual stress. This different trend in area ratio was in agreement with Suresh & Giannokoplous [11] who reported a non-linear trend of area ratio and used different area ratios to extract residual stresses from their model.

From Fig.6.10, it can be seen that a separate set of equations is required to define the compressive and tensile region behaviour so data can be described as;

$$\frac{A_{c'}}{A_c} = a_C \frac{\sigma_r}{\sigma_Y} + b_C \quad \text{(6.11a)} \qquad , \qquad \frac{A_{c'}}{A_c} = a_T \frac{\sigma_r}{\sigma_Y} + b_T \quad \text{(6.11b)}$$

Values for a and b are given in Table 6.1. It can be seen that the values of the slope i.e. a were the same for both materials in compression and tension but the intercept values b were different and were higher for the Al-cladding.

Using the constants from Table 6.1, eq. 6.11 (a) and (b) can be used to estimate the residual stress for the Al-cladding and Al 2024-T351, if the area of contact including pile-up $A_{c'}$, is known. This particular equation is only useful for finite element studies, and has less importance for experimental studies in which measurement of area by means of optical microscopy or AFM is challenging, and the change in area of contact with residual stress requires measurement of contact area at every single location which is a tedious task.

This relationship shows that whenever experimental indentation is performed on any unknown residual stress region, piling up of the material has to be calculated to allow the correct area of the contact obtained from the O-P model. For very local residual stress fields e.g. a near surface region, this pile-up would change at every location and AFM or some other technique is required to accurately measure the true area of contact, which itself is a source of error.

6.3.3 Empirical Model for Estimation of Residual Stress

The area obtained from indentation was directly related to the change in final depth h_f of the indentation. Any change in residual stress introduced a change in the area of contact and consequently in final depth h_f of the indentation. This change in h_f resulted in a change in W_p/W_t. When plotting W_p/W_t with $A_{c'}/A_c$, a direct relation was obtained as shown in Fig.6.11. Again a non-linear trend was obtained due to the non-linearity of pile-up height in both the compressive and tensile regions.

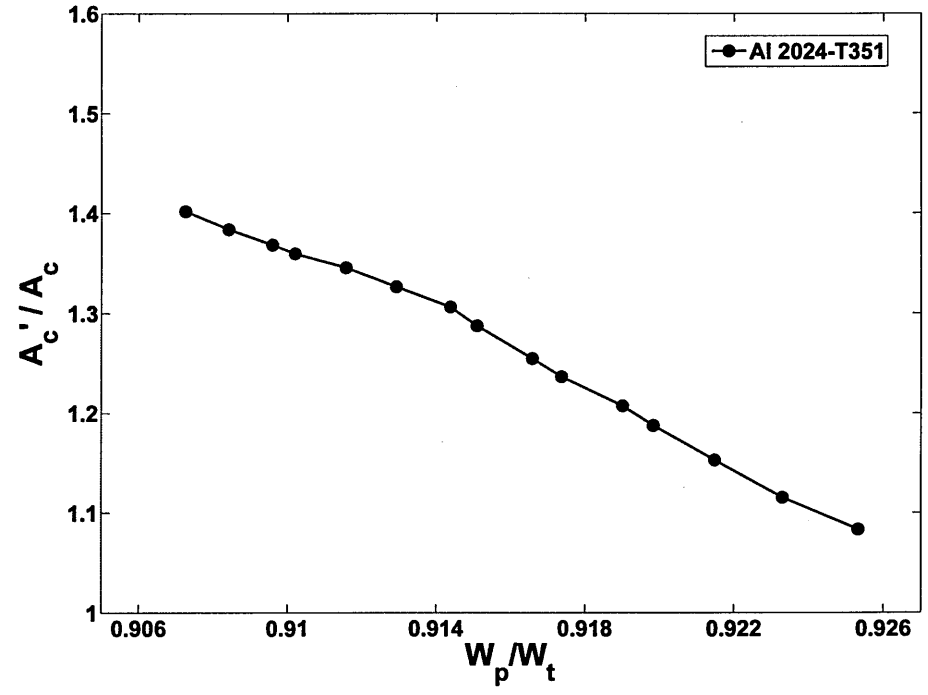

(a)

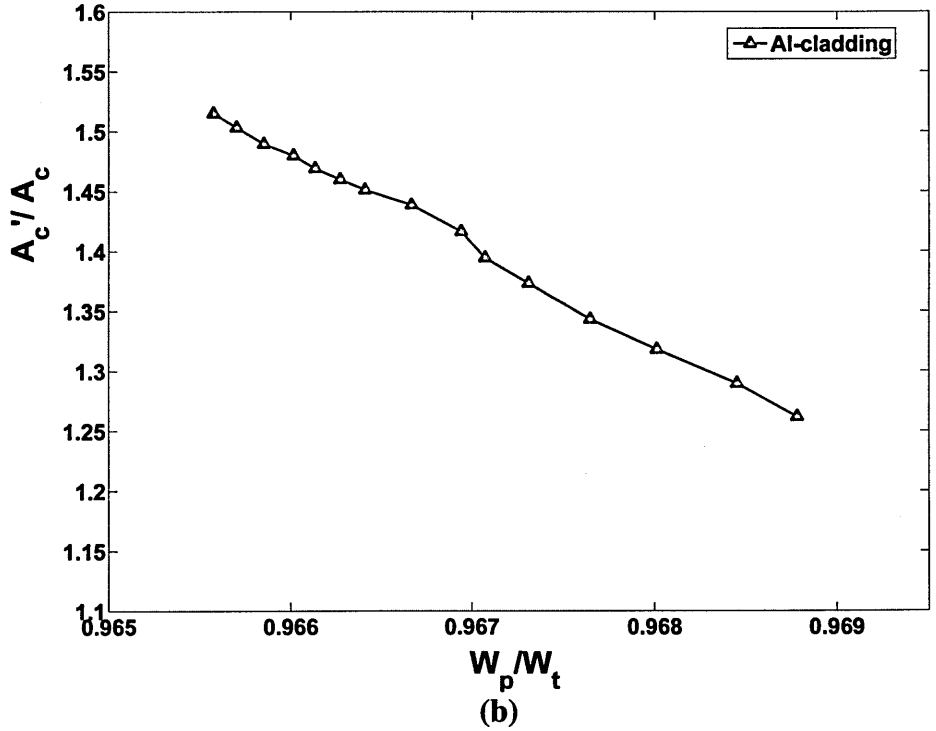

(b)

Fig. 6.11 - Relation between work ratio and area ratio for (a) Al 2024-T351 (b) Al-cladding

To calculate the area of contact, including pile-up, the data of Fig.6.11 can be described as,

$$\frac{A_{c'}}{A_c} = a_C \frac{W_p}{W_t} + b_C \quad \text{(6.12 a)} \qquad , \qquad \frac{A_{c'}}{A_c} = a_T \frac{W_p}{W_t} + b_T \quad \text{(6.12 b)}$$

Values for a and b are given in Table 6.1. Different slope and intercept values were obtained for both materials in compression and tension.

So for extraction of residual stresses from experimental load-displacement curves eq. 6.12 can be used to obtain the area ratio $A_{c'}/A_c$ from W_p/W_t ratio, and then eq. 6.11 can be used to obtain residual stress σ_r/σ_Y based on $A_{c'}/A_c$.

Material	Coefficient	Relation between						
		P_{max} and σ_r/σ_Y	C and σ_r/σ_Y	W_p/W_t and σ_r/σ_Y	$A_{c'}/A_c$ and σ_r/σ_Y		$A_{c'}/A_c$ and W_p/W_t	
Al-cladding	a	-0.5284	-1.5636	0.0024	C	-0.1163	C	-70.8436
					T	-0.2798	T	69.9161
	b	5.0674	14.0600	0.9669	C	1.4387	C	-82.1432
					T	1.4431	T	80.8367
Al 2024-T351	a	-2.545	-8.2633	0.0134	C	-0.1636	C	-13.6242
					T	-0.3076	T	-20.3904
	b	12.347	34.1612	0.9155	C	1.2954	C	13.7617
					T	1.2886	T	19.5442

Table 6.1 - Slope and intercept values obtained from fitting of data for Al-cladding and Al 2024-T351.

6.4 Conclusions

Finite element simulations have been carried out to study the effect of residual stress on nanoindentation response of Al-cladding and Al-2024-T351. It has been found that nanoindentation properties including maximum load of indentation, curvature of the loading curve, elastically recovered depth, final depth, work of indentation and area of contact were affected by the presence of residual stresses. Expressions were derived to extract residual stresses from change in nanoindentation parameters including maximum

load, curvature, ratio of work of indentation and ratio of contact area. When plotting W_p/W_t with $A_{c'}/A_c$ maximum load, curvature of loading curve, to estimate residual stresses. Pile-up height and area of contact showed a non-linear behaviour for its variation in compression and tension.

For experimental indentation, where measurement of the true area of contact including pile-up is a challenging task, the area of contact can be extracted from its relation with W_p/W_t from eq. 6.12. Once true area of contact is known then residual stress can be extracted based on relations described in eq. 6.11. The developed technique will be applied on scribe marks from different tools and subsequently residual stresses will be extracted from load-displacement data.

6.5 References

[1] Bhattacharya, A. K. and W. D. Nix. Finite element simulation of indentation experiments. International Journal of Solids and Structures 24(9), 1988, pp 881-891.

[2] Pelletier, H., J. Krier, A. Cornet and P. Mille. Limits of using bilinear stress-strain curve for finite element modeling of nanoindentation response on bulk materials. Thin Solid Films 379(1-2), 2000, pp 147-155.

[3] Lichinchi, M., C. Lenardi, J. Haupt and R. Vitali. Simulation of Berkovich nanoindentation experiments on thin films using finite element method. Thin Solid Films 312(1-2), 1998, pp 240-248.

[4] Hainsworth, S. V., H. W. Chandler and T. F. Page. Analysis of nanoindentation load-displacement loading curves. Journal of Materials Research 11(8), 1996, pp 1987-1995.

[5] Oliver, W. C. and G. M. Pharr. An Improved Technique for determining hardness and elastic modulus using load and displacement senssing indentation experiments." Journal of Materials Research 7(6), 1992, pp 1564-1583.

[6] Khan, M. K., S. V. Hainsworth, M. E. Fitzpatrick and L. Edwards. Application of the work of indentation approach for the characterization of aluminium 2024-T351 and Al cladding by nanoindentation. Journal of Materials Science 44(4), 2009, pp 1006-1015.

[7] Bolshakov, A. and G. M. Pharr. Influences of pileup on the measurement of mechanical properties by load and depth sensing indentation techniques. Journal of Materials Research 13(4), 1998, pp 1049-1058.

[8] Taljat, B. and G. M. Pharr. Development of pile-up during spherical indentation of elastic-plastic solids. International Journal of Solids and Structures 41(14), 2004, pp 3891-3904.

[9] Tsui, T. Y., W. C. Oliver and G. M. Pharr. Influences of stress on the measurement of mechanical properties using nanoindentation. Experimental studies in an aluminium alloy. Journal of Materials Research 11(3), 1996, pp 752-759.

[10] Swadener, J. G., B. Taljat and G. M. Pharr. Measurement of residual stress by load and depth sensing indentation with spherical indenters. Journal of Materials Research 16(7), 2001, pp 2091-2102.

[11] Suresh, S. and A. E. Giannakopoulos. A new method for estimating residual stresses by instrumented sharp indentation. Acta Materialia 46(16), 1998, pp 5755-5767.

[12] Lee, Y. H., W. J. Ji and D. Kwon. Stress measurement of SS400 steel beam using the continuous indentation technique. Experimental Mechanics 44(1), 2004, pp 55-61.

[13] Lee, Y. H. and D. Kwon. Measurement of residual-stress effect by nanoindentation on elastically strained (100) W. Scripta Materialia 49(5), 2003, pp 459-465.

[14] Lee, Y. H. and D. Kwon. Estimation of biaxial surface stress by instrumented indentation with sharp indenters. Acta Materialia 52(6), 2004, pp 1555-1563.

[15] Carlsson, S. and P. L. Larsson. On the determination of residual stress and strain fields by sharp indentation testing. Part I: Theoretical and numerical analysis. Acta Materialia 49(12), 2001, pp 2179-2191.

[16] Xu, Z. H. and X. Li. Estimation of residual stresses from elastic recovery of nanoindentation. Philosophical Magazine 86(19), 2006, pp 2835-2846.

[17] Xu, Z. H. and X. D. Li. Influence of equi-blaxial residual stress on unloading behaviour of nanoindentation. Acta Materialia 53(7), 2005, pp 1913-1919.

[18] Zhao, M. H., X. Chen, J. Yan and A. M. Karlsson, Determination of uniaxial residual stress and mechanical properties by instrumented indentation. Acta Materialia 54(10), 2006, pp 2823-2832.

[19] Khan, M. K., M.E. Fitzpatrick., S. V. Hainsworth and L.E. Edwards. Effect of tool profile and fatigue loading on the local hardness around scratches in clad and unclad aluminium alloy 2024. Materials Science and Engineering A, Volume 527, Issues 1-2, 2009, pp 297-304.

Chapter 7: Measurement of Strain and Stress Fields and Local Hardening around Scribe Marks of Different Geometries in Aluminium alloy 5091 and 2024-T351

7.1 Introduction

The growth of fatigue cracks from small defects is of tremendous importance and of primary concern in structural integrity of aerospace structures. In fatigue, a crack initiates from a stress concentration location and can cause premature failure. The fatigue life for scribes is a function of the stress concentration around the root which depends upon the depth and root radius of the scribe, the associated microstructure, the residual stress field, work hardening from plastic deformation during scribing and relaxation or redistribution of these residual stresses in fatigue [6-8, 11-12]. Several investigations have been done in the past to address the issues associated with stress concentration and microstructural distortion around small damages [1-2, 4, 6, 8-10] but a thorough understanding of the effect of the residual stress around scribe marks and scratches is yet to be obtained.

The distribution of damage controls the initiation and early growth of fatigue cracks. Under fatigue residual stresses are responsible for changing the mean stress value and thus may accelerate or retard the crack growth if they are tensile or compressive respectively. Unfortunately the ability to measure local residual stress-strain fields around scribes is a difficult experimental problem due to the presence of high stress gradients around the scribe root. To probe these local residual stress fields experimental techniques are required that have spatial resolution of the order of a few microns, for which synchrotron X-ray diffraction is an ideal technique. Synchrotron X-ray methods are well suited to the investigation of residual stresses in the near-surface regions of engineered components [13]. The high intensity and low divergence allows small gauge volumes to be defined in order to study stress fields existing over a range of several hundred microns.

In the past, there have not been many studies carried out which focussed on the effect of submillimetre deep notches, scribes, gouges or scratches on fatigue life. Most of the research has been towards characterization of the effect of foreign object damage (FOD) on turbine engine blades in titanium. FOD were created with impact on specimen with projectiles of different size and shapes with different velocities. In these studies several aspects including residual stresses has been discussed and in almost every study residual stresses has been termed as very important factor in affecting fatigue lives However, very little contribution has been made on measurement of initial residual stresses around these FODs and the effect of fatigue loading in relaxation of these residual stresses [4-10]. First time Boyce et al. [11] measured residual stress field around FOD from synchrotron X-ray diffraction and found that initial residual stress around the damage was high tensile and was 40% of the yield stress. They emphasized that initial residual stress state is substantially reduced by relaxation or distribution during fatigue loading and may reduce by 30-50% of its initial value after the first fatigue cycle. In another study [12], focussing on relaxation of these residual stresses, they concluded that initial residual stress state around FOD can decay significantly in fatigue depending upon the applied stress. For Ti-6Al-4V, they obtained very little relaxation for $0.35\sigma_Y$ but for higher applied stress of $0.54\sigma_Y$ this relaxation reached to 50%. They observed that decay of the residual stress state was only during the first cycle and subsequent cycles showed very little further relaxation.

Overall, it was observed that to successfully predict, fatigue lives of any foreign object damage, scribe marks, scratches, gouges etc. important parameters are stress concentration associated with the geometry of damage, associated microstructural distortion, residual stress field induced by the damage and subsequent plastic damage distribution and relaxation of such residual stresses upon fatigue loading. This chapter presents investigation of residual stress field around scribe marks of different geometries in

aluminium alloy 5091 and 2024-T351 induced by different tools. Residual strain fields were measured by synchrotron X-ray diffraction at ID31 beam line of European Synchrotron Radiation Facility (ESRF), Grenoble, France

7.2 Materials, Specimen and Experimental Details

7.2.1 Materials Details

Due to the large grain size (~20 μm) of Al 2024-T351, it was decided that measurements will be made using 2mm thick sample of aluminium alloy 5091, produced by a powder metallurgy process, which is ideal for synchrotron measurement owing to its fine grain size (~0.6 μm). Material properties for aluminium alloy 5091 are already given in chapter 3.

One scribe of 100 μm depth in unclad Al 2024-T351 was also measured. With much larger grain size of clad (~70 μm), it was very difficult to measure residual stress field from diffraction and hence none of the samples with clad Al 2024-T351 was measured.

7.2.2 Specimen Details

For both of the materials, 2mm thick plates were used. In total four scribes were produced with different tools in different aluminium alloys as discussed previously. Scribe marks of 125 μm depth and 5 μm root radius were produced in aluminium alloy 5091 with two different tools designated as tool A and B. One scribe mark was produced with tool A in aluminium alloy 2024-T351 with 100 μm depth and 5 μm root radius. Another tool designated as 'tool D' was used to produce scribes in aluminium alloy 5091 with the same depth of 125 μm but with a root radius of 50 μm. Details of the scribe marks are given in Table 7.1 and cross-sections of these scribes are shown in Fig.7.1. For measurement using synchrotron X-rays sample size of 50mm x 50mm x 2mm was used with the scribe mark exactly at the centre of the sample.

Sample #	Material	Tool	Depth d (μm)	Root radius ρ (μm)	d/ρ
1	Al 5091	A	125	5	25
2	Al 5091	B	125	5	25
3	Al 2024	A	100	5	20
4	Al 5091	D	125	50	2.5

Table 7.1 - Scribe marks used in measurements.

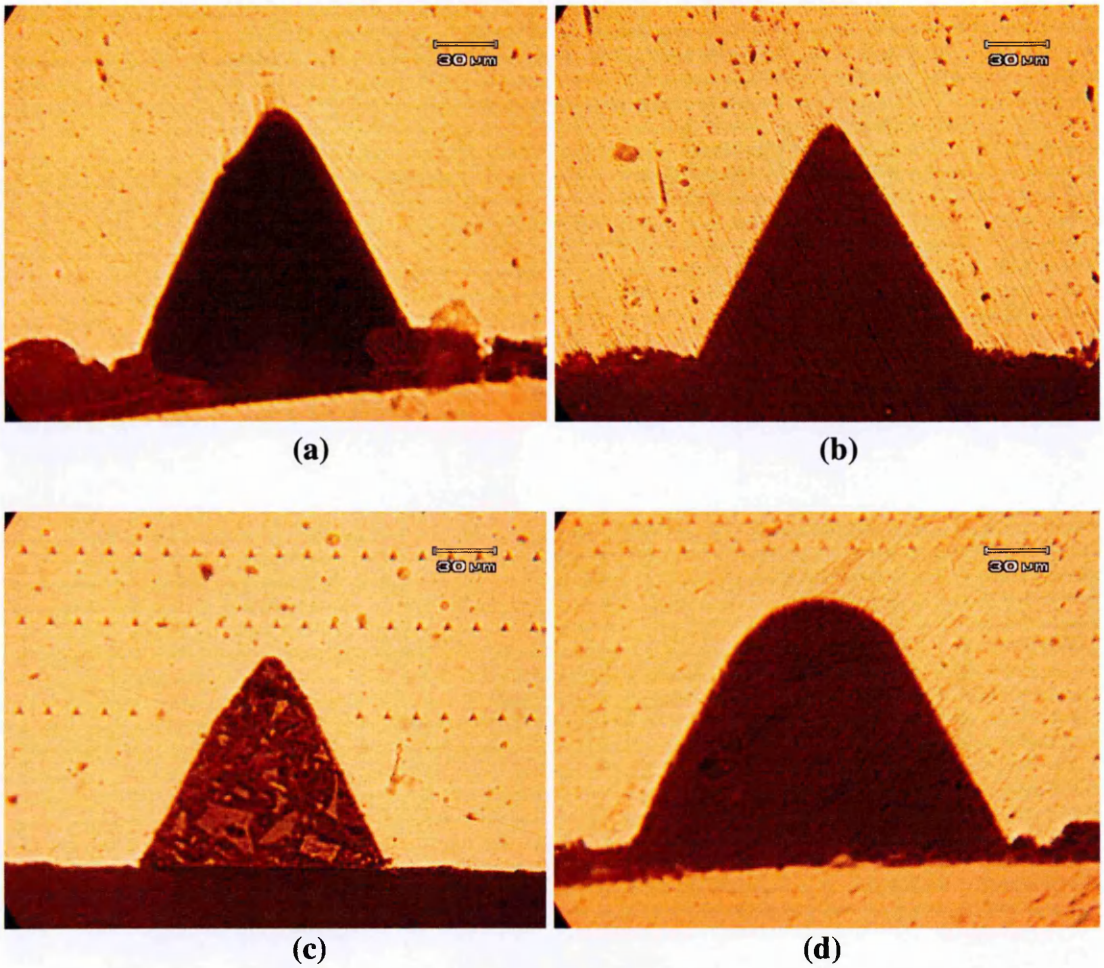

(a) **(b)**

(c) **(d)**

Fig. 7.1 - Cross-section of scribes (a) Sample 1(b) Sample 2 (c) Sample 3 (d) Sample 4

7.2.3 Experimental Setup

At the ID31 beam line of ESRF, a monochromatic beam is generated using Si 111 crystals. The diffractometer, as shown in Fig.7.2, uses a bank of nine detectors to measure diffracted

intensity as a function of 2θ. Each detector is preceded by a Si 111 an analyser crystal and the detector channels are approximately 2° apart. The use of analyser crystal helps to avoid any near surface measurement effects due to partially filled gauge volumes. The energy range of ID31 is 5keV to 60keV which corresponds to wavelengths of 2.48 Å to 0.21 Å.

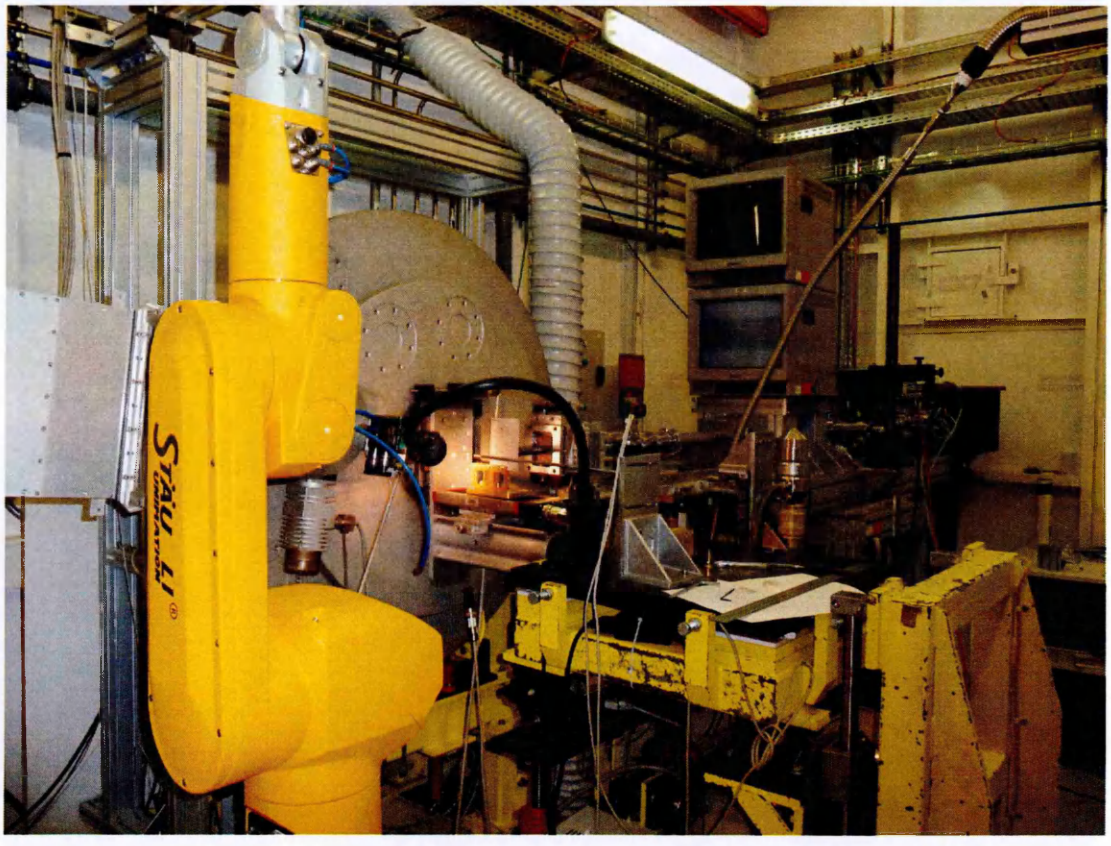

Fig. 7.2 - Diffractometer at ID31 of ESRF

For measurements, the sample was mounted on a translation mounting rig by which the sample can be translated in all the x, y and z axes as shown in Fig.7.3. Monochromatic radiation of 60keV was used. This corresponds to a wavelength of 0.21Å. Different crystallographic planes vary in their deformation mechanism and give different response for elastic residual stresses and in consideration of this, the 311 reflection was used [17]. As aluminium is FCC (face centred cubic) polycrystalline so the 311 reflection, which is most suitable for FCC polycrystals for least elastic anisotropy and best representation of the average macroscopic strain within the measurement volume, was used to determine inter-planar spacing [18]. The diffraction angle 2θ of 9.6° was used. An angular range of

0.065° for aluminium alloy 5091 and 0.1° for Al 2024-T351 was scanned to locate the exact angular position of the peak. The diffraction peak obtained was fitted assuming as a Gaussian distribution function using LAMP (Large Array Manipulation Program) [13].

In diffraction, at a particular diffraction angle, the geometry of the gauge volume depends upon the vertical opening of the incident beam slit and the opening of the receiving detector slit. Due to the very small and local residual strain field associated with scribes in an area of 500μm x 500μm, a very small gauge volume was used. Reflection and transmission modes of diffraction were used to measure different component of the strain. For measurement in reflection, the horizontal slit gap was 50μm and the vertical slit gap was 80μm for aluminium alloy 5091 while these gaps were 50μm and 100μm respectively for Al 2024-T351 due to its relatively large grain size. Similarly for measurements in transmission, the horizontal and vertical gap was 80μm and 100μm for aluminium alloy 5091 while these gaps were 80μm and 150μm respectively for Al 2024-T351.

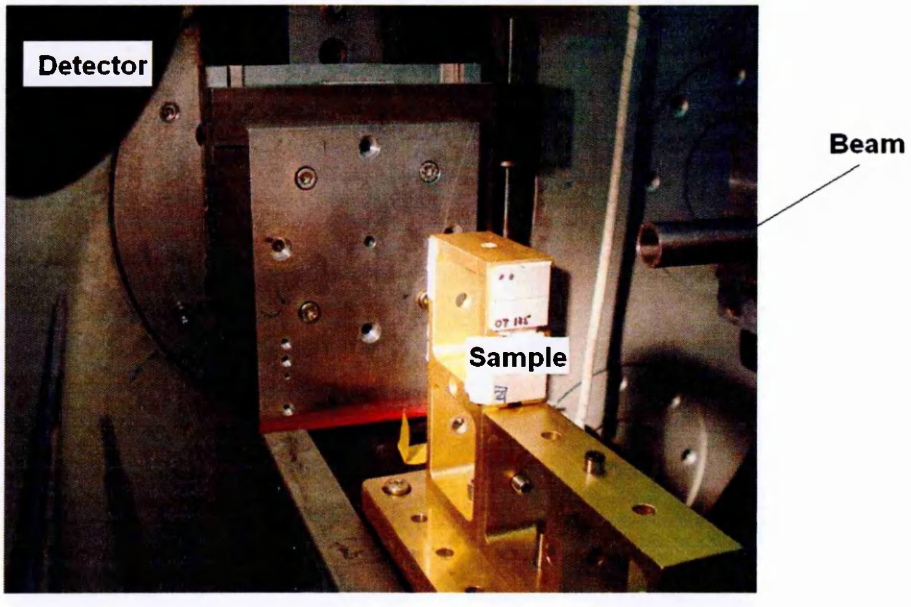

Fig. 7.3 - Sample in reflection mode of diffraction

Spatial resolution of the measured volume inside a material depends upon the geometry of the gauge volume and material characteristics. One consequence of low scattering angles

using high energy X-rays is an elongated gauge volume. The gauge volume was aligned such that the long axis was always parallel to the scribe, as in this direction the strain gradient can be assumed to be zero. Hence there was no significant averaging of the strain as a consequence of the elongated gauge volume. In the plane perpendicular to the scribe the gauge was ~ 80 x 50 μm. The scatter in strain measurements was found in the order of 20 με. The components of the strains are defined in Fig.7.4. The coordinate system has been chosen with $x = y = z = 0$ at the scribe root tip and at the centre of the sample. The x-direction was parallel to the crack propagating direction while the y-direction was perpendicular to the scribe plane and lay in the crack opening direction. The z-direction was parallel to the scribe length and this coordinate measured the depth from the scribe centre and z=0 was exactly at the centre of the sample. Two components of the strains, ε_{xx} and ε_{yy} were measured for every scribe while ε_{zz} was extracted from a possible plane stress or plane strain assumption which will be discussed later in this chapter. ε_{xx} is the crack propagating component of strain and ε_{xx} is the crack opening component of strain.

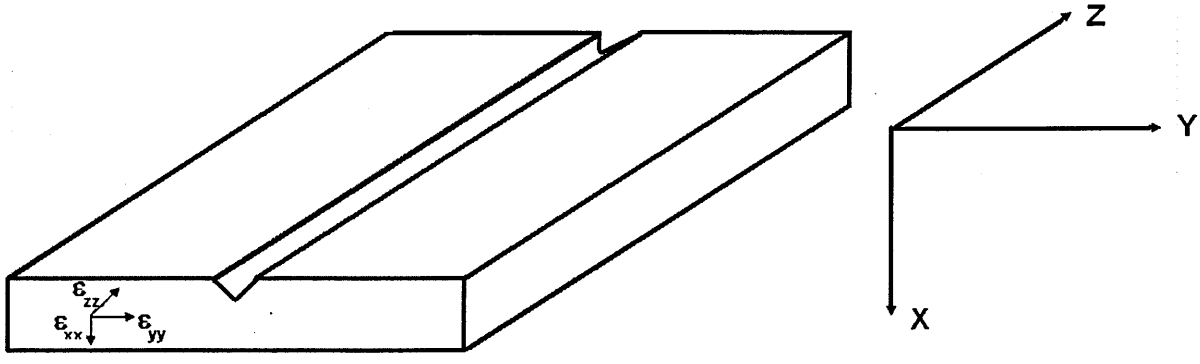

Fig. 7.4 - Strain component's geometry for scribe

To measure ε_{yy}, reflection mode of diffraction was used and sample was placed as shown in Fig.7.5 (a) while to measure ε_{xx}, transmission mode of diffraction was used and sample was twisted to a new orientation as shown in Fig.7.5 (b).

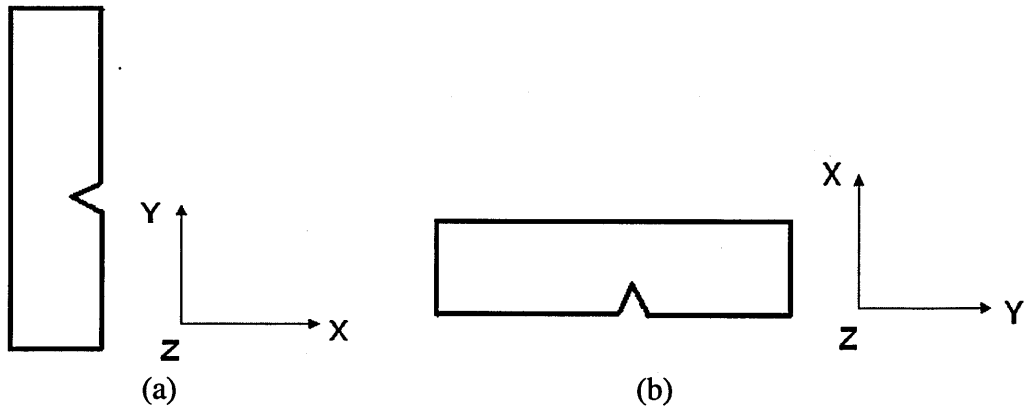

Fig. 7.5 - Sample Orientation to measure (a) in reflection for ε_{yy} (b) in transmission for ε_{xx}

7.3. Results and Discussion

7.3.1 Residual Strains from Synchrotron X-ray Diffraction

Determination of the actual internal stresses is dependent upon measurement of all three strain components. Experimentally, this required multiple sample orientations and alignments. Because our samples were only 2mm in thickness and scribe was long so keeping in consideration of a possible plane stress or plane strain assumption, two components of the strain ε_{xx} and ε_{yy} were measured. Third component of the strain ε_{zz} was not measured due to very high spatial resolution requirement hence it was extracted from elastic strain equations.

A stress free inter-planar lattice spacing d_o value was obtained from a region far from the scratch root which could be considered as stress-free. Strains were calculated from the method discussed in chapter 2. The exact position of the scribe root was difficult to identify so surface scans were carried out for every scribe to find exact position of its root. In principle, the Bragg line intensity starts from zero in air, rises rapidly as the diffraction volume enters the material, and reaches a maximum when the diffraction volume is fully immersed in the specimen. Once the scribe root's position was precisely determined, measurement started with a coarse scanning pitch of 200 μm on a large region of 1500 μm each side in the y-direction across scribe root. Three series of measurements in the y-

direction were carried out at different x-locations to determine the strain. Scanning was carried out in the peak strain region with a fine pitch of 20 μm in x-direction through the scribe root with different y-locations.

7.3.1.1 Sample 1

For sample 1, coarse scanning with a pitch of 200 μm was carried out in the y-direction with different x-locations of x=+5 μm, +80 μm, and +130 μm (arbitrarily chosen) to observe strain gradient. ε_{xx} and ε_{yy} were measured and the strain profiles for these measurements are shown in Fig.7.6. It can be seen that both of the components were tensile residual strain condition with ε_{yy} much higher as compared to ε_{xx} for this scribe. At x=+5 μm, below the scribe root i.e. at $y=0$, ε_{yy} reached its maximum tensile strain value of +1700 micro-strains and started to decrease as distance from scribe root increased in +x-direction. ε_{yy} decreased down to +600 με at x=+80 μm and +400 με at x=+130 μm. On the other side, ε_{xx} reached its maximum value of +200 με at x=+5 μm and decreased to 100 με at x=+130 μm. For each scan in the y-direction, a variation in strain was present until 500 μm on either side of scribe root and after this region a strain free condition was present.

One important result of this measurement was that the strain components were not symmetric across the scribe root and the profile of the strain showed a deviation from symmetric behaviour in the $+y$-direction of the scribe root. This irregular behaviour was due to the irregular profile of the scribe as shown in Fig.7.1(a). This irregular profile of the scribe was a characteristic of tool A, and every scribe produced from this tool had this irregular feature as discussed in chapter 3. It was found that strains jumped to slightly higher values under this feature of the scribe.

This coarse pitch scanning revealed that in the x-direction a high gradient of strain is present and the strain field extends 200 μm from scribe root.

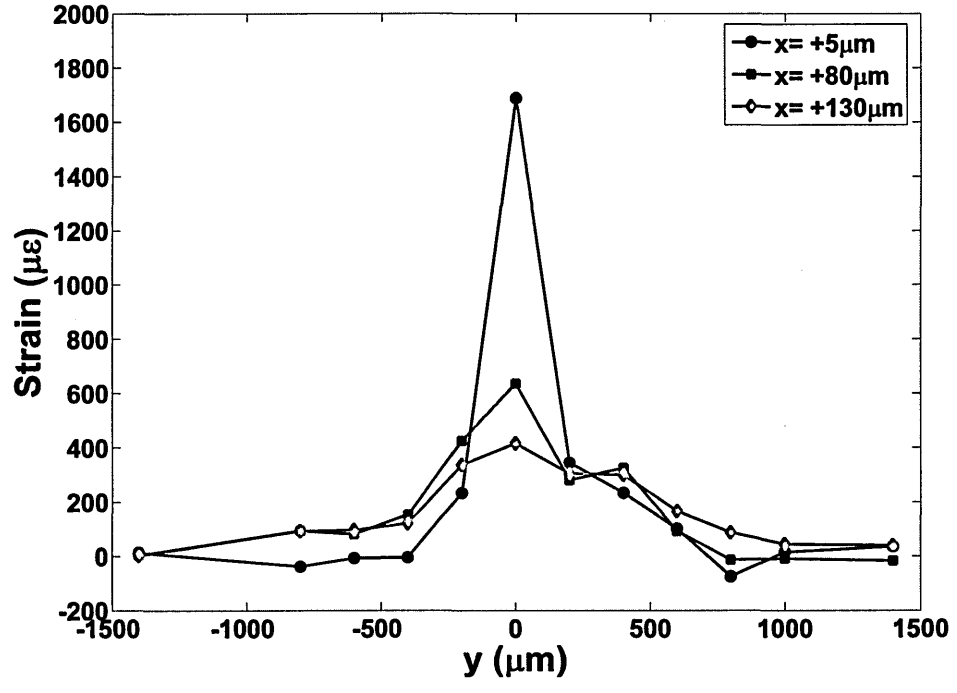

(a)

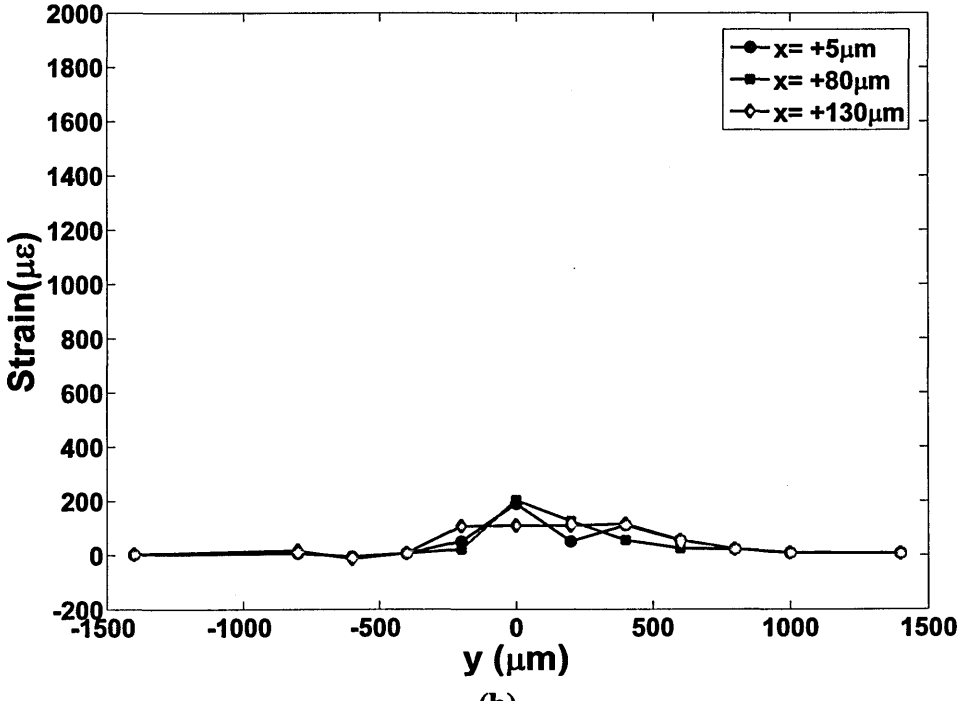

(b)

Fig. 7.6 - Strain profiles across scribe for sample 1.
(a) Transverse component (b) Longitudinal component

Scanning with a fine pitch of 30 μm was carried out in the x-direction with different y-locations and the strain profiles for these measurements are shown in Fig.7.7. It was discovered that for sample 1, ε_{yy} reached a maximum strain of +1700 micro-strain below the scribe root at y=0. With increase in distance in the x-direction from the scribe root, ε_{yy} started to decrease and became compressive after x=+100 μm and reached to -2800 με. However, ε_{xx} remained the same for all scans at a tensile strain of about +200 με.

There was considerable difference between the strain profiles of ε_{yy} at y=+75 μm and y=-75 μm and maximum value of strain was +1000 με and +200 με respectively at x=50 μm.

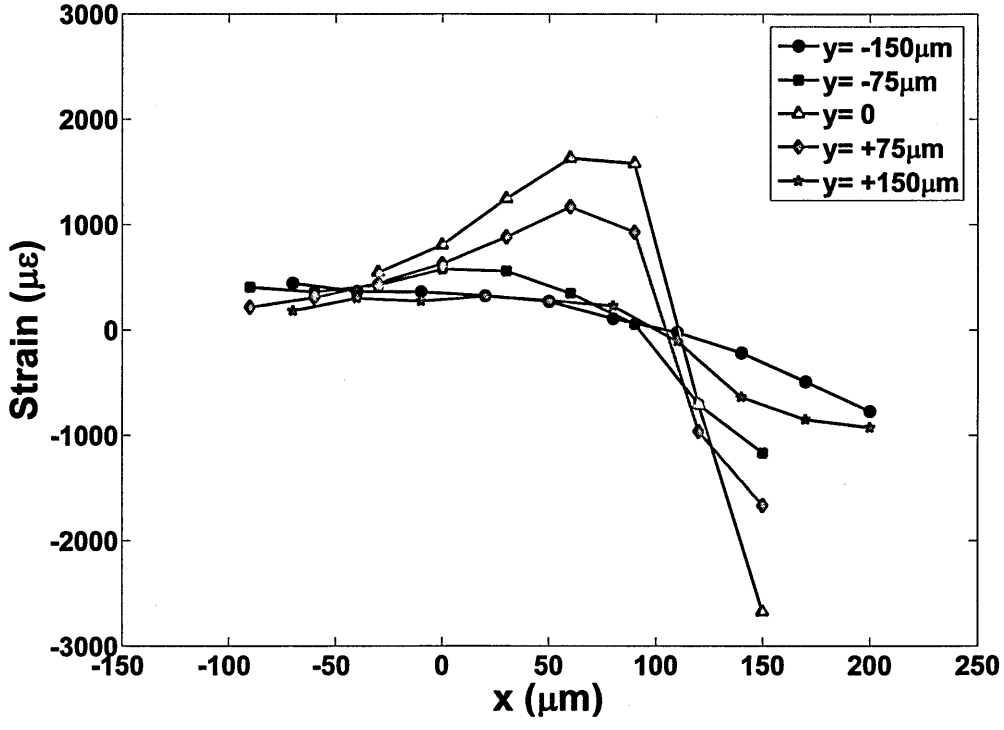

(a)

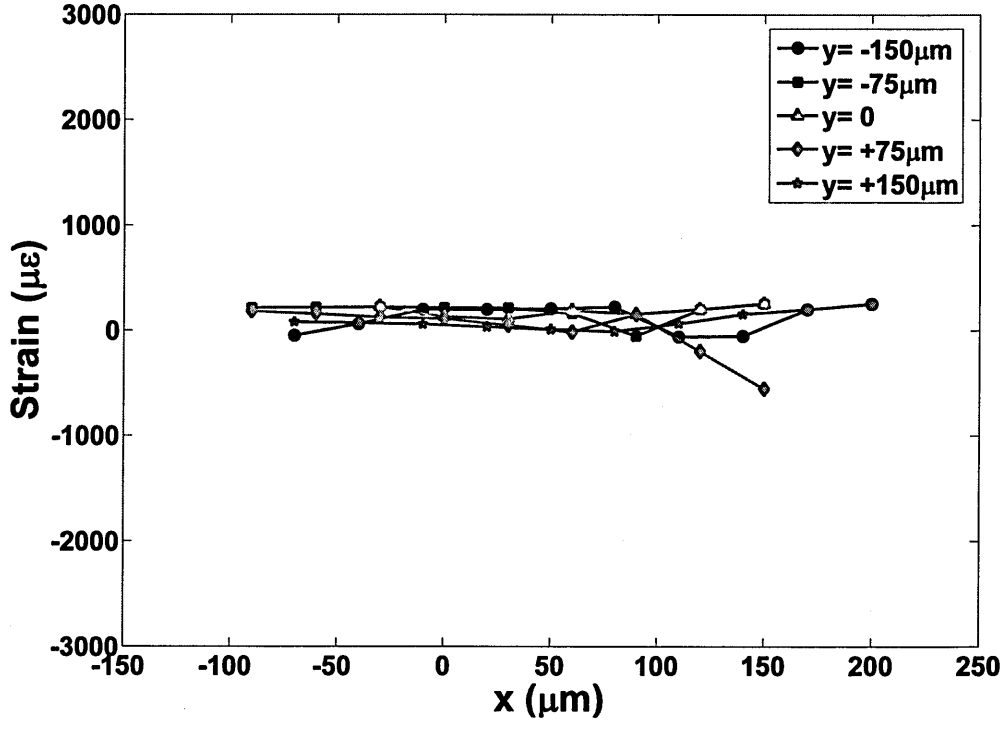

(b)

Fig. 7.7 - Strain profile around sample 1.
(a) Transverse component (b) Longitudinal component

So it was found that sample 1 had a high tensile residual strain field around the scribe root in which tensile residual strain reached as high as 1800 με. The tensile field was present up to 100 μm in +x-direction below the scribe root and to balance this tensile residual strain compressive residual strains were present after x=+100 μm.

7.3.1.2 Sample 2

For sample 2, coarse scanning was carried out in the y-direction with different x-locations at x=-45 μm, +30 μm and +75 μm. Both ε_{xx} and ε_{yy} were measured. Fig.7.8 shows the strain profiles for these measurements. There was not a considerable difference between ε_{xx} and ε_{yy} for this scribe, primarily due to the reason that no measurement point was carried out at $y = 0$. At x=+30 μm, ε_{yy} reached a maximum value of +200 με. For every

scan in the y-direction, a variation in strain was present up to 500 μm on either side of the scribe root and after this region a strain free condition was present.

So this coarse pitch scanning didn't disclose peak tensile strain values correctly but provided a good estimate of the area in which fine pitch scanning were required.

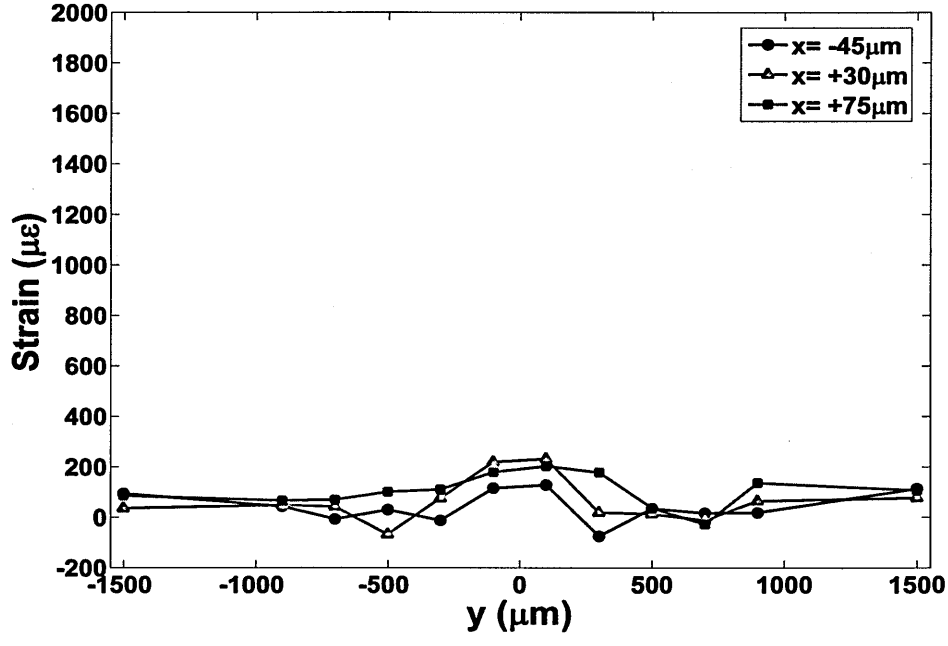

(a)

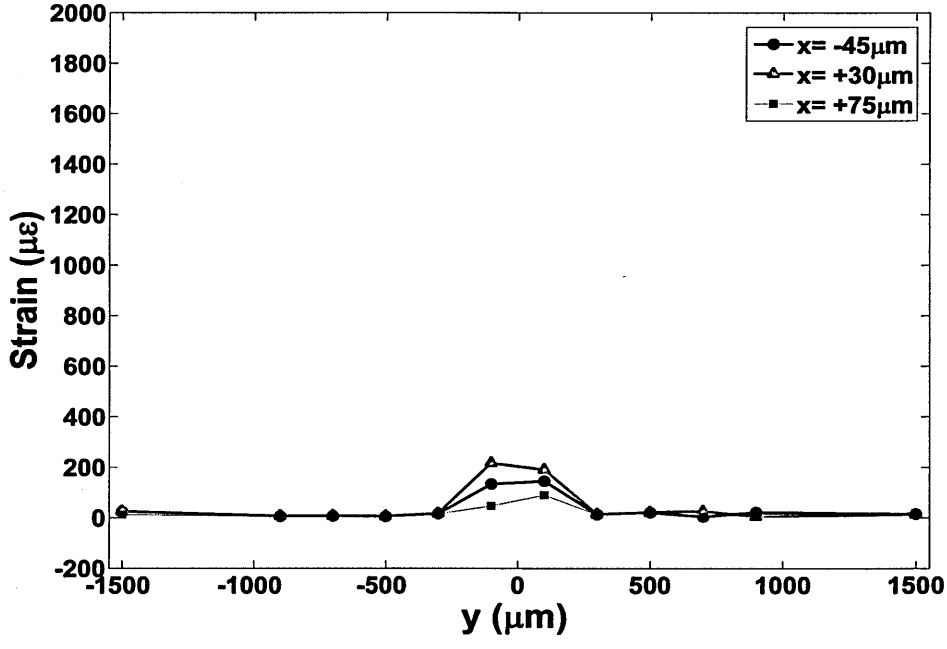

(b)

Fig. 7.8 - Strain profile around the sample 2
(a) Transverse component (b) Longitudinal component

Scanning with a fine pitch was carried out in the x-direction at different y-locations on both sides of the scribe centre. Fig.7.9 shows strain profiles for these measurements. ε_{yy} was much higher than ε_{xx} as was the case with the tool A scribe, but the ε_{yy} values were below than for sample1. Here ε_{yy} reached a maximum strain of +1000 με below the scribe root centre i.e. y=0. As the distance from scribe increased in the +x direction, the ε_{yy} strain component decreased down to +200 με at x=+60 μm. However, ε_{xx} remained same for all scans at a tensile strain of about +200 με.

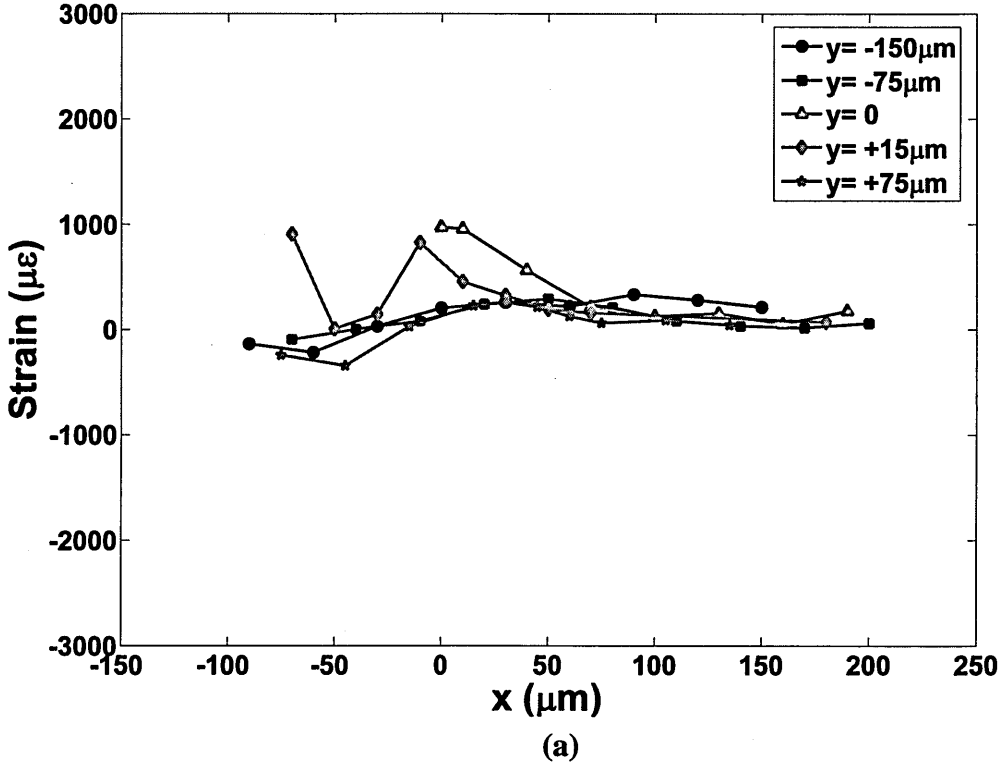

(a)

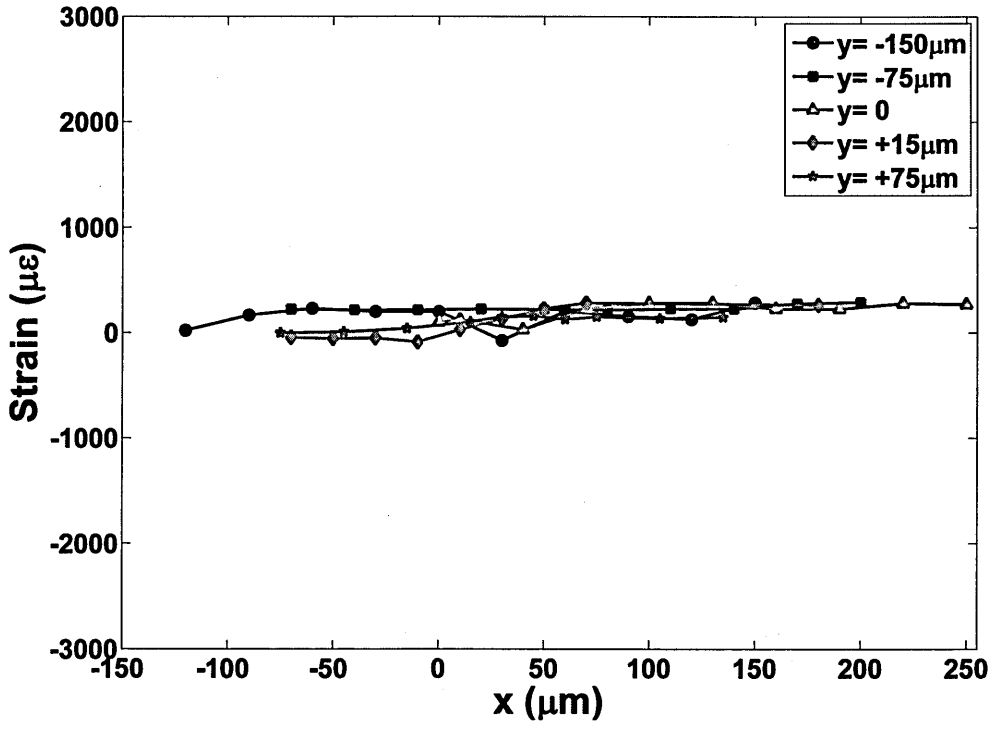

(b)

Fig. 7.9 - Strain profile through sample 2
(a) Transverse component (b) Longitudinal component

So it was found that sample 2 had a high tensile residual strain field as sample 1, but peak tensile values were less than sample 1. The peak tensile strain reached 1000 με. Not only the peak strain values were low but the spatial extent of the residual strains were less as compared to tool A, being only 60 μm below the scribe compared to 100 μm for sample 1.

7.3.1.3 Sample 3

Sample 3 was a similar scribe as sample 1 but in Al 2024-T351 and of slightly less depth of 100 μm. With larger slit gaps for aluminium alloy 2024-T351 as discussed earlier, coarse and fine pitch scanning adopted for samples 1 and 2 was not carried out, because of the larger gauge volume so fine pitch scanning would have no advantage here. Scanning with a pitch of 100 μm was carried out in y-direction at different x-locations at x=-30 μm, 0, +50 μm and +100 μm. More time was required for measurement in Al 2024-T351 due to

the larger gauge volume used for Al 2024-T351 and due to shortage of beamtime only transverse component of the strain i.e. ε_{yy} was measured as shown in Fig.7.10. Due to large gauge volume, residual strains at $x = 0$ did not show any reliable information about the residual strains due to the fact that it represented average value of the strain for a partially filled gauge volume included behind the root area. It can be seen that ε_{yy} for this sample was very much similar to that obtained for sample 1. For a scan at x=+50μm, below the scribe root at $y = 0$, ε_{yy} reached maximum value of +2000με and started to decrease with increase in distance from scribe root. One line of the scan was carried out behind the scribe root at x=-30μm and this region was in overall compression and the maximum value of strain was -1700με. With the same values for ε_{yy} for this scribe as obtained for sample 1 and because beamtime was limited, it was assumed that the other component, ε_{xx}, would show a similar trend as was obtained for sample 1.

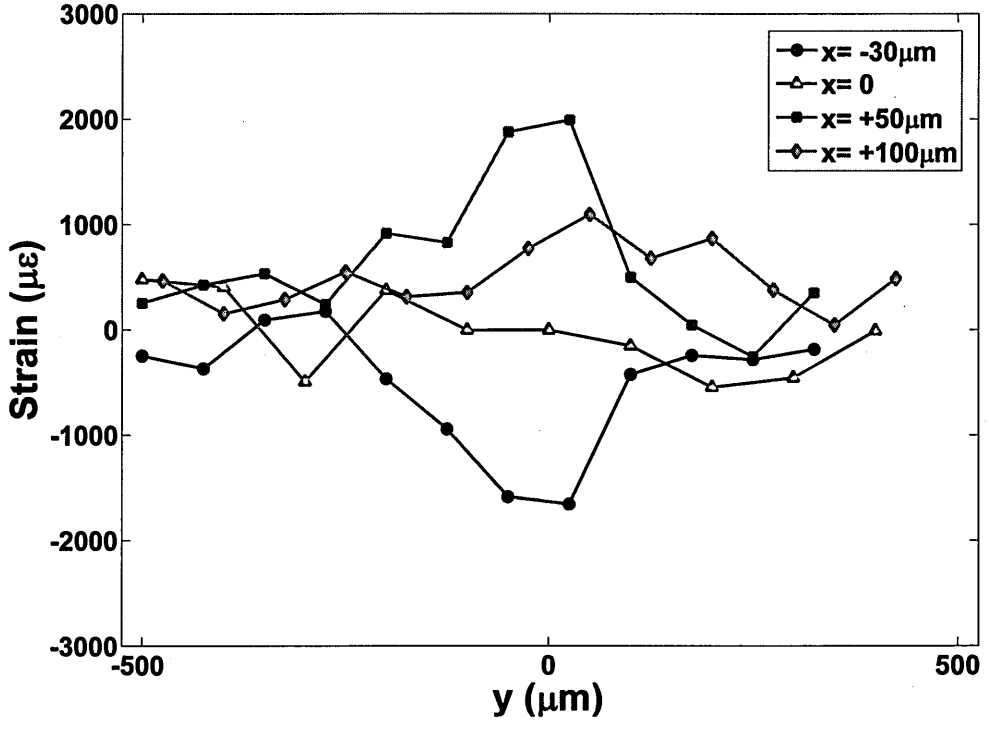

Fig. 7.10 - Strain profile of transverse component through scribe for sample 3.

So it was revealed that for sample 3, a high tensile residual strain field around scribe root was present in which tensile residual strain reached as high as 2000 με. The tensile field was present up to 100 μm ahead of the scribe root and to balance the tensile residual strain compressive residual strains were present behind the scribe root.

7.3.1.4 Sample 4

For sample 4, coarse scanning was not carried out as low strains were expected in view of the larger root radius. Scanning with a fine pitch was carried out in the x-direction at different y-locations. Fig.7.11 shows the strain profiles for these measurements. It was discovered that for this scribe, very low values of ε_{yy} were obtained even just below the scribe root. A maximum value of +300 με was measured. With this information in hand, sample was not aligned to measure ε_{xx} and it was expected that this component of the strains would be very less.

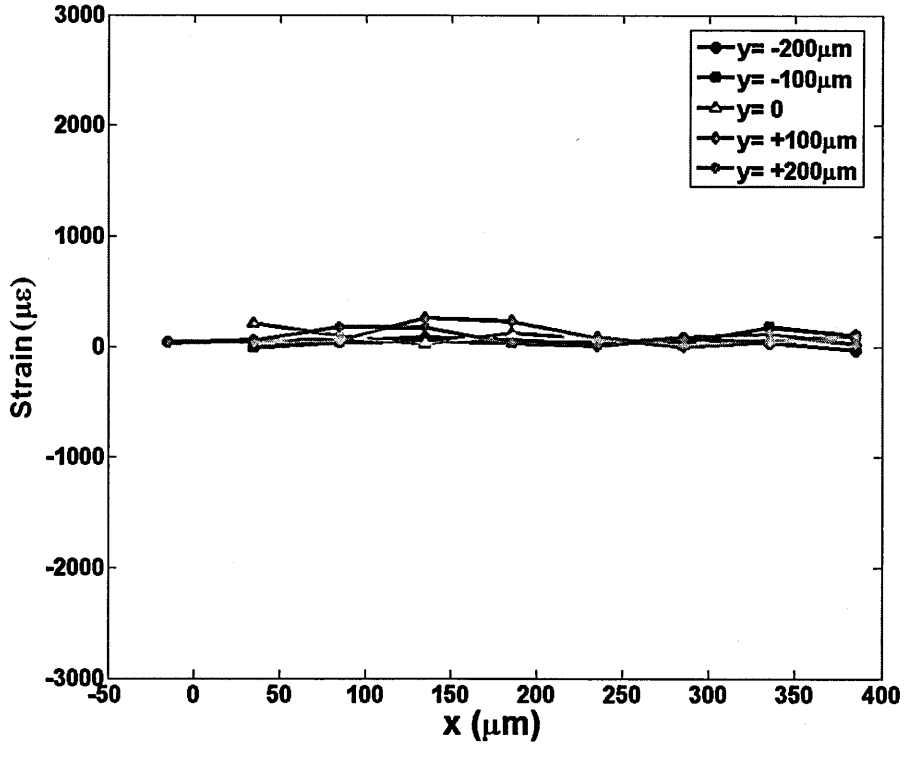

Fig. 7.11 - Strain profile of transverse component through scribe for sample 4.

The only difference in sample 4 was the larger root radius as compared to sample 1 and 2. It was found that an increase in root radius significantly decreases the residual strains around root.

7.3.2 Stress Analysis

Elastic stress-strain relations can be written as,

$$\sigma_{xx} = \frac{E}{(1+\nu)(1-2\nu)}\left[(1-\nu)\varepsilon_{xx} + \nu\varepsilon_{yy} + \nu\varepsilon_{zz}\right] \quad (7.1)$$

$$\sigma_{yy} = \frac{E}{(1+\nu)(1-2\nu)}\left[(1-\nu)\varepsilon_{yy} + \nu\varepsilon_{xx} + \nu\varepsilon_{zz}\right] \quad (7.2)$$

$$\sigma_{zz} = \frac{E}{(1+\nu)(1-2\nu)}\left[(1-\nu)\varepsilon_{zz} + \nu\varepsilon_{xx} + \nu\varepsilon_{yy}\right] \quad (7.3)$$

In many structural problems, stress analysis can be simplified with possible assumption of plane stress or plane strain condition. For all scribes, plate thickness was considerably less as compared to the lateral dimensions of the plate. So a plane stress condition could be assumed in which all the stresses parallel to the thickness direction could be assumed as zero. On the other hand the scribe itself was a long scratch as compared to its other two directions i.e. thickness and width of the sample. So a plane strain condition could be assumed in which all of the strains parallel to the scribe length could be considered as zero. Each condition was considered one by one and the viability of each condition was assessed.

7.3.2.1 Plane Strain Condition

If a plane strain condition around the scribe is assumed then the strain component in the z-direction can be assumed to be zero. i.e.

$$\varepsilon_{zz} = 0$$

So elastic stress-strain relation for stress component in z-direction can be written as,

$$\sigma_{xx} = \frac{E}{(1+\nu)(1-2\nu)}\left[(1-\nu)\varepsilon_{xx} + \nu\varepsilon_{yy}\right] \quad (7.4)$$

$$\sigma_{yy} = \frac{E}{(1+\nu)(1-2\nu)}\left[(1-\nu)\varepsilon_{yy} + \nu\varepsilon_{xx}\right] \quad (7.5)$$

$$\sigma_{zz} = \frac{E}{(1+\nu)(1-2\nu)}\left[\nu\varepsilon_{xx} + \nu\varepsilon_{yy}\right] \quad (7.6)$$

So equations (7.4), (7.5) and (7.6) were used to obtain the stress components of stress around scribe marks.

Sample 1

Fig.7.12. shows all three stress components obtained from plane strain condition for sample 1. It can be seen that σ_{yy} was the highest all of the stress components in which the peak tensile residual stress was below the scribe root. The peak value was +180MPa and it decreased as the distance from the scribe root increased in +x- direction. Behind the scribe root most of the region was under compressive residual stress. σ_{xx} and σ_{zz} were similar to each other but about half of the value of σ_{yy}. Peak tensile residual stress for these components was +100MPa below the scribe root. Here as well, behind the scribe root most of the region was under compressive residual stress.

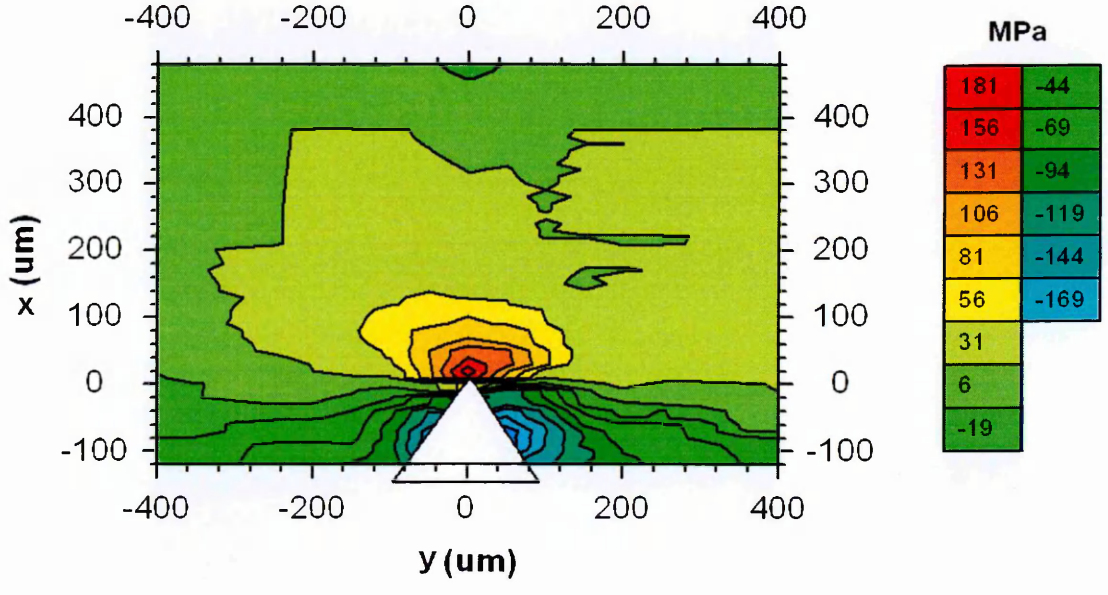

(a)

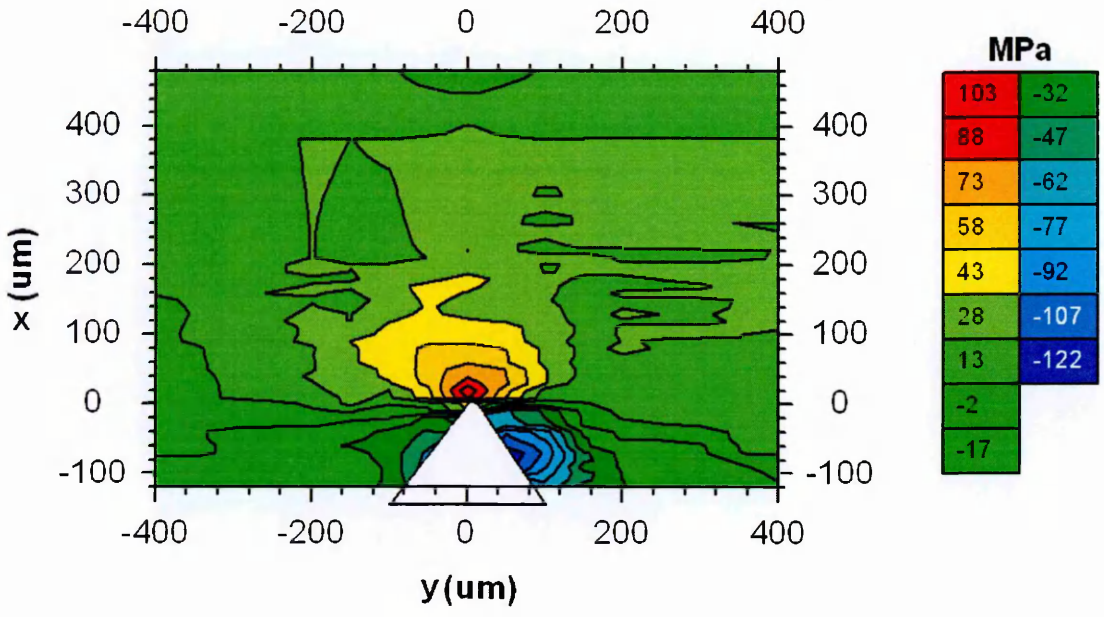

(b)

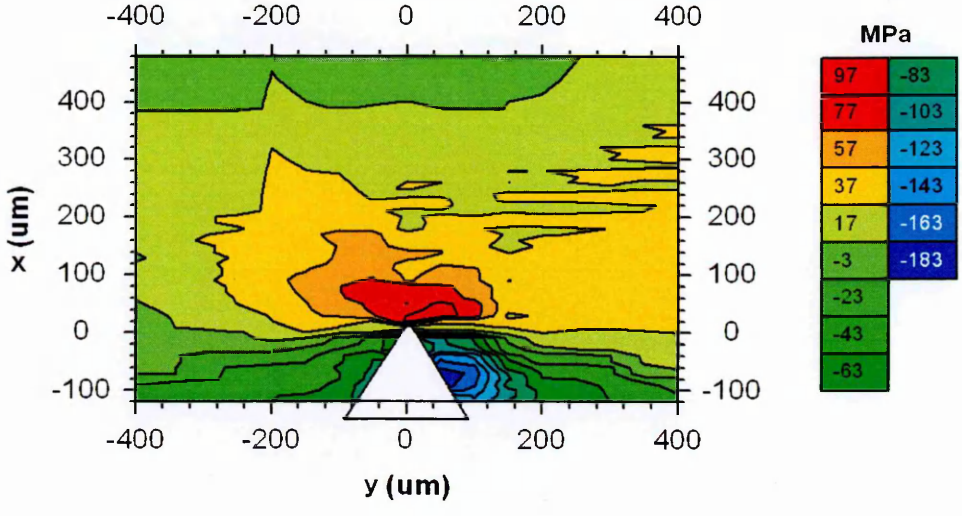

(c)

Fig. 7.12 - Stress profile for sample 1 (a) Transverse component (b) Longitudinal component (c) Normal component

Sample 2

Fig.7.13 shows all three stress components obtained using the plane strain condition for sample 2. It can be seen that σ_{yy} was the highest in all of the stress components. The peak tensile residual stress was again just below the scribe root. The peak value was +100MPa. The region behind the scribe root was under low compressive residual stress. σ_{xx} and σ_{zz}

were similar but less than σ_{yy}. In fact these two components were almost half of σ_{yy}. The peak tensile residual stress was +60MPa just below the scribe root for these components. The peak stress started to decrease with distance from the scribe root. This showed that tool B produced a stress field in sample 2 with every component of the stress half than that tool A produced in sample 1. Not only the stress components but the extent of the stress field ahead of scribe root in x-direction was about half as compared to sample 1.

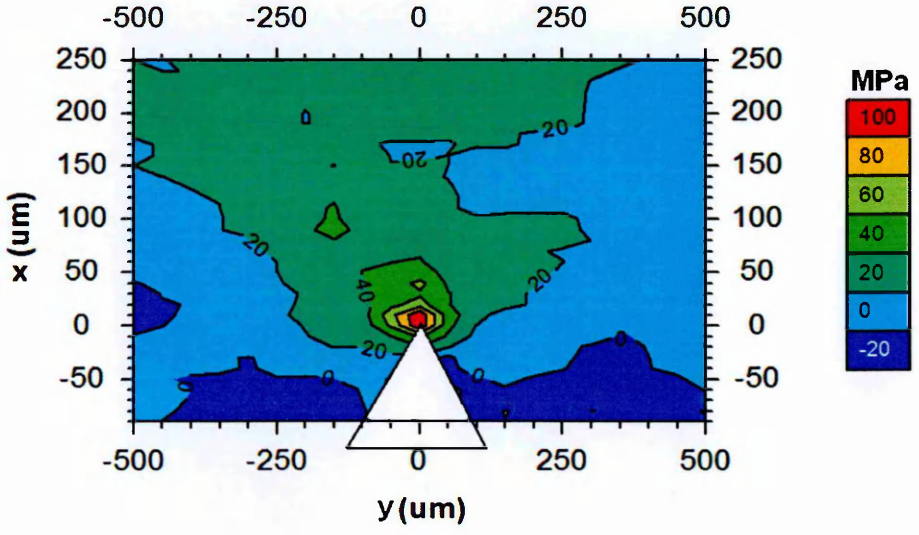

(a)

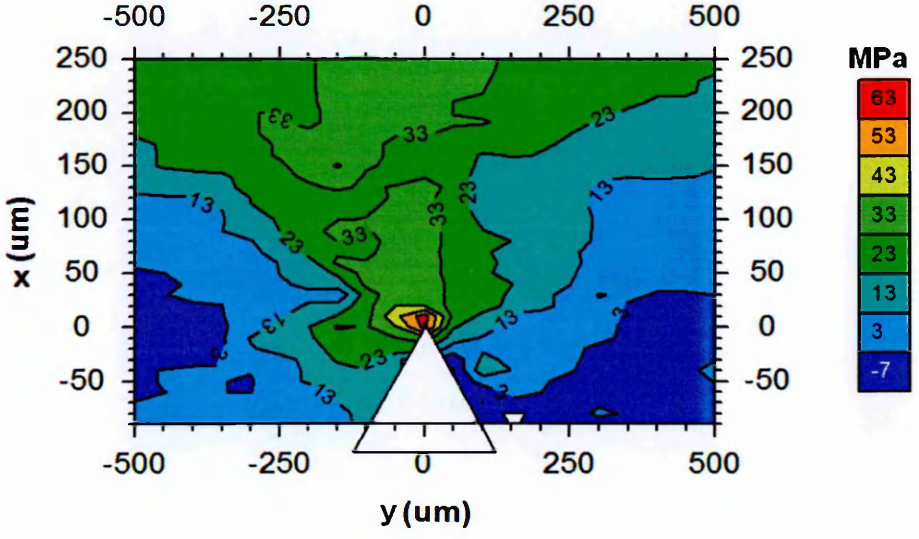

(b)

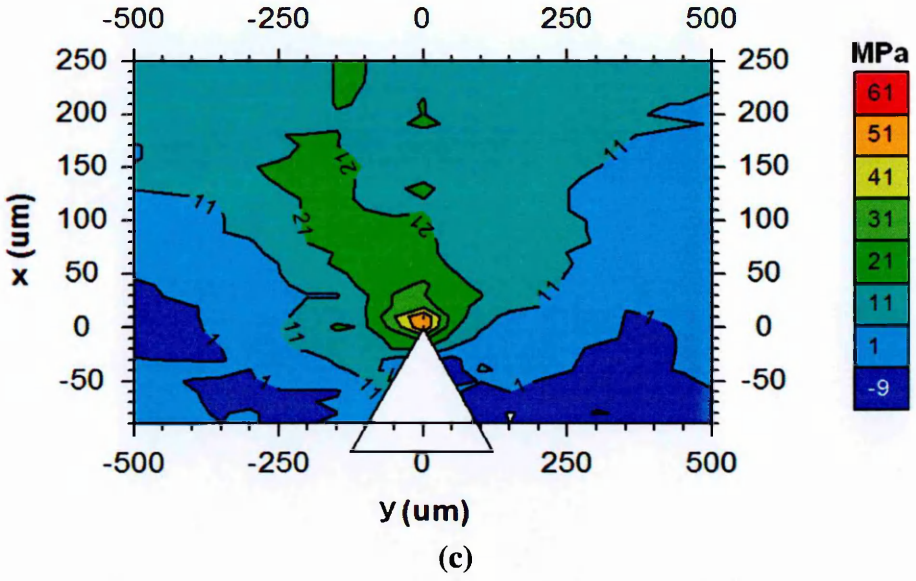

(c)

Fig. 7.13 - Stress profile for sample 2 (a) Transverse component (b) Longitudinal component (c) Normal component

Sample 3

This sample was almost the same as sample 1 but it was produced in Al 2024-T351 and the scribe depth was slightly less. Information in a very small area in +x-direction was obtained, additionally only transverse component of the strain was calculated hence stress analysis was not possible here. It was clear that a very similar transverse strain component was found here as was obtained for sample 1 so it can be said that this scribe would show a similar stress field as sample 1 but it requires further measurement of longitudinal component of the strain.

Sample 4

As in sample 3, due to limitation of beamtime, only transverse component was measured hence stress analysis was not possible here. The most important result is that the transverse strain component was very low as compared to the 5 μm root radius and on measurement longitudinal component would show very low strain. This would result in very nominal stress profiles.

7.3.2.2 Plane Stress

Another possible assumption which can be made here is plane stress condition. As measurements were carried out very near to the surface and on top of that thickness of plate was small as compared to the lateral dimensions of the plate, so all the stresses parallel to the thickness direction can be assumed as zero. i.e.

$\sigma_{xx} = 0$

So eq. (7.1) can be written as,

$$0 = \frac{E}{(1+\nu)(1-2\nu)}\left[(1-\nu)\varepsilon_{xx} + \nu\varepsilon_{yy} + \nu\varepsilon_{zz}\right]$$

or,

$$\varepsilon_{zz} = -\frac{1}{\nu}\left[(1-\nu)\varepsilon_{xx} + \nu\varepsilon_{yy}\right] \qquad (7.7)$$

With the measured ε_{xx} and ε_{yy} for every scribe, eq. (7.7) can be used to extract ε_{zz}. Then based on eq. (7.2) and (7.3) σ_{yy} and σ_{zz} can be obtained.

Sample 1

Fig.7.14 shows σ_{yy} and σ_{zz} obtained using the plane stress condition for sample 1. For σ_{yy}, plane stress condition showed lower peak stress values as compared to the plane strain assumption. The distribution and extent of the stress field was very similar as obtained from plane strain condition but the peak values of the stress were less. Peak tensile residual stress for this component reached a maximum value of +80MPa below the scribe root. It decreased with distance from the scribe root and reached +20MPa at 100 μm in both the +x-direction and y-direction. Behind the scribe root most of the region was under compressive residual stress. For σ_{zz}, below scribe root, instead of tensile residual stress, compressive residual stress was obtained which was unusual. Compressive residual

stress of -125MPa was found below scribe root. The region of the compressive stresses was large and high compressive residual stresses of -65MPa were present in an area of 200 μm x 200 μm around scribe root.

This analysis showed that plane stress condition produced a very conservative stress field for σ_{yy} and qualitatively opposite for σ_{zz}. This could be attributed to ignoring the crack propagating component of the stress i.e σ_{xx} which was assumed zero in plane stress condition. For most of the engineering problems on thin plates, the assumption of plane stress condition works very well but here these scribes had very small and local residual stress field which in most of the scribes was up to 200 μm along x-axis. This 200 μm is a very small portion of the all over 2mm thickness of the plate and it can be assumed that stresses in the x-direction may occur. And indeed from plane strain assumption it was discovered that there were significant residual stresses present in the x-direction as shown in Fig.7.12 (a) and hence $\sigma_{xx} = 0$ is not a viable condition to assume.

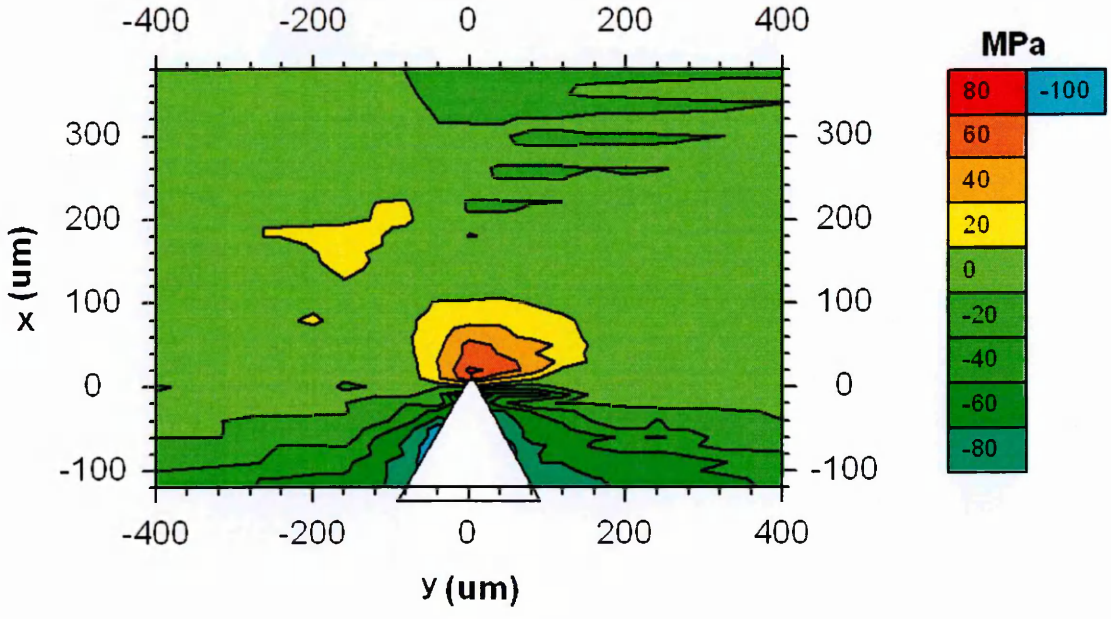

(a)

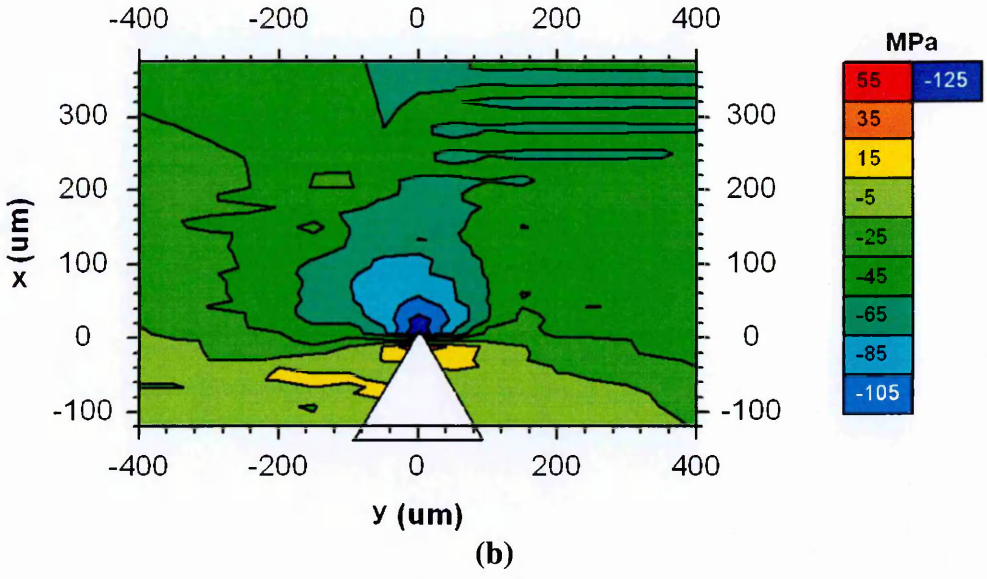

(b)

Fig. 7.14 - Stress profile for sample 1
(a) Transverse component (b) Longitudinal component

Sample 2

Fig.7.15 shows σ_{yy} and σ_{zz} obtained using the plane stress condition for sample 2. Here again σ_{yy} obtained showed a lower peak tensile stress value. The distribution and extent of the stress field was very similar as obtained from the plane strain condition but quantitatively peak values for stress were less. The peak tensile stress for σ_{yy} reached to a maximum value of only +45MPa below the scribe root. For σ_{xx}, below the scribe root, instead of tensile residual stress, compressive residual stress was obtained. A compressive residual stress of -70MPa was found below scribe root.

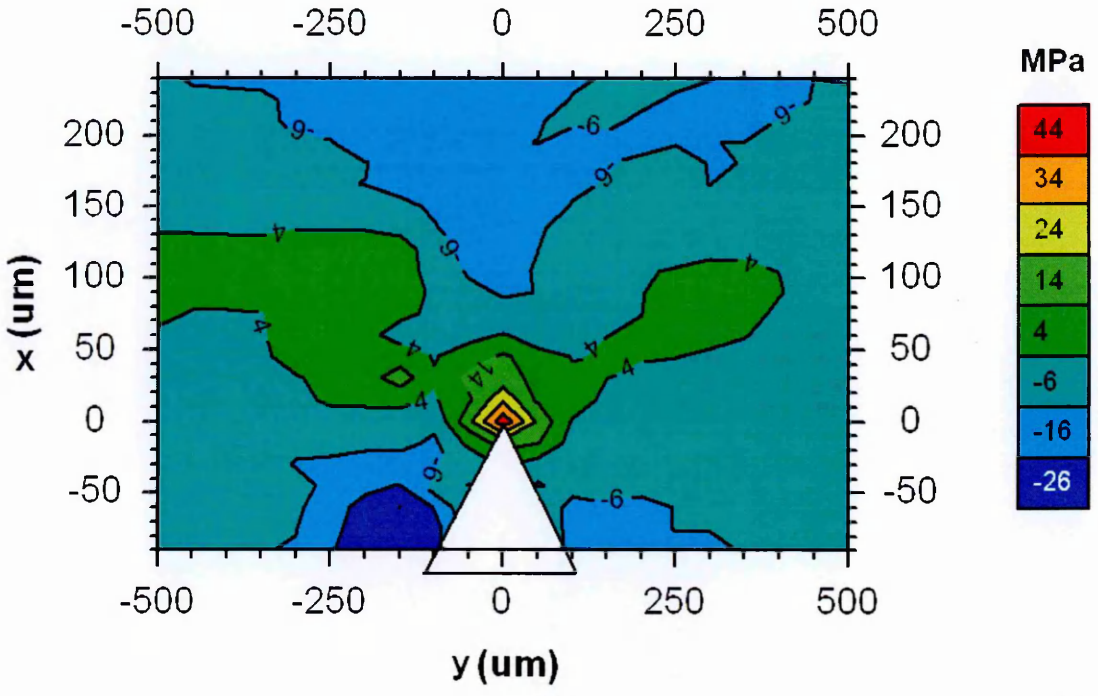

(a)

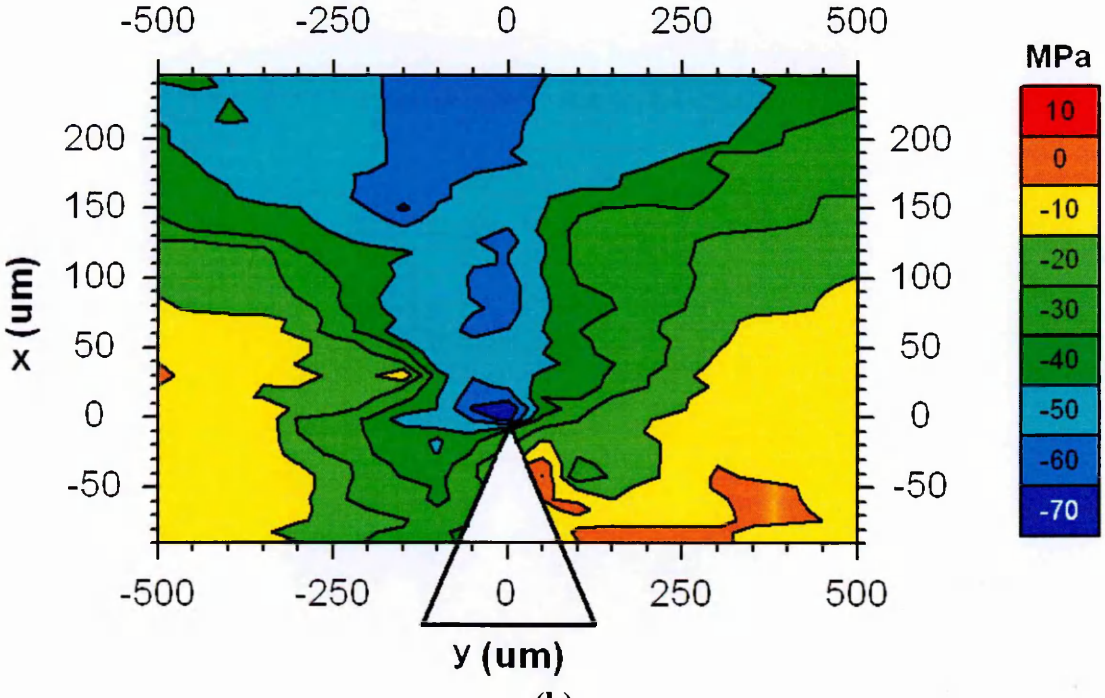

(b)

Fig. 7.15 - Stress profile for sample 2
(a) Transverse component (b) Longitudinal component

For sample 3 and 4 similar conditions were obtained for σ_{yy} and σ_{zz} so results for these scribes from plane stress conditions are not reported here. It was concluded that the plane stress assumption is not viable for assessment of residual stress field around these scribes

and hence the plane strain assumption provides best estimate of stresses around scribe marks.

7.3.3 Peak Width Analysis

Different stress profiles obtained from the different tools showed that the tools which were used to produce the scribes are different and produce different stress field around scribes. With the different behaviour of these tools it was anticipated that there would be a different level of work hardening and local plasticity present around scribe roots. This information could be obtained from the diffraction peaks obtained.

In peak width analysis peaks obtained from diffraction are fitted with a Gaussian profile, and for every peak its characteristic width is calculated. The width of the diffraction peak is directly related to the density of dislocations due to work hardening in the process of producing the scribes. Regions of heavy deformation reflect considerably broad diffraction peaks.

The full width at half maximum (FWHM) is a parameter commonly used to describe the width of a curve or function. It can be calculated by the distance between points on the curve at which the function reaches half its maximum value. A Gaussian profile can be described by the function,

$$f(x) = \frac{1}{\sigma\sqrt{2\pi}} e^{\frac{-(x-x_0)^2}{2\sigma^2}}$$

Where σ is the standard deviation and x_0 can be any value (the width of the function does not depend on translation). The relationship between FWHM and the standard deviation is,

$$\text{FWHM} = 2\sqrt{2\ln 2}\,\sigma$$

So if the standard deviation of the curve is known then the FWHM for every peak can be obtained.

FWHM profiles for peaks were calculated for all of the scribes as shown in Fig.7.16. FWHM for aluminium alloy 5091 for most of the peaks was around 10 x 10^{-3} while for 2024-T351 it was 15 x 10^{-3}. The difference in FWHM values for these two materials was most likely due to the grain size of the materials. Whenever there was work hardening or a hard region was encountered, the FWHM increased from this number.

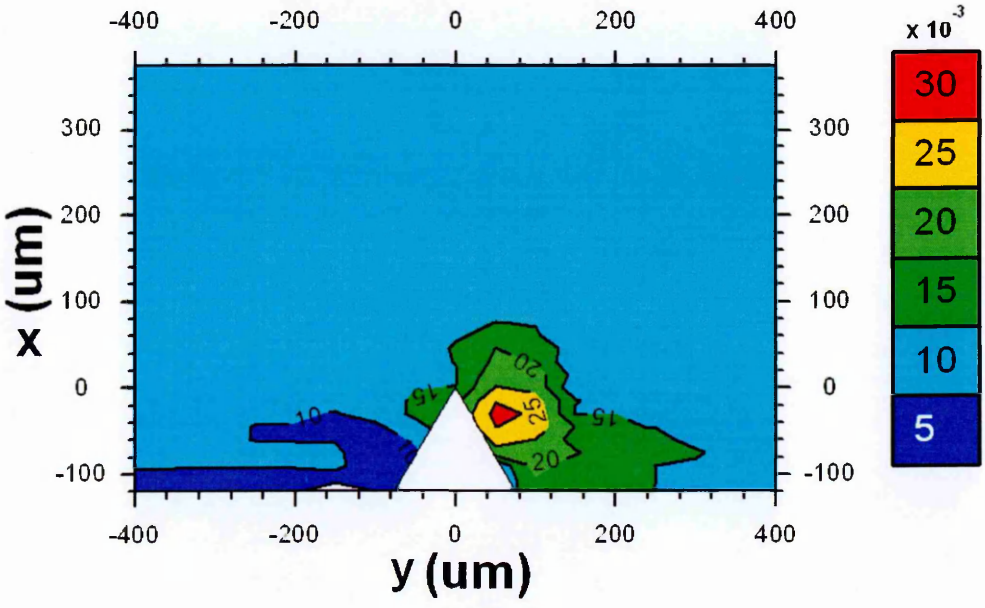

(a)

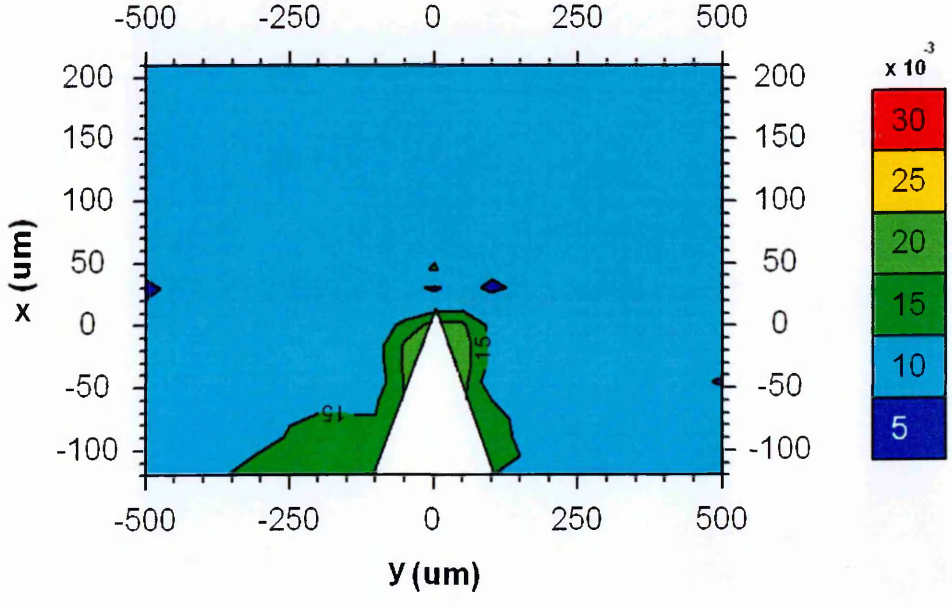

(b)

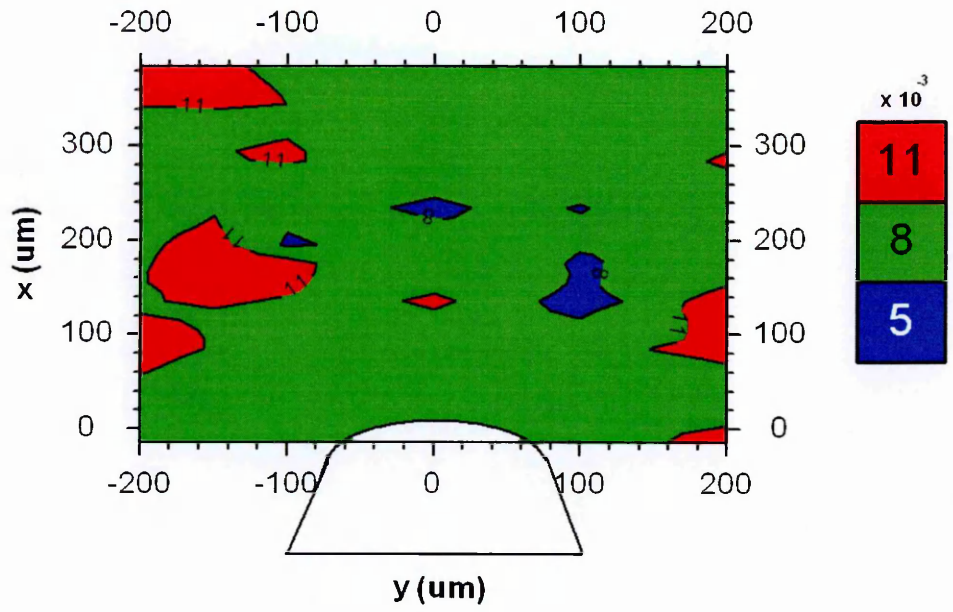

(d)

Fig. 7.16 - FWHM profiles for (a) Sample 1 (b) Sample 2 (c) Sample 4

Sample 1

For sample1, as shown in Fig.7.16 (a), a heavily deformed region was observed around scribe root. Very wide peaks were obtained for these regions. FWHM in these regions increased significantly and reached a maximum of 30 x 10^{-3}. Regions close to the scribe root showed higher values of FWHM as compare to regions far from scribe root. This revealed that during scribing material removed was ploughed around the scribe root. This plastically deformed region was higher in strength as compared to regions far from the scribe root and larger values for FWHM were obtained. Another interesting aspect was the non-symmetric FWHM profiles around root and it was observed that highest value of FWHM was not below the scribe root. Although there was an increase in FWHM below root as well, it increased more under the irregular feature. The area of the highest deformation was 50 μm away from the scribe root in x-direction and towards the region

behind scratch root in y-direction as shown in Fig.7.16 (a). This was the irregular profile which was present for sample 1 that has been discussed in earlier sections.

Because FWHM gives just a number in terms of increase in width of peak and does not provide any qualitative information so nanoindentation was used to obtain hardness profile around scribe to study the increase in hardness of these deformed regions around scribe root. Fig.7.17 (a) shows the hardness profile obtained for this scribe from nanoindentation and it can be seen that the hardness increased from 1.9 GPa to 2.15 GPa below scribe root.

Sample 2

For the scribe produced from tool B (Fig.7.16 (b)), the FWHM around the scribe root remained the same but a small increase was obtained behind scribe root in –x-direction in which FWHM increased to 15 x 10^{-3}. This revealed that during scribing with tool B material which was removed was not deposited around the scribe root but had been cut away. To confirm the absence of a hard plastically deformed region, nanoindentation was used to obtain the hardness profile around scribe. Fig.7.17 (b) shows the hardness distribution for sample 2 and it can be seen that no such increase in hardness was there around scribe root and the entire region had almost same hardness of 1.9 GPa.

Sample 3

Diffraction data for this sample was obtained in a very small region hence like stress analysis, FWHM for this sample was not calculated. Nanoindentation was used to obtain the hardness profile around the scribe. Fig.7.17 (c) shows the hardness profile obtained for this scribe from nanoindentation and it can be seen that hardness below the scribe root increased significantly from 1.9GPa to 2.3GPa. Scribe root was surrounded by this hard plastically deformed region which was spread 100μm ahead and sideways of scribe root as was obtained for sample 1.

Sample 4

Fig.7.16 (c) shows the FWHM distribution for sample 4 and it can be seen that no such increase in FWHM was obtained near the scribe root. To confirm absence of hard plastically region, nanoindentation was used. Fig.7.17 (d) shows hardness profile obtained for this scribe from nanoindentation and it can be seen that a very small hard patch was present above the scribe root which could be due to the very small work hardening, the presence of a hard particle above the root of scribe, but nothing was conclusively clear.

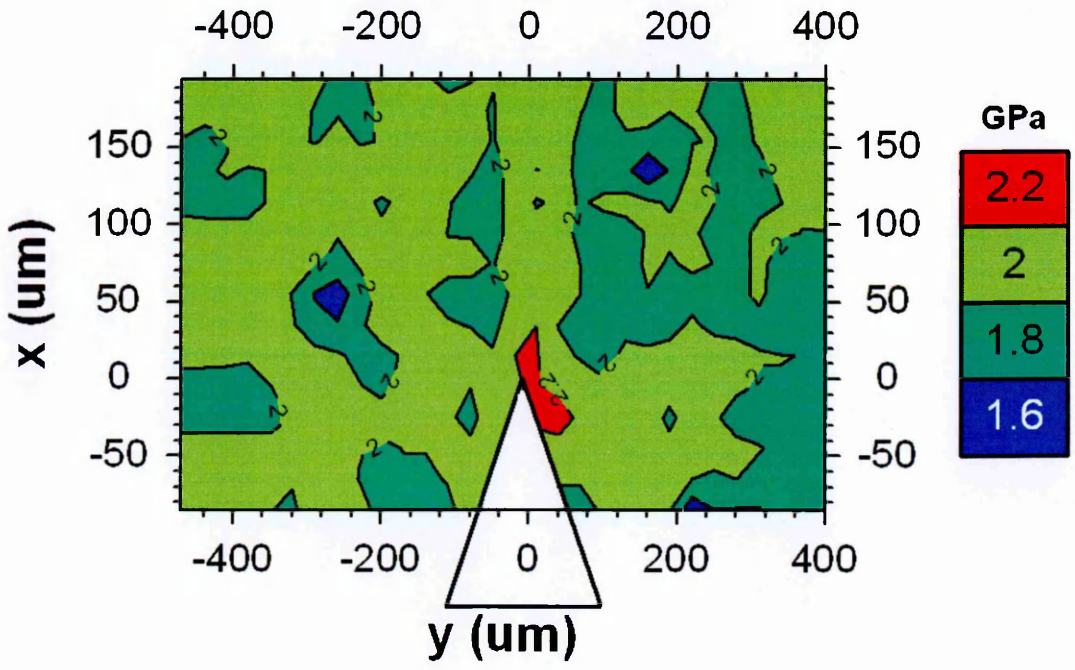

(a)

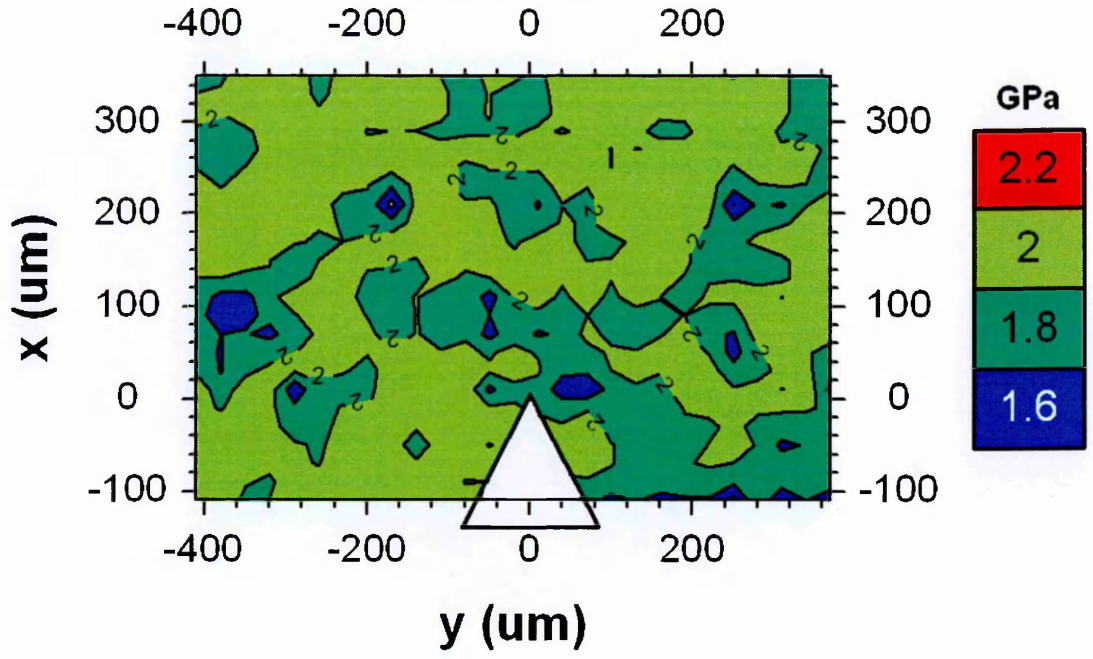
-400
-200
0
200
300
200
100
0
-100
x (um)
y (um)
GPa
2.2
2
1.8
1.6

(b)

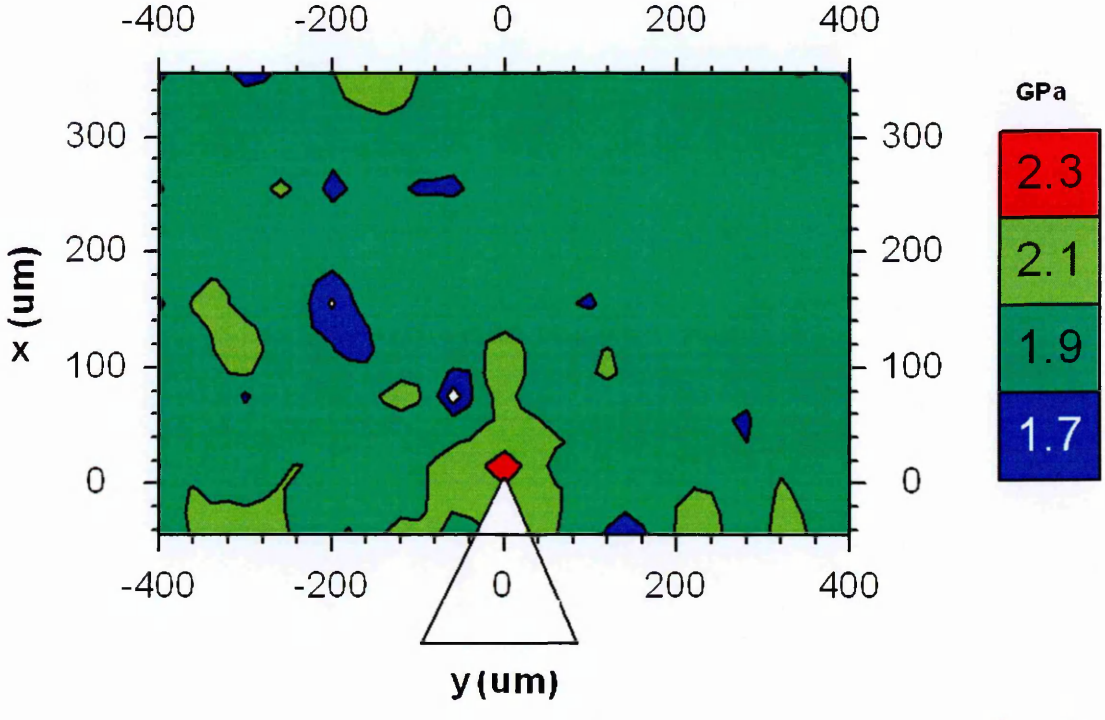
-400
-200
0
200
400
300
200
100
0
x (um)
y (um)
GPa
2.3
2.1
1.9
1.7

(c)

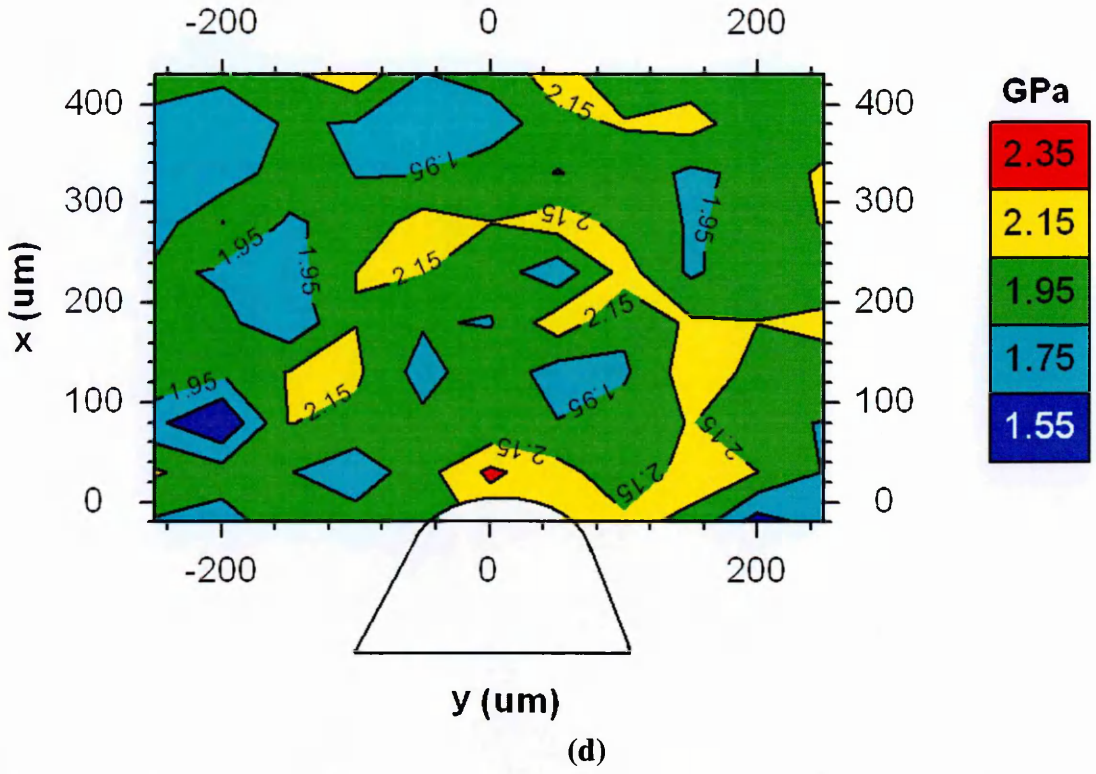

(d)

Fig. 7.17 - Hardness profiles for (a) Sample 1 (b) Sample 2 (c) Sample 3 (d) Sample 4

7.4. Discussion

7.4.1. Relation between Components of Strain & Stress

Strain and stress field around scribe marks of different depth and root radius produced from different tools in aluminium alloy 5091 and 2024-T351 have been presented and discussed. In total the strain fields for four scribe marks were measured at ID31 of ESRF, France. Two components of the strain i.e. ε_{xx} and ε_{yy} were measured. It was learnt that for all scribes, the strain component in the crack opening direction ε_{yy} was high as compared to the strain component in the crack propagation direction ε_{xx}.

For sample 1, peak tensile stress of +200MPa was obtained for σ_{yy} and +100MPa for the other two components σ_{xx} and σ_{zz}. The extent of the tensile stress field was up to 100μm both in the +x-direction and either side of y-direction. For sample 2, another scribe with a similar geometry and material but produced from a different tool, peak tensile stress of +100MPa was obtained for σ_{yy} and +50MPa for σ_{xx}. It was clear that this tool created a residual stress field in which the stress components were almost half as compared to tool

A for sample 1. Not only the stress components were lower but the extent of the tensile stress field was half as compared to sample 1 and the stress field was confined in a region up to 50 μm in the +x-direction.

In sample 3, when the material was changed to aluminium alloy 2024-T351 from 5091 and the same tool A was used to produce scribe of slightly less depth than sample 1, it was revealed that changing material did not create any significant difference in strain profiles. Only one component of the strain was measured and hence stress field was not calculated but measured component showed almost same peak value of strain as showed in sample 1. The extent of the tensile strain was confined in a similar region of 100 μm ahead of the scribe root in the +x-direction and 200 μm on either side of the scribe root in the y-direction as in sample 1.

In sample 4, when the root radius of the scribe was changed to 50 μm from 5 μm in aluminium alloy 5091 it was observed that the strain field diminished significantly and only a nominal amount of strains were found ahead the scribe root.

These sets of results for first two scribes revealed that for all of the scribes, the crack opening component of the stress i.e. σ_{yy} is always greater than the other two components of the stress. Additionally, σ_{yy} was always found twice as large as σ_{xx} and σ_{zz} for all of the scribes.

$$\sigma_{yy} = 2\sigma_{xx} = 2\sigma_{yy}$$

7.4.2. Effect of Tool

When scribes of similar depth and root radius were produced from tool A and B, some differences were found for these scribes which are given below;

1- Tool A scribes were 10% greater in depth and width as compared to tool B scribes.

2- Scribe profile produced from tool A had irregular feature and this feature produced higher tensile stresses and hardening around the scribe root.

3- As discussed in chapter 4, attack angle of Tool A was 40° while for tool B it was 30° which created a wide profile for tool A scribes as compare to tool B.

This information reveals that these two tools are very different in terms of their ability to produce scribes, and consequently they generate different residual stress fields. To acquire a particular depth, tool A requires more force and speed and produced more severe tensile stress field as compared to tool B. Peters et al. [8-9] studied the pile-up around damage in titanium alloy produced by impact at different velocities and found that impact above 250m/s velocity produced pile-up and microcracking around damage and every velocity below than this never produced pile-up. Here tool A attacks differently on material in producing scribe and cuts the material which deposits around scribe root. This mechanism of removing material is termed as 'ploughing' in which not all of the material which was 'cut' was removed but most of the material was displaced around the edges of the scribe profile. FWHM analysis and nanoindentation hardness profiles for all scribes showed that there was significant work hardening around tool A. High tensile stresses are generated when scribes are produced from with this tool with peak tensile stress of +200MPa and the extent of the stress field goes up to 100μm in the +x-direction.

On the other hand, tool B cuts the material with a lower attack angle and the mechanism of removing material was different. To acquire a particular depth, it does not require as much of force as tool A. No ploughing was found for this tool and there was no evidence of displacement of the material, as confirmed from FWHM and nanoindentation hardness profiles. All of the material which was removed had been cut away and the mechanism of removing material was 'cutting'. Tensile stresses were found under scribe root for tool B scribes as well. However, strength and extent of the tensile stress components were half as compare to tool A stress field. Table 7.2 shows every component of the stress obtained for

first two scribes and it can be seen that effect of tool A for sample 1 is twice as compare to tool B for sample 2 i.e.

$$\sigma_A = 2\sigma_B$$

Sample #	Depth d (μm)	Root radius ρ (μm)	d/ρ	σ_{yy} (MPa)	σ_{xx} (MPa)	σ_{zz} (MPa)
1	125	5	25	+180	+100	+100
2	125	5	25	+100	+60	+60

Table 7.2 - Stress components obtained for all samples

7.4.3 Effect of Material

With very similar strain profiles obtained for sample 1 and 3 it was concluded that the behaviour of the tool for both of the materials was same. Although there was difference in the yield strength of these two aluminium alloys as shown in chapter 3, but the effect of the same tool on different alloys was the same. This evidence reflects that residual stress around these scribe marks are highly influenced by the tool and not affected by the material on which scribes were made.

7.4.4 Effect of Root Radius

Stress and strain profiles obtained for 5 μm and 50 μm root radius showed that there is significant difference in stress profiles for these two root radius scribes. Scribes in similar material and of same depth but different root radius showed that with increase in root radius, residual stress around scribe root decreased significantly. It was observed that

although relation between the stress components remained same i.e $\sigma_{yy} = 2\sigma_{xx} = 2\sigma_{zz}$ but the peak strains decrease significantly and it can be concluded that;

$$\sigma \alpha \frac{1}{\rho}$$

7.5 Conclusions

This chapter discusses strain and stress field associated with scribes of different geometries produced by different tools in different aluminium alloys. Strain fields were determined by synchrotron X-rays. It has been shown that the residual stress field around these marks is dependent upon the tool by which they were produced. Behaviour of the tool has been found to be the same on different aluminium alloys. It was concluded that tool A produces severe tensile stress field and work hardening around the root of the scribe as compared to tool B, and the magnitude and extent of the tool A residual stress field is twice that of tool B. With an increase in root radius of the scribe, this residual stress field vanishes and no effect of work hardening was obtained as well for larger root radius scribes.

All of the scribes which were tested were not loaded in fatigue. Knowledge of the initial residual stress distribution induced by scribing is not sufficient to evaluate the driving force for a crack to form and propagate. Although tool A initially exhibits high tensile stresses around the scribe root as compared to tool B, however that doesn't necessarily mean that tool A scribe would initiate and propagate earlier in fatigue loading as compare to tool B scribe. The initiation and propagation of crack from scribe marks depends upon the redistribution of these tensile stresses under fatigue loading[11]. The magnitude and rate of relaxation of residual stresses in fatigue strongly depends on the applied loading. Boyce et al. [12], focussing on relaxation of these residual stresses, concluded that the initial residual stress state around FOD can decay significantly in fatigue depending upon the applied stress. For Ti-6Al-4V, they obtained very little relaxation for $0.35\sigma_Y$ but for higher applied stress of $0.54\sigma_Y$ this relaxation reached to 50%. They observed that decay

of the residual stress state was only during the first cycle and subsequent cycle showed very little further relaxation. Hence for this reason it is recommended to determine residual stresses after first cycle of loading as most of the relaxation of residual stresses occurs in this stage.

7.6 References

[1] Walmsley S.W. Fatigue potential of tool scratches on clad 2024-T351 alumnium alloy. 2007, Cranfield University MSc. Thesis.

[2] Morency, R. Fatigue Crack Initiation and Growth from Scratches in 2024-T351 Aluminium. 2006, Cranfield University MSc Thesis.

[3] Dini, D., D. Nowell and I. N. Dyson. The use of notch and short crack approaches to fretting fatigue threshold prediction: Theory and experimental validation. 4th International Symposium on Fretting Fatique, 2004, Lyon, FRANCE, Elsevier Sci Ltd.

[4] Nowell, D., P. Duo, I. F. Stewart. Prediction of fatigue performance in gas turbine blades after foreign object damage. 4th International Conference on Fatigue Damage of Structural Materials, Hyannis, 2002, Massachusetts, Elsevier Sci Ltd.

[5] Ruschau, J. J., T. Nicholas and S. R. Thompson. Influence of foreign object damage (FOD) on the fatigue life of simulated Ti-6Al-4V airfoils. International Journal of Impact Engineering 25(3), 2001, pp 233-250.

[6] Oakley, S. Y. and D. Nowell. Prediction of the combined high- and low-cycle fatigue performance of gas turbine blades after foreign object damage." International Journal of Fatigue 29(1), 2007, pp 69-80.

[7] Thompson, S. R., J. J. Ruschau and T. Nicholas. Influence of residual stresses on high cycle fatigue strength of Ti-6Al-4V subjected to foreign object damage. 3rd International Conference on Fatigue Damage of Structural Materials, 2000, Hyannis, Massachusetts, Elsevier Sci Ltd.

[8] Peters, J. O., B. L. Boyce, Chen X, J. M. McNaney, J. W. Hutchinson and R. O Ritchie. On the application of the Kitagawa-Takahashi diagram to foreign-object damage and high-cycle fatigue. Engineering Fracture Mechanics 69(13), 2002, pp 1425-1446.

[9] Peters, J. O. and R. O. Ritchie. Foreign-object damage and high-cycle fatigue of Ti-6Al-4V. 12th Meeting of the International Conference on the Strength of Materials (ICSMA 12), 2000, Asilomar, California, Elsevier Science Sa.

[10] J. O. Peters, O. Roder, B. L. Boyce, A. W. Thompson and R. O. Ritchie. Role of foreign-object damage on thresholds for high-cycle fatigue in Ti-6Al-4V. Metallurgical and Materials Transactions a-Physical Metallurgy and Materials Science 31(6), 2000, pp 1571-1583.

[11] Boyce, B. L., X. Chen, J. W. Hutchinson and R. O. Ritchie. The residual stress state due to a spherical hard-body impact. Mechanics of Materials 33(8), 2001, pp 441-454.

[12] Boyce, B. L., X. Chen, J. O. Peters, J. W. Hutchinson and R. O. Ritchie. Mechanical relaxation of localized residual stresses associated with foreign object damage. Materials Science and Engineering a-Structural Materials Properties Microstructure and Processing 349(1-2), 2003, pp 48-58.

[13] Steuwer, A., L. Edwards, S. Pratihar, S. Ganguly, M. Peel, M. E. Fitzpatrick et al. In situ analysis of cracks in structural materials using synchrotron X-ray tomography and diffraction. Nuclear Instruments and Methods in Physics Research B 246, 2006, pp 217–225 .

[14] D. Richard, M. Ferrand and G.J. Kearley, J. Neutron Research 4, 33-39, 1996.

Large array manipulation program (LAMP), the Large Array Manipulation Program. http://www.ill.fr/data_treat/lamp/lamp.html.

[15] Croft, M., Z. Zhong, N. Jisrawi, I. Zakharchenko, R. L. Holtz, J. Skaritka, T. Fast et al. Strain profiling of fatigue crack overload effects using energy dispersive X-ray diffraction. International Journal of Fatigue 27, 2005, pp 1408–1419.

[16] Materials Handbook, Ninth Edition, Vol. 2, Properties and Selection: Nonferrous Alloys and Pure Metals. American Society for Metals, Metals Park, Ohio 44073.

[17] Determination of residual stresses by X-ray diffraction- Issue 2. Measurement Good Practice Guide No. 52, National Physical Laboratory, Teddington, Middlesex, UK, September 2005.

[18] B. Clausen, T. Lorentzen and T. Leffers. Self-consistent modelling of the plastic deformation of F.C.C. polycrystals and its implications for diffraction measurements of internal stresses, Acta Mater, 1998, Vol 46, pp 3087-3098.

Chapter 8: Determination of Residual Stress around Scribe Marks from Nanoindentation

8.1 Introduction

It has been shown in chapter 7 that the determination of residual stress around scribe marks using diffraction methods is challenging due to the fact that the grain size of Al 2024-T351 is large (20~100 μm) compared to the scale of the stress field, which prevents the use of the small gauge volume required for the measurement of a small and local residual stress field around scribes. Although a finite element based study has been carried out in chapter 6 showing that the response to equibiaxial stresses can be extracted based on the variation of maximum load of indentation or ratio of work of indentation, such variations in indentation response are also sensitive to any local plastic deformation.

Residual stresses around scribe marks are generated during scratching of the material. These stresses are only developed when the material is deformed plastically. It was discussed in chapter 4 that both 'cutting' and 'ploughing' deformations are possible and every tool introduces a different level of elastic residual stress. Whenever a technique like nanoindentation is applied around scribe marks, it measures the response of the elastic residual stress field and plastic deformation of the material. This means that the hardness information around scribe roots obtained in chapter 4 contains not only the effect of plastically deformed hard material but also of residual stresses.

This problem of the convoluted response of a hard plastically deformed material and tensile residual stresses requires separation for accurate calculation of residual stresses from nanoindentation response, and for this a comprehensive analytical model is required. In this study it has been assumed that any increase in hardness of the material around scribe root is only due to the plastic deformation. Based on this assumption, it can be said

that if the increase in hardness can be separated from the nanoindentation response around scribe, the rest of the response can be treated as response of elastic residual stresses.

Another approach to extract residual stresses could be the development of a finite element model of the production of these scribes. This could give the expected residual stress field generated due to the scribe formation and then nanoindentation response could be measured to verify the modelled residual stresses. As presented in chapter 4, even scribes of the same depth and root radius created by different tools (A and B) can be of different profiles, so the development of finite element modelling of 'cutting' and 'ploughed' scribes would require inclusion of tool profiles and geometry which will be computationally impractical. Hence in this study the methodology used in chapter 6 has been used to extract residual stresses with some assumptions which are discussed in detail.

Indentation load-displacement curves are sensitive to residual stresses. Compared to a stress-free region, the path of the loading curve shifts up and consequently shows higher slope for compressive stresses, while the loading curve shifts down and shows a lower slope for tensile residual stresses. To attain a particular indentation depth the maximum load of indentation P_{max} increases for compressive residual stress and decreases for tensile residual stress [3-13]. It was shown in chapter 6 that the indentation maximum load P_{max} changes twice as much for an equi-biaxial stress state ($\sigma_{xx} = \sigma_{yy} \neq 0$) as compared to an equivalent uniaxial stress state($\sigma_{xx} \neq 0, \sigma_{yy} = 0$) whilst a pure shear stress state $(\sigma_{xx} = -\sigma_{yy} \neq 0)$ does not produce any change in P_{max}. For the pure shear stress state, the increase in indentation maximum load P_{max} for compressive stress in one axis negates the load decrease for tensile stress on the orthogonal axis [9]. This means that whenever a stressed region is indented, both components of in-plane stress play a part. The variation in load-displacement curves is sensitive to the individual components but the overall response is not unique and gives a response dependent upon the overall resultant residual stress state.

In chapter 7, measurements from synchrotron X-ray diffraction were carried out exactly at the centre of the scratch, where a plane strain condition was assumed. It was found that the stress field around the scribe marks in that region was not equi-biaxial and in fact the crack opening component of the stress σ_{yy} was twice the crack propagating σ_{xx} and parallel to scribe σ_{zz} components of the stress.

For nanoindentation, the measurements were carried around the cross-section of the scribe as shown in Fig.8.1, for which a plane strain condition cannot be assumed. Due to the very small indentation depth used in this study, i.e. 600nm, only the effect of σ_{xx} and σ_{yy} can be sampled by indentation. There are some techniques from which individual stress components can be extracted if the ratio of stress components $(\sigma_{yy}/\sigma_{xx})$ is known [7-9]. In this study, an equi-biaxial stress state was assumed around the scribe marks for extraction of residual stresses from nanoindentation. It was found that stresses obtained from nanoindentation method using this assumption are similar in magnitude to the component with highest component of the stress as measured by synchrotron X-rays diffraction.

This chapter discusses the application of nanoindentation for determination of residual stresses around scribe marks. Initially, all four scribes for which residual stress fields have been obtained from synchrotron X-rays were indented and a comparison of residual stresses from synchrotron X-rays and nanoindentation has been presented. Later in the chapter, residual stress fields around scribe marks of different geometries produced from different tools are presented. Scribes of 5μm, 25μm and 50μm root radii were nanoindentation tested before and after fatigue and the residual stress fields were measured. Before fatigue 15 scribes were tested, called 'virgin scribes' while 10 scribes were tested after fatigue. Two modes of fatigue loading were used; four point bending (FPB) and tension-tension. All together this chapter reports residual stress fields extracted from nanoindentation load-displacement curves for 29 scribes. Assumptions were made for

extraction of residual stresses for the scribes generated with significant work hardening. It was found that with these assumptions extracted residual stresses are similar in magnitude of the highest component of the stress as obtained from synchrotron X-rays results.

8.2 Materials, Samples and Experimental Details

8.2.1 Materials and Sample Details

Aluminium alloys 2024-T351 and 5091 were used, for which material properties have already been presented. Four samples were the same as used in the synchrotron X-ray diffraction experiments. Details of these samples have already been given in chapter 7. Further new scribes were tested for which synchrotron data was not available. These scribes of different root radii were produced in the same aluminium alloys Al 2024-T351 and 5091 with different tools. Details of these scribes are given later in this chapter in section 8.5.

8.2.2 Experimental Details

Nanoindentation was carried out to 600nm depth with the same experimental procedure as presented in earlier chapters. Indentations were made in an array around the scratch cross-section with 10μm spacing between the indentations. Load-displacement data was obtained for every indentation. Mapping of indentations was the same as discussed in chapter 4 and shown in Fig.4.3. Here Fig.8.1 shows the arrangement of indentations in greater detail. Indentation in a stress free region was carried out far from the scribe root and 10 indentations were carried out in this region to reduce any scatter in stress free load-displacement curve.

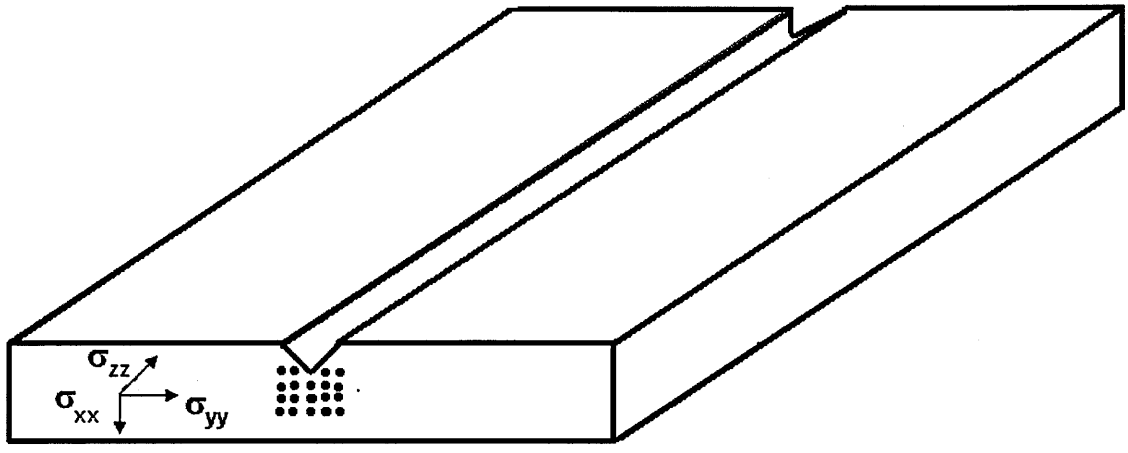

Fig. 8.1 – Schematic of indentation with marks showing indentation

8.3 Load-displacement Curve Analysis

8.3.1 Sample 1 (125 μm deep scribe from tool A)

Fig.8.2 shows nanoindentation load-displacement curves obtained for sample 1 at y=0, +15 μm and -15 μm. From synchrotron X-ray diffraction it was known that there were high tensile stresses of around 180MPa present around the scribe root. Based on this, in principle the loading curves for the near scribe root region should have shifted downwards, but it can be seen that at all values of y, not all of the loading curves were below the stress free loading curve and a mixed trend of loading curves above and below the stress free curve was observed. This was due to the hard plastically deformed region around the scribe root for tool A [14] as discussed in chapters 4 and 7. This harder region prevented the loading curves from moving down significantly and a convoluted response of increased hardness (loading curve moves up) and high tensile stresses (loading curve moves down) was obtained. Although, as discussed in chapter 6, the maximum load of indentation is directly related to the residual stresses, the presence of a hard deformed plastic region prevented this effect in the case of the tool A scribes. At some locations, the loading curve moved down which was a clear indication of tensile residual stresses but for most of the regions load-displacement curves showed a hardening response which was greater than the

response of the tensile residual stresses. This effect revealed that the dependence of P_{max} on the residual stresses may give misleading information in the presence of hard plastically deformed regions. Hence, another parameter such as C or W_p/W_t as discussed in chapter 6, should be used for extraction of residual stresses from the load-displacement curves around scribes, although these parameters are also affected by the increase in hardness. The detailed method for separation of this hardness increase from residual stresses will be discussed later in this chapter.

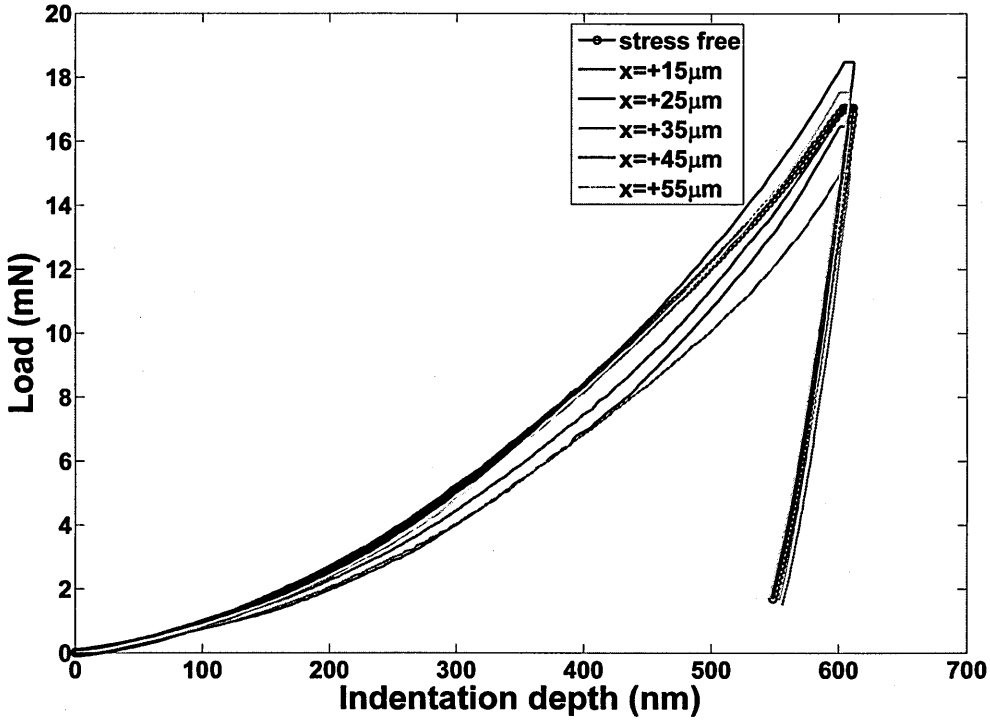

(a)

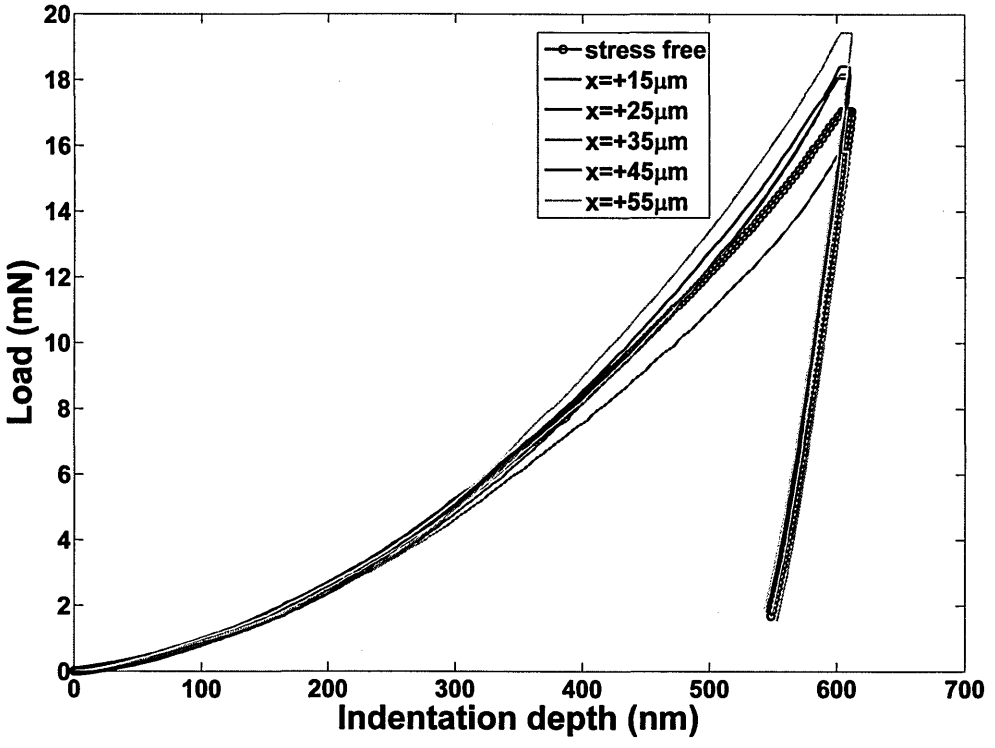

(b)

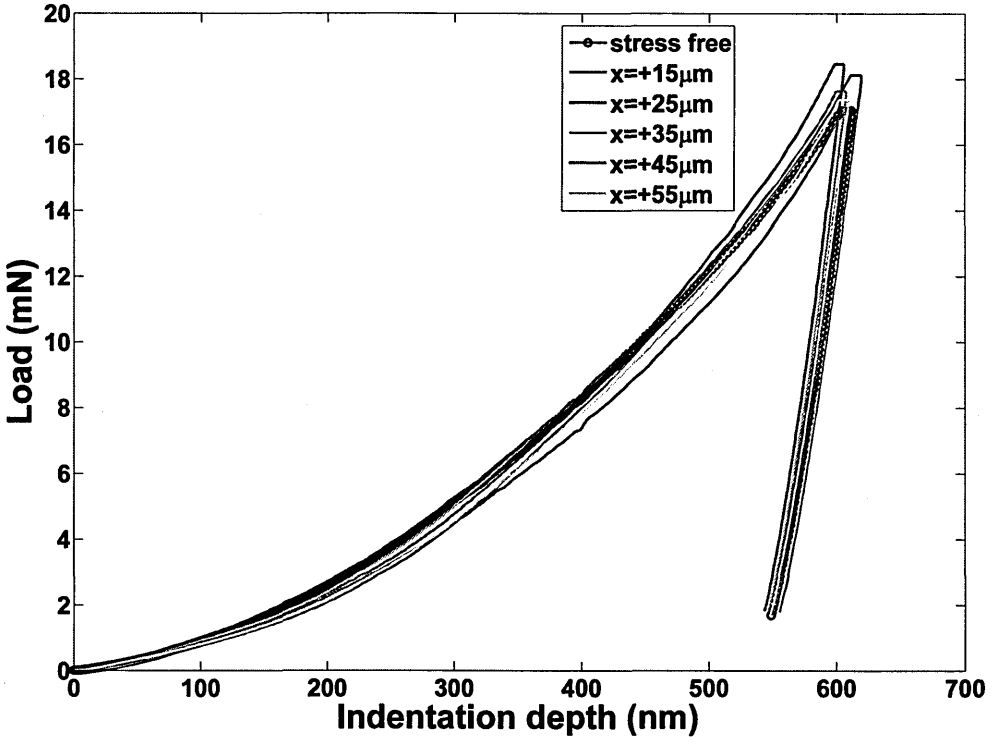

(c)

Fig. 8.2 - Nanoindentation load-displacement curve for sample 1 at (a) y=0 (b) y=+15 μm and (c) y=-15 μm

8.3.2 Sample 2 (125 µm deep scribe from tool B)

Fig.8.3 shows nanoindentation load-displacement curves obtained for sample 2 at y=0, +15 µm and -15 µm. It can be seen that for the near scribe root some of the loading curves obtained for y-locations were below the stress free loading curve. This was a clear indication that there were tensile residual stresses present below the scribe root in the +x-direction but the response was not that significant. This low difference from the stress free loading curve was due to the less severe tensile residual stresses for this scribe. From synchrotron X-ray diffraction it was already known that 100MPa of tensile residual stresses were present for this scribe which was almost half of the peak tensile residual stresses obtained for sample 1.

From the FWHM analysis for this scribe no high work hardening was seen around the scribe and all of the material which was removed during scribing was cut away. In the absence of any work hardening around the scribe root it was evident that all of the response from the variation in loading curve was due to residual stresses. It can be seen that the response of tensile stresses were not as much directly below the scribe root i.e. y=0 as compared to y=+15 µm and -15 µm. This could be attributed to low work hardening levels below the scribe root in a very local region where the magnitude and extent is not as high in the case of sample 1. At y=+15 µm and -15 µm the response of residual stress was easily visible with the loading curves for the near root regions moved down significantly. Altogether, the load-displacement curves successfully detected the presence of tensile residual stresses around the scribe root for this sample as compared to tool A in which some regions could not show tensile residual stresses in the highly deformed plastic regions.

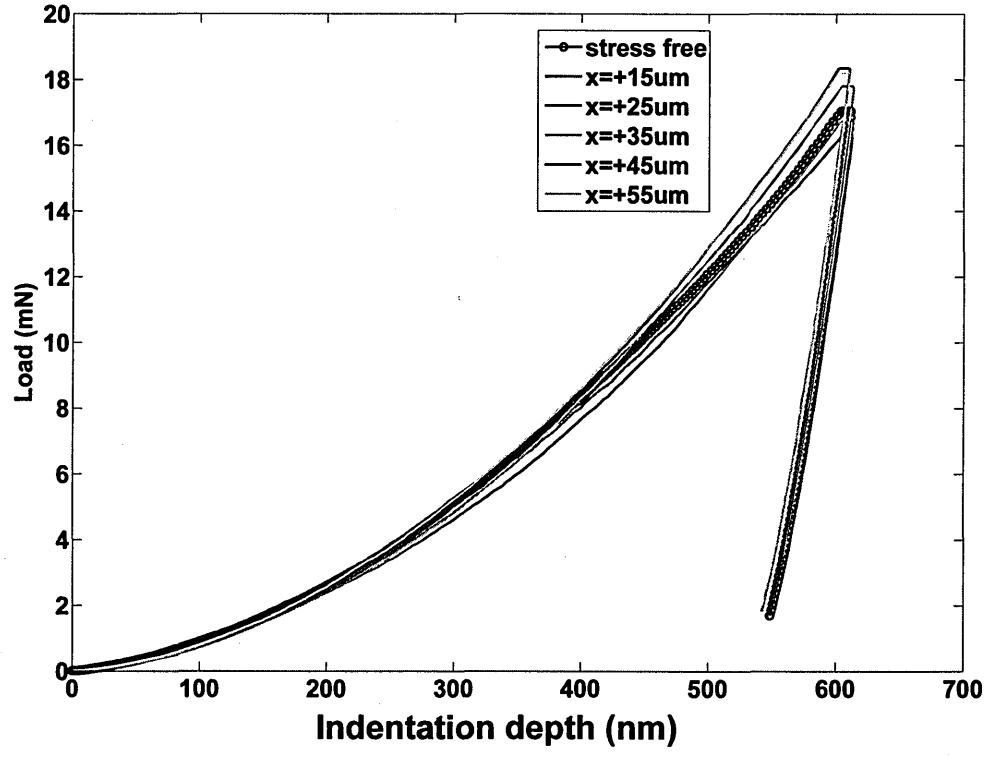
stress free
x=+15um
x=+25um
x=+35um
x=+45um
x=+55um
Load (mN)
Indentation depth (nm)
0
2
4
6
8
10
12
14
16
18
20
0
100
200
300
400
500
600
700

(a)

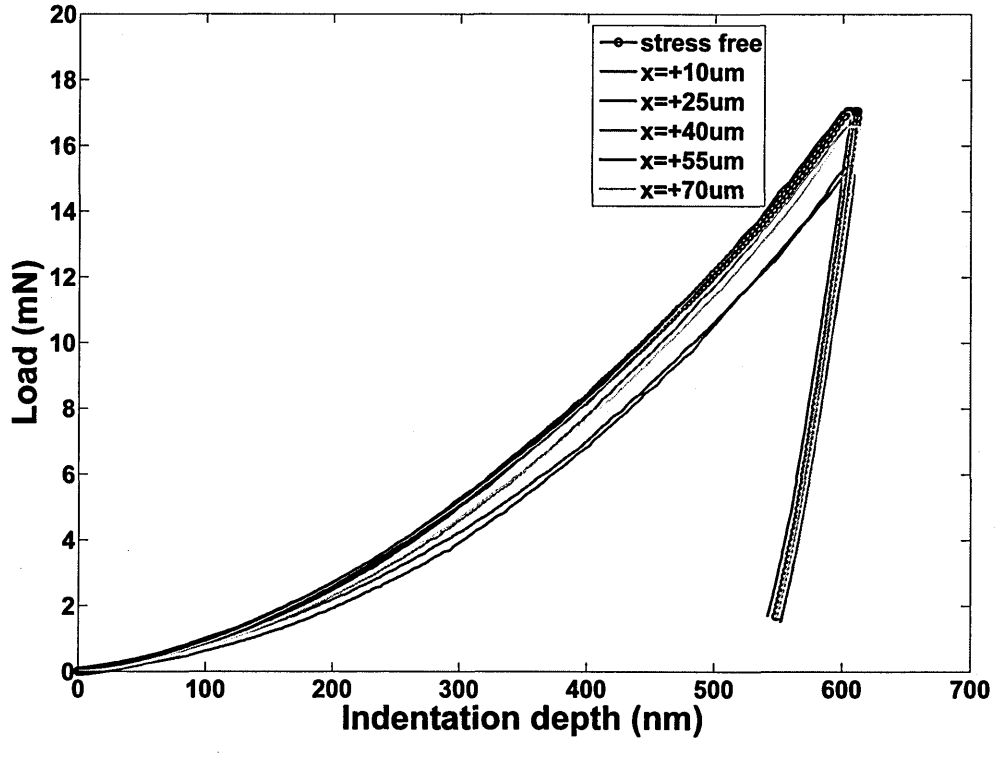
stress free
x=+10um
x=+25um
x=+40um
x=+55um
x=+70um
Load (mN)
Indentation depth (nm)
0
2
4
6
8
10
12
14
16
18
20
0
100
200
300
400
500
600
700

(b)

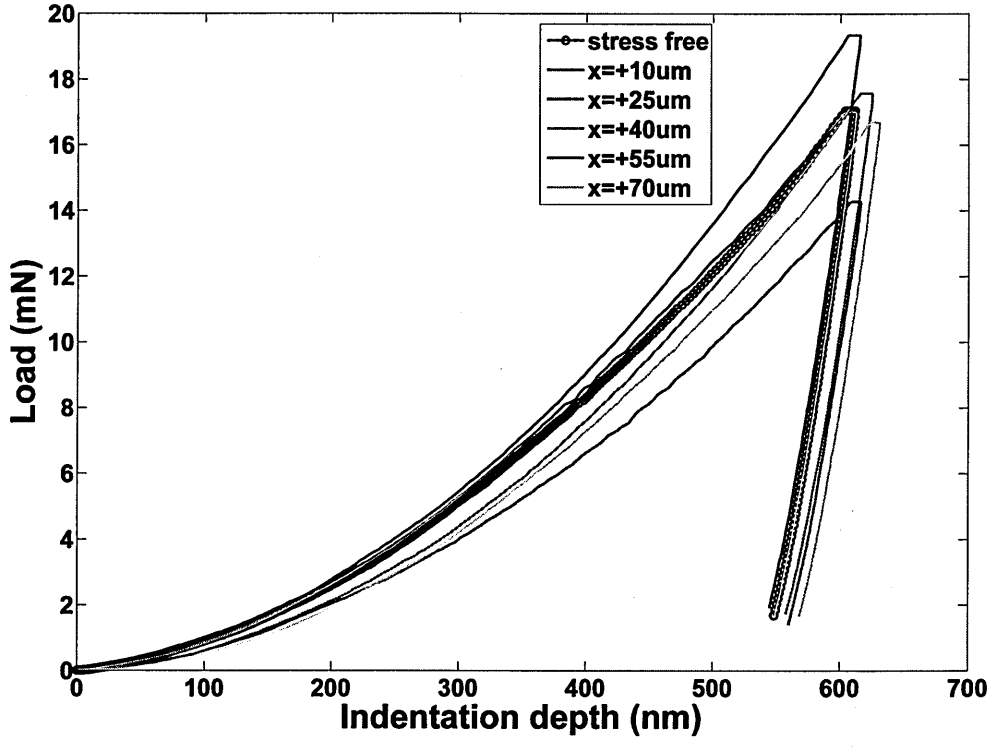

(c)

Fig. 8.3 - Nanoindentation load-displacement curve for sample 2 at (a) y=0 (b) y=+15 μm and (c) y=-15 μm

8.3.3 Sample 3 (100 μm deep scribe from tool A)

Fig.8.4 shows load-displacement curves obtained for sample 3 at y=0, +15 μm and -15 μm. It can be seen that at all locations, the loading curves were above or equivalent to the stress free loading curve. This scribe was created in Al 2024-T351 using tool A, which creates severe work hardening around the scribe root, and the indentation load-displacement curve showed again a cumulative effective response of hardening and tensile residual stresses. The hardening was so severe here that the load-displacement curve did not show any response of tensile residual stresses and all of the loading curves moved up and showed a response typical of a hard deformed material.

The response of the load-displacement curve is therefore misleading here as from the synchrotron X-ray diffraction results, high tensile strains of 2000 με were present around the scribe root. From the hardness map for this scribe, it was evident that the hard

deformed plastic region overcome the response of tensile residual stresses and to extract residual stresses from this load-displacement curves as discussed in section 8.3.2 another parameter such as W_p/W_t should be used.

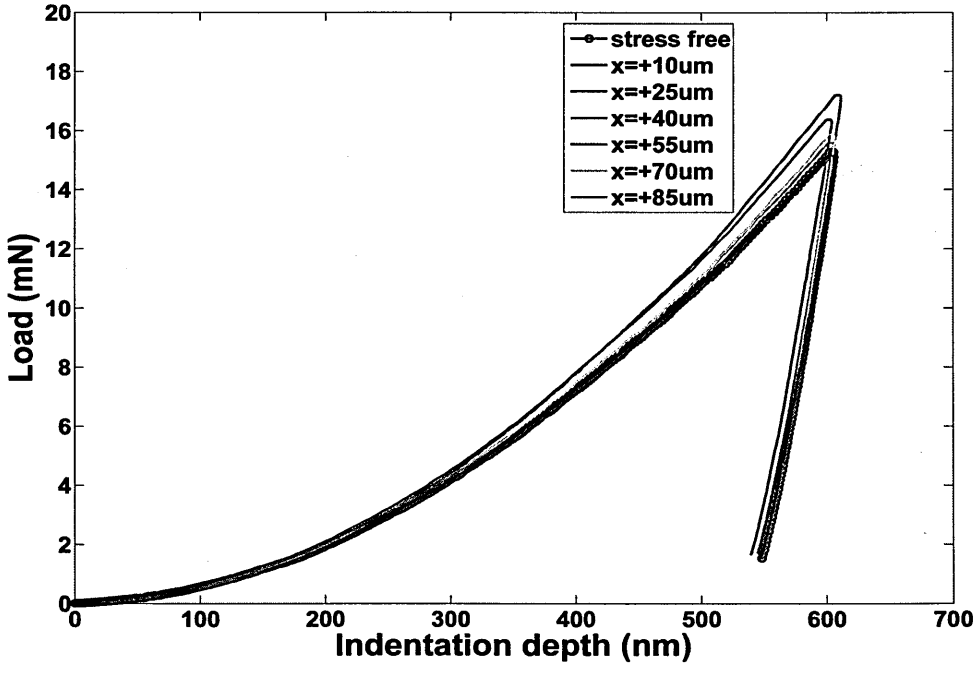

(a)

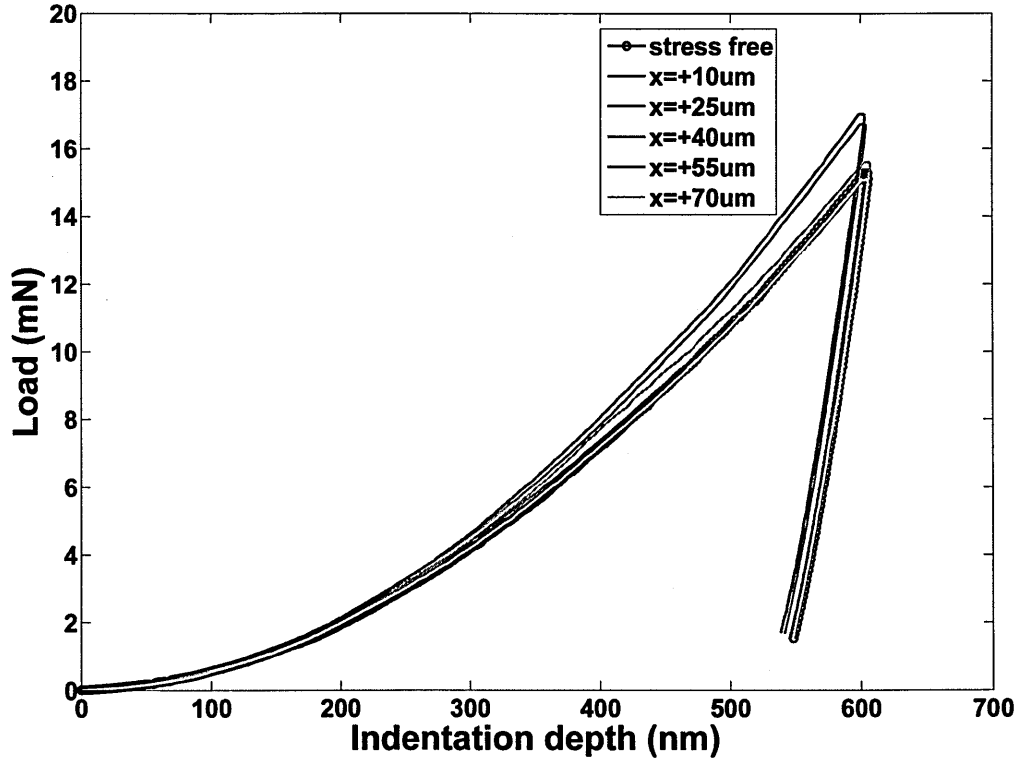

(b)

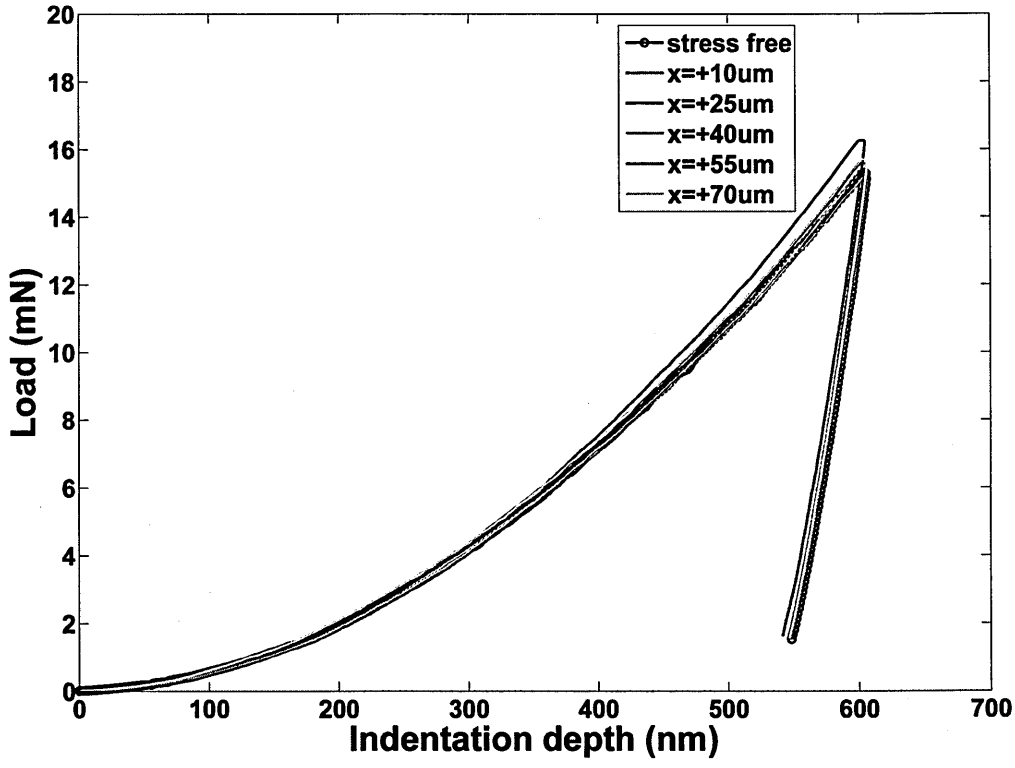

(c)

Fig. 8.4 - Nanoindentation load-displacement curve for sample 3 at (a) y=0 (b) y=+15 μm and (c) y=-15 μm

8.3.4 Sample 4 (125 μm deep scribe from tool D)

Fig.8.5 shows nanoindentation load-displacement curves obtained for sample 4 at y=0, +15 μm and -15 μm. It can be seen from the loading curves at y=0 that there are tensile stresses present below the scribe root. However, this response was not apparent for indentations at y=+15 μm and -15 μm. From FWHM and hardness maps from nanoindentation, no evidence of work hardening was obtained for this scribe. This indicated that there are tensile stresses present just below the root, and these stresses are very local, having decayed at y=+15 μm and -15 μm.

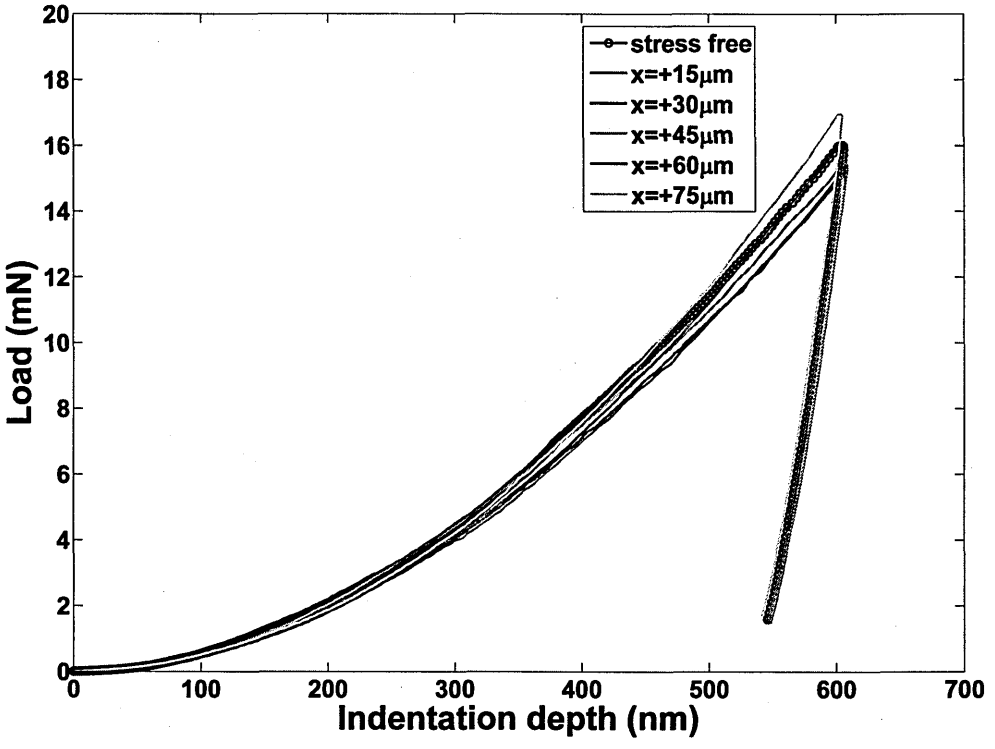
stress free
x=+15μm
x=+30μm
x=+45μm
x=+60μm
x=+75μm
Load (mN)
Indentation depth (nm)
0
2
4
6
8
10
12
14
16
18
20
0
100
200
300
400
500
600
700

(a)

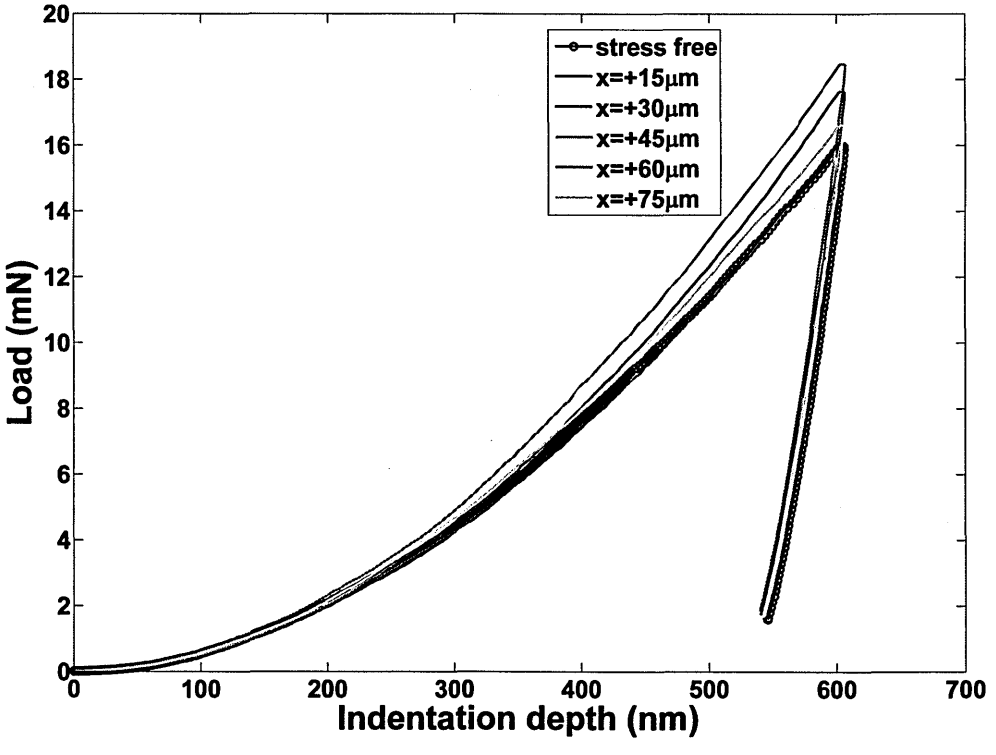
stress free
x=+15μm
x=+30μm
x=+45μm
x=+60μm
x=+75μm
Load (mN)
Indentation depth (nm)
0
2
4
6
8
10
12
14
16
18
20
0
100
200
300
400
500
600
700

(b)

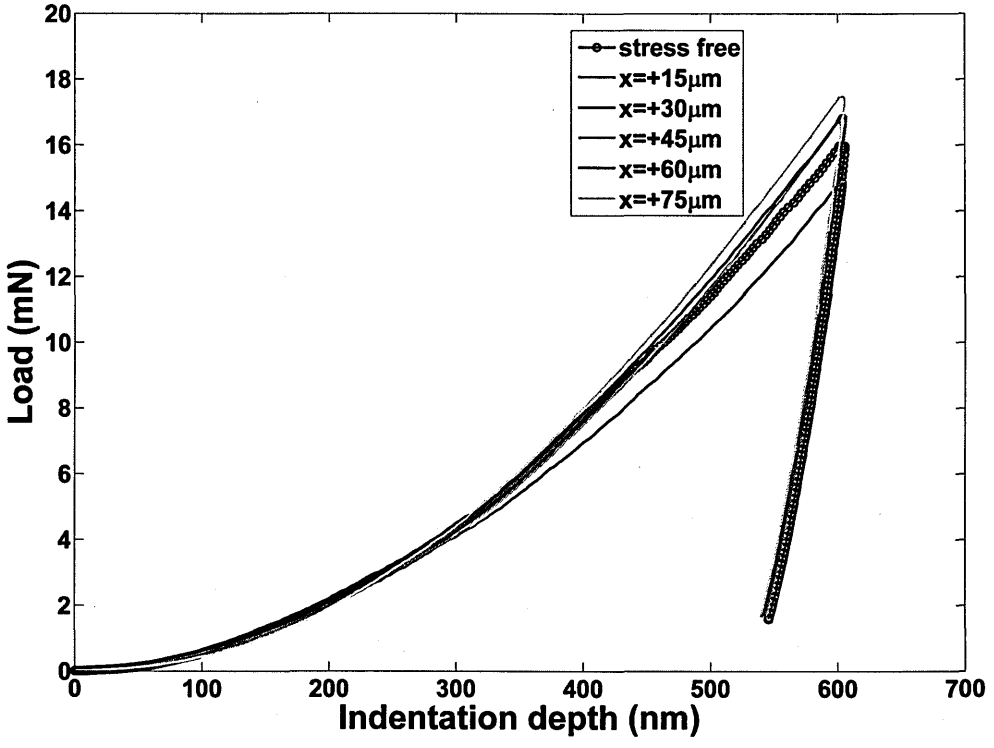

(c)

Fig. 8.5 - Nanoindentation load-displacement curve for sample 4 at (a) y=0 (b) y=+15 μm and (c) y=-15 μm

8.4 Determination of Residual Stresses from Load-displacement Curve

8.4.1 The Method

There are some methods which can be used to extract residual stresses from load-displacement curves [6-10] however, these methods were developed with finite element studies for ideal materials and to date no such study has been carried out on real engineering alloys like aluminium. Engineering alloys may show pile-up even at small loads of indentation [1-3] and the behaviour of the pile-up changes with the type and magnitude of the residual stress state. Another problem with engineering alloys like Al 2024-T351 is texture, in which grains of different orientation exhibit anisotropy in mechanical properties. In addition during scribing, hard plastically deformed material deposits around scribe root for 'ploughing' kind of scribes for which maximum load of indentation P_{max} does not show linearity with the residual stresses as was observed in chapter 6.

Most importantly there is a hard plastically deformed region present around scribe root (especially tool A scribes). Whenever indents are made in this region the loading curve moves up and the maximum load of indentation increases. The unloading curve moves towards the loading curve and the plastic work decreases which results in a decrease in W_p/W_t. This decrease in W_p/W_t is a convoluted response of the elastic residual stresses and plastic deformation of the material. Because the actual increase in hardness due to plastic deformation is unknown, and will vary with position around the scribe, (some increase in hardness has been balanced by tensile residual stresses around scribe root), hence one can never know that what proportion of the shift in W_p/W_t is due to hardness. As discussed in chapter 4, this plastically deformed region diminishes with distance from the scribe root. This indicates that there will not be a constant change in hardness (or W_p/W_t) around the scribe root and it will vary with position.

In chapter 6 it was discussed that the true area of contact A_c' can be related to W_p/W_t as given below;

$$\frac{A_c'}{A_c} = a\frac{W_p}{W_t} + b \tag{8.1}$$

And once A_c' is known then residual stress can be obtained from the relation,

$$\frac{\sigma_r}{\sigma_Y} = a\frac{A_c'}{A_c} + b \tag{8.2}$$

So for scribes with work hardening around root, eq. (8.1) can be written as;

$$\frac{A_c'}{A_c} = a(\frac{W_p}{W_t} + \text{hardening}) + b \tag{8.3}$$

Here in this study a correction factor ϕ is introduced which will account for the effect of hardening. So eq. (8.3) can be written in simplified form as;

$$\frac{A_c'}{A_c} = \text{a}\frac{W_p}{W_t} + \text{b} + \phi \tag{8.4}$$

Where $\phi = a \times hardening$ is a correction factor which tries to separate work hardening from the response of residual stresses on area contact ratio. It is a number which depends upon the work hardening induced by the tool which produced the scribes. In this study ϕ is higher for tool A scribes as it generates more work hardening and it is very low for tool B which does not generate any work hardening around the scribes.

Choosing a value of ϕ is a very challenging problem. The actual increase in hardness at any point around the scribe root cannot be separated from the effect of tensile residual stresses. Additionally the increase in hardness varies with position around the scribe root and hence a single value for the correction factor can not be defined.

To observe the effectiveness of the model developed in chapter 6 it has been assumed here that the increase in hardness is only due to plastic deformation, and that the hardening is uniform in a 50 μm region around the scribe root. For tool A the peak increase in hardness was 30% over the bulk hardness values. This increase in hardness decreased W_p/W_t by ~0.02. For tensile residual stress, the slope a was obtained as -20.4 so correction factor can be obtained as,

$$\phi = a \times hardening$$

$$\phi = -20.4 \times 0.02$$

$$\phi = -0.40 \qquad (8.5)$$

So for tool A, which generates work hardening the correction factor for peak hardness was -0.40 and for tool B and other tools which does not generate significant work hardening around scribe roots this factor was considered to be zero.

From table 6.1 which gives values of a and b, eq. 8.4 can be written as,

For tensile residual stresses;

$$\frac{A_c'}{A_c} = -20.4\frac{W_p}{W_t} + 19.64 + \phi \qquad (8.6)$$

For tool A and B, the correction factor ϕ was taken as -0.4 and 0 respectively and eq. (8.6) becomes;

$$\frac{A_c'}{A_c} = -20.4\frac{W_p}{W_t} + 19.24 \quad \text{(For Tool A)} \tag{8.7}$$

$$\frac{A_c'}{A_c} = -20.4\frac{W_p}{W_t} + 19.64 \quad \text{(For Tool B)} \tag{8.8}$$

For compressive residual stresses no correction factor was used and 8.4 remained the same;

$$\frac{A_c'}{A_c} = -13.62\frac{W_p}{W_t} + 13.76 \quad \text{(For Tool A and B)} \tag{8.9}$$

And then residual stress can be extracted based on the true contact area from the equations below, which have already been discussed in chapter 6.

For tensile residual stresses;

$$\frac{A_c'}{A_c} = -1.17 \times 10^9 \left(\frac{\sigma_r}{\sigma_Y} - 1.28\right) \tag{8.10}$$

For compressive residual stresses;

$$\frac{A_c'}{A_c} = -2.2 \times 10^9 \left(\frac{\sigma_r}{\sigma_Y} - 1.3\right) \tag{8.11}$$

Based on the fact that some measurements were carried out on aluminium alloy 5091, a similar exercise was carried out for aluminium alloy 5091 and new values of constants a and b were obtained. For relation between $\frac{A_c'}{A_c}$ and $\frac{W_p}{W_t}$, these values of a and b are given below.

a = -27.36, b=26.4 (For tensile residual stresses)

And

a = -12.09, b=12.54 (For compressive residual stresses)

The increase in hardness decreased W_p/W_t by ~0.02 for Al 5091. For tensile residual stress, the slope a was obtained as -27.36 and correction factor ϕ obtained was -0.5. The equations so obtained are given below;

For tensile residual stresses;

$$\frac{A_c'}{A_c} = -27.36\frac{W_p}{W_t} + 26.4 + \phi \qquad (8.12)$$

$$\frac{A_c'}{A_c} = -27.36\frac{W_p}{W_t} + 25.9 \qquad \text{(For Tool A)} \qquad (8.13)$$

$$\frac{A_c'}{A_c} = -27.36\frac{W_p}{W_t} + 26.4 \qquad \text{(For Tool B)} \qquad (8.14)$$

For compressive residual stresses;

$$\frac{A_c'}{A_c} = -12.09\frac{W_p}{W_t} + 12.54 \qquad \text{(For Tool A and B)} \qquad (8.15)$$

For relation between $\frac{A_c'}{A_c}$ and $\frac{\sigma_r}{\sigma_Y}$, these values of a and b are given below.

a = -0.57, b=1.41 (For tensile residual stresses)

And

a = -0.21, b=1.41 (For compressive residual stresses)

And then residual stress can be extracted based on true contact area from the equations below;

For tensile residual stresses;

$$\frac{A_c'}{A_c} = -0.82 \times 10^9 \left(\frac{\sigma_r}{\sigma_Y} - 1.41\right) \qquad (8.14)$$

For tensile residual stresses;

$$\frac{A_c'}{A_c} = -2.23 \times 10^9 \left(\frac{\sigma_r}{\sigma_Y} - 1.41\right) \qquad (8.15)$$

Equations (8.7) to (8.11) were used to extract residual stress for scribes in Al 2024-T351 and (8.12) to (8.15) were used for aluminium alloy 5091.

8.4.2 Assumptions and Limitations

A number of assumptions were made for the extraction of residual stresses from the load-displacement curves:

1- The set of equations discussed above is based on the response to equibiaxial residual stresses; however, it is already known that the tensile residual stress field obtained around scribe root is not equibiaxial as shown in chapter 7.

2- The equations were derived from finite element modelling results in which tip bluntness effect were not considered.

3- Al 2024-T351 is an anisotropic material which has weak texture. It was assumed that the response of the load-displacement curve is only affected by residual stresses and no effect of grain orientation was considered.

4- It has been assumed that the change in hardness obtained for the deformed material around the scribe root is entirely due to the plastic deformation.

5- It has been assumed that there is no variation in hardness beyond 50 μm around scribe root.

As discussed in section 8.1, formation of a scribe results in a complex interaction of elastic residual stress field and plastic deformation of the material which does not allow nanoindentation to extract the true change in hardness around scribe root. Hence the method used to deal with increase in hardness with the help of ratio of work of indentation in section 8.4.1 will provide qualitative data at best but quantitatively it can not provide the uncertainty in stress values due to the assumption about the hardness increase around the scribe root.

The sensitivity of the nanoindentation load-displacement curves and the extraction of the residual stress based on these curves are dependent upon the response of the material. As

discussed in chapter 3, Al 2024-T351 is a textured material and has anisotropy from grain to grain. There is some difference in terms of the hardness of grains and some grains due to this higher hardness required more load to penetrate up to the same depth of 600nm. Whenever a region of low residual stress (<50MPa) is indented in Al 2024-T351, different load-displacement curves are obtained due to the different response of different grains as shown in Fig.8.6 (a). When indents are made in a region with high residual stresses (>50MPa), the load-displacement curves show a definite response of the residual stresses (Fig.8.6 (b)) and the scatter between indentations decreases markedly.

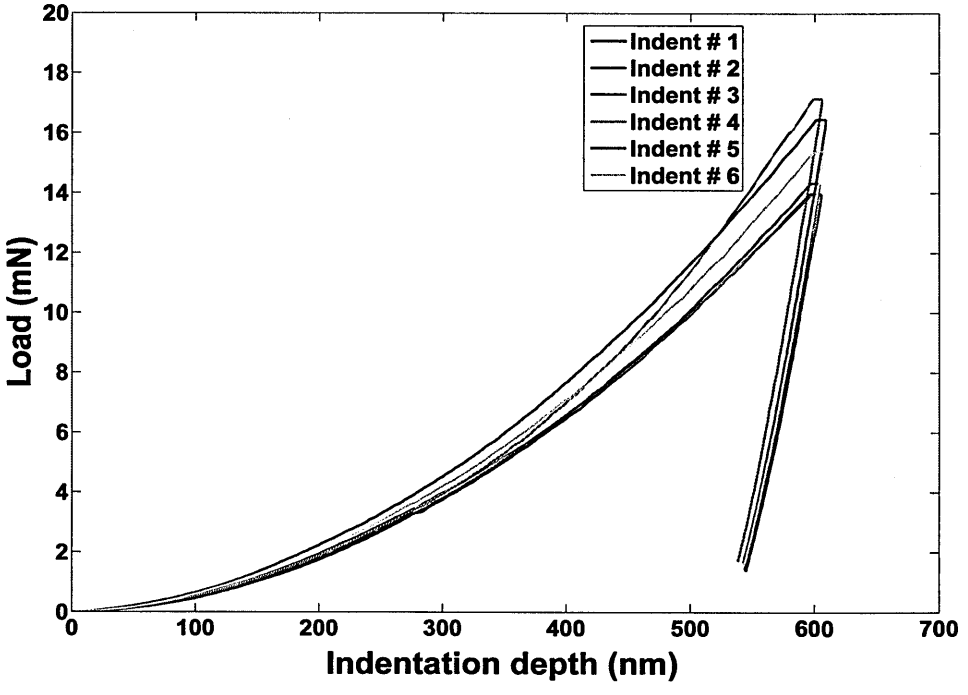

(a)

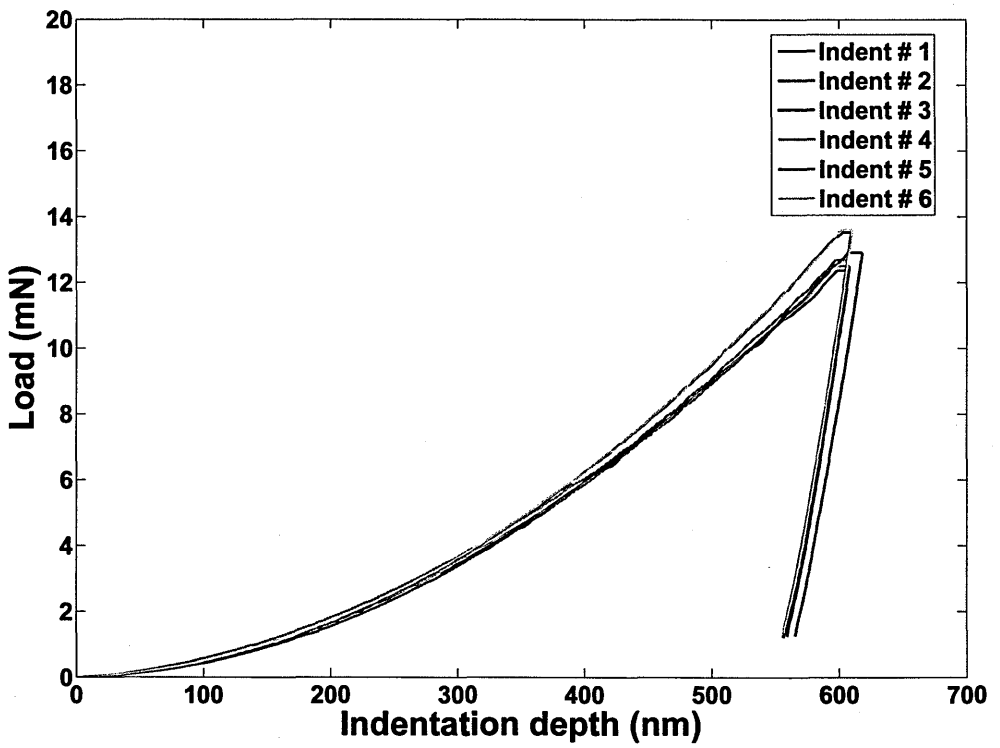

(b)

Fig. 8.6 - Nanoindentation load-displacement curve (a) For the region of +30MPa residual stress (b) For the region of +100MPa residual stress.

So if the model is applied on a region of no or low residual stresses (<50MPa), the extracted values of residual stresses can be expressed to give high scatter in the data (Fig.8.7 (a)). However, when the same model is applied on the load-displacement curves for the region of the higher stresses, less scattered data is obtained for the residual stresses (Fig.8.7 (b)).

So high scatter in the residual stress values extracted from the model can be attributed partly to zero or low residual stress. Unfortunately, the peak residual stresses around scribe marks are of the order of +100-200MPa in a very small region near the root of the scribe and start to decrease away from the scribe root very quickly. Hence it is expected that the near scribe root regions are ideal for extraction of residual stresses from the model and far from the scribe root, more scatter in the data will be obtained as a consequence of this effect.

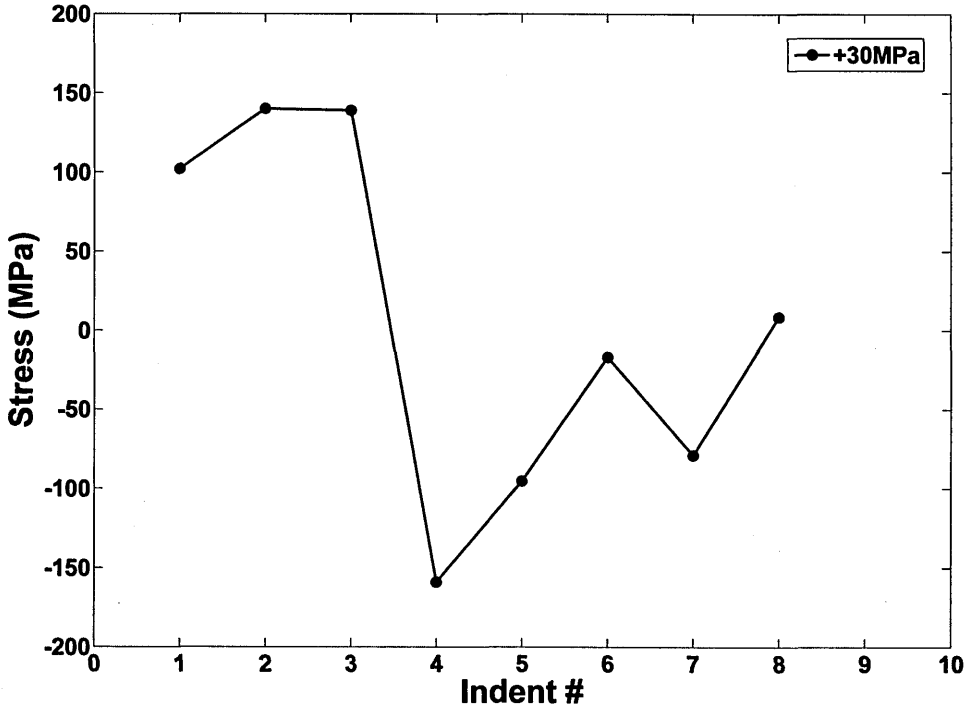

(a)

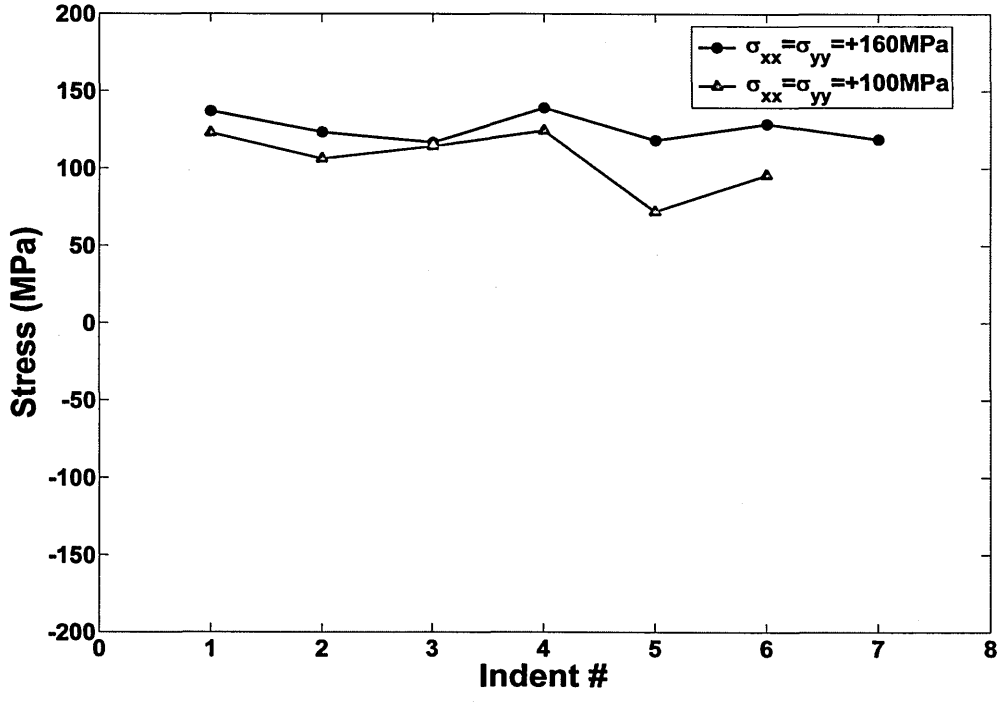

(b)

Fig. 8.7 – Residual stress values obtained from model (a) For the region of +30MPa (b) For the region of +160MPa and +100MPa.

Based on these assumptions and limitations, scribe marks in aluminium alloys 2024-T351 and 5091 were indented from nanoindentation at different y-locations in +x-direction up to 150 μm and eq. 8.7 to 8.15 were used to extract residual stresses from load-displacement data.

8.4.3 Application on Scribes

8.4.3.1 Sample 1 to 4 (used in Synchrotron measurements)

Initially four samples for which the data from synchrotron X-rays was known were nanoindentation tested. The synchrotron X-ray diffraction results were an average over the gauge volume and the nanoindentation extraction was for very localized regions, so to compare the results of synchrotron X-ray diffraction, the average value of residual stress up to +50 μm was calculated. Table 8.1 shows a comparison of residual stresses obtained from synchrotron X-ray diffraction and nanoindentation for sample 1 and 2 for which stress analysis was carried out in chapter 7. For sample 1 produced with tool A, stresses were calculated with and without the correction factor. It can be seen that with correction factor, nanoindentation extracted residual stress values were in close agreement with the synchrotron results while without correction compressive residual stresses were found. For sample 2 produced with tool B, no correction was necessary, and residual stresses were found in fair agreement with the synchrotron X-ray diffraction results.

Sample #	**Tool**	**Depth *d* (μm)**	**Residual Stress (MPa)**		
			Synchrotron X-rays (σ_{yy})	**Nanoindentation**	
				Without Correction	**With Correction**
1	A	125	+180	-247	+163
2	B	125	+100	+77	Not applied

Table 8.1 - Comparison of residual stress results from Synchrotron X-rays diffraction and Nanoindentation.

For sample 3 and 4 only one component of the strain was measured from synchrotron X-rays diffraction hence comparison was not possible. From nanoindentation method average tensile stress of +210MPa and +180MPa was found sample 3 and 4 respectively.

8.5 Extraction of Residual Stresses on Additional Scribes

Since the magnitude of the biaxial residual stresses calculated from nanoindentation are similar to the σ_{yy} obtained from synchrotron X-rays diffraction, further scribe marks of different depths and root radius were produced in Al 2024-T351. Because for these scribes synchrotron data was not available for validation, to ensure reproducibility of results for every scribe indentation was carried out for three samples and extraction of residual stress was applied every time. Furthermore, scribes of same depth and root radius were produced in aluminium alloy 5091 to ensure confidence on accuracy of the results.

In total 10 scribes of different depths with $5\,\mu m$ root radius were produced from tool A and B in aluminium alloy 2024-T351 and 5091. Details of these samples are given in Table 8.2. Similarly five scribes of different depths with $25\,\mu m$ and $50\,\mu m$ root radii were produced and details of these samples are given in Table 8.3. A further 10 scribes were extracted from fatigued samples which will be discussed later in this chapter. Indentations were made at $y = 0$ for every scribe with a similar procedure as discussed earlier.

Sample #	Material	Tool	Depth d (μm)	Root radius ρ (μm)	d/ρ
5	Al 2024-T351	A	50	5	10
6	Al 2024-T351	A	75	5	15
7	Al 2024-T351	A	100	5	20
8	AA 5091	A	50	5	10
9	AA 5091	A	100	5	20
10	Al 2024-T351	B	50	5	10
11	Al 2024-T351	B	100	5	20
12	Al 2024-T351	B	150	5	30
13	AA 5091	B	50	5	10
14	AA 5091	B	100	5	20

Table 8.2 - Scribe marks of 5 μm root radius used in measurements.

Sample #	Material	Tool	Depth d (μm)	Root radius ρ (μm)	d/ρ
15	Al 2024-T351	C	100	25	4
16	Al 2024-T351	C	110	25	4.4
17	Al 2024-T351	D	15	50	0.3
18	Al 2024-T351	D	50	50	1
19	Al 2024-T351	D	100	50	0.5

Table 8.3 - Scribe marks of 25 μm & 50 μm root radius used in measurements.

8.5.1 Scribes from Tool A and B (5 μm Root Radius)

Nanoindentation method was applied to scribe marks of 5 μm produced from tool A and B and results are shown in Table 8.4. These results showed that there were tensile residual

stresses around all scribe marks generated from tool A. The peak tensile residual stresses were in the range of +154 to +210MPa for tool A which compares to +200MPa from synchrotron X-rays diffraction. For tool B, residual stresses the peak stresses were less than tool A scribes. Peak tensile stresses fell in the range of +67 to +120MPa which compares to +100MPa from synchrotron X-rays diffraction. Despite of the assumptions made for the model, the results from the nanoindentation method found similar with synchrotron X-rays.

Sample #	Tool	Depth *d* (μm)	Residual Stress (MPa)	Average Stress (MPa)
5	A	50	+154	+172
6	A	75	+160	
7	A	100	+210	
8	A	50	+155	
9	A	100	+205	
10	B	50	+120	+81
11	B	100	+71	
12	B	150	+67	
13	B	50	+75	
14	B	100	+73	

Table 8.4 - Residual stress in Al 2024-T351 from nanoindentation for 5 μm root radius scribes from different tools.

Fig.8.8 shows residual stresses obtained for scribes produced from tools A and B and it can be seen there was a significant difference in the magnitude of residual stresses from both tools. Tool A showed higher residual stresses, and in agreement from synchrotron results

discussed in chapter 7, the peak tensile stress for tool A were almost twice as compared to tool B scribes. This difference in peak tensile stresses is understandable as tools A and B were very different in the production of scribes, ploughing and cutting the material respectively. These two different mechanisms of removing the material induce different amounts of residual stresses around the scribe root.

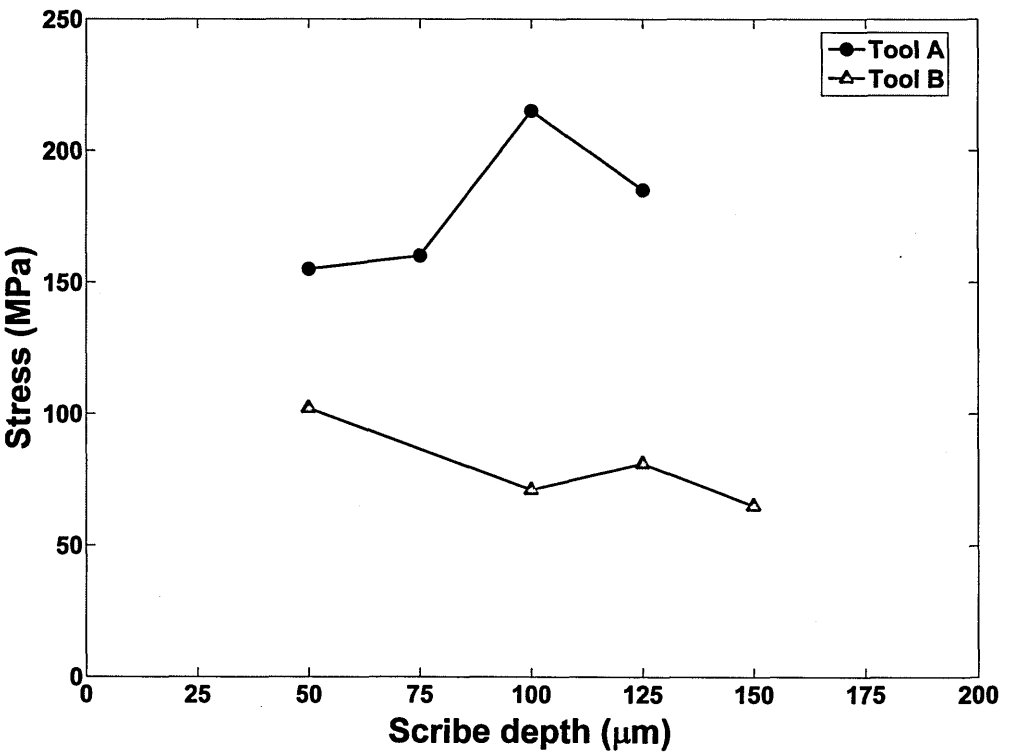

Fig. 8.8 - Residual stress values for scribes of different depths from tool A and B

8.5.2 Scribes from Tool C and D (25 and 50 μm Root Radius)

Residual stress values obtained for scribes produced from tool C and D are given in Table 8.5 and Fig.8.9 shows residual stress obtained for tool D for different depths of scribes. The average tensile stress was found as ~+110MPa for tool C and ~+80MPa for tool D.

Sample #	Tool	Depth d (μm)	Root radius ρ (μm)	Residual Stress (MPa)	Average stress (MPa)
15	C	100	25	+90	+109
16	C	110	25	+127	
17	D	15	50	+72	+78
18	D	50	50	+56	
19	D	100	50	+106	

Table 8.5 - Residual stress results from nanoindentation for 25 μm and 50 μm root radius scribes.

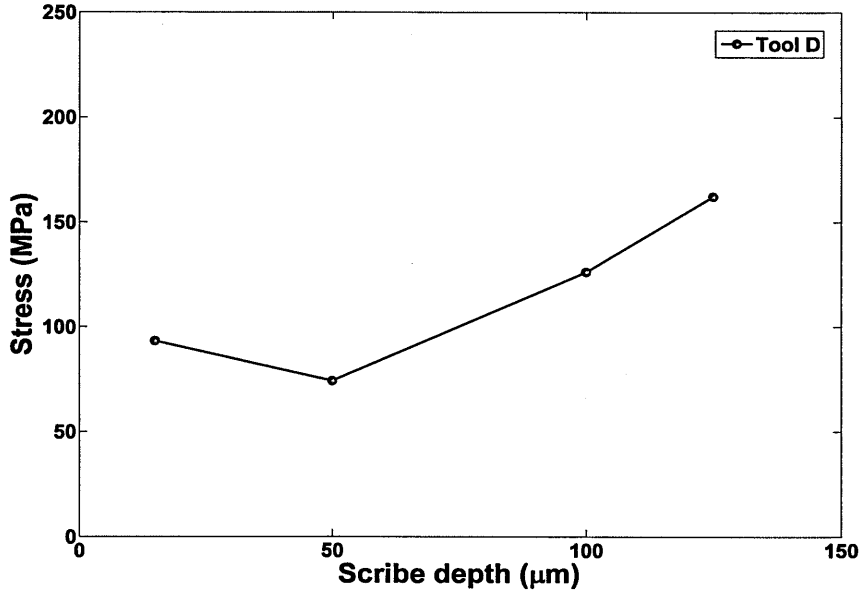

Fig. 8.9 - Residual stress values for scribes of 50 μm root radius from tool D

It can be seen that due to the same 'cutting' mechanism of tool C & D as tool B, same level of residual stress was obtained as for tool B. It can be seen that from Table 8.5 tensile stresses of +90 to +127MPa for tool C and +56 to +106MPa for tool D were obtained.

8.6 Effect of Fatigue on Residual Stress

It has been discussed that residual stress around scribe marks may reach up to +200MPa which can help cracks to initiate from scribes and further aid in propagation of these cracks under fatigue loading. But knowledge of the initial residual stress distribution induced by scribing is not sufficient to evaluate the driving force for a crack under fatigue loading [15]. The magnitude and rate of relaxation of the residual stresses after fatigue cycles strongly depends upon on the applied loading.

To assess the role of residual stresses on scribes to propagate a crack in fatigue, some scribes were tested which had already been loaded in fatigue. Only scribes of 5 μm root radius were tested as it was assumed that there would be the same behaviour of relaxation of residual stresses with different root radii.

In total 10 samples were tested in different conditions of fatigue with eight in four point bending and two in tension without being taken to failure to preserve scribes for nanoindentation testing. The fatigue conditions were the same as used in chapter 4 when local hardness around fatigued scribe marks was discussed. Table 8.6 shows details of the samples used in fatigue and subsequently nanoindentation testing.

Sample #	Tool	Depth d (μm)	Fatigue Mode	Fatigue cycles
20	A	50	FPB	250,000
21	A	50	FPB	500,000
22	A	50	FPB	1,250,000
23	A	75	FPB	500,000
24	A	100	FPB	250,000
25	A	100	FPB	500,000
26	B	100	FPB	100,000
27	B	100	FPB	200,000
28	A	50	Tension	107,000
29	A	100	Tension	414,000

Table 8.6 - Details of the samples tested in fatigue

8.6.1 Scribes from Tool A and B (5 μm Root Radius)

Residual stress values obtained for scribes from tool A and B after fatigue testing is given in Table 8.7. These results revealed that for all scribes, in general, there was no relaxation of residual stresses after fatigue cycles.

Sample #	Depth *d* (μm)	Tool	Fatigue Mode	Fatigue cycles	Residual Stress (MPa)	
					Before fatigue	After fatigue
20	50	A	FPB	250000	+154	+163
21	50	A	FPB	500000	+154	+178
22	50	A	FPB	125000	+154	+153
23	75	A	FPB	500000	+160	+134
24	100	A	FPB	250000	+210	+194
25	100	A	FPB	500000	+210	+188
26	100	B	FPB	100000	+71	+82
27	100	B	FPB	200000	+71	+93
28	50	A	Tension	107000	+154	+175
29	100	A	Tension	414000	+210	+186

Table 8.7 – Residual stresses obtained from nanoindentation after different fatigue cycles

8.7 Conclusions

This chapter presents application of a technique developed for extraction of residual stresses using nanoindentation. In total 29 scribes of different depths and root radius produced from different tools were tested and their residual stress field were reported.

It was found that tool A scribes were difficult to measure due to the plastic deformation around the scribe root. To separate the response of work hardening from residual stress a correction factor was introduced which gave the similar stress values in magnitude as found with the highest component of the stress obtained from the synchrotron X-rays diffraction. For tool B due to the absence of work hardening no amendment in the developed method was required. The residual stress was independent of depth and root radius of the scribe and was found to be tensile for every scribe. Depending upon the tool

and root radius, residual stresses were different in magnitude and were found in the range of +100MPa to +200MPa.

The effect of fatigue loading on relaxation of pre-existing residual stresses was studied. Two different modes of fatigue loading included four point bending and tension-tension were used. It was found that there was no significant effect of fatigue loading on the scribes.

It was concluded that fatigue life of these scribes should be examined with consideration of residual stresses which were +200MPa to +100MPa depending upon the tool. Any crack initiation and propagation model without supplementation of residual stress fields may predict more conservative lives in fatigue.

8.8 References

[1] Bolshakov, A. and G. M. Pharr. Influences of pileup on the measurement of mechanical properties by load and depth sensing indentation techniques. Journal of Materials Research 13(4), 1998, pp 1049-1058.

[2] Taljat, B. and G. M. Pharr. Development of pile-up during spherical indentation of elastic-plastic solids. International Journal of Solids and Structures 41(14), 2004, pp 3891-3904.

[3] Khan, M. K., S. V. Hainsworth, M. E. Fitzpatrick and L. Edwards. Application of the work of indentation approach for the characterization of aluminium 2024-T351 and Al cladding by nanoindentation. Journal of Materials Science 44(4), 2009, pp 1006-1015.

[4] Tsui, T. Y., W. C. Oliver and G. M. Pharr. Influences of stress on the measurement of mechanical properties using nanoindentation. Experimental studies in an aluminium alloy. Journal of Materials Research 11(3), 1996, pp 752-759.

[5] Swadener, J. G., B. Taljat and G. M. Pharr. Measurement of residual stress by load and depth sensing indentation with spherical indenters. Journal of Materials Research 16(7), 2001, pp 2091-2102.

[6] Suresh, S. and A. E. Giannakopoulos. A new method for estimating residual stresses by instrumented sharp indentation. Acta Materialia 46(16), 1998, pp 5755-5767.

[7] Lee, Y. H., W. J. Ji and D. Kwon. Stress measurement of SS400 steel beam using the continuous indentation technique. Experimental Mechanics 44(1), 2004, pp 55-61.

[8] Lee, Y. H. and D. Kwon. Measurement of residual-
stress effect by nanoindentation on elastically strained (100) W. Scripta Materialia 49(5), 2003, pp 459-465.

[9] Lee, Y. H. and D. Kwon. Estimation of biaxial surface stress by instrumented indentation with sharp indenters. Acta Materialia 52(6), 2004, pp 1555-1563.

[10] Carlsson, S. and P. L. Larsson. On the determination of residual stress and strain fields by sharp indentation testing. Part I: Theoretical and numerical analysis. Acta Materialia 49(12), 2001, pp 2179-2191.

[11] Xu, Z. H. and X. Li. Estimation of residual stresses from elastic recovery of nanoindentation. Philosophical Magazine 86(19), 2006, pp 2835-2846.

[12] Xu, Z. H. and X. D. Li. Influence of equi-biaxial residual stress on unloading behaviour of nanoindentation. Acta Materialia 53(7), 2005, pp 1913-1919.

[13] Zhao, M. H., X. Chen, J. Yan and A. M. Karlsson, Determination of uniaxial residual stress and mechanical properties by instrumented indentation. Acta Materialia 54(10), 2006, pp 2823-2832.

[14] Khan, M. K., M.E. Fitzpatrick., S. V. Hainsworth and L. Edwards. Effect of tool profile and fatigue loading on the local hardness around scratches in clad and unclad aluminium alloy 2024. Materials Science & Engineering A, Volume 527, Issues 1-2, 2009, pp 297-304.

[15] Boyce, B. L., X. Chen, J. W. Hutchinson and R. O. Ritchie. The residual stress state due to a spherical hard-body impact. Mechanics of Materials 33(8), 2001, pp 441-454.

Chapter 9: Overall Conclusions and Suggestions for Future Work

9.1 Conclusions

The overall aim of the project was to investigate the residual stress fields around scribes of different geometries produced from different tools. It was a challenging task in consideration of the very small and local residual stress fields for scribe marks. Synchrotron X-ray diffraction has been used to measure residual stress fields on a model aluminium alloy 5091 and the aerospace alloy 2024-T351. Four samples with scribe marks of different depths and root radii were investigated. The nanoindentation technique has also been used to extract the residual stresses from the load-displacement data and it was found that results from the two methods were in excellent agreement with each other.

- Work in the initial part of the thesis showed that nanoindentation load-displacement curves can be used to extract the true hardness of soft materials like aluminium alloys. Pile-up is an important issue which not only develops in stress-free conditions but changes with the state of residual stresses. To extract hardness from load-displacement data, the work of indentation technique gives best estimation.
- Wear around scribe marks have been investigated with scanning electron microscopy. It was revealed that the two tools A and B used to create the scribe marks of 5 μm root radius produced 'ploughed' and 'cut' scribes respectively. Due to this difference in the type of the scribes, different levels of plastic deformation were obtained. Scribes of 25 and 50 μm root radius were investigated as well and was found to produce 'cut' scribes.
- Finite element simulations have been carried out to model load-displacement curves. Forward and reverse analysis techniques were used to compare with experimental results of nanoindentation. Excellent agreement was obtained

between experimental and simulated nanoindentation properties. Pile-up characterization was performed and it was found that the true area of contact can be calculated with simulations.

- Finite element simulations have been carried out to study the effect of residual stresses on nanoindentation properties of Al-cladding and Al 2024-T351. It has been found that nanoindentation properties including maximum load of indentation, curvature of the loading curve, elastically recovered depth, final depth, work of indentation and area of contacts were affected by the presence of residual stresses. Pile-up height and area of contact showed a non-linear behaviour with residual stresses in compression and tension. For experimental indentation, where measurement of the true area of contact included the pile-up was difficult, the area of contact has been extracted from its relation with W_p/W_t. Once the true area of contact was known then residual stress has been calculated based on relations described.
- Strain and stress fields around scribes of different geometries produced by the different tools in aluminium alloys have been measured with the synchrotron X-ray diffraction. It has been found that the residual stress fields around scribes are dependent upon the tool by which they were produced. It was concluded that tool A produces a severe tensile stress field and work hardening around the root of the scribe as compared to tool B. The magnitude and extent of the stress field produced by tool A was twice that of tool B. With an increase in root radius of the scribe, this residual stress field vanishes and no effect of work hardening was obtained.
- A nanoindentation method for the extraction of residual stresses around the scribe marks has been developed. In total 29 scribes of different depths and root radii produced from different tools were tested with nanoindentation and their residual stress fields have been reported. It was found that tool A scribes were difficult to

measure due to the plastic deformation around the scribe root. To separate the response of work hardening from residual stress a correction factor was used. For tool B due to the absence of work hardening no amendment in the method was required. The form of the residual stress was independent of depth and root radius of the scribe and was found to be tensile for every scribe. Depending upon the tool and root radius, residual stresses were different in magnitudes and found to be in the range of +100 to +200MPa.

- The effect of fatigue loading on relaxation of pre-existing residual stresses was studied. Two different modes of fatigue loading, four point bending and tension-tension, were used. It was found that there was no significant effect of fatigue loading due to the scribes from any tool. It was concluded that the fatigue life of these scribes should be examined with consideration of residual stresses. These residual stresses depend upon the tool which produced the scribe along with the root radius and depth of the scribe. Any crack initiation and propagation model without inclusion of residual stress fields may predict very conservative lives in fatigue.

9.2 Future Work

Although this study has provided in-depth knowledge of scribes of different geometries and detailed method of extraction of residual stresses from nanoindentation load-displacement data, yet some issues need to be studied further.

A PhD project [1] is currently underway at Cranfield University to provide detailed information on the influence of different scratch geometries on the initiation and growth of fatigue cracks from scratches in clad 2024-T351 aluminium alloy. It is very important to use calculated residual stresses from this study in to the developed model of fatigue lives prediction from scratches and scribes in Cranfield project. This will reveal the role of residual stresses in initiation and propagation of fatigue cracks from these scratches and

scribes. It is highly expected that addition of the results for residual stresses would enable a comprehensive model of the structural integrity of scribe or scratch defects to be developed as cracks.

Although a significant number of scribes were investigated in this study with synchrotron X-ray diffraction and nanoindentation, no scribes in clad Al 2024-T351 have been studied. Due to the large grain size (~70-100 μm) of the cladding, the synchrotron X-ray diffraction method can not be applied, and additionally, presence of cladding in very thin form (~100 μm) makes it difficult to analyse with nanoindentation. On the cross-section of samples, the effect of the substrate started to appear after 10% of the thickness of the cladding from the top surface. It would be very useful to study the scribe marks in cladding with some other technique e.g. Raman spectroscopy.

The incapability of experimental rigs to induce artificial stresses in a wide range necessitated the study of the effects of residual stresses on the nanoindentation response from finite element modelling. Finite element studies were carried out for equi-biaxial stresses so an improved design of experimental rig would provide an opportunity to explore the non-equibiaxial stress response of material more thoroughly.

9.3 References

[1] Cini, A. Scribe Marks at Fuselage Joints- Initiation and propagation of cracks from mechanical defects in aluminium alloys. PhD Thesis, Cranfield University, 2009.